QUANTUM PLASMONIC EFFECTS OF DOUBLE RAMAN SYSTEMS

LOH WAI MING

FACULTY OF SCIENCE
UNIVERSITY OF MALAYA
KUALA LUMPUR

2017

QUANTUM PLASMONIC EFFECTS OF DOUBLE RAMAN SYSTEMS

LOH WAI MING

THESIS SUBMITTED IN FULFILMENT OF THE REQUIREMENTS FOR THE DEGREE OF DOCTOR OF PHILOSOPHY

DEPARTMENT OF PHYSICS
FACULTY OF SCIENCE
UNIVERSITY OF MALAYA
KUALA LUMPUR

2017

UNIVERSITY OF MALAYA

ORIGINAL LITERARY WORK DECLARATION

Name of Candidate: **LOH WAI MING**

Matric No: **SHC160024**

Name of Degree: **DOCTOR OF PHILOSOPHY**

Title of Project Paper/Research Report/Dissertation/Thesis ("this Work"):

QUANTUM PLASMONIC EFFECTS OF DOUBLE RAMAN SYSTEMS

Field of Study:

THEORETICAL PHYSICS

I do solemnly and sincerely declare that:

(1) I am the sole author/writer of this Work;
(2) This Work is original;
(3) Any use of any work in which copyright exists was done by way of fair dealing and for permitted purposes and any excerpt or extract from, or reference to or reproduction of any copyright work has been disclosed expressly and sufficiently and the title of the Work and its authorship have been acknowledged in this Work;
(4) I do not have any actual knowledge nor do I ought reasonably to know that the making of this work constitutes an infringement of any copyright work;
(5) I hereby assign all and every rights in the copyright to this Work to the University of Malaya ("UM"), who henceforth shall be owner of the copyright in this Work and that any reproduction or use in any form or by any means whatsoever is prohibited without the written consent of UM having been first had and obtained;
(6) I am fully aware that if in the course of making this Work I have infringed any copyright whether intentionally or otherwise, I may be subject to legal action or any other action as may be determined by UM.

Candidate's Signature Date:

Subscribed and solemnly declared before,

Witness's Signature Date:

Name:

Designation:

ABSTRACT

An analytical theory to study the optical properties of a hybrid nanostructure comprising of a metallic nanoparticle (MP) in close proximity with a quantum system (QS) in double Raman configuration is presented. In particular, the spectra of the quantum fields emitted by the system is computed to gain insights into the plasmonic effects caused by the nearby MP. Using Heisenberg-Langevin formalism, the quantum spectra of the Stokes and anti-Stokes fields emitted by a mesoscopic spherical particle (which consists of quantum particles in double Raman scheme) without the presence of a nearby MP is first computed. The dependence of the spectra on the particle size, laser configuration and angle of observation is then analyzed and studied. It is found that the mesoscopic nature of the microparticle hides or modifies the spectral peaks originally formed due to quantum coherence and laser interaction effects. The analytical calculation is then extended to include the plasmonic effects from a nearby MP, where the MP-QS interaction is modelled using a semiclassical approach in which the MP is treated as a classical spherical dielectric particle while the QS is treated quantum-mechanically using Heisenberg-Langevin formalism. Spectra of the quantum fields emitted by the hybrid nanostructure exhibit cavity interference effect which manifests itself as oscillations across interparticle distances. Besides, Fano dip in the central peak of the spectra is observed at sufficiently weak laser fields strengths, indicating enhancement of the local Stokes and anti-Stokes fields to the extent that the quantum fields become comparable to or greater than the incident laser fields strengths. Also, the MP-QS coupling, which is affected by the size of the MP and the number density of the QS, changes the angular dependence of the spectra by breaking the angular rotational symmetry. In the presence of Surface Plasmon Resonance (SPR) the oscillatory dependence of the spectra on the interparticle distance and angles of

observation becomes even stronger due to the plasmonic enhancement effect. The study also includes the derivation of a general expression for the scattered electric field formula which takes into account the multipole effects and is valid for arbitrary size of the component particles as well as arbitrary observation distance. This expression is then applied to the study of MP-QS interaction with the aim of deriving a scattered field formula that is valid for any energy level configuration of the QS.

ABSTRAK

Suatu teori analitik telah dibentangkan untuk mengkaji ciri-ciri optik satu struktur nano hibrid yang terdiri daripada satu nanopartikel logam yang berdekatan dengan satu zarah kuantum dalam konfigurasi Raman ganda. Khususnya, spektrum medan-medan kuantum yang dipancarkan oleh sistem tersebut telah dikira untuk mendapatkan maklumat mengenai kesan plasmonik yang disebabkan oleh nanopartikel logam yang berhampiran. Dengan mengunakan formalisme Heisenberg-Langevin, spektrum kuantum medan Stokes dan anti-Stokes yang dipancarkan oleh satu zarah sfera mesoskopik (yang mengandungi zarah-zarah kuantum dalam skim Raman ganda) tanpa kehadiran nanopartikel logam yang berhampiran dikira terlebih dahulu. Seterusnya, pergantungan spektrum pada saiz zarah, konfigurasi laser dan sudut pemerhatian adalah dianalisa dan dikaji. Didapati bahawa sifat-sifat mesoskopik zarah sfera menyembunyikan atau mengubah puncak spektrum yang asalnya terbentuk kesan daripada kepaduan dan interaksi laser kuantum. Pengiraan analitik kemudiannya diperluaskan untuk merangkumi kesan plasmonik dari nanopartikel logam berhampiran, di mana interaksi nanopartikel logam-zarah kuantum dianalisa menggunakan pendekatan klasik separuh yang memerlukan nanopartikel logam dianggap sebagai zarah dielektrik sfera klasik manakala zarah kuantum dianalisa secara kuantum-mekanikal menggunakan formalisme Heisenberg-Langevin. Spektrum medan-medan kuantum yang dipancarkan oleh struktur nano hybrid itu menunjukkan kesan interferens rongga yang boleh dilihat sebagai ayunan yang bergantung pada jarak antara nanopartikel logam dan zarah kuantum. Selain itu, kejunaman Fano di puncak tengah spektrum juga diperhatikan apabila kekuatan medan laser input lemah. Ini menunjukkan peningkatan kekuatan medan Stokes dan anti-Stokes tempatan kesan daripada nanopartikel logam sehingga kekuatan medan-medan kuantum itu menjadi setanding dengan atau

lebih tinggi daripada kekuatan medan laser. Selain itu, interaksi nanopartikel logam-zarah kuantum yang bergantung pada saiz nanopartikel logam serta ketumpatan zarah kuantum mengubah pergantungan spektrum pada sudut permerhatian dengan memecahkan simetri putaran sudut. Dengan kehadiran resonans plasmon permukaan (SPR), ayunan spektrum yang bergantung pada jarak antara nanopartikel logam dan zarah kuantum serta sudut pemerhatian menjadi lebih kuat disebabkan kesan peningkatan medan plasmonik. Kajian ini juga merangkumi pencarian ungkapan umum bagi medan elektrik bertaburan yang mengambil kira kesan multipole dan sah bagi apa-apa nilai saiz zarah komponen serta jarak pemerhatian. Ungkapan ini kemudiannya digunakan untuk mengkaji interaksi nanopartikel logam-zarah kuantum dengan tujuan untuk memperoleh formula medan bertaburan yang sah untuk sebarang konfigurasi tahap tenaga zarah kuantum.

TABLE OF CONTENTS

LIST OF FIGURES

LIST OF TABLES

LIST OF SYMBOLS AND ABBREVIATIONS

Ag	:	Silver.
Au	:	Gold.
HHG	:	High Harmonic Generation.
HRTEM	:	High Resolution Transmission Electron Microscopy.
LSP	:	Localized Surface Plasmon.
LSPR	:	Localized Surface Plasmon Resonance.
MP	:	Metallic Nanoparticle.
QD	:	Quantum dot.
QS	:	Quantum System.
RHS	:	Right-hand side.
SEM	:	Scanning Electron Microscopy.
SPR	:	Surface Plasmon Resonance.
SQD	:	Semiconductor Quantum Dot.

CHAPTER 1: INTRODUCTION

1.1 Issues and Motivations

Humans have been for centuries fascinated by the interesting optical properties exhibited by Metallic Nanoparticles (MPs) which are dramatically different from those of either the corresponding bulk materials or the atomic and molecular systems. One of the oldest examples is the famous Lycurgus Cup from about 400 AD which is made of glass embedded with gold-silver bimetallic nanoparticles. Due to the nanoparticles' strong absorption of green light, this cup shows a striking red colour when light is shone into the cup and transmitted through the glass, while appears green when viewed in reflected light (Kumar, 2013). Other earlier examples include the red glasses of the late Bronze Age (1200-1000 BCE) from Frattesina di Rovigo, Italy which contains copper nanoparticles that cause the glasses to exhibit bright red colour (Angelini et al., 2004). While nanoparticles were usually used for colouring glasses during ancient times, today, they have brought about a revolution in physics, chemistry, material, biomedical and life sciences.

One of the areas in which MPs play a promising role is optoelectronics. Most of the current optoelectronic technologies necessitate the ability to control light phenomena for achieving various functionalities. Perpetual competition in size reduction of the optoelectronic components together with rapid advancement in nanotechnology have brought a tremendous amount of attention to the study and design of nanostructured devices capable of controlling light-matter interaction at the nanoscale (Novotny & Hecht, 2006). Metallic nanostructures such as MPs are ideally suited to this end due to their ability to enhance and confine optical fields beyond the classical diffraction limit. Such fascinating optical properties of the MP stem from the occurrence of non-propagating collective oscillations

of free electrons on its surface, known as Localized Surface Plasmons (LSPs) when coupled to the electromagnetic field. From theoretical point of view, these LSP modes arise naturally from the light scattering problem (Figure 1.1) of a small, subwavelength conductive nanoparticle in an electrostatic field. The curved surface of the nanoparticle exerts an effective restoring force on the driven conduction electrons, giving rise to Localized Surface Plasmon Resonances (LSPRs) which lead to field amplification both inside and in the near-field zone outside the nanostructure (Maier, 2007). The LSPR of the MP, which usually lies in the frequency range from the infrared to visible region of the electromagnetic spectrum are highly dependent on the geometric parameters of the MP such as its size and shape (Figure 1.2 (b)) as the oscillations of the free electrons are confined by the particle boundaries over finite nanoscale dimensions (Kumar, 2013). Other parameters that affect the LSPR frequency include the electronic properties of the constituent metal (Figure 1.3) as well as the dielectric properties of the surrounding medium.

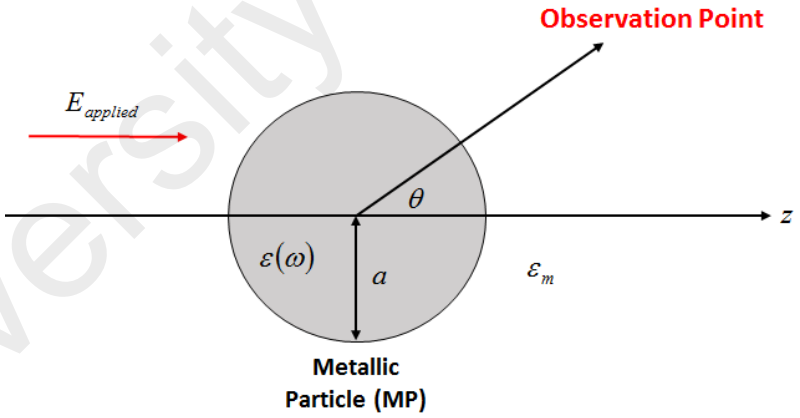

Figure 1.1: Schematic diagram of the scattering problem of a homogeneous metallic sphere placed into an electrostatic field. Here, a is the radius of the metallic sphere, $E_{applied}$ is the incident electrostatic field which is parallel to the $z-$axis while $\varepsilon(\omega)$ and ε_m represent the dielectric function of the homogeneous sphere and permitivity of the surrounding medium, respectively.

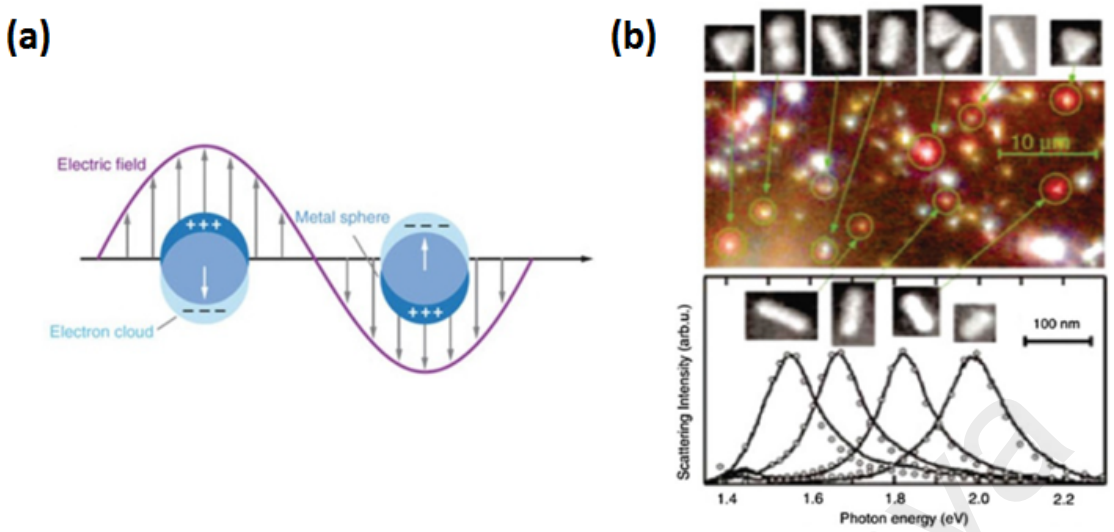

Figure 1.2: (a) Schematic illustration of LSPR of a metallic nanosphere, (b) Dark-field microscopy image with the corresponding SEM images, and light-scattering spectra of Au nanocrystals of different sizes and shapes. Note that different sizes and shapes of the Au nanocrystals yield different spectral position of the peak of the spectra (which corresponds to LSPR frequency) (Willets & Duyne, 2007; Kuwata et al., 2003).

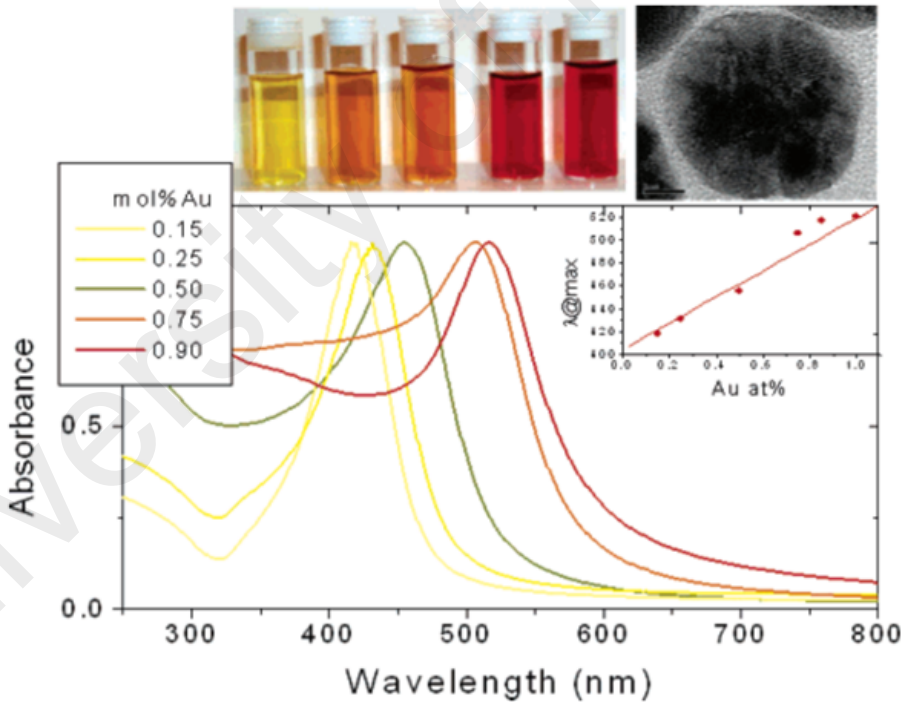

Figure 1.3: Plot of the absorption spectra showing the variation in the optical properties of Au-Ag alloy nanoparticle colloids with varying compositions. In the graph inset, the position of the experimental absorption band (dots) is plotted as a function of composition and the solid line is the linear fit to the values obtained using Mie theory. The HRTEM image shows the homogeneous distribution of Au and Ag atoms within the particles (Liz-Marzán, 2006).

The large fields and high confinement of the MP due to the presence of the LSPR (Alvarez-Puebla et al., 2010) enable strong interaction of the MP with other photonic elements such as quantum emitters (Zhang et al., 2006; Artuso & Bryant, 2008), thus opening wide horizons for new designs and applications in the novel area of quantum plasmonics. For this reason, the interaction between plasmonic MP and quantum emitters such as molecules (Davis et al., 2010) and quantum dots (QDs) (Zhang et al., 2006; Zhang & Govorov, 2011; Ridolfo et al., 2010; Artuso & Bryant, 2010; Govorov, 2010; Sadeghi, 2009) has been the subject of a tremendous number of studies over the past decade. Many interesting results from the strong exciton-plasmon coupling (Manjavacas et al., 2011) have been reported, which include nonlinear Fano effect (Zhang et al., 2006; Zhang & Govorov, 2011), exciton-induced transparency (Artuso & Bryant, 2010), effects on photon statistics (Ridolfo et al., 2010), effects on spin coupling in the presence of magnetic fields (Govorov, 2010), inhibition of optical excitations and enhancement of Rabi oscillations (Sadeghi, 2009), enhancement of fluorescence emission rate of nanocrystals (Shimizu et al., 2002), increase in the efficiency of photosynthesis systems (Govorov & Carmeli, 2007), etc.

The importance of this field of research is highlighted by its ground-breaking and diverse applications in various fields such as in the development of biological markers (Boyer et al., 2002) and nanosensors (Alivisatos, 2004; Rindzevicius et al., 2005; Govorov & Carmeli, 2007), ultrasensitive spectroscopy (Li et al., 2010), nanoscale laser cavities (spaser) (Noginov et al., 2009), surface enhanced Raman scattering (SERS) (Félidj et al., 2002; Xu et al., 1999; Talley et al., 2005; Theiss et al., 2010), optical filters and sensors (Genet & Ebbesen, 2007; Maier & Atwater, 2005), subwavelength optical waveguides (Gantzounis & Stefanou, 2006) as well as optical nanoantennas (Mühlschlegel et al., 2005; Bharadwaj et al., 2009) that allow control of radiation from single quantum emitters

(Taminiau et al., 2008) and generation of extreme ultraviolet pulses via High Harmonic Generation (HHG) (Kim et al., 2008). Also, it has been demonstrated that MP can act as a nanopulse controller and functional amplifier for QD in the presence of a coherent field (Sadeghi, 2010). The radiative rate of exciton and the nonradiative energy transfer rate can also be controlled by coherent exciton-plasmon interaction (Govorov et al., 2006). The LSPR of MP also plays an important role in the fundamental studies on the control of emission from semiconductor nanocrystals (Matsuda et al., 2008; Pons et al., 2007; Govorov et al., 2006; Shimizu et al., 2002). In addition, bottom-up fabrication techniques of plasmonic nanoparticle clusters are promising towards the realization of low-cost photonic nanodevices, such as optical nanocircuits (Ozbay, 2006; Engheta, 2007; Chang et al., 2007) that can merge electronics and photonics at the nanoscale.

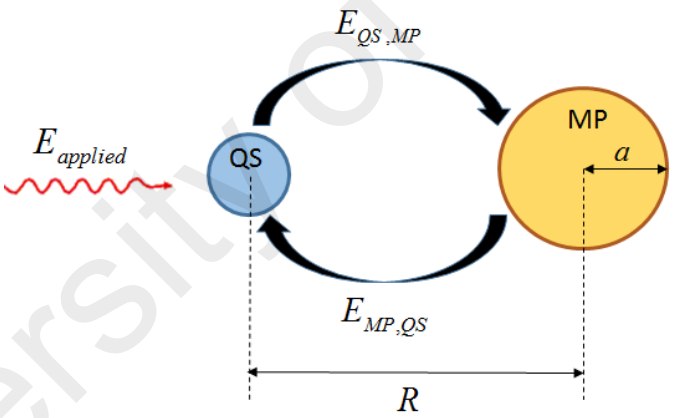

Figure 1.4: Schematic diagram of the typical model for studying MP-QS interaction. Here, $E_{QS,MP}$ represents the field scattered from the QS to MP whereas $E_{MP,QS}$ is the field scattered from MP to QS. The applied field $E_{applied}$ induces a polarization in both MP and QS which in turn allows dipole-dipole coupling to take place.

So far, all the existing works on plasmonic MP-quantum system (QS) interaction have not considered quantum systems in double Raman scheme emitting correlated photons which carry novel quantum properties useful for quantum metrology (Huver et al., 2008) and ultrafast quantum information processing (Hammerer et al., 2010). This scheme has remarkable features and has been widely studied in the context of quantum erasers (Scully

& Drühl, 1982), quantum information (Kuzmich et al., 2003; Chou et al., 2004; van der Wal et al., 2003; Jiang et al., 2004), quantum entanglement (Moiseev & Ham, 2005; Lia et al., 2005; Yang & Wu, 2005; André et al., 2002; Yang et al., 2005), nonlinear optics (Lukin et al., 1999; Lukin et al., 1998) and subwavelength resolution microscopy (Scully, 1994). It has been shown that the photons generated from double Raman scheme exhibit nonclassical properties such as squeezing (Lukin et al., 1999), violation of the Cauchy-Schwartz inequality (Balić et al., 2005; Kolchin et al., 2006), and antibunching with Rabi oscillations in $G^{(2)}$ for the single-atom case (Scully & Ooi, 2004). Various systems in this scheme have been studied, including single atoms (Patnaik et al., 2005), two atoms with dipole-dipole interaction (Ooi, 2007b; Ooi et al., 2007), an array of atoms (Ooi & Lan, 2010), a single-atom two-photon laser (Ooi, 2007a; Benkert et al., 1990) and a one-dimensional amplifier (Ooi et al., 2007). These systems are relevant for the generation of nonclassical photons in quantum information (Bennett & Shor, 1998). For example, double Raman scheme enables efficient mapping of the quantum information (Kozhekin et al., 2000; Fleischhauer & Lukin, 2002) carried by the input Stokes photon into the atomic ensembles and reading off the information as an anti-Stokes photon after a controllable time delay up to 2μs (Jiang et al., 2004), which is much longer than those produced in cascade scheme and in parametric down-conversion (Wu et al., 1987; Kurtsiefer et al., 2001).

Motivated by the previous works on MP-QS interaction and double Raman scheme, in this thesis, the optical properties of a hybrid nanostructure consisting of a spherical MP in close proximity with a QS in four-level double Raman configuration is theoretically studied. A semiclassical approach is adopted in which the MP is treated as a classical spherical dielectric particle while the QS is treated quantum-mechanically using quantum Langevin formalism with noise operators (Ooi et al., 2007). In such system the laser field

excites the discreet transitions in the QS as well as the surface plasmons (with continuous spectral response) of the MP. Though there is no direct coupling between the MP and QS, a long-range Coulomb interaction exists between them which couples the two particles and leads to excitation transfer. The coupling between the continuum excitations (plasmons) of the MP and the discreet excitations (excitons) of the QS will lead to a novel effect called nonlinear Fano effect (Zhang et al., 2006). Such effect arises from the interference between the external field and the induced internal field in the hybrid nanostructure and usually manifests itself in the form of an asymmetric shape of the optical absorption spectra.

In this thesis the quantum properties of the photons emitted by the above-mentioned hybrid nanostructure will be explored. The quantum coherences associated with the Stokes and anti-Stokes transitions will be analytically solved using Heisenberg-Langevin formalism. Then, the spectra of the Stokes and anti-Stokes fields will be computed and analyzed. The dependence of the spectra on various parameters such as the laser fields strengths, interparticle distance, etc. will also be studied. Besides, the angular/directional dependence of the spectra will be explored. It is hoped that this research will have implications on the study and design of nanophotonics devices and quantum information tools that rely on plasmon-exciton interactions.

1.2 Aim and Objectives

In this thesis, the quantum optical properties of a hybrid nanostructure comprising of a MP in close proximity with a QS in double Raman configuration is studied and solved using quantum Langevin formalism with noise operators. The objectives of this study are

1. To solve for the coherences associated with the Stokes and anti-Stokes fields emitted by a QS in double Raman scheme using quantum Langevin formalism with noise

operators.

2. To study the effects caused by the finite size of a mesoscopic micro-particle on the properties of the quantum fields.

3. To investigate the effects of MP-QS coupling on the spectra of the Stokes and anti-Stokes fields emitted by a hybrid nanostructure consisting of a MP located near a QS in double Raman configuration.

4. To study the dependence of the spectra of Raman photon pairs on various parameters including the angles of observation.

1.3 Outline

The following are the main topics that will be covered in this thesis:

1. **Double Raman scheme:** The focus will be on the analytical solution for four-level double Raman scheme based on quantum Langevin formalism with noise operators. The aim is to compute the coherences associated with the Stokes and anti-Stokes transitions which will be useful for deriving the expression of the scattered electric field.

2. **Scattered field formula:** The focus will be on the integral solution of the scattered field formula which is derived from the Maxwell equations taking into account the optical nonlinear polarization and the finite size of the source particle. Also, the general expression for the scattered electric field formula which takes into account the multipole effects and is valid for arbitrary size of the source particle as well as arbitrary observation distance will be derived. The expression will then be applied to the study of MP-QS interaction with the aim of deriving a scattered field formula which is valid for any energy level configuration of the QS.

3. **Quantum spectra:** The spectra of the Stokes and anti-Stokes fields emitted from two systems: (i) A mesoscopic spherical particle and (ii) A hybrid nanostructure comprising of a MP in close proximity with a QS will be computed and analyzed. Both mesoscopic particle and QS consists of quantum particles in double Raman configuration which emit Stokes and anti-Stokes photons. The quantum spectra obtained will provide insights into the quantum properties of the photons emitted by both systems. In particular, the variation of the spectra with various parameters will be studied and explanation for the underlying physical mechanisms responsible for the variations will be provided.

4. **MP-QS interaction:** The Coulomb interaction between MP and QS will be analytically studied by computing the local fields of each particle and the scattered field from both MP and QS at arbitrary distance. Then, the plasmonic effects caused by the MP on the QS will be analyzed by interpreting the results of the simulated Stokes and anti-Stokes spectra.

1.4 Organization of the thesis

This thesis is organized as follow. The first chapter is the introductory chapter which gives an account on the issues concerned in this study as well as the motivations behind the research. It also contains the aim and objectives of the study, the outline of the research approach as well as a summary on the structure of the thesis.

Chapter 2 is concerned with the literature review. This chapter contains the theories as well as findings from various published works which are relevant to our study of MP-QS interaction. Specifically, quantum Langevin formalism with noise operators as well as its application in solving for the QS in four-level double Raman scheme will be reviewed. Also, in this chapter, the normal- and antinormal-order spectra which is the

physical quantity that will be employed throughout this thesis to study the properties of the quantum fields will be defined. This chapter is ended with reviews on the study of MP-QS interaction in other revelent works based on both semiclassical and fully quantum-mechanical approach.

The next chapter, Chapter 3, contains the analytical theory of quantum spectra of Raman photon pairs emitted by a mesoscopic spherical particle. In this chapter, the analytical solution of the coherences associated with the Stokes and anti-Stokes transitions is obtained based on the quantum Langevin formalism reviewed in Chapter 2. Then, analytical derivation of the quantum spectra of the Stokes and anti-Stokes fields emitted from the mesoscopic spherical particle without the presence of MP will be shown. The mesoscopic particle in this study contains atoms or molecules in four-level double Raman configuration.

Chapter 4 covers the main body of this thesis, which is the interaction between MP and QS in four-level double Raman scheme. The long-range Coulomb interaction between MP and QS will be analyzed using the local fields of both particles which will be helpful in the search for the explicit expression of scattered fields at arbitrary point. As in Chapter 3, the Stokes and anti-Stokes spectra are computed and will be simulated and analyzed in Chapter 6.

This is followed by Chapter 5 which comprises of the derivation of the general expression of the scattered field formula from a MP-QS hybrid nanostructure similar to one studied in Chapter 4. The scattered field formula derived includes multipole effects and is valid for arbitrary size of QS and MP, arbitrary observation distance as well as any energy-level configuration of the QS.

The results and discussions of this study are covered in Chapter 6. Here simulation results of the quantum spectra derived in Chapter 3 and 4, particularly their dependence on various parameters such as the size of the particle, strengths of the laser fields, etc. will be shown. This is followed by interpretation of the results based on existing theories and some well-known physical phenomena.

Finally, this thesis is concluded in Chapter 7. In this chapter, the key findings of this study will be summarized and their implications discussed. This chapter also includes suggestions for future work.

CHAPTER 2: REVIEW OF RELEVANT THEORIES AND STUDIES ON METALLIC PARTICLE-QUANTUM SYSTEM INTERACTION

In this chapter, some of the theories as well as findings from various published works which are relevant to our study on metallic nanoparticle-quantum system (MP-QS) interaction will be reviewed. In the first section of this chapter quantum Langevin formalism with noise operators which is the theoretical tool that will be used for obtaining the quantum-mechanical solution for the QS in double Raman scheme will be the introduced. The focus will be on solving a simple problem using Heisenberg-Langevin approach with the aim of providing readers a simple example of the application of this mathematical method. In section 2.2, the analytical solution for the four-level double Raman scheme based on quantum Langevin formalism will be provided. This is followed by section 2.3 which gives the definitions of normal- and antinormal-order spectra that will be employed throughout this thesis and their connection to the first-order correlation functions. A review on the theoretical treatment of MP-QS interaction based on semiclassical theory comes next in section 2.4. This chapter ends with a section on full quantum-mechanical treatment of the MP-QS interaction based on two approaches, namely the density matrix method and Zubarev's Green's function formalism, both of which enable us to fully account for the quantum aspects of the optical response of our system.

2.1 Quantum Langevin Formalism

In real experiments, the quantum system of interest actually couples to the environment which normally has more degrees of freedom compared to the system of interest. This coupling leads to a phenomenon in the system of interest known as *damping* which plays an important role in describing, for example, the decay of an atom in an excited state to a lower state. However, while the dynamics of the system of interest is profoundly changed by this coupling, in general, it is assumed that the quantum statistical state

(i.e. density operator) of the environment remains unchanged due to its many degrees of freedom.

The problem of damping is usually attacked by separating the complete system into a system of primary interest (termed *system*) and a system of secondary interest (termed *reservoir*) with a huge number of degrees of freedom. Usually, one is interested in the stochastic dynamics of the system alone. This leads to the need to obtain the equations of motion associated with only the system after eliminating the reservoir degrees of freedom by tracing over the reservoir variables. Two different approaches are usually presented to deal with this problem. In the Schrödinger (or interaction) picture, this is achieved via the master equation techniques in which the reservoir variables are eliminated by using the reduced density operator for the system. In the Heisenberg picture, the damping of the system will be considered using the noise operators method in which the system dynamics are governed by the Heisenberg-Langevin equations (Scully & Zubairy, 1997; Yamamoto & Imamoglu, 1999). In this thesis the focus will only be on the Heisenberg-Langevin approach as it provides a particularly simple method for the calculation of two-time correlation functions of the atomic coherences operators which are required for the computation of the quantum fields spectra.

In the subsections that follow insights into the description of damping mechanism based on Heisenberg-Langevin approach (also known as quantum Langevin formalism in this thesis) will be obtained by considering the decay of a single-mode field inside a cavity with lossy mirrors. In this case, the system is the single-mode field whereas the reservoir consists of a large number of phonon-like modes in the mirrors. The single-mode field may be considered as a single harmonic oscillator interacting with many other simple harmonic oscillators (phonon-modes). The first subsection gives the theoretical treatment of this problem based on quantum Langevin formalism starting from

the Hamiltonian up to the equations of motion for the operators associated with the system. This is followed by subsection 2.1.2 where various correlation functions associated with the noise operators are computed. This is important for this study particularly for the calculation of the field spectra which is actually the Fourier transform of the first-order correlation function. Subsection 2.1.3 concerns the Einstein diffusion equation which is necessary for the computation of diffusion coefficients that appear in the calculation of correlation functions in subsection 2.1.2.

2.1.1 Simple Treatment of Damping Based on Heisenberg-Langevin Approach

Consider a system which consists of a single-mode field of frequency ν and annihilation operator $\hat{a}(t)$. The reservoir consists of many oscillators with closely spaced frequencies ν_k and annihilation (and creation) operators $\hat{b}_{\mathbf{k}}$ (and $\hat{b}_{\mathbf{k}}^{\dagger}$). The total Hamiltonian of the field-reservoir system is

$$\hat{H} = \hat{H}_0 + \hat{H}_1, \tag{2.1}$$

where the free Hamiltonian

$$\hat{H}_0 = \hbar\nu\hat{a}^{\dagger}\hat{a} + \sum_{\mathbf{k}} \hbar\nu_k \hat{b}_{\mathbf{k}}^{\dagger}\hat{b}_{\mathbf{k}} \tag{2.2}$$

consists of the energy of the free field and the reservoir modes and

$$\hat{H}_1 = \hbar \sum_{\mathbf{k}} g_{\mathbf{k}} \left(\hat{b}_{\mathbf{k}}^{\dagger}\hat{a} + \hat{a}^{\dagger}\hat{b}_{\mathbf{k}} \right) \tag{2.3}$$

is the interaction Hamiltonian where the usual rotating wave approximation has been made. The Heisenberg equations of motion for the operators are

$$\frac{d}{dt}\hat{a}(t) = \frac{i}{\hbar}\left[\hat{H}, \hat{a}(t)\right] = -i\nu\hat{a}(t) - i\sum_{\mathbf{k}} g_{\mathbf{k}}\hat{b}_{\mathbf{k}}(t), \tag{2.4}$$

$$\frac{d}{dt}\hat{b}_{\mathbf{k}}(t) = -i\nu_k\hat{b}_{\mathbf{k}}(t) - ig_{\mathbf{k}}\hat{a}(t). \tag{2.5}$$

Now, the field operator $\hat{a}(t)$ has to be solved. Firstly, Equation 2.5 is integrated to get

$$\hat{b}_{\mathbf{k}}(t) = \hat{b}_{\mathbf{k}}(0)\, e^{-i\nu_k t} - ig_{\mathbf{k}}\int_0^t dt'\hat{a}(t')\, e^{-i\nu_k(t-t')}. \tag{2.6}$$

The first term in Equation 2.6 represents the free evolution of the reservoir modes whereas the second term represents their interaction with the system. Eliminating $\hat{b}_{\mathbf{k}}(t)$ in Equation 2.4 by substituting Equation 2.6 into Equation 2.4 will lead to

$$\frac{d}{dt}\hat{a}(t) = -i\nu a(t) - \sum_{\mathbf{k}} g_{\mathbf{k}}^2\int_0^t dt' a(t')\, e^{-i\nu_k(t-t')} + f_a(t), \tag{2.7}$$

where

$$f_a(t) = -i\sum_{\mathbf{k}} g_{\mathbf{k}}\hat{b}_{\mathbf{k}}(0)\, e^{-i\nu_k t} \tag{2.8}$$

is the noise operator as it depends on the reservoir operator $\hat{b}_{\mathbf{k}}(0)$. The evolution of the expectation values of the system operators will therefore be affected by the fluctuations in the reservoir. The presence of all the reservoir frequencies causes the noise operator to vary rapidly. The fast frequency dependence of $\hat{a}(t)$ can be removed by transforming to the slowly varying annihilation operator

$$\tilde{a}(t) = \hat{a}(t)\, e^{i\nu t}. \tag{2.9}$$

Note that the commutation relation

$$\left[\tilde{a}(t), \tilde{a}^{\dagger}(t)\right] = 1 \tag{2.10}$$

still holds true. Equation 2.7 now reduces to

$$\frac{d}{dt}\tilde{a}(t) = -\sum_{\mathbf{k}} g_{\mathbf{k}}^2 \int_0^t dt' \tilde{a}(t') e^{-i(\nu_k - \nu)(t'-t)} + \hat{F}_{\tilde{a}}(t) \tag{2.11}$$

with

$$\hat{F}_{\tilde{a}}(t) = e^{i\nu t} f_a(t) = -i \sum_{\mathbf{k}} g_{\mathbf{k}} \hat{b}_{\mathbf{k}}(0) e^{-i(\nu_k - \nu)t}. \tag{2.12}$$

As in the Weisskopf-Wigner approximation (Scully & Zubairy, 1997), by assuming that the modes of the reservoir are closely spaced in frequency, one can replace the summation $\sum_{\mathbf{k}}$ by an integral

$$\sum_{\mathbf{k}} \rightarrow 2\frac{V}{(2\pi)^3} \int_0^{2\pi} d\phi \int_0^{\pi} \sin\theta d\theta \int_0^{\infty} k^2 dk, \tag{2.13}$$

where V is the quantization volume. Using $k = \frac{\nu_k}{c}$ and the Dirac delta function

$$\int_{-\infty}^{\infty} d\nu_k e^{i(\omega - \nu_k)(t-t')} = 2\pi\delta(t - t'), \tag{2.14}$$

the first term of Equation 2.11 then becomes

$$\sum_{\mathbf{k}} g_{\mathbf{k}}^2 \int_0^t dt' \tilde{a}(t') e^{-i(\nu_k - \nu)(t'-t)} \simeq \frac{1}{2} C \tilde{a}(t), \tag{2.15}$$

where the damping constant

$$C = 2\pi \left[g(\nu)\right]^2 D(\nu) \tag{2.16}$$

with $g(\nu)$ as the coupling constant evaluated at $k = \frac{\nu}{c}$ and

$$D(\nu) = \frac{V\nu^2}{\pi^2 c^3} \tag{2.17}$$

as the density of states. Hence, Equation 2.11 can be reduced to the Langevin equation

$$\frac{d}{dt}\tilde{a}(t) = -\frac{1}{2}C\tilde{a} + \hat{F}_{\tilde{a}}(t), \tag{2.18}$$

where $\hat{F}_{\tilde{a}}(t)$ is the noise operator which depends on reservoir variables. Note that the presence of the noise operator in Equation 2.18 is necessary for the preservation of the commutation relation in Equation 2.10. If the noise term ($\hat{F}_{\tilde{a}}(t) = 0$) is not considered in Equation 2.18, one will get the solution

$$\tilde{a}(t) = \tilde{a}(0)\, e^{-Ct/2}. \tag{2.19}$$

If operator $\tilde{a}(0)$ satisfies the commutation relation in Equation 2.10, then

$$\left[\tilde{a}(t), \tilde{a}^{\dagger}(t)\right] = e^{-Ct}, \tag{2.20}$$

which is the violation of the commutation relation. This shows that the noise operators are necessary to help maintain the commutation relation at all times. Equation 2.18 is in fact a manifestation of the *fluctuation-dissipation theorem* (i.e. dissipation is always accompanied by fluctuations) as it contains a damping term along with a noise term.

2.1.2 Correlation Functions of Noise Operators

It was mentioned earlier that quantum Langevin approach is chosen in this study because it is convenient for the calculation of the correlation functions. Here in this

subsection the focus will be on the computation of various correlation functions associated with the noise operator $\hat{F}_{\tilde{a}}(t)$. The procedures outlined in this subsection will later be useful for reference when the field correlation function will be derived in Chapter 3 and 4.

We assume that the reservoir is in thermal equilibrium, so that

$$\left\langle \hat{b}_{\mathbf{k}}(0) \right\rangle_R = \left\langle \hat{b}^{\dagger}_{\mathbf{k}}(0) \right\rangle_R = 0, \tag{2.21}$$

$$\left\langle \hat{b}^{\dagger}_{\mathbf{k}}(0)\, \hat{b}_{\mathbf{k}'}(0) \right\rangle_R = \bar{n}_{\mathbf{k}} \delta_{\mathbf{k}\mathbf{k}'}, \tag{2.22}$$

$$\left\langle \hat{b}_{\mathbf{k}'}(0)\, \hat{b}^{\dagger}_{\mathbf{k}}(0) \right\rangle_R = (\bar{n}_{\mathbf{k}} + 1)\, \delta_{\mathbf{k}\mathbf{k}'}, \tag{2.23}$$

$$\left\langle \hat{b}_{\mathbf{k}'}(0)\, \hat{b}_{\mathbf{k}}(0) \right\rangle_R = \left\langle \hat{b}^{\dagger}_{\mathbf{k}'}(0)\, \hat{b}^{\dagger}_{\mathbf{k}}(0) \right\rangle_R = 0. \tag{2.24}$$

Using Equation 2.12 and Equations 2.21-2.24, one can evaluate various correlation functions involving $\hat{F}_{\tilde{a}}(t)$ as follows. First of all, from Equation 2.21,

$$\left\langle \hat{F}_{\tilde{a}}(t) \right\rangle_R = \left\langle \hat{F}^{\dagger}_{\tilde{a}}(t) \right\rangle_R = 0. \tag{2.25}$$

Next, using Equation 2.22, one obtains

$$\begin{aligned} \left\langle \hat{F}^{\dagger}_{\tilde{a}}(t)\, \hat{F}_{\tilde{a}}(t') \right\rangle_R &= \sum_{\mathbf{k}} \sum_{\mathbf{k}'} g_{\mathbf{k}} g_{\mathbf{k}'} \left\langle \hat{b}^{\dagger}_{\mathbf{k}}(0)\, \hat{b}_{\mathbf{k}'}(0) \right\rangle_R \exp\left[i(\nu_k - \nu)\, t - i(\nu_{k'} - \nu)\, t' \right] \\ &= \sum_{\mathbf{k}} g^2_{\mathbf{k}} \bar{n}_{\mathbf{k}} \exp\left[i(\nu_k - \nu)(t - t') \right] \\ &= \int_0^{\infty} D(\nu_k) \left[g(\nu_k) \right]^2 \bar{n}(\nu_k)\, e^{i(\nu_k - \nu)(t' - t)} d\nu_k, \end{aligned} \tag{2.26}$$

where the usual continuous representation of $\sum_{\mathbf{k}}$ have been applied. Now, the slowly varying terms $D(\nu_k)$, $[g(\nu_k)]^2$ and $\bar{n}(\nu_k)$ at $\nu_k = \nu$ can be pulled out from the integral

and the remaining integral can be replaced by a $\delta-$function to arrive at

$$\left\langle \hat{F}_{\tilde{a}}^{\dagger}(t)\,\hat{F}_{\tilde{a}}(t')\right\rangle_{R} = C\bar{n}_{th}\delta(t-t')\,. \tag{2.27}$$

In analogy with classical Langevin theory, the diffusion coefficient $D_{\tilde{a}^{\dagger}\tilde{a}}$ is defined as follows

$$\left\langle \hat{F}_{\tilde{a}}^{\dagger}(t)\,\hat{F}_{\tilde{a}}(t')\right\rangle_{R} = 2\left\langle D_{\tilde{a}^{\dagger}\tilde{a}}\right\rangle_{R}\delta(t-t')\,. \tag{2.28}$$

According to Equation 2.27, the diffusion coefficient for $\tilde{a}^{\dagger}\tilde{a}$ is given by

$$2\left\langle D_{\tilde{a}^{\dagger}\tilde{a}}\right\rangle_{R} = C\bar{n}_{th}. \tag{2.29}$$

Similarly, following the same procedures one can show that

$$\left\langle \hat{F}_{\tilde{a}}(t)\,\hat{F}_{\tilde{a}}^{\dagger}(t')\right\rangle_{R} = C(\bar{n}_{th}+1)\,\delta(t-t') \tag{2.30}$$

and

$$\left\langle \hat{F}_{\tilde{a}}(t)\,\hat{F}_{\tilde{a}}(t')\right\rangle_{R} = \left\langle \hat{F}_{\tilde{a}}^{\dagger}(t)\,\hat{F}_{\tilde{a}}^{\dagger}(t')\right\rangle_{R} = 0, \tag{2.31}$$

from which one may deduce that

$$2\left\langle D_{\tilde{a}\tilde{a}^{\dagger}}\right\rangle_{R} = C(\bar{n}_{th}+1), \tag{2.32}$$

$$\left\langle D_{\tilde{a}\tilde{a}}\right\rangle_{R} = \left\langle D_{\tilde{a}^{\dagger}\tilde{a}^{\dagger}}\right\rangle_{R} = 0. \tag{2.33}$$

Now the correlation functions $\left\langle \hat{F}_{\tilde{a}}^{\dagger}(t)\,\tilde{a}(t)\right\rangle$ and $\left\langle \tilde{a}^{\dagger}(t)\,\hat{F}_{\tilde{a}}(t)\right\rangle$ shall be determined. These two correlation functions will be useful for the derivation of equations of motion

for $\left\langle \tilde{a}^{\dagger}(t)\,\tilde{a}(t)\right\rangle_R$ in subsection 2.1.3. Solving Equation 2.18, one gets

$$\tilde{a}(t) = \tilde{a}(0)\exp\left(-\frac{C}{2}t\right) + \int_0^t dt' \exp\left[-\frac{C}{2}(t-t')\right]\hat{F}_{\tilde{a}}(t')\,. \tag{2.34}$$

Multiplying $\hat{F}^{\dagger}_{\tilde{a}}(t)$ from the left and taking the expectation, one obtains

$$\begin{aligned}\left\langle \hat{F}^{\dagger}_{\tilde{a}}(t)\,\tilde{a}(t)\right\rangle_R &= \left\langle \hat{F}^{\dagger}_{\tilde{a}}(t)\right\rangle_R \tilde{a}(0)\exp\left(-\frac{C}{2}t\right) \\ &\quad + \int_0^t dt' \exp\left[-\frac{C}{2}(t-t')\right]\left\langle \hat{F}^{\dagger}_{\tilde{a}}(t)\,\hat{F}_{\tilde{a}}(t')\right\rangle. \end{aligned}\tag{2.35}$$

If one assumes $\tilde{a}(0)$ and $\hat{F}_{\tilde{a}}(t')$ to be statistically independent, it follows that from Equations 2.25 and 2.28,

$$\left\langle \hat{F}^{\dagger}_{\tilde{a}}(t)\,\tilde{a}(t)\right\rangle_R = \frac{C}{2}\bar{n}_{th} = \langle D_{\tilde{a}^{\dagger}\tilde{a}}\rangle_R\,. \tag{2.36}$$

Similarly, one can show that

$$\left\langle \tilde{a}^{\dagger}(t)\,\hat{F}_{\tilde{a}}(t)\right\rangle_R = \frac{C}{2}\bar{n}_{th}. \tag{2.37}$$

2.1.3 Einstein Relation

In this subsection, the Einstein relation will be derived from the results obtained in subsection 2.1.1.and 2.1.2. This relation will be needed later in the evaluation of diffusion coefficients in Chapter 3 and 4. The equation of motion for the mean of $\tilde{a}(t)$ and of the number operator $\tilde{a}^{\dagger}(t)\,\tilde{a}(t)$ will first be derived. One knows from Equations 2.25 and 2.18 that

$$\frac{d}{dt}\langle \tilde{a}(t)\rangle_R = -\frac{1}{2}C\,\langle \tilde{a}(t)\rangle_R, \tag{2.38}$$

which shows that the mean value of the system operator goes to zero in time. Meanwhile, the mean time development of the field number operator is

$$\begin{aligned}\frac{d}{dt}\left\langle \tilde{a}^{\dagger}(t)\,\tilde{a}(t)\right\rangle_R &= \left\langle \frac{d\tilde{a}^{\dagger}(t)}{dt}\tilde{a}(t)\right\rangle_R + \left\langle \tilde{a}^{\dagger}(t)\,\frac{d\tilde{a}(t)}{dt}\right\rangle_R \\ &= -C\left\langle \tilde{a}^{\dagger}(t)\,\tilde{a}(t)\right\rangle_R + \left\langle \hat{F}_{\tilde{a}}^{\dagger}(t)\,\tilde{a}(t)\right\rangle_R + \left\langle \tilde{a}^{\dagger}(t)\,\hat{F}_{\tilde{a}}(t)\right\rangle_R \\ &= -C\left\langle \tilde{a}^{\dagger}(t)\,\tilde{a}(t)\right\rangle_R + C\bar{n}_{th}, \end{aligned} \tag{2.39}$$

which shows that the steady-state value of the number operator $\left\langle \tilde{a}^{\dagger}(t)\,\tilde{a}(t)\right\rangle_R$ is $\bar{n}_{th}$ (times the identity operator).

Next, one may use Equation 2.29 to write Equation 2.39 as

$$2\left\langle D_{\tilde{a}^{\dagger}\tilde{a}}\right\rangle_R = \frac{d}{dt}\left\langle \tilde{a}^{\dagger}(t)\,\tilde{a}(t)\right\rangle_R + C\left\langle \tilde{a}^{\dagger}(t)\,\tilde{a}(t)\right\rangle_R. \tag{2.40}$$

From Equation 2.18 and its conjugate, one gets the relations

$$\frac{1}{2}C\left\langle \tilde{a}^{\dagger}(t)\,\tilde{a}(t)\right\rangle_R = -\left\langle \tilde{a}^{\dagger}(t)\left[\frac{d\tilde{a}(t)}{dt} - \hat{F}_{\tilde{a}}(t)\right]\right\rangle_R, \tag{2.41}$$

$$\frac{1}{2}C\left\langle \tilde{a}^{\dagger}(t)\,\tilde{a}(t)\right\rangle_R = -\left\langle \left[\frac{d\tilde{a}^{\dagger}(t)}{dt} - \hat{F}_{\tilde{a}}^{\dagger}(t)\right]\tilde{a}(t)\right\rangle_R. \tag{2.42}$$

Adding up Equations 2.41 and 2.42 will give the second term on the right-hand side (RHS) of Equation 2.40. Hence, Equation 2.40 may be written as

$$\begin{aligned}2\left\langle D_{\tilde{a}^{\dagger}\tilde{a}}\right\rangle_R &= \frac{d}{dt}\left\langle \tilde{a}^{\dagger}(t)\,\tilde{a}(t)\right\rangle_R - \left\langle \left[\frac{d\tilde{a}^{\dagger}}{dt} - \hat{F}_{\tilde{a}}^{\dagger}(t)\right]\tilde{a}(t)\right\rangle_R \\ &\quad - \left\langle \tilde{a}^{\dagger}(t)\left[\frac{d\tilde{a}(t)}{dt} - \hat{F}_{\tilde{a}}(t)\right]\right\rangle_R. \end{aligned} \tag{2.43}$$

Equation 2.43 is called the *Einstein relation* which provides an extremely simple way

to determine the diffusion coefficient $2\langle D_{\tilde{a}^\dagger \tilde{a}}\rangle_R$. Although in this thesis this relation is derived from the problem of damped harmonic oscillator, this relation is actually valid for many general system-reservoir problems. In general, the diffusion coefficient $2D_{A,B}$ associated with any two operators A and B can be determined from the relation

$$2D_{A,B} = \left\langle \frac{d(AB)}{dt} - A\left(\frac{dB}{dt} - F_B\right) - \left(\frac{dA}{dt} - F_A\right)B \right\rangle. \tag{2.44}$$

This relation will be revisited again in Appendix C for the determination of normal- and antinormal-order diffusion coefficients required in the evaluation of the fields spectra.

2.2 Quantum-Mechanical Solution for Four-Level Double Raman Scheme

The QS considered in our study of MP-QS interaction in chapter 4 consists of quantum particles in four-level double Raman configuration as shown in Figure 2.1(a). For this reason, this section focuses on the analytical solution for the double Raman scheme based on Heisenberg-Langevin formalism. The results obtained in this section will be revisited again in Chapter 3 for the evaluation of quantum coherences and fields.

In this scheme, the incident laser field (called "pump") first excites the system from its ground state $|c\rangle$ to $|d\rangle$ where a Stokes photon is later generated via a spontaneous Raman process while the system decays to level $|b\rangle$. It is possible to generate another photon, called the anti-Stokes photon, which is strongly correlated to the Stokes photon by applying a strong resonant control field which couples level $|b\rangle$ to $|a\rangle$. The quantum Stokes and anti-Stokes fields generated by this scheme are sometimes referred to as *Raman photon pairs*.

In the Schrödinger picture, the total Hamiltonian describing the four-level double Raman scheme is given by

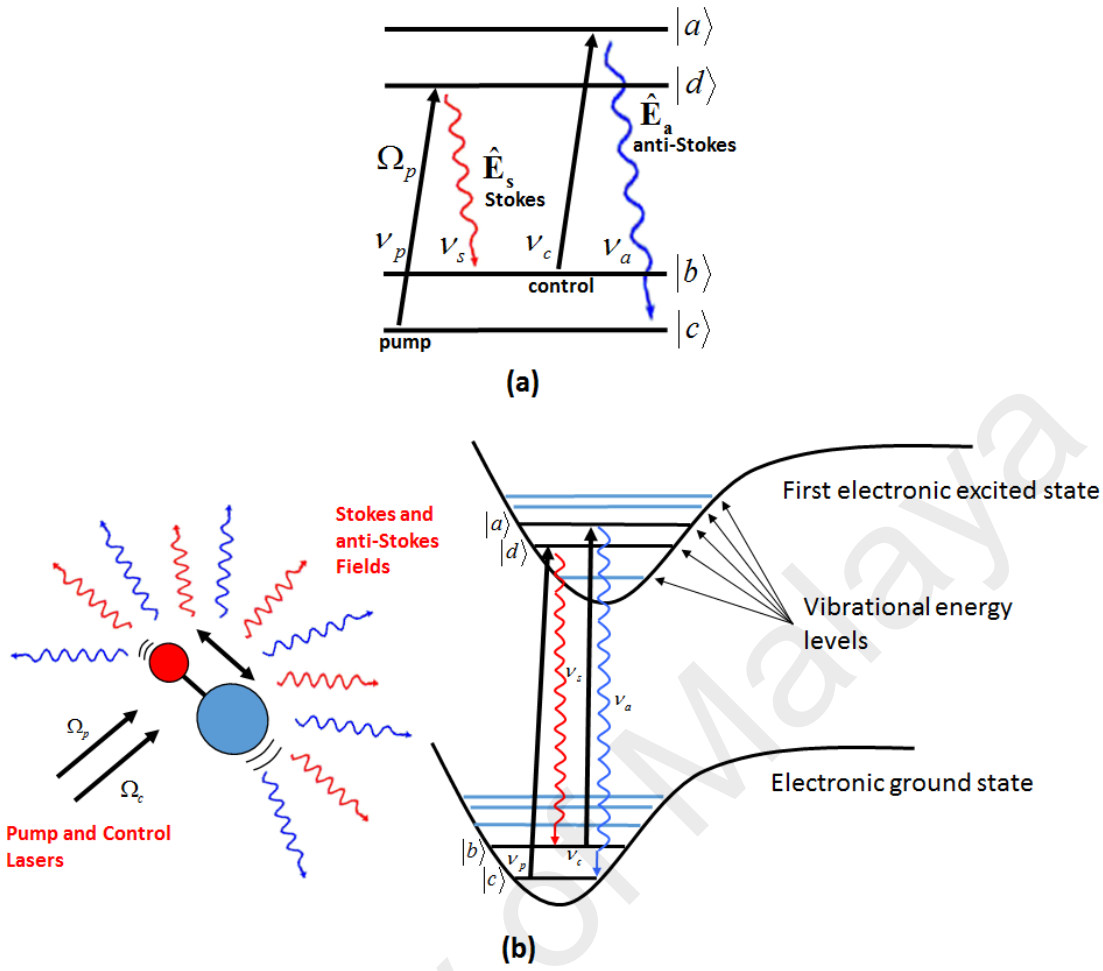

Figure 2.1: (a) Energy level diagram for the four-level double Raman scheme. The QS interacts with pump Ω_p and control Ω_c lasers (solid arrows) and emits quantized Stokes $\hat{E}_s$ and anti-Stokes $\hat{E}_a$ fields (wavy arrows) with their respective frequencies given by ν_i $(i = p, s, c, a)$. (b) Vibrational energy levels of a molecule as the four energy levels in double Raman scheme.

$$\hat{H} = \hat{H}_0 + \hat{V}, \tag{2.45}$$

where

$$\hat{H}_0 = \sum_{\varsigma=a,b,c,d} \hbar\omega_\varsigma \left|\varsigma\right\rangle \left\langle\varsigma\right| + \sum_{\mathbf{k},\lambda} \left(\hat{a}^\dagger_{\mathbf{k}\lambda}\hat{a}_{\mathbf{k}\lambda} + \frac{1}{2}\right)\hbar\nu_{\mathbf{k}\lambda} \tag{2.46}$$

is the free Hamiltonian and

$$\begin{aligned}\hat{V} &= -\hbar \sum_{\mathbf{k},\varsigma=b,c} \left(g_{\mathbf{k}}^{a\varsigma} |a\rangle \langle\varsigma| + g_{\mathbf{k}}^{d\varsigma} |d\rangle \langle\varsigma| \right) \hat{a}_{\mathbf{k}}(t)\, e^{i(\mathbf{k}\cdot\mathbf{r}-\nu_{\mathbf{k}}t)} \\ &\quad -\hbar \left(\Omega_p |d\rangle \langle c|\, e^{i(\mathbf{k}_p\cdot\mathbf{r}-\nu_p t)} + \Omega_c |a\rangle \langle b|\, e^{i(\mathbf{k}_c\cdot\mathbf{r}-\nu_c t)} \right) \\ &\quad -\hbar \left(\mathbf{g}_s\cdot\hat{\mathbf{E}}_s |d\rangle \langle b|\, e^{i(\mathbf{k}_s\cdot\mathbf{r}-\nu_s t)} + \mathbf{g}_a\cdot\hat{\mathbf{E}}_a |a\rangle \langle c|\, e^{i(\mathbf{k}_a\cdot\mathbf{r}-\nu_a t)} \right) + \text{adj.} \qquad (2.47)\end{aligned}$$

is the interaction Hamiltonian after the usual rotating wave approximation has been made. The first term on the RHS of Equation 2.46 is the atomic Hamiltonian of the QS (system) whereas the second term represents the Hamiltonian due to the environment (reservoir) which is treated as a large number of harmonic oscillators as in section 2.1. Here, $\mathbf{g}_s = \frac{1}{\hbar}\vec{\wp}_{bd}, \mathbf{g}_a = \frac{1}{\hbar}\vec{\wp}_{ca}$, $g^{a\varsigma} = \frac{1}{\hbar}\,\wp_{a\varsigma}$ and $g^{d\varsigma} = \frac{1}{\hbar}\,\wp_{d\varsigma}$ are the coupling strengths, Ω_p and Ω_c are respectively the Rabi frequency of the pump and control laser fields, $\hat{\mathbf{E}}_s$ and $\hat{\mathbf{E}}_a$ are respectively the quantum Stokes and anti-Stokes fields operators and $E_{\mathbf{k}} = \sqrt{\frac{\hbar\nu_{\mathbf{k}}}{2\varepsilon_0 V}}$ where $\nu_{\mathbf{k}}$ and V are the mode frequency and quantization volume, respectively. Here, $\mathbf{k}$ and λ are respectively the wavevector and polarization associated with the harmonic oscillators of the reservoir in the Langevin formalism. $\nu_i\,(i, j = p, s, c, a)$ is the carrier frequency of the pump, Stokes, control and anti-Stokes field, respectively whereas $\mathbf{k}_i$ is the corresponding wavevector.

Instead of studying the time-evolution of the density matrix elements, here the equations of motion for the atomic operators $\hat{\sigma}_{\alpha\beta}\,(\alpha, \beta = a, b, c, d)$ in the Heisenberg representation will be derived. In the Heisenberg representation, it is the operators which represent the observables that carry the time-dependence instead of the state vectors. The atomic operators already contain an implicit trace over the reservoir variables and the inverse is also true (Berman & Malinovsky, 2011). Hence, Heisenberg representation can greatly simplify calculations especially when one is interested in the atomic variables

only. This also justifies the choice of Heisenberg-Langevin formalism in the evaluation of the atomic populations and coherences for double Raman scheme in Chapter 3.

The equations of motion are derived from the Heisenberg equation given by

$$\frac{d\hat{O}}{dt} = \frac{i}{\hbar}\left[\hat{H}, \hat{O}\right], \tag{2.48}$$

where in this case the operator is $\hat{O} = \hat{\sigma}_{\alpha\beta}\,(\alpha, \beta = a, b, c, d)$, since one is only interested in solving for the populations and coherences of the QS though the same is also applicable to the field (reservoir) operators $\hat{a}^{\dagger}$ and $\hat{a}$. One may add the phenomenological decay terms

$$\left(\frac{d\hat{\sigma}_{\alpha\beta}}{dt}\right)_{decay} = -\gamma_{\alpha\beta}\hat{\sigma}_{\alpha\beta} \tag{2.49}$$

to each of the 16 equations describing the time-evolution of the atomic operators $\hat{\sigma}_{\alpha\beta}$ to account for the possible radiative and non-radiative relaxation processes and define the slowly-varying envelop operators as $\hat{p}_{ab} = \hat{\sigma}_{ab}e^{-i\nu_c t}, \hat{p}_{ac} = \hat{\sigma}_{ac}e^{-i\nu_a t}, \hat{p}_{ad} = \hat{\sigma}_{ad}e^{-i\nu_{cs} t}, \hat{p}_{bc} = \hat{\sigma}_{bc}e^{-i\nu_{ac} t}, \hat{p}_{bd} = \hat{\sigma}_{bd}e^{i\nu_s t}$ and $\hat{p}_{cd} = \hat{\sigma}_{cd}e^{i\nu_p t}$. Here, $\nu_{ij} = \nu_i - \nu_j$ and $\nu_i\,(i, j = p, s, c, a)$ denotes the carrier frequency of the pump, Stokes, control and anti-Stokes fields, respectively. The results are 16 Langevin equations with 10 of them shown below

$$\begin{aligned}\frac{d}{dt}\hat{p}_{aa} &= i\left(\Omega_c\hat{p}_{ab} - \Omega_c^{*}\hat{p}_{ba}\right) + i\left(\mathbf{g}_a\cdot\tilde{\mathbf{E}}_a\hat{p}_{ac} - \mathbf{g}_a^{*}\cdot\tilde{\mathbf{E}}_a^{\dagger}\hat{p}_{ca}\right)\\ &\quad -T_{aa}\hat{p}_{aa} + \Gamma_{ab}\bar{n}_{ab}\hat{p}_{bb} + \Gamma_{ac}\bar{n}_{ac}\hat{p}_{cc} + \hat{F}_{aa}(t),\end{aligned} \tag{2.50}$$

$$\begin{aligned}\frac{d}{dt}\hat{p}_{ab} &= -T_{ab}\hat{p}_{ab} - i\mathbf{g}_a^{*}\cdot\tilde{\mathbf{E}}_a^{\dagger}\hat{p}_{cb} + i\mathbf{g}_s^{*}\cdot\tilde{\mathbf{E}}_s^{\dagger}\hat{p}_{ad}\\ &\quad +i\Omega_c^{*}\left(\hat{p}_{aa} - \hat{p}_{bb}\right) + e^{-i\nu_c t}\hat{F}_{ab}(t),\end{aligned} \tag{2.51}$$

$$\frac{d}{dt}\hat{p}_{ac} = -T_{ac}\hat{p}_{ac} - i\Omega_c^*\hat{p}_{bc} + i\mathbf{g}_a^*\cdot\tilde{\mathbf{E}}_a^\dagger\left(\hat{p}_{aa} - \hat{p}_{cc}\right) + i\Omega_p^*\hat{p}_{ad} + \hat{F}_{ac}\left(t\right)e^{-i\nu_a t}, \tag{2.52}$$

$$\frac{d}{dt}\hat{p}_{ad} = -T_{ad}\hat{p}_{ad} - i\mathbf{g}_a^*\cdot\tilde{\mathbf{E}}_a^\dagger\hat{p}_{cd} + i\mathbf{g}_s\cdot\tilde{\mathbf{E}}_s\hat{p}_{ab} - i\Omega_c^*\hat{p}_{bd} + i\Omega_p\hat{p}_{ac} + \hat{F}_{ad}\left(t\right)e^{-i\nu_{cs}t}, \tag{2.53}$$

$$\frac{d}{dt}\hat{p}_{bb} = -i\left(\Omega_c\hat{p}_{ab} - \Omega_c^*\hat{p}_{ba}\right) - i\left(\mathbf{g}_s\cdot\tilde{\mathbf{E}}_s\hat{p}_{db} - \mathbf{g}_s^*\cdot\tilde{\mathbf{E}}_s^\dagger\hat{p}_{bd}\right) - T_{bb}\hat{p}_{bb} + \Gamma_{ab}\left(\bar{n}_{ab}+1\right)\hat{p}_{aa} + \Gamma_{db}\left(\bar{n}_{db}+1\right)\hat{p}_{dd} + \hat{F}_{bb}\left(t\right), \tag{2.54}$$

$$\frac{d}{dt}\hat{p}_{bc} = -T_{bc}\hat{p}_{bc} - i\mathbf{g}_s\cdot\tilde{\mathbf{E}}_s\hat{p}_{dc} + i\mathbf{g}_a^*\cdot\tilde{\mathbf{E}}_a^\dagger\hat{p}_{ba} - i\Omega_c\hat{p}_{ac} + i\Omega_p^*\hat{p}_{bd} + e^{-i\nu_{ac}t}\hat{F}_{bc}\left(t\right), \tag{2.55}$$

$$\frac{d}{dt}\hat{p}_{bd} = -T_{bd}\hat{p}_{bd} - i\mathbf{g}_s\cdot\tilde{\mathbf{E}}_s\left(\hat{p}_{dd} - \hat{p}_{bb}\right) - i\Omega_c\hat{p}_{ad} + i\Omega_p\hat{p}_{bc} + e^{i\nu_s t}\hat{F}_{bd}\left(t\right), \tag{2.56}$$

$$\frac{d}{dt}\hat{p}_{cc} = -i\left(\Omega_p\hat{p}_{dc} - \Omega_p^*\hat{p}_{cd}\right) - i\left(\mathbf{g}_a\cdot\tilde{\mathbf{E}}_a\hat{p}_{ac} - \mathbf{g}_a^*\cdot\tilde{\mathbf{E}}_a^\dagger\hat{p}_{ca}\right) - T_{cc}\hat{p}_{cc} + \Gamma_{ac}\left(\bar{n}_{ac}+1\right)\hat{p}_{aa} + \Gamma_{dc}\left(\bar{n}_{dc}+1\right)\hat{p}_{dd} + \hat{F}_{cc}\left(t\right), \tag{2.57}$$

$$\frac{d}{dt}\hat{p}_{cd} = -T_{cd}\hat{p}_{cd} - i\mathbf{g}_a\cdot\tilde{\mathbf{E}}_a\hat{p}_{ad} + i\mathbf{g}_s\cdot\tilde{\mathbf{E}}_s\hat{p}_{cb} - i\Omega_p\left(\hat{p}_{dd} - \hat{p}_{cc}\right) + e^{i\nu_p t}\hat{F}_{cd}\left(t\right), \tag{2.58}$$

$$\frac{d}{dt}\hat{p}_{dd} = i\left(\Omega_p\hat{p}_{dc} - \Omega_p^*\hat{p}_{cd}\right) + i\left(\mathbf{g}_s\cdot\tilde{\mathbf{E}}_s\hat{p}_{db} - \mathbf{g}_s^*\cdot\tilde{\mathbf{E}}_s^\dagger\hat{p}_{bd}\right)$$
$$-T_{dd}\hat{p}_{dd} + \Gamma_{db}\bar{n}_{db}\hat{p}_{bb} + \Gamma_{dc}\bar{n}_{dc}\hat{p}_{cc} + \hat{F}_{dd}(t), \tag{2.59}$$

and the remaining 6 equations can be obtained via the relation $\hat{p}_{\alpha\beta}^\dagger = \hat{p}_{\beta\alpha}$. The complex decoherences $T_{\alpha\beta}\,(\alpha,\beta = a,b,c,d)$ in Equations 2.50-2.59 are given in Appendix F whereas $\Gamma_{\alpha\beta}$ denotes the spontaneous emission rate. The explicit form of the noise operators are

$$\hat{F}_{aa}(t) = i\left(g_{\mathbf{k}}^{ab}\hat{\sigma}_{ab} + g_{\mathbf{k}}^{ac}\hat{\sigma}_{ac}\right)\hat{a}_{\mathbf{k}}(t)\,e^{i(\mathbf{k}\cdot\mathbf{r}-\nu_{\mathbf{k}}t)} + \text{adj.}, \tag{2.60}$$

$$\hat{F}_{ab}(t) = ig_{\mathbf{k}}^{ba}\left(\hat{\sigma}_{aa} - \hat{\sigma}_{bb}\right)\hat{a}_{\mathbf{k}}^\dagger(t)\,e^{-i\left(\mathbf{k}\cdot\mathbf{r}_j-\nu_{\mathbf{k}}t\right)}$$
$$+i\left(g_{\mathbf{k}}^{bd}\hat{\sigma}_{ad} - g_{\mathbf{k}}^{ca}\hat{\sigma}_{cb}\right)\hat{a}_{\mathbf{k}}^\dagger(t)\,e^{-i(\mathbf{k}\cdot\mathbf{r}-\nu_{\mathbf{k}}t)}, \tag{2.61}$$

$$\hat{F}_{ac}(t) = i\left(g_{\mathbf{k}}^{cd}\hat{\sigma}_{ad} - g_{\mathbf{k}}^{ba}\hat{\sigma}_{bc}\right)\hat{a}_{\mathbf{k}}^\dagger(t)\,e^{-i(\mathbf{k}\cdot\mathbf{r}-\nu_{\mathbf{k}}t)}$$
$$+ig_{\mathbf{k}}^{ca}\left(\hat{\sigma}_{aa} - \hat{\sigma}_{cc}\right)\hat{a}_{\mathbf{k}}^\dagger(t)\,e^{-i(\mathbf{k}\cdot\mathbf{r}-\nu_{\mathbf{k}}t)}, \tag{2.62}$$

$$\hat{F}_{ad}(t) = -i\left(g_{\mathbf{k}}^{ba}\hat{\sigma}_{bd} + g_{\mathbf{k}}^{ca}\hat{\sigma}_{cd}\right)\hat{a}_{\mathbf{k}}^\dagger(t)\,e^{-i(\mathbf{k}\cdot\mathbf{r}-\nu_{\mathbf{k}}t)}$$
$$+i\left(g_{\mathbf{k}}^{db}\hat{\sigma}_{ab} + g_{\mathbf{k}}^{dc}\hat{\sigma}_{ac}\right)\hat{a}_{\mathbf{k}}(t)\,e^{i(\mathbf{k}\cdot\mathbf{r}-\nu_{\mathbf{k}}t)}, \tag{2.63}$$

$$\hat{F}_{bb} = -i\left(g_{\mathbf{k}}^{ab}\hat{\sigma}_{ab} + g_{\mathbf{k}}^{db}\hat{\sigma}_{db}\right)\hat{a}_{\mathbf{k}}(t)\,e^{i(\mathbf{k}\cdot\mathbf{r}-\nu_{\mathbf{k}}t)} + \text{adj.}, \tag{2.64}$$

$$\hat{F}_{bc}(t) = -i\left(g_{\mathbf{k}}^{ab}\hat{\sigma}_{ac} + g_{\mathbf{k}}^{db}\hat{\sigma}_{dc}\right)\hat{a}_{\mathbf{k}}(t)\,e^{i(\mathbf{k}\cdot\mathbf{r}-\nu_{\mathbf{k}}t)}$$
$$+i\left(g_{\mathbf{k}}^{ca}\hat{\sigma}_{ba} + g_{\mathbf{k}}^{cd}\hat{\sigma}_{bd}\right)\hat{a}_{\mathbf{k}}^\dagger(t)\,e^{-i(\mathbf{k}\cdot\mathbf{r}-\nu_{\mathbf{k}}t)}, \tag{2.65}$$

$$\hat{F}_{bd}(t) = i\left(g_{\mathbf{k}}^{dc}\hat{\sigma}_{bc} - g_{\mathbf{k}}^{ab}\hat{\sigma}_{ad}\right)\hat{a}_{\mathbf{k}}(t)\,e^{i(\mathbf{k}\cdot\mathbf{r}-\nu_{\mathbf{k}}t)} - ig_{\mathbf{k}}^{db}\left(\hat{\sigma}_{dd} - \hat{\sigma}_{bb}\right)\hat{a}_{\mathbf{k}}(t)\,e^{i(\mathbf{k}\cdot\mathbf{r}-\nu_{\mathbf{k}}t)}, \tag{2.66}$$

$$\hat{F}_{cc}(t) = i\left(g_{\mathbf{k}}^{ca}\hat{\sigma}_{ca} + g_{\mathbf{k}}^{cd}\hat{\sigma}_{cd}\right)\hat{a}_{\mathbf{k}}^{\dagger}(t)\,e^{-i(\mathbf{k}\cdot\mathbf{r}-\nu_{\mathbf{k}}t)} + \text{adj.}, \tag{2.67}$$

$$\hat{F}_{cd}(t) = -i\left(g_{\mathbf{k}}^{ac}\hat{\sigma}_{ad} + g_{\mathbf{k}}^{dc}\hat{\sigma}_{dd}\right)\hat{a}_{\mathbf{k}}(t)\,e^{i(\mathbf{k}\cdot\mathbf{r}-\nu_{\mathbf{k}}t)} + i\left(g_{\mathbf{k}}^{db}\hat{\sigma}_{cb} + g_{\mathbf{k}}^{dc}\hat{\sigma}_{dc}\right)\hat{a}_{\mathbf{k}}(t)\,e^{i(\mathbf{k}\cdot\mathbf{r}-\nu_{\mathbf{k}}t)}, \tag{2.68}$$

$$\hat{F}_{dd}(t) = -i\left(g_{\mathbf{k}}^{bd}\hat{\sigma}_{bd} + g_{\mathbf{k}}^{cd}\hat{\sigma}_{cd}\right)\hat{a}_{\mathbf{k}}^{\dagger}(t)\,e^{-i(\mathbf{k}\cdot\mathbf{r}-\nu_{\mathbf{k}}t)} + \text{adj.}, \tag{2.69}$$

while the remaining 6 noise operators can be derived from the relation $\hat{F}_{\alpha\beta}^{\dagger} = \hat{F}_{\beta\alpha}$.

Equations 2.50-2.59 will be revisited again in Chapter 3 where the coherences $\hat{p}_{bd}$ and $\hat{p}_{ac}$ associated with the Stokes and anti-Stokes transitions, respectively will be solved analytically. In general, seeking for the analytical solution to a set of Langevin equations is extremely challenging, if not impossible due to the highly nonlinear nature of the equations. Approximations are usually needed to arrive at the final analytical solution of the atomic operators and this will be discussed in Chapter 3.

2.3 Quantum Spectra and First-Order Correlation Function

This section is concerned with the definition of quantum spectra and their relation to the first-order correlation function. A characteristic of the light fields of utmost interest has traditionally been its spectrum. Quantum spectra carry useful information on the quantum properties of the scattered fields which could provide insights into the optical properties of the source. For this reason, throughout this thesis, the MP-QS interaction will be studied by computing and analyzing the quantum spectra of the fields emitted from the MP-QS system. Here, clarification on the definitions of normal- and antinormal-order

spectra that will be applied in our study will be provided.

One may start from the definition of the Fourier transform of the electric field polarized in the $q-$direction

$$E_q(\omega) = \frac{1}{\sqrt{2\pi}} \int_{-\infty}^{\infty} E_q(t)\, e^{i\omega t} dt, \tag{2.70}$$

$$E_q^{\dagger}(-\omega) = \frac{1}{\sqrt{2\pi}} \int_{-\infty}^{\infty} E_q^{\dagger}(t)\, e^{-i\omega t} dt, \tag{2.71}$$

where $E_q(t)$ and $E_q^{\dagger}(t)$ are scalar. In classical electrodynamics, the power spectrum in the $q-$direction is proportional to the absolute square of the $q-$polarized electric field in frequency domain (Puri, 2001)

$$\begin{aligned} S_q(\omega) &= \left|E_q(\omega)\right|^2 = E_q^*(-\omega)\, E_q(\omega) \\ &= \frac{1}{2\pi} \int_{-\infty}^{\infty} E_q^*(t)\, e^{-i\omega t} dt \int_{-\infty}^{\infty} E_q(t')\, e^{i\omega t'} dt' \\ &= \frac{1}{2\pi} \int_{-\infty}^{\infty} e^{i\omega(t'-t)} \int_{-\infty}^{\infty} E_q^*(t)\, E_q(t')\, dt dt'. \end{aligned} \tag{2.72}$$

By defining $\tau = t' - t$, one gets

$$S(\omega) = \frac{1}{2\pi} \int_{-\infty}^{\infty} e^{i\omega\tau} C_q(\tau)\, d\tau, \tag{2.73}$$

where

$$C_q(\tau) = \int_{-\infty}^{\infty} E_q^*(t)\, E_q(t+\tau)\, dt \tag{2.74}$$

is the first-order (field-field) correlation function for the $q-$polarized electric field. Hence, the power spectrum is actually the Fourier transform of the first-order correlation function.

However, since the fields emitted by our MP-QS system are quantum fields, the power spectrum defined above cannot be applied to our study. There is a need to find the

quantum-mechanical version of the power spectrum. One may do so by first representing the $q-$polarized electric field as a quantum-mechanical operator $\hat{E}_q(t)$. According to the Wiener-Khintchine theorem, the power spectrum $S_q(\omega)$ in the $q-$direction is related to the two-time correlation function of the $q-$polarized electric field $\hat{E}_q(t)$ by (Scully & Zubairy, 1997)

$$S_q(\omega) = \frac{1}{2\pi} \lim_{T\to\infty} \frac{1}{T} \int_0^T dt \int_0^T dt' \left\langle \hat{E}_q^\dagger(t)\, \hat{E}_q(t') \right\rangle e^{-i\omega(t-t')}, \tag{2.75}$$

By assuming that the fields are statistically stationary, i.e. the field correlation function $\left\langle \hat{E}_q^\dagger(t)\, \hat{E}_q(t') \right\rangle$ is independent of the origin of time and depends only on the time difference $\tau = t - t'$., Equation 2.75 will become

$$S_q(\omega) = \frac{1}{2\pi} \lim_{T\to\infty} \frac{1}{T} \int_0^T dt \left(\int_0^t dt' + \int_t^T dt' \right) \left\langle \hat{E}_q^\dagger(t)\, \hat{E}_q(t') \right\rangle e^{-i\omega(t-t')}$$

$$= \frac{1}{2\pi} \lim_{T\to\infty} \frac{1}{T} \int_0^T dt \left[\int_0^t \left\langle \hat{E}_q^\dagger(\tau)\, \hat{E}_q(0) \right\rangle e^{-i\omega\tau} d\tau + \int_t^{T-t} \left\langle \hat{E}_q^\dagger(0)\, \hat{E}_q(\tau) \right\rangle e^{i\omega\tau} d\tau \right], \tag{2.76}$$

If the field operators are correlated for only a short period of time, one may extend the upper limit of the $\tau-$integration to infinity without bringing significant change. Using the relation $\left\langle \hat{E}_q^\dagger(\tau)\, \hat{E}_q(0) \right\rangle = \left\langle \hat{E}_q^\dagger(0)\, \hat{E}_q(\tau) \right\rangle^*$, one arrives at

$$S_q(\omega) = \frac{1}{\pi} \mathrm{Re} \left[\int_0^\infty e^{i\omega\tau} \left\langle \hat{E}_q^\dagger(0)\, \hat{E}_q(\tau) \right\rangle d\tau \right]. \tag{2.77}$$

The normal- and antinormal-order spectra in the $q-$direction may be defined as

$$S_q^n(\omega) = \left\langle \hat{E}_q^\dagger(-\omega)\, \hat{E}_q(\omega) \right\rangle = \frac{1}{\pi} \mathrm{Re} \left[\int_0^\infty \left\langle \hat{E}_q^\dagger(0)\, \hat{E}_q(\tau) \right\rangle d\tau \right], \tag{2.78}$$

$$S_q^{an}(\omega) = \left\langle \hat{E}_q(\omega)\, \hat{E}_q^{\dagger}(-\omega) \right\rangle = \frac{1}{\pi} \mathrm{Re}\left[\int_0^{\infty} \left\langle \hat{E}_q(\tau)\, \hat{E}_q^{\dagger}(0) \right\rangle d\tau \right], \tag{2.79}$$

respectively. For unpolarized detection in the Cartesian coordinate, one may compute the spectra due to all $q-$components ($q = x, y, z$) as follows

$$S^{n}(\omega) = \sum_{q=x,y,z} \left\langle \hat{E}_q^{\dagger}(-\omega)\, \hat{E}_q(\omega) \right\rangle = \left\langle \hat{\mathbf{E}}^{\dagger}(-\omega) \cdot \hat{\mathbf{E}}(\omega) \right\rangle, \tag{2.80}$$

$$S^{an}(\omega) = \sum_{q=x,y,z} \left\langle \hat{E}_q(\omega)\, \hat{E}_q^{\dagger}(-\omega) \right\rangle = \left\langle \hat{\mathbf{E}}(\omega) \cdot \hat{\mathbf{E}}^{\dagger}(-\omega) \right\rangle. \tag{2.81}$$

Normal- and antinormal-order correlations can be understood as follows. Normal-order correlation functions are used to describe photodetection experiments based on the photoelectric effect which detect photons by absorbing them. Due to the ubiquity of this photodetection technique, normal-order correlation functions are more frequently used (Glauber, 1963). On the other hand, antinormal-order correlation functions describe photodetection using quantum counter introduced by Mandel (Mandel, 1966) which functions by stimulated emission rather than by absorption of photons. In this case, it is the creation operator instead of the annihilation operator that plays the central role. Comparison between the two distinct correlations is interesting in the photodetection theory.

In Chapter 3 and 4, the spectra of the quantum fields will be computed based on Equations 2.80 and 2.81.

2.4 Metallic Nanoparticle-Quantum System Interaction: Semiclassical Treatment

In this section, a brief review on the theoretical treatment of the MP-QS interaction based on previous works (Zhang et al., 2006; Artuso & Bryant, 2008) will be provided. The problem of MP-QS interaction has been theoretically studied by many research groups, with most of them focusing on the changes in the absorption spectrum of the hybrid nanostructure induced by the plasmonic effects of the MP. In most of the cases, the QS is

modelled as a spherical semiconductor quantum dot (SQD) with only two energy levels (ground and excited states) whereas the MP is treated as a spherical dielectric particle. A semiclassical approach is usually employed where the QS is treated quantum-mechanically via density matrix formalism while the metallic nanoparticle (MP) is described using classical electrodynamics and quasistatic approach.

The basic excitations in the MP are the surface plasmons with a continuous spectrum whereas the excitations in SQD are the discreet interband excitons. Although there is no direct tunneling between the MP and the SQD, a long-range Coulomb interaction couples the excitons and plasmons, leading to the formation of hybrid excitons and Förster energy transfer. Such effects of coupling between the excitons and plasmons become particularly strong near resonance when the exciton energy lies in the vicinity of the plasmon peak. In the final part of this section the reader will see that the coupling between the continuum excitations (plasmon) and discreet excitations also leads to a novel effect called nonlinear Fano effect which manifests itself in the form of asymmetrical shape of the absorption spectrum.

While the theoretical treatment given below was taken from a previous work (Zhang et al., 2006) which focuses on nonlinear Fano effect, the formalism used can be employed to study other aspects of MP-QS interaction.

2.4.1 Analytical Solution of MP-SQD Interaction

The system considered here consists of a hybrid molecule (Figure 2.2) which is made of a spherical MP of radius a and a spherical SQD with radius r in the presence of a polarized external field $E = E_0 \cos(\omega t)$. The center-to-center distance between MNP and SQD is denoted as R and is aligned along the $z-$axis. Since the size of the hybrid molecule is much smaller (i.e. tens of nanometers) than the wavelength of the incident light, we can neglect retardation effects. Also, due to the symmetry of the spherical

SQD, it has three bright excitons with dipoles parallel to the direction α, where α can be x, y,and z. Although the dark exciton states are not excited in the dipole limit, they do provide a nonradiative decay channel for the bright excitons which contribute to the exciton lifetime. Given the symmetry of the molecule and the linearly polarized field one obtains the Hamiltonian

$$\hat{H}_{SQD} = \sum_{i=1,2} \epsilon_i c_i^\dagger c_i - \mu E_{SQD} \left(c_1^\dagger c_2 + c_2^\dagger c_1 \right), \tag{2.82}$$

where $c_1^\dagger$ and $c_2^\dagger$ are the creation operators for the vacuum ground state and α-exciton state, respectively, μ is the interband dipole matrix element, and E_{SQD} is the total field (local field) felt by the SQD which is given by

$$E_{SQD} = E + \frac{s_\alpha P_{MP}}{\varepsilon_{eff1} R^3}, \tag{2.83}$$

with $\varepsilon_{eff1} = \frac{2\varepsilon_0 + \varepsilon_s}{3\varepsilon_0}$, ε_0 and ε_s are the dielectric constants of the background and SQD, respectively, E is the external field, $s_\alpha = 2\,(-1)$ for electric field polarization $\alpha = z\,(x, y)$ and P_{MP} is the polarization resulted from the charges induced on the surface of the MP. Equation 2.83 shows that the total field felt by the SQD is a combination of the external field and the field scattered from the MP. By the same reasoning, the field felt by the MP is due to the external field and the field scattered from the SQD. Thus, one can write the polarization of the MP as

$$P_{MP} = \gamma a^3 \left(E + \frac{s_\alpha P_{SQD}}{\varepsilon_{eff2} R^3} \right), \tag{2.84}$$

where the relation $P_{MP} = \gamma a^3 E_{MP}$ has been used, with $\gamma = \frac{\varepsilon_m(\omega) - \varepsilon_0}{2\varepsilon_0 + \varepsilon_m(\omega)}$, $\varepsilon_{eff2} = \frac{2\varepsilon_0 + \varepsilon_s}{3}$ and $\varepsilon_m\,(\omega)$ as the dielectric function of the MP from the Drude model. The polarization of

the SQD is expressed as

$$P_{SQD} = \mu\left(\rho_{21} + \rho_{12}\right), \tag{2.85}$$

where ρ_{21} and ρ_{12} are the transition matrix elements that can be solved from the master equation

$$\frac{d\hat{\rho}}{dt} = \frac{i}{\hbar}\left[\hat{\rho}, \hat{H}_{SQD}\right] - \Gamma\hat{\rho}. \tag{2.86}$$

The diagonal and off-diagonal relaxation matrix elements are given by

$$\Gamma_{12} = \Gamma_{21} = \frac{1}{T_{20}}, \tag{2.87}$$

$$\Gamma_{22} = -\Gamma_{11} = \frac{1}{\tau_0}, \tag{2.88}$$

where τ_0 includes the nonradiative decay via the dark states. To solve the coupled equations in a self-consistent manner, the high frequency part is first separated by writing ρ_{12} and ρ_{21} as $\rho_{12} = \bar{\rho}_{12}e^{i\omega t}$ and $\rho_{21} = \bar{\rho}_{21}e^{-i\omega t}$, respectively. After applying the rotating wave approximation, the solution for the steady-state coherence is obtained as

$$\bar{\rho}_{21} = A + iB, \tag{2.89}$$

where A and B form a system of nonlinear equations

$$A = -\frac{\left(\Omega_I + K\Omega_R\right)T_2}{1 + K^2}\Delta, \tag{2.90}$$

$$B = \frac{\left(\Omega_R - K\Omega_I\right)T_2}{1 + K^2}\Delta, \tag{2.91}$$

$$\frac{1 - \Delta}{\tau_0} = 4\Omega_R B - 4\Omega_I A - 4G_I\left(A^2 + B^2\right), \tag{2.92}$$

with

$$\Delta = \rho_{11} - \rho_{22}, \tag{2.93}$$

$$K = \left[(\omega - \omega_0) + G_R \Delta\right] T_2, \tag{2.94}$$

$$\omega_0 = \frac{\varepsilon_2 - \varepsilon_1}{\hbar}, \tag{2.95}$$

$$\frac{1}{T_2} = \frac{1}{T_{20}} + G_I, \tag{2.96}$$

$$G = \frac{s_a^2 \gamma a^3 \mu^2}{\hbar \varepsilon_{eff1} \varepsilon_{eff2} R^6}, \tag{2.97}$$

$$G_R = \mathrm{Re}\left[G\right], \tag{2.98}$$

$$G_I = \mathrm{Im}\left[G\right], \tag{2.99}$$

$$\Omega_{eff} = \Omega_0 \left[1 + s_\alpha \gamma \left(\frac{a}{R}\right)^3\right], \tag{2.100}$$

$$\Omega_0 = \frac{\mu E_0}{2\hbar \varepsilon_{eff1}}, \tag{2.101}$$

$$\Omega_R = \mathrm{Re}\left[\Omega_{eff}\right], \tag{2.102}$$

and

$$\Omega_I = \mathrm{Im}\left[\Omega_{eff}\right]. \tag{2.103}$$

If one assumes the external field to be weak ($\Omega_0 << \frac{1}{T_2}, \frac{1}{\tau}$), steady state solution in the following form will result

$$\bar{\rho}_{12} = -\frac{\Omega_{eff}}{(\omega - \omega_0 + G_R) - i\left(\Gamma_{12} + G_I\right)}. \tag{2.104}$$

The interpretation of Equation 2.104 is as follows. The interaction between the plasmon and the exciton leads to the formation of hybrid exciton with shifted exciton frequency

and decreased lifetime determined by G_R and G_I, respectively. The long-range Coulomb coupling leads to incoherent energy transfer at the rate G_I via Förster mechanism while the exciton shift G_R shows the partially coherent nature of the interaction.

2.4.2 Energy Absorption Spectra

In this subsection, the effect of plasmon-exciton interaction on the energy absorption rate of the hybrid nanostructure in both the weak and strong field regime will be studied. The total energy absorption rate of the hybrid nanostructure is given by

$$Q = Q_{MP} + Q_{SQD}, \tag{2.105}$$

where

$$Q_{MP} = \left\langle \int \mathbf{j}\mathbf{E} dV \right\rangle, \tag{2.106}$$

$$Q_{SQD} = \frac{\hbar\omega_0 \rho_{22}}{\tau_0} \tag{2.107}$$

are the absorption rate of the MP and SQD, respectively. Here, $\mathbf{j}$ is the current, $\langle ... \rangle$ is the average over time and ω_0 is the bare exciton frequency. After rigorous calculations, the expression of total energy absorption becomes

$$Q = C\Omega_0^2 \left[\frac{(K-q)^2}{1+K^2} + \alpha \frac{1}{1+K^2} \right] + \beta \frac{\hbar\omega_0}{1+K^2}, \tag{2.108}$$

where

$$q = \frac{s_\alpha \mu^2 \Omega_R T_2 \Delta}{\hbar \varepsilon_{eff1} \varepsilon_{eff2} R^3 \Omega_0}, \tag{2.109}$$

$$C = \frac{1}{6} \left(\frac{2\hbar}{\mu} \right)^2 a^3 \omega \left| \frac{3\varepsilon_0}{2\varepsilon_0 + \varepsilon_m} \right|^2 \mathrm{Im}\left(\varepsilon_m\right) \tag{2.110}$$

as well as K and Ω_0 are given in Equations 2.94 and 2.101, respectively. For the weak field regime, $\alpha = \left(\frac{1}{1+G_I T_{20}}\right)^2$ and $\beta = \left|4\Omega_{eff}\right|^2 \frac{T_2^2}{T_{20}}$ while for the strong field regime, $\alpha = 1$ and $\beta = \frac{1}{2\tau_0}$. In the discussion that follows, gold (Au) MP with bulk dielectric constant $\varepsilon(\omega)$ taken from Palik (1985) will be used as our example. The values for the rest of the parameters are provided in Table 2.1.

Table 2.1: Numerical values of various parameters used in Figures 2.2-2.4.

Parameters	Numerical Values
a	7.5 mm
ε_0	1.0
ε_s	6.0
ω_0	2.5 eV
τ_0	0.8 ns
T_{20}	0.3 ns
r_0	0.65 nm

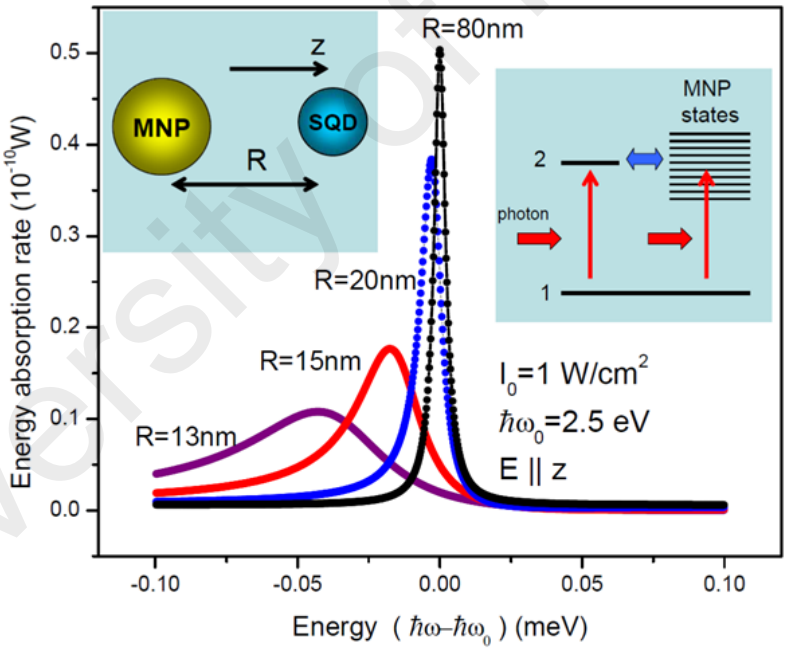

Figure 2.2: Absorption spectra in the weak field regime with light intensity $I = 1$ W/cm^2 for different interparticle distances. Here, ω denotes the frequency of the incident laser light whereas $\hbar\omega_0$ is the bare exciton energy. Left inset: The model of the system under study. Right inset: Quantum transitions in the system; the vertical (horizontal) arrows represent light (Coulomb)-induced transitions (Zhang et al., 2006).

Figure 2.2 shows the spectrum of the total energy absorption rate in the weak field regime where the intensity of the incident light is $I_0 = 1$ W/cm^2. Red shifting and

broadening of the energy absorption peak with decreasing interparticle distance R can be clearly observed from the figure. This behavior is due to the formation of hybrid exciton with shifted frequency and shortened lifetime at relatively small R. The results in Figure 2.2 predicts the frequency shift to be about 40 μeV for small separations of $R \simeq 15$ nm.

The energy absorption spectrum in the strong field regime shown in Figure 2.3 exhibits a different behavior where asymmetrical Fano shape and substantial suppression of energy absorption at higher frequencies are observed. The asymmetric shape of the spectrum which vanishes at large R originates from the Coulomb coupling between the MP and the SQD. This asymmetry is interesting because in the usual linear Fano effect, the interference effect causes the absorption rate to become zero for certain range of frequencies (Fano, 1961) yet such is not the case in Figure 2.3 where nonvanishing energy absorption at any light frequency is found. This is actually due to the nonlinear nature of the interference effect (Finkelstein-Shapiro, 2016). To understand this, one has to examine Equations 2.83 and 2.84 where it can be deduced that the effective field applied to SQD and MP is the superposition of the external and the induced internal field. The nonlinear interference of the external and induced field as represented by the nonlinear coupled equations in Equations 2.90-2.92 gives rise to the asymmetric Fano shape. Note that in Figure 2.3 one can again observe red shift in the resonant frequency as R decreases.

To explain why symmetric shape is observed for the weak field regime in Figure 2.2 but nonlinear Fano shape is observed for the strong field regime in Figure 2.3, one has to first look at the analytical form of the total absorption rate in Equation 2.108. In the weak field regime $\left(\Omega_0 << \frac{1}{T_2}, \frac{1}{\tau}\right)$, Q has the Fano function form in the limit $T_{20} \rightarrow \infty$. For a finite T_{20}, the finite broadening of the exciton peak destroys the linear Fano effect, giving rise to the symmetric peak (Figure 2.2). When the SQD is driven by strong field $\left(\Omega_0 >> \frac{1}{T_2}, \frac{1}{\tau}\right)$, the absorption peak becomes strongly suppressed as in an atom (Yariv,

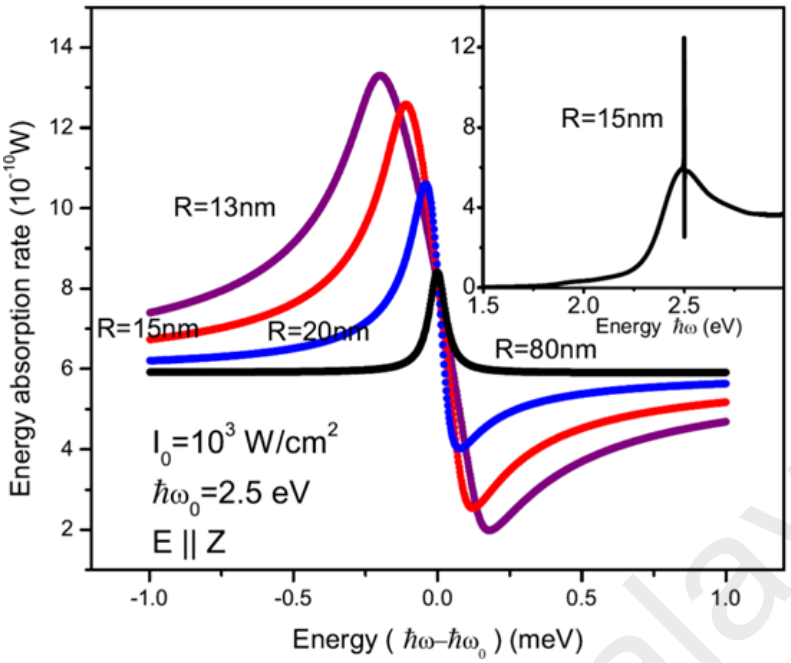

Figure 2.3: Absorption spectra in the strong field regime with light intensity $I = 10^3$ W/cm^2 for different interparticle distances. Inset: Absorption spectra for $R = 15$ nm in a wider frequency regime. Note that the exciton feature is within the plasmon peak (Zhang et al., 2006).

1989). As for the MP, it is assumed that the plasmon is not strongly excited due to the short lifetime of the plasmon (of order 10 fs). In general, the ac dipole moments of the MP and SQD increase simultaneously with the increase in the intensity. When this happens, the interference between the two channels of plasmon excitation in the MP (which corresponds to the first and second field terms in Equation 2.84) increases and thus greatly enhances the peak asymmetry even up to the point where the minimum of the absorption curve becomes comparable to peak height (Figure 2.3).

Finally, it is shown in Figure 2.4 the polarization dependence of the energy absorption spectrum. It is observed that the Fano absorption intensity has the opposite shape for the electric field polarization along the $z-$ and $x\,(y)-$directions. This is predictable since $s_\alpha\,(\alpha = x, y, z)$ in Equations 2.83 and 2.84 changes sign depending on the polarizations (z yields positive sign while x, y give negative sign), thus dictating the enhancement or suppression of the effective field.

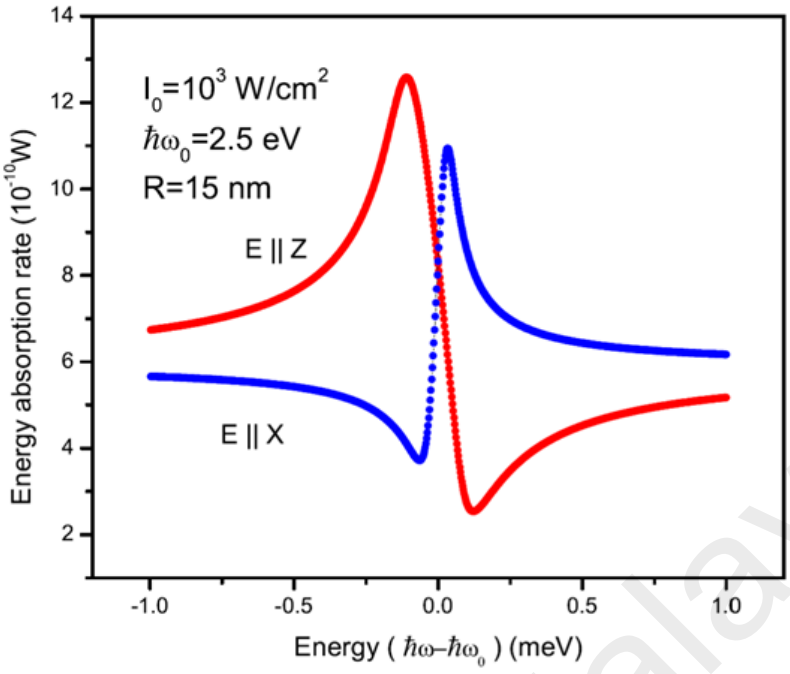

Figure 2.4: Absorption spectra in the strong field regime showing dependence on the polarization of the incident laser field (Zhang et al., 2006).

In short, the optical properties of a hybrid nanostructure composed of a MP and a SQD is studied from the energy absorption spectrum. The analytical theory predicts several interesting effects caused by the plasmon-exciton interaction such as exciton energy shift, Förster energy transfer and nonlinear interference effect. Nonlinear Fano absorption shape is observed in the strong field regime which has striking differences to the usual Fano effect. A point to note here is that the analytical theory developed here is based on semiclassical approach where the two-level SQD is treated quantum-mechanically via density matrix formalism while the MP is treated using classical electrodynamics. However, there are also cases where fully quantum-mechanical approach is necessary in the study of MP-SQD interaction. This approach will be reviewed in the next section.

2.5 Metallic Nanoparticle-Quantum System Interaction: Full Quantum Treatment

The analytical theory on MP-SQD interaction reviewed in section 2.4 was based on semiclassical treatment. Since the Fano effect in quantum systems is a consequence of

quantum interference, a full quantum theory is necessary for a reliable description of the nonlinear Fano effect. Here in this section, the full quantum treatment of the problem of MP-SQD interaction where both the exciton and plasmon are treated on equal footing will be reviewed. It will later be shown that the absorption spectra obtained from semiclassical and quantum theories exhibits striking differences in the strong nonlinear regime. Two quantum approaches will be presented, one based on density matrix formalism and another on Zubarev's Green function approach (Manjavacas et al., 2011). The full quantum theory reviewed here can be applied to other systems where quantum nature is important, for example, systems with discreet spectrum showing confined Fano effect.

2.5.1 Density Matrix Formalism

The model in this study is the same as the one highlighted in 2.4.1 (Figure 2.5), except that the plasmon is now treated quantum-mechanically. One can see from Figure 2.5(b) that both exciton and plasmon are assumed to share a common ground state $|0\rangle$. The excited state $|e\rangle$ of the exciton is coupled to $|0\rangle$ through a dipole transition with moment μ. The plasmon, on the other hand, has a large number of excited states denoted by $|j\rangle$ which are coupled to the ground state via dipole moment μ_j. The total Hamiltonian of the hybrid nanostructure is given by

$$H = H_0 + H_{int}, \tag{2.111}$$

where

$$\begin{aligned} H_0 &= \varepsilon_0 c_0^\dagger c_0 + \varepsilon_e c_e^\dagger c_e - \frac{E\mu}{\varepsilon_{eff1}}\left(c_0^\dagger c_e + c_e^\dagger c_0\right) \\ &\quad + \sum_j \varepsilon_j c_j^\dagger c_j - E\sum_j \mu_j \left(c_0^\dagger c_j + c_j^\dagger c_0\right), \end{aligned} \tag{2.112}$$

$$H_{int} = \sum_j \left(H_{je} c_j^\dagger c_e + H_{ej} c_e^\dagger c_j \right), \tag{2.113}$$

and c_0 is the annihilation operator for the common ground state, c_e (c_j) is the annihilation operator for the excited state of the exciton (plasmon), μ (μ_j) is the dipole moment between the ground state and the exciton-excited state (plasmon-excited state), $\varepsilon_{eff1} = \frac{2\varepsilon_0 + \varepsilon_s}{3\varepsilon_0}$ with ε_0 and ε_s as the dielectric constants of the background and SQD, respectively and H_{ej} is the interaction amplitude between the exciton and plasmon. Note that the effective dielectric constant of the MP has been absorbed into μ_j.

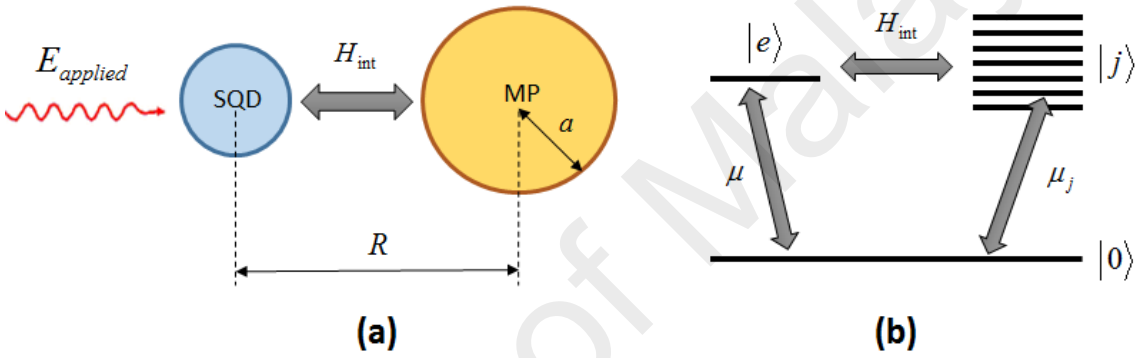

Figure 2.5: (a) The model of the hybrid nanostructure under study and (b) Energy level diagram of the hybrid system.

The dynamics of the system is governed by master equation of the form

$$\frac{d\rho}{dt} = -\frac{i}{\hbar}[H, \rho] - \frac{1}{2}\{\Gamma, \rho\}, \tag{2.114}$$

where the second term on the RHS describes possible dissipation effects. Applying the rotating wave approximation, one will arrive at the coupled equations

$$\frac{d\bar{\rho}_{ee}}{dt} = i\Omega_1 (\bar{\rho}_{0e} - \bar{\rho}_{e0}) + \frac{i}{\hbar} \sum_j \left(H_{je}\bar{\rho}_{ej} - H_{ej}\bar{\rho}_{je} \right) - \Gamma_e \bar{\rho}_{ee}, \tag{2.115}$$

$$\frac{d\bar{\rho}_{0e}}{dt} = i(\omega_0 - \omega)\bar{\rho}_{0e} + i\Omega_1 (\bar{\rho}_{ee} - \bar{\rho}_{00}) + \frac{i}{\hbar} \sum_j H_{je}\bar{\rho}_{0j} + i \sum_j \Omega_j \bar{\rho}_{je} - \Gamma_{0e}\bar{\rho}_{0e}, \tag{2.116}$$

$$\frac{d\bar{\rho}_{ej}}{dt} = i\left(\omega_j - \omega_0\right)\bar{\rho}_{ej} - i\Omega_j\bar{\rho}_{e0} + \frac{i}{\hbar}\sum_j H_{ej}\bar{\rho}_{ee} - \frac{i}{\hbar}H_{ek}\bar{\rho}_{kj} + i\Omega_1\bar{\rho}_{0j} - \Gamma_{ej}\bar{\rho}_{ej}, \quad (2.117)$$

$$\frac{d\bar{\rho}_{0j}}{dt} = i\left(\omega_j - \omega\right)\bar{\rho}_{0j} + i\sum_k \Omega_k\rho_{kj} - i\Omega_j\bar{\rho}_{00} + \frac{i}{\hbar}H_{ej}\bar{\rho}_{0e} + i\Omega_1\bar{\rho}_{ej} - \Gamma_{0j}\bar{\rho}_{0j}, \quad (2.118)$$

$$\frac{d\bar{\rho}_{jj}}{dt} = i\Omega_j\left(\bar{\rho}_{0j} - \bar{\rho}_{j0}\right) + \frac{i}{\hbar}\left(H_{ej}\bar{\rho}_{je} - H_{je}\bar{\rho}_{ej}\right) - \Gamma_j\bar{\rho}_{jj}. \quad (2.119)$$

Here the slow variables are defined as $\rho_{ee} = \bar{\rho}_{ee}, \rho_{0e} = \bar{\rho}_{0e}e^{i\omega t}, \rho_{0j} = \bar{\rho}_{0j}e^{i\omega t}, \rho_{ej} = \bar{\rho}_{ej}$ and $\rho_{kj} = \bar{\rho}_{kj}$. The frequency $\omega_j = \frac{\varepsilon_j - \varepsilon_0}{\hbar}$ and the Rabi frequencies are $\Omega_1 = \frac{\mu E_0}{2\hbar\varepsilon_{eff1}}$ and $\Omega_j = \frac{\mu_j E_0}{2\hbar}$. Here, steady-state solution is considered for the case with large dissipation in MP such that $\Gamma_{ej} \approx \frac{\Gamma_e + \Gamma_j}{2} \approx \frac{\Gamma_j}{2}$ and $\Gamma_{0j} \approx \frac{\Gamma_j}{2}$, as well as for the near resonant regime, i.e. $\omega \approx \omega_0$,

$$\gamma\rho_{ee} = -i\Omega_{eff}\bar{\rho}_{e0} + \text{H.c.}, \quad (2.120)$$

$$\left(\omega_0 - \omega + \gamma_{0e}\right)\bar{\rho}_{0e} = \Omega_{eff}\Delta, \quad (2.121)$$

where $\Delta = \rho_{00} - \rho_{ee}, \Omega_{eff} = \Omega_1 - \sum_j \frac{\Omega_j H_{je}}{\hbar\omega'_j}$ is the normalized field felt by the SQD with $\Omega_R = \text{Re}\left(\Omega_{eff}\right), \Omega_I = \text{Im}\left(\Omega_{eff}\right), \omega'_j = \omega_j - \omega + i\Gamma_{0j}$,

$$\gamma_{0e} = \sum_j \left[\frac{\Omega_j^2}{\omega_j'^*} - \frac{\left|H_{ej}\right|^2}{\hbar^2\omega'_j} + 4\,\text{Im}\left(\frac{1}{\hbar\omega'_j}\right)\frac{H_{je}\Omega_j\Omega_1}{\gamma}\right] + i\Gamma_{0e}, \quad (2.122)$$

and

$$\gamma = \Gamma_e + \sum_j \frac{2\left|H_{ej}\right|^2\Gamma_{ej}}{\hbar^2\left[\left(\omega_j - \omega_0\right)^2 + \Gamma_{ej}^2\right]}. \quad (2.123)$$

Hence, the steady-state solution for ρ_{ee} and $\bar{\rho}_{0e}$ is obtained as

$$\rho_{ee} = \frac{Y\left|\Omega_{eff}\right|^2}{K^2 + \tilde{\Gamma}_{0e}^2 + 2Y\left|\Omega_{eff}\right|^2}, \quad (2.124)$$

$$\bar{\rho}_{0e} = \frac{\left(K\Omega_R + \tilde{\Gamma}_{0e}\Omega_I\right) + i\left(K\Omega_I - \tilde{\Gamma}_{0e}\Omega_R\right)}{K^2 + \tilde{\Gamma}_{0e}^2 + 2Y\left|\Omega_{eff}\right|^2}, \quad (2.125)$$

where $K = \omega_0 - \omega + \delta, \delta = \mathrm{Re}(\gamma_{0e}), \tilde{\Gamma}_{0e} = \mathrm{Im}(\gamma_{0e})$ and $Y = \frac{2\tilde{\Gamma}_{0e}}{\gamma}$. Due to the fast dissipation of the MP, it is assumed that $\rho_{00} + \rho_{ee} \approx 1$. Just as in section 2.4, the MP-SQD interaction will be studied from the absorption spectra. After some calculations, the total energy absorption of the hybrid nanostructure is found to be

$$Q_{tot} = Q_{MP} + Q_{SQD}, \tag{2.126}$$

where

$$Q_{SQD} = \Gamma_e \rho_{ee} \hbar\omega_0, \tag{2.127}$$

$$Q_{MP} = \sum_j \Gamma_j \rho_{jj} \hbar\omega_j = \sum_j \frac{2\Gamma_{0j}\mu_j^2 \hbar\omega_j}{\left(\omega_j - \omega_0\right)^2 + \Gamma_{0j}^2} \frac{E_0^2}{(2\hbar)^2} F(K), \tag{2.128}$$

with

$$F(K) = \frac{(K - \beta_R)^2 + \left(\tilde{\Gamma}_{0e} - \beta_I\right)^2 + \left[\beta^2 (Y-1) + Y\right] \left|\Omega_{eff}\right|^2}{K^2 + \tilde{\Gamma}_{0e}^2 + 2Y \left|\Omega_{eff}\right|^2}. \tag{2.129}$$

Here, $\beta_R = \beta\Omega_R, \beta_I = \beta\Omega_I$ and $\beta = \frac{H_{ej}}{\hbar\Omega_j}$. Alternatively, one may write Equation 2.129 as

$$F = \frac{|\varepsilon + q|^2}{1 + \varepsilon^2} = \frac{(\varepsilon + q_R)^2}{1 + \varepsilon^2} + \frac{q_I^2}{1 + \varepsilon^2}, \tag{2.130}$$

where

$$\varepsilon = \frac{\omega - \omega_0 - \delta}{\sqrt{\tilde{\Gamma}_{0e}^2 + 2Y \left|\Omega_{eff}\right|^2}}, \tag{2.131}$$

$$q = q_R + i q_I, \tag{2.132}$$

$$q_R = \frac{H_{ej}\Omega_R}{\hbar\Omega_j} \frac{1}{\sqrt{\tilde{\Gamma}_{0e}^2 + 2Y \left|\Omega_{eff}\right|^2}}, \tag{2.133}$$

and

$$q_I = \sqrt{\frac{\left(\tilde{\Gamma}_{0e} - \beta_I\right)^2 + \left[\beta^2 (Y-1) + Y\right] \left|\Omega_{eff}\right|^2}{\tilde{\Gamma}_{0e}^2 + 2Y \left|\Omega_{eff}\right|^2}}. \tag{2.134}$$

The absorption rate of the entire hybrid nanostructure will be dominated by the absorption of MP under two conditions: strong laser field and short interparticle distance. This is due to the saturation effect of SQD (for strong laser field) and/or the fast dissipation of MP (for short interparticle distance). Due to the huge value of Γ_{0j}, the absorption line shape is largely determined by F, the Fano function.

A comparison is made in Figure 2.6 between the total energy absorption rate obtained from semiclassical theory and quantum theory. At the same time, the dependence of the absorption rate on the dipole moment, $\mu = er_0$ of the SQD as well as the laser intensity is also shown in the figure. The numerical values of all the related parameters are given in Table 2.2. It can be clearly observed from Figure 2.6 that there is a good agreement for the total absorption rate between the semiclassical theory and quantum theory for the case of weak field or strong field off-resonance (left panel of Figure 2.6 with $\Delta \approx 1$). However, for the case with strong field (right panel of Figure 2.6 where $\Delta << 1$), the quantum results are significantly different from the semiclassical results. Generally speaking, the absorption line shape in quantum theory is more symmetrical than the one in semiclassical theory.

Table 2.2: Numerical values of various parameters used in Figure 2.6.

Parameters	**Numerical Values**
ε_b	2.0 (polymer)
ε_s	7.2 (CdTe)
R	15 nm
a	7.5 nm

Furthermore, one can observe another peculiar behavior in the absorption spectrum in Figure 2.6(f) for the case of strong field and large exciton dipole. It is shown that the semiclassical theory exhibits instabilities in the small energy window near resonance. In this near resonance regime, there are three steady-state solutions with different values of exciton excited state population and absorption rate for each frequency. These three

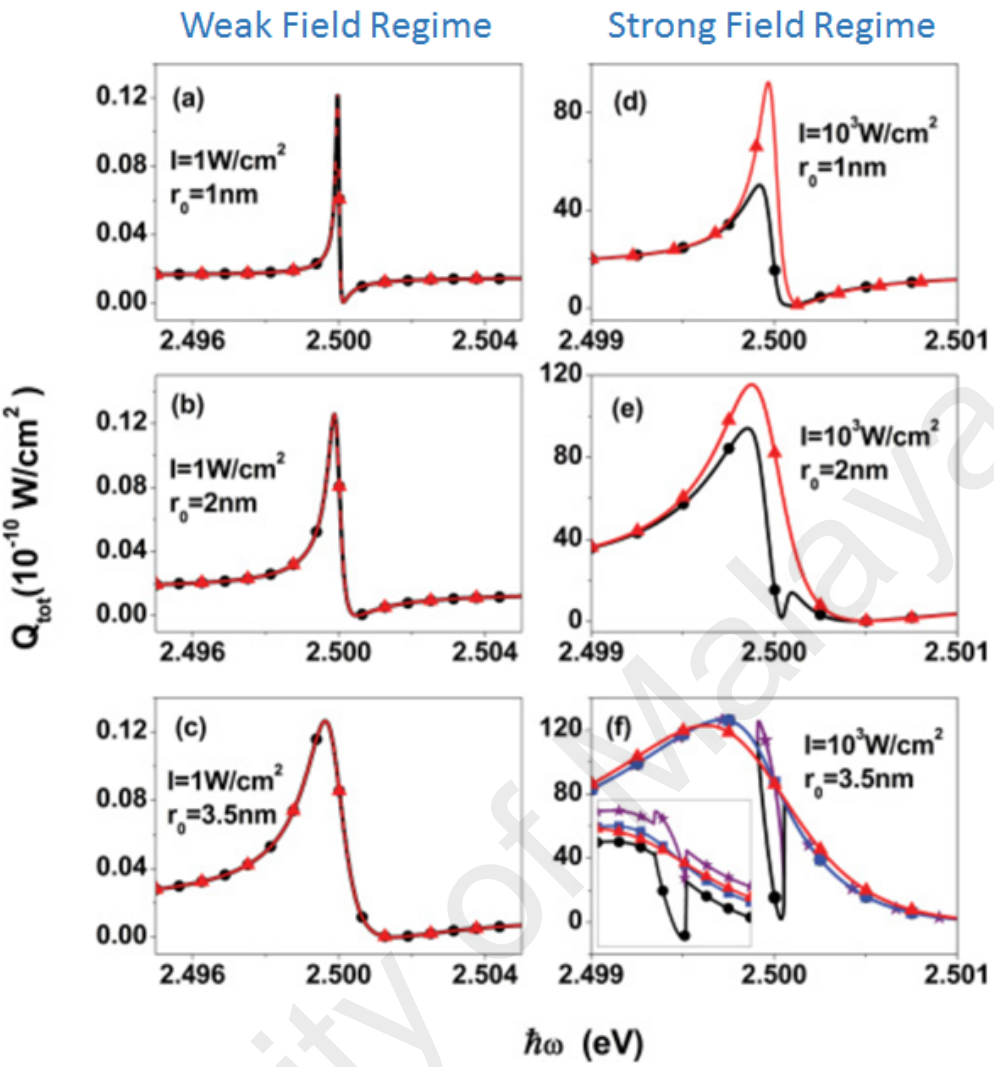

Figure 2.6: Total energy absorption spectra obtained from semiclassical theory (black curves with dots) and fully quantum theory (red curves with triangles) for different values of dipole moment of the SQD in both weak and strong field regime. (a)-(c) are for the weak regime and (d)-(f) are for the strong field regime. In (f), the black curve with dots, blue curve with squares and purple curve with stars represent the three nonlinear steady states solutions obtained from the semiclassical theory. The inset in (f) is the magnification of the curves in the near resonance regime. Note that the curves in the inset have been shifted for clearer view (Zhang & Govorov, 2011).

steady-state solutions are represented by the black curve with dots, blue curve with squares and purple curve with stars in Figure 2.6(f). Beyond the near resonance energy window, all three curves collapse to only one curve. Another interesting observation is in Figure 2.6(e) where the black curve shows zero total absorption (induced transparency effect). In contrast, the absorption spectrum from quantum theory (red lines with triangles) does not show instabilities and transparency effects for any values of dipole moment and laser

field strengths. The explanation for the absence of instability and transparency effects in quantum theory is that the continuum states cannot be heavily populated since the population nonlinearity for the MP cannot be achieved at the light power considered here.

The main result of this subsection is the striking difference between semiclassical and full quantum theory in terms of their absorption spectra in the strong field regime. This result shows that full quantum theory is needed in explaining the behavior of the MP-SQD when the laser field is strong. Now that the problem has been solved via density matrix method it is appropriate to look at another interesting full quantum approach in solving MP-SQD interaction termed "Zubarev's Green function formalism".

2.5.2 Zubarev's Green Function Formalism

This subsection presents a fully quantum-mechanical approach for modelling the optical response of plasmons interacting with a quantum emitter based on Zubarev's Green functions (Zubarev, 1960). While this method has been successfully applied to different problems in statistical physics and linear response theory (Tsukada & Brenig, 1985; Pike & Swain, 1971; Nordlander & Avouris, 1986), it has recently been adapted to study the optical absorption rate of a hybrid nanostructure formed by a metallic nanoparticle and a quantum emitter (such as SQD) (Manjavacas et al., 2011) similar to the system in section 2.4 and subsection 2.5.1. This approach enables us to describe the internal evolution of such quantum systems beyond the perturbative regime, thus helping us to take advantage of their quantum features, such as collective and single-particle excitations, and quantum correlations and interferences.

Below shows the application of Zubarev's Green functions to the problem of MP-SQD interaction as illustrated in Figure 2.5(a). The absorption spectra obtained from the retarded Zubarev's Green function of the quantum operators that mediate the photon absorption process will be computed. Before that, the basics of this formalism and how

it could lead us to the analytical form of the absorption spectrum will be reviewed first.

The retarded Zubarev Green function of the annihilation and creation operators, A and $A^\dagger$ of a quantum system is defined in the frequency domain as

$$\left\langle\left\langle A(\omega); A^\dagger(\omega)\right\rangle\right\rangle_{\omega+i0^+} = -\frac{i}{\hbar}\int_{-\infty}^{\infty} dt e^{i(\omega+i0^+)t}\theta(t)\left\langle\left[A(t), A^\dagger(0)\right]_\eta\right\rangle, \tag{2.135}$$

where $A(t)$ is the Heisenberg representation of operator A, $\theta(t)$ is the Heaviside step function, $\left[A, A^\dagger\right]_\eta = AA^\dagger - \eta A^\dagger A$ is the commutator of bosonic operators ($\eta = 1$) or the anticommutator of fermionic operators ($\eta = -1$), $i0^+$ is added to ensure convergence of the integral and $\langle\langle ... \rangle\rangle$ is just a notation to represent the Zubarev Green function (not related to expectation value). The time-evolution of $A(t)$ is described by the Heisenberg equation of motion, which for fixed excitation energy ε_f leads to the solution

$$A(t) = A(0)\, e^{-i\varepsilon_f t/\hbar}. \tag{2.136}$$

Using Equation 2.136, one can now write Equation 2.135 as

$$\left\langle\left\langle A(\omega); A^\dagger(\omega)\right\rangle\right\rangle_{\omega+i0^+} = -\frac{i}{\hbar}\int_{0}^{\infty} dt e^{-i\left[(\varepsilon_f-\hbar\omega-i0^+)t\right]/\hbar}\left[\left\langle A(0)\, A^\dagger(0)\right\rangle - \eta\left\langle A^\dagger(0)\, A(0)\right\rangle\right], \tag{2.137}$$

where $\left\langle A(0)\, A^\dagger(0)\right\rangle$ and $\left\langle A^\dagger(0)\, A(0)\right\rangle$ denote the expectation values associated with the initial state $|i\rangle$ of the system. In our system, the initial state is assumed to be the ground state (at $T = 0$ K). In this case, the second term on the RHS of Equation 2.137 vanishes since $\langle i|\, A^\dagger(0)\, A(0)\, |i\rangle = 0$. Solving the integral in Equation 2.137, one arrives at

$$\left\langle\left\langle A(\omega); A^\dagger(\omega)\right\rangle\right\rangle_{\omega+i0^+} = -\frac{\left\langle A(0)\, A^\dagger(0)\right\rangle}{\varepsilon_f - \hbar\omega - i0^+}, \tag{2.138}$$

The optical absorption cross section is given by Fermi's Golden rule as

$$\sigma(\omega) = \frac{2\pi\rho}{\hbar\phi} \sum_f |\langle f; n-1| H_{int} |i; n\rangle|^2 \, \delta\left(\varepsilon_f - \hbar\omega\right), \tag{2.139}$$

where $|i\rangle$ and $|f\rangle$ represent the initial and final state of the system, respectively, ε_f is the energy difference between the initial and final state, n is the number of external photons with frequency ω, ρ is the density of final state (number of states per unit energy), ϕ is the photon flux through the target (with the dimension of per unit area per unit time) (Perkins, 2000) and H_{int} is the interaction Hamiltonian that couples the system to the external photon given by

$$H_{int} = \Delta_{Aa}\left(Aa^\dagger + A^\dagger a\right), \tag{2.140}$$

where a and $a^\dagger$ are the annihilation and creation operators for the external photons, respectively. Using the interaction Hamiltonian in Equation 2.140 and the identity

$$\delta(x) = \mathrm{Im}\left(\frac{1}{x - i0^+}\right), \tag{2.141}$$

Equation 2.139 becomes

$$\sigma(\omega) = \frac{2\pi\rho}{\hbar\phi} \mathrm{Im}\left\{\sum_f \frac{\langle i; n| H_{int} |f; n-1\rangle \langle f; n-1| H_{int} |i; n\rangle}{\varepsilon_f - \hbar\omega - i0^+}\right\}. \tag{2.142}$$

Equation 2.142 can be further simplified using $a|n\rangle = \sqrt{n}|n-1\rangle$ as well as the orthogonality of the photonic states $\langle n|n'\rangle = \delta_{n,n'}$ into

$$\sigma(\omega) = \frac{2\pi\rho}{\hbar\phi} \mathrm{Im}\left\{\sum_f \frac{\langle i| A |f\rangle \langle f| A^\dagger |i\rangle}{\varepsilon_f - \hbar\omega - i0^+}\right\}. \tag{2.143}$$

Here, it is assumed that $A^\dagger$ connects the initial ground state to a set of final states separated

by a common energy ε_f. This assumption is good enough for this study in which the external photons couple through the excitation of a single particle plasmon. Hence, one may extract the ε_f from the sum over final states and using the closure relation $\sum_f |f\rangle \langle f| = \hat{I}$ (within the ε_f reachable-energy shell), Equation 2.143 becomes

$$\sigma(\omega) = \frac{2\pi\rho}{\hbar\phi} \operatorname{Im}\left\{\frac{\langle i| AA^{\dagger} |i\rangle}{\varepsilon_f - \hbar\omega - i0^{+}}\right\}. \tag{2.144}$$

Finally, by realizing that $\langle i| AA^{\dagger} |i\rangle$ in Equation 2.144 and $\left\langle A(0) A^{\dagger}(0)\right\rangle$ in Equation 2.138 carry the same magnitude in the Schrödinger and Heisenberg picture, respectively, one can substitute Equation 2.138 into Equation 2.144 to obtain

$$\sigma(\omega) = -\frac{2\pi\rho}{\hbar\phi} \operatorname{Im}\left\{\left\langle\left\langle A(\omega); A^{\dagger}(\omega)\right\rangle\right\rangle_{\omega+i0^{+}}\right\}, \tag{2.145}$$

which relates the Zubarev's Green function to the absorption spectra.

The Green function on the RHS of Equation 2.145 is usually calculated by writing its equation of motion. To derive the equation of motion, it is necessary to first obtain the retarded Zubarev Green function $\left\langle\left\langle A; A^{\dagger}\right\rangle\right\rangle$ in time domain by performing inverse Fourier transformation on Equation 2.135. This leads us to

$$\left\langle\left\langle A(t); A^{+}(0)\right\rangle\right\rangle = -\frac{i}{\hbar}\theta(t)\left\langle\left[A(t), A^{\dagger}(0)\right]_{\eta}\right\rangle. \tag{2.146}$$

Multiplying each term by i and differentiating with respect to time, one gets

$$i\frac{d}{dt}\left\langle\left\langle A(t); A^{+}(0)\right\rangle\right\rangle = \frac{1}{\hbar}\frac{d\theta(t)}{dt}\left\langle\left[A(t), A^{\dagger}(0)\right]_{\eta}\right\rangle + \left\langle\left\langle i\frac{dA(t)}{dt}; A^{\dagger}(0)\right\rangle\right\rangle, \tag{2.147}$$

which can be simplified using Heisenberg equation of motion $\frac{dA}{dt} = \frac{i}{\hbar}[H, A]$ to yield

$$\hbar \frac{d}{dt} \left\langle\left\langle A(t) ; A^{+}(0)\right\rangle\right\rangle = \delta(t) \left\langle\left[A(t), A^{\dagger}(0)\right]_{\eta}\right\rangle + \left\langle\left\langle [A, H] ; A^{\dagger}(0)\right\rangle\right\rangle . \tag{2.148}$$

where H is the Hamiltonian of the system and $[A, H] = AH - HA$. Taking the Fourier transform of Equation 2.148, one will arrive at

$$\hbar\omega \left\langle\left\langle A(\omega) ; A^{+}(\omega)\right\rangle\right\rangle_{\omega+i0^{+}} = \left\langle\left[A(\omega), A^{\dagger}(\omega)\right]_{\eta}\right\rangle + \left\langle\left\langle [A(\omega), H(\omega)] ; A^{\dagger}(\omega)\right\rangle\right\rangle, \tag{2.149}$$

which is the most simplified version of the equation of motion for $\langle\langle A; A^{+}\rangle\rangle$ in frequency domain from which the analytical form of $\langle\langle A; A^{+}\rangle\rangle$ can be found. However, Equation 2.149 depends on another Green function $\left\langle\left\langle [A, H] ; A^{\dagger}\right\rangle\right\rangle$, which can also be calculated by writing down it equation of motion. Iterating this process, one obtains a hierarchy of equations that have to be truncated at some point via application of a physical approximation. The result is a linear system of equations from which after solving, $\langle\langle A; A^{+}\rangle\rangle$ (and therefore $\sigma(\omega)$) is obtained.

Now the results in Equations 2.135, 2.145 and 2.149 will be applied to our study of MP-SQD interaction. The system considered here comprises of a small MP (with diameter of tens of nanometers) located close to a SQD. The coupled plasmon-exciton system will result in a hybrid plasmonic excitonic modes referred to as Plexcitons (Manjavacas et al., 2011). Here, it is assumed that the MP support a well-defined dipolar plasmon mode whereas the SQD is a fermionic system with only two possible states (ground and excited states). Also, the usual dipole approximation will be applied to the MP where higher-multipole modes are neglected. This approximation is reasonable for noble-metal particle with radius much smaller than the wavelength.

The total Hamiltonian of the system is given by

$$H = H_0 + H_{int} + H_{decay} \tag{2.150}$$

where

$$H_0 = \varepsilon_d d^\dagger d + \varepsilon_c c^\dagger c \tag{2.151}$$

is the free Hamiltonian,

$$H_{int} = -\Delta_{dc}\left[d^\dagger c + c^\dagger d\right] \tag{2.152}$$

is the interaction Hamiltonian and

$$\begin{aligned} H_{decay} &= \int \hbar\omega f_d^\dagger(\omega) f_d(\omega) d\omega + \int \hbar\omega f_c^\dagger(\omega) f_c(\omega) d\omega \\ &\quad - \int \left[\nu_d(\omega) f_d(\omega) d^\dagger + \nu_d^*(\omega) f_d^\dagger(\omega) d\right] d\omega \\ &\quad - \int \left[\nu_c(\omega) f_c(\omega) c^\dagger + \nu_c^*(\omega) f_c^\dagger(\omega) c\right] d\omega \end{aligned} \tag{2.153}$$

is the Hamiltonian describing the decay of plasmon and exciton. This decay term is used to realistically account for the finite lifetime in the excitations of the system which originates from the inelastic interaction of the excitations with a continuum of modes. For example, a plasmon can decay radiatively by emitting a photon and nonradiatively through generation of electron-hole pairs, phonons, etc. Here, d and c ($d^\dagger$ and $c^\dagger$) are the annihilation (creation) operators for the MP plasmon and SQD fermion of energies ε_d and ε_c, respectively, Δ_{dc} is the plasmon-exciton coupling strength (taken to be real), and $f_d(\omega)$ and $f_c(\omega)$ are the annihilation operators of the continuum modes coupled to the plasmon and fermion with coupling constant $\nu_d(\omega)$ and $\nu_c(\omega)$, respectively.

Since the absorption cross section of the MP is generally much larger than that of the

SQD, one may obtain the absorption spectrum from the Green function $\langle\langle d; d^{+}\rangle\rangle$ via

$$\sigma(\omega) = -\frac{2\pi\rho}{\hbar\phi}\,\mathrm{Im}\left\{\left\langle\left\langle d; d^{+}\right\rangle\right\rangle_{\omega+i0^{+}}\right\}, \tag{2.154}$$

From Equations 2.149 and 2.150, the equation of motion for $\langle\langle d; d^{+}\rangle\rangle$ is

$$(\hbar\omega - \varepsilon_d)\left\langle\left\langle d; d^{\dagger}\right\rangle\right\rangle = 1 - \Delta_{dc}\left\langle\left\langle c; d^{\dagger}\right\rangle\right\rangle - \int \nu_d(\omega')\left\langle\left\langle f_d(\omega'); d^{\dagger}\right\rangle\right\rangle d\omega'. \tag{2.155}$$

Now, there is a need to compute $\left\langle\left\langle c; d^{\dagger}\right\rangle\right\rangle$ and $\left\langle\left\langle f_d(\omega'); d^{\dagger}\right\rangle\right\rangle$ to get $\left\langle\left\langle d; d^{\dagger}\right\rangle\right\rangle$. The equation of motion for $\left\langle\left\langle c; d^{\dagger}\right\rangle\right\rangle$ is given by

$$\begin{aligned}(\hbar\omega - \varepsilon_c)\left\langle\left\langle c; d^{\dagger}\right\rangle\right\rangle &= -\Delta_{dc}\left\langle\left\langle\left(1 - 2c^{\dagger}c\right) d; d^{\dagger}\right\rangle\right\rangle \\ &\quad - \int \nu_c(\omega')\left\langle\left\langle\left(1 - 2c^{\dagger}c\right) f_c(\omega'); d^{\dagger}\right\rangle\right\rangle d\omega'. \end{aligned}\tag{2.156}$$

Again, new Green functions $\left\langle\left\langle\left(1 - 2c^{\dagger}c\right) d; d^{\dagger}\right\rangle\right\rangle$ and $\left\langle\left\langle\left(1 - 2c^{\dagger}c\right) f_c(\omega'); d^{\dagger}\right\rangle\right\rangle$ emerge. If one continues to iterate this process he will produce an infinite hierarchy of equations of motion. Here this process will be truncated at this point by approximating $c^{\dagger}c$ by its expectation value $\left\langle c^{\dagger}c\right\rangle = n_c$, which is the result of the fermionic character of the SQD. However, one still needs to deal with $\left\langle\left\langle f_d(\omega'); d^{\dagger}\right\rangle\right\rangle$ and $\left\langle\left\langle f_c(\omega'); d^{\dagger}\right\rangle\right\rangle$. Derivations of their equations of motion gives

$$(\hbar\omega - \hbar\omega')\left\langle\left\langle f_d(\omega'); d^{\dagger}\right\rangle\right\rangle = -\nu_d^{*}(\omega')\left\langle\left\langle d; d^{\dagger}\right\rangle\right\rangle, \tag{2.157}$$

$$(\hbar\omega - \hbar\omega')\left\langle\left\langle f_c(\omega'); d^{\dagger}\right\rangle\right\rangle = -\nu_c^{*}(\omega')\left\langle\left\langle c; d^{\dagger}\right\rangle\right\rangle, \tag{2.158}$$

which show that they only depend on Green functions derived above. Thus, one now has a set of four closed coupled equations given by Equations 2.155, 2.156, 2.157 and 2.158.

There is a need to solve for the integral terms in Equations 2.155 and 2.156. Substitution of Equation 2.157 into Equation 2.155 and introduction of the positive infinitesimal imaginary part of the frequency which appears in Equation 2.135 gives the result

$$\begin{aligned}\int \nu_d(\omega')\left\langle\left\langle f_d(\omega');d^\dagger\right\rangle\right\rangle d\omega' &= \left\langle\left\langle d;d^\dagger\right\rangle\right\rangle\int\frac{|\nu_d(\omega')|^2}{(\hbar\omega'-\hbar\omega-i0^+)}d\omega' \\ &= \left\langle\left\langle d;d^\dagger\right\rangle\right\rangle\left[\mathcal{P}\int d\omega'\frac{|\nu_d(\omega')|^2}{\hbar\omega'-\hbar\omega}+i\pi|\nu_d(\omega')|^2\right] \\ &= \left\langle\left\langle d;d^\dagger\right\rangle\right\rangle\left[\delta\omega_d+i\frac{\Gamma_d}{2}\right], \end{aligned} \tag{2.159}$$

where the Sokhatsky-Weierstrass theorem has been used, $\mathcal{P}$ is Cauchy principal value, $\delta\omega_d$ is frequency shift and $\Gamma_d = 2\pi|\nu_d(\omega')|^2$ inelastic decay rate of dipolar plasmon. If one solves in a similar way for the integral term in Equation 2.156, Equations 2.155 and 2.156 will become

$$\left(\hbar\omega-\varepsilon_d+\delta\omega_d+i\frac{\Gamma_d}{2}\right)\left\langle\left\langle d;d^\dagger\right\rangle\right\rangle = 1-\Delta_{dc}\left\langle\left\langle c;d^\dagger\right\rangle\right\rangle, \tag{2.160}$$

$$\left(\hbar\omega-\varepsilon_c+(1-2n_c)\left[\delta\omega_c+i\frac{\Gamma_c}{2}\right]\right)\left\langle\left\langle c;d^\dagger\right\rangle\right\rangle = -\Delta_{dc}(1-2n_c)\left\langle\left\langle d;d^\dagger\right\rangle\right\rangle, \tag{2.161}$$

which form two closed coupled equations from which $\left\langle\left\langle d;d^\dagger\right\rangle\right\rangle$ and thus $\sigma(\omega)$ can be calculated. After a simple calculation, the absorption spectrum will become

$$\sigma(\omega) = -\frac{2\pi\rho}{\hbar\phi}\,\mathrm{Im}\left(\hbar\omega-\varepsilon_d+\delta\omega_d+i\frac{\Gamma_d}{2}-\frac{\Delta_{dc}^2(1-2n_c)}{\hbar\omega-\varepsilon_c+(1-2n_c)\left[\delta\omega_c+i\frac{\Gamma_c}{2}\right]}\right)^{-1}. \tag{2.162}$$

Figures 2.7-2.9 show the absorption spectrum for the MP-SQD system computed for different values of the exciton resonance energy ε_c, exciton resonance width Γ_c and plasmon-exciton coupling strength Δ_{dc}, respectively. A comparison is made between the spectra obtained from Zubarev Green function method (black continuous line) and with

that obtained from density matrix formalism (red dashed line) highlighted in subsection 2.5.1. Here, $\varepsilon_d = 2.5$ eV which is the plasmon resonance energy for gold nanoparticle and $\Gamma_d = 86$ meV as the corresponding dipolar plasmon width. Also, is it assumed that the frequency shifts $\delta\omega_d \approx \delta\omega_c \approx 0$ is negligible and the photon number is calculated from $n_c = [\exp(\varepsilon_c/k_BT) - 1]^{-1}$ at temperature $T = 300K$. The values for other parameters are given in the caption of each figures.

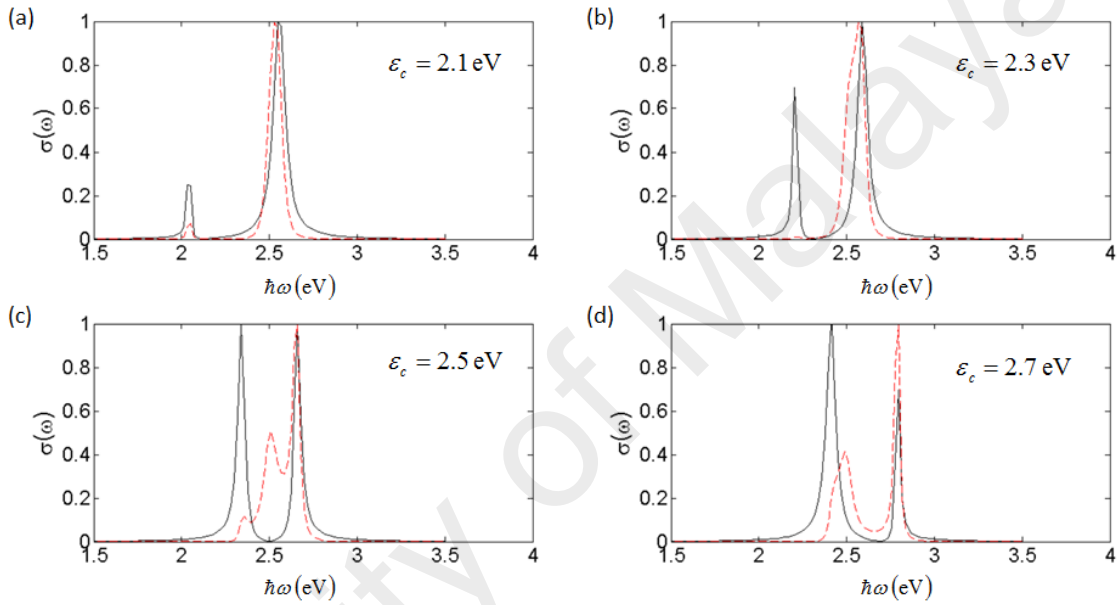

Figure 2.7: Dependence of the absorption spectrum of the MP-SQD system on the exciton resonance energy, ε_c. The black continuous line is the absorption spectrum obtained from Zubarev Green function formalism whereas the red dashed line is the absorption spectrum obtained from density matrix method developed in subsection 2.5.1. Here, we use the value $\Gamma_c = 4$ meV for the exciton resonance width and $\Delta_{dc} = 160$ meV for the plasmon-exciton coupling strength. A Fano resonance is clearly visible as a result of the plasmon-exciton coupling.

By looking at the black curve, one can easily identify the origin of the absorption peaks in Figure 2.7(a),(b),(d): dipolar plasmon mode at around $\varepsilon_d = 2.5$ eV and excitonic mode ε_c. One can also observe from Figure 2.7(c) that when the exciton resonance energy matches the plasmon resonance energy, i.e. $\varepsilon_c = \varepsilon_d = 2.5$ eV, Fano resonance occurs. This Fano resonance is a result of the interaction between the continuum modes of the plasmons and the narrow discreet mode of the exciton. The line shape of the Fano

resonance depends strongly on the resonance energy of the exciton as shown in Figure 2.7. The spectra obtained using density matrix formalism (red dashed line) also exhibit Fano resonances but the line shapes are less symmetrical. It can also be observed from Figure 2.7 that the red curves show larger deviations from the black ones at higher exciton energy.

Figure 2.8 shows the dependence of the Fano resonance on the width of the exciton. Both black and red curves show that the Fano resonance is the strongest when exciton resonance width is the smallest and slowly disappears when the width grows larger. The coupling strength also plays an important role in determining the shape of the Fano resonance, as shown in Figure 2.9. For both black and red curves, the dip associated with the Fano resonance disappears when the plasmon-exciton coupling is weak (Δ_{dc} is small). As Δ_{dc} increases, the Fano dip becomes deeper and the separation between the resulting peaks becomes more pronounced. Actually, when Δ_{dc} is larger than $\frac{\Gamma_d}{2}$ one can alternatively interpret the resulting line shape as vacuum Rabi splitting (Savasta et al., 2010). One may also observe from Figure 2.9(d) that density matrix formalism predicts the emergence of additional broader peaks which are believed to be a manifestation of the formation of hybrid excitons with shifted frequency and shortened lifetime.

The discrepancies between the spectra obtained from density matrix formalism and those from Zubarev's Green function may be due to the following reasons:

1. The standard density matrix formalism reviewed in subsection 2.5.1 considers some realistic effects on the absorption spectrum due to various parameters such as the background permittivity, incident laser fields strengths, interparticle distance, etc. On the other hand, such parameters are not considered in the Zubarev's Green function formalism in which only Δ_{dc} (which depends on dipole moment), Γ_c and ε_c dictate the degree to which plasmon and exciton interact and thus determine the

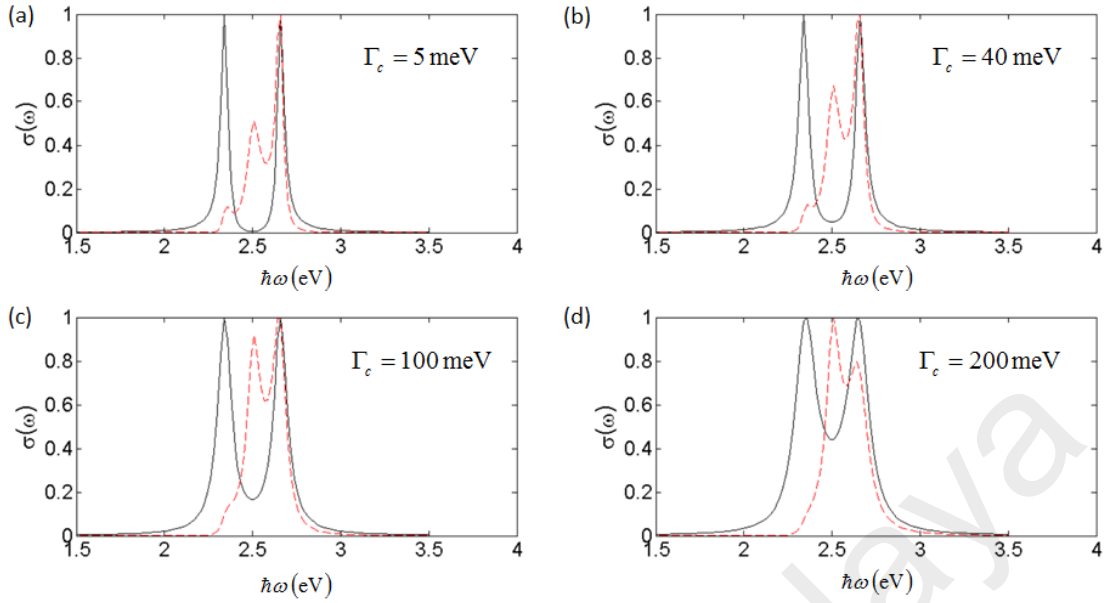

Figure 2.8: Dependence of the absorption spectrum of the MP-SQD system on the exciton resonance width, Γ_c. The black continuous line is the absorption spectrum obtained from Zubarev Green function formalism whereas the red dashed line is the absorption spectrum obtained from density matrix method developed in subsection 2.5.1. Here, we use the value $\varepsilon_c = 2.5$ eV for the exciton resonance energy and $\Delta_{dc} = 160$ meV for the plasmon-exciton coupling strength. Fano resonance disappears as Γ_c increases.

spectral line shape. In other words, in Zubarev's formalism it is assumed that the strength of the incident field is strong and the interparticle distance is small enough for the exciton and plasmon to interact efficiently and that other parameters such as background permittivity, shape and size of the metallic nanoparticle, etc. do not affect the absorption spectrum significantly.

2. In the Zubarev's Green function formalism, the direct coupling of the emitter (which supports excitons) to the incident light is neglected and it is assumed that only the plasmons couple efficiently to the external photons. Therefore, the optical absorption spectrum of the hybrid nanostructure is assumed to depend only on the Green function associated with the creation and annihilation operators of the plasmons (see Equation 2.154). In contrast, such approximation was not made in the semiclassical theory as the total absorption rate depends on contribution from both SQD and MP (see Equation 2.126). In fact, such approximation is only valid

in the case of strong laser field (due to saturation effect of SQD) or weak laser field with short interparticle distance (due to fast dissipation of the plasmons in MP). This means that in the case of weak field and long interparticle distance prediction from the Zubarev's Green function formalism will not be accurate.

3. The approximation $\langle c^{\dagger}c \rangle = n_c$ made in Equation 2.156 in order to truncate the infinite hierarchy of equations of motions may also contribute to the discrepancies. The price one pays when making such approximation is that he will be unable to fully account for the nonlinearity of the equations of motion in Equations 2.155-2.158 which represents the complexity of the plasmon-exciton interaction. This is in contrast to the density matrix formalism where the density matrix elements are solved self-consistently without truncating any one of the equations of motion.

In general, the density matrix formalism provides a more accurate description of the plasmon-exciton interaction as it analyses the complex nonlinear interaction more realistically and self-consistently. Absorption spectrum obtained from Zubarev's Green function is only sufficient to describe strongly interacting plasmon-exciton systems (with strong external input field and small interparticle distance) without taking into account other practical factors that may affect the spectrum qualitatively and quantitatively. Despite this, Zubarev formalism also offers several advantages over the density matrix formalism in solving MP-QS interaction problem.

The major advantage of the Zubarev's Green function method is that it is conceptually much simpler than the density matrix formalism since the only calculations required is the evaluation of simple commutation relations between operators. Furthermore, since the dynamics are obtained nonperturbatively directly from the Hamiltonian, this formalism can be generalized to include more complex interactions such as coupling between two

quantum emitters, coupling to phonons, etc. The simplicity of this formalism could make it a powerful tool for studying plasmon-exciton interactions in plasmonic transistors, modulators and quantum information devices.

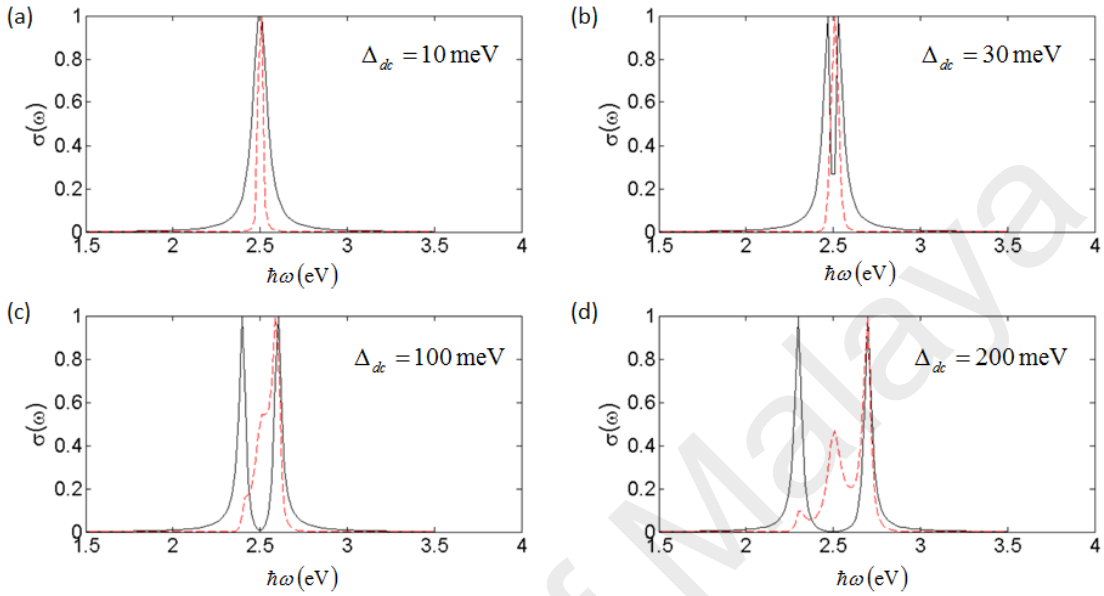

Figure 2.9: Dependence of the absorption spectrum of the MP-SQD system on the plasmon-exciton coupling strength, Δ_{dc}. The black continuous line is the absorption spectrum obtained from Zubarev Green function formalism whereas the red dashed line is the absorption spectrum obtained from density matrix method developed in subsection 2.5.1. Here, we use the value $\varepsilon_c = 2.5$ eV for the exciton resonance energy and $\Gamma_c = 4$ meV for the exciton resonance width. Fano dip becomes more pronounced at large Δ_{dc}.

To summarize, the quantum Langevin formalism with noise operators as well as their applications in solving for double Raman scheme are reviewed. The results in section 2.2 will be useful for the derivation of the quantum coherences and fields in Chapter 3. Also, the definitions of normal- and antinormal-order spectra and their relations to the first-order correlation functions have also been covered. The fields spectra will be the final outcome of our formalism in Chapter 3 and 4 and the spectra obtained will be simulated and analyzed in Chapter 6. Then, several previous studies on the interaction between a MP and a two-level QS based on both semiclassical and fully quantum-mechanical theory were also reviewed. The formalism and the results of these previous studies will serve as a guide for our study of MP-QS interaction in Chapter 4, 5 and 6.

CHAPTER 3: MESOSCOPIC SPHERICAL PARTICLE: QUANTUM SPECTRA OF RAMAN PHOTON PAIR FROM LANGEVIN THEORY

In this chapter, the quantum properties of the Raman photon pairs emitted by a mesoscopic spherical particle composed of quantum particles (atoms/molecules) in double Raman configuration will be studied. Quantum Langevin formalism (Sargent et al., 1974; Scully & Zubairy, 1997) will be used to describe the interaction of the quantum particles with pump and control laser fields inside the small spherical particle with arbitrary dimension. In this formalism, the Stokes and anti-Stokes electric fields are expressed as quantum operators in terms of noise operators, thus enabling the computation of the quantum-mechanical expressions for the field-field correlation functions in a transparent manner. In particular, both the normal- and antinormal-order spectra (Puri, 2001) of the Stokes and anti-Stokes electric fields are obtained. As described earlier in section 2.3, the normal-order spectrum plays an important role in the description of experimentally observed quantities such as photoelectron statistics whereas the antinormal-order spectrum describes a photodetection method introduced by Mandel (Mandel, 1966) which functions based on stimulated emission.

This chapter is organized in the following manner. First, the model of the system under study as well as the various assumptions made will be described in detail. Then, the analytical expression of the scattered electric field from a spherical particle with arbitrary size will be derived starting from the Maxwell's equations. This is followed by the solution of the coherences operators associated with the Stokes and anti-Stokes fields based on quantum Langevin formalism with noise operators highlighted in section 2.2. The coherences operators obtained will then be used to derive the analytical forms of the Stokes and anti-Stokes electric fields. Finally, the chapter is concluded with the expressions of the normal- and antinormal-order spectra of the Stokes and anti-Stokes

fields. The simulation results of the spectra and their interpretations will be discussed in Chapter 6.

3.1 Model

The model considered here consists of a single mesoscopic spherical particle with radius ρ comprising of quantum particles (atoms/molecules) in double Raman configuration (Figure 3.1). In this study, the center of the mesoscopic particle is assumed to be at the origin of the Cartesian coordinate system. As shown in Figure 3.1, **R** is denoted as the vector of the observation point and **r** as the position of the dipole within the mesoscopic particle. The mesoscopic particle is assumed to be isolated, i.e. without the presence of a nearby particle and upon interacting with the pump and control laser fields, it emits Stokes and anti-Stokes fields which are quantum fields of which the electric fields can be represented by quantum-mechanical operators. It is assumed that both incident pump and control laser fields propagate along the $+z-$direction and are polarized along the $x-$axis. Both laser fields are also assumed to be continuous wave (cw) lasers of which temporal dependence is not important and can thus be neglected. Also, in this system the detection distance is sufficiently large, i.e. $R >> \rho$ such that the far-field approximation can be made. In this study however, the dipole approximation commonly used in studying laser interaction with small particles will not be applied so as to ensure our results to be valid for arbitrary size of the particle.

3.2 Integral Solution of the Scattered Field in Far Zone

In this section, the analytical expression of the electric field emitted by a spherical particle with arbitrary size will be derived starting from the Maxwell's equations for the macroscopic fields. The results obtained will be revisited in section 3.4 for the derivation of the analytical form of the Stokes and anti-Stokes fields.

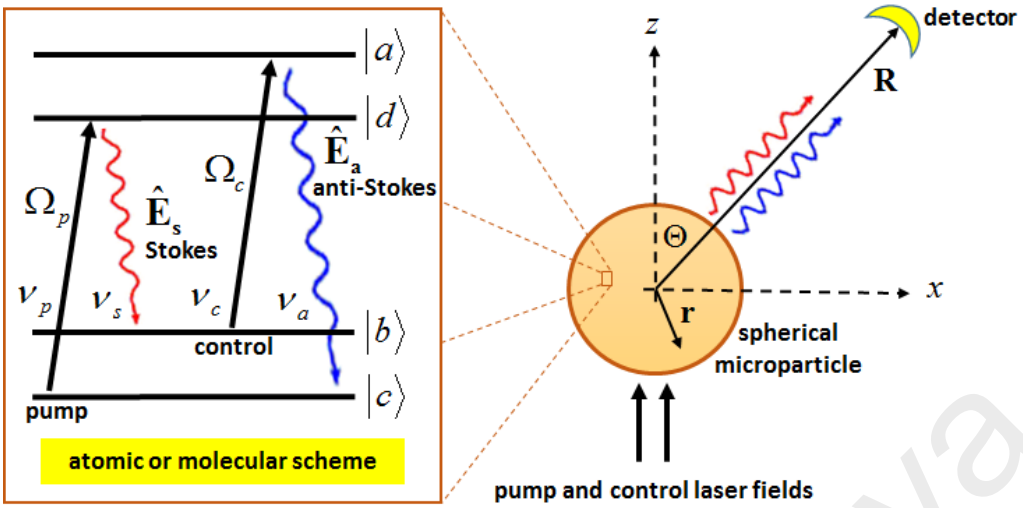

Figure 3.1: Illustration of a spherical microparticle composed of atoms in double Raman configuration. Inset on the left shows the energy-level diagram which describes the four-level double Raman scheme. The particle interacts with pump Ω_p and control Ω_c lasers (solid arrows) which are incident along the $z-$direction and emits quantized Stokes $\hat{E}_s$ and anti-Stokes $\hat{E}_a$ fields (wavy arrows) with their respective frequencies given by ν_i $(i = p, c, s, a)$.

The Maxwell's equations which describe the relation between the four electromagnetic fields vectors ($\mathbf{D}, \mathbf{B}, \mathbf{E}$ and $\mathbf{H}$) and their sources, namely the free charge density ρ and the free current density $\mathbf{J}$ are given by

$$\nabla \cdot \mathbf{D} = \rho_f, \tag{3.1}$$

$$\nabla \cdot \mathbf{B} = 0, \tag{3.2}$$

$$\nabla \times \mathbf{E} = -\frac{\partial \mathbf{B}}{\partial t}, \tag{3.3}$$

$$\nabla \times \mathbf{H} = \frac{\partial \mathbf{D}}{\partial t} + \mathbf{J}_f. \tag{3.4}$$

Here, $\mathbf{E}$ and $\mathbf{B}$ are the electric and magnetic field strengths, respectively whereas $\mathbf{D}$ and $\mathbf{H}$ are the auxiliary fields (termed electric displacement and magnetic induction)

which are related to the original fields strengths via

$$\mathbf{D} = \varepsilon_0 \mathbf{E} + \mathbf{P}, \tag{3.5}$$

$$\mathbf{H} = \frac{\mathbf{B}}{\mu_0}. \tag{3.6}$$

where the macroscopic polarization $\mathbf{P}$ is defined as electric dipole moment per unit volume. In our system, this polarization arises from the linear and nonlinear interaction of the external fields (laser fields) with the atoms/molecules within the spherical particle. Note also that in Equation 3.6 any effects arising from magnetization have been neglected. This assumption is reasonable since at optical frequency, the magnetic response is too slow as it takes time much longer than the period of the optical wave (Fox, 2006). It should also be understood that all the fields quantities ($\mathbf{D}, \mathbf{B}, \mathbf{E}$ and $\mathbf{H}$) depend on space and time, though they are not explicitly shown. The situation which will be focused here contains no free currents or free charges in the particle volume, i.e. $\rho_f = \mathbf{J}_f = 0$, so that the Maxwell's equations become

$$\nabla \cdot (\varepsilon_0 \mathbf{E} + \mathbf{P}) = 0, \tag{3.7}$$

$$\nabla \cdot \mathbf{B} = 0, \tag{3.8}$$

$$\nabla \times \mathbf{E} = -\frac{\partial \mathbf{B}}{\partial t}, \tag{3.9}$$

$$\nabla \times \mathbf{B} = \mu_0 \frac{\partial (\varepsilon_0 \mathbf{E} + \mathbf{P})}{\partial t}. \tag{3.10}$$

Taking the curl of Equation 3.9 and using Equation 3.10,

$$\nabla \times (\nabla \times \mathbf{E}) = -\frac{1}{c^2} \frac{\partial^2}{\partial t^2} \mathbf{E} - \mu_0 \frac{\partial^2}{\partial t^2} \mathbf{P}, \tag{3.11}$$

where the following relation has been used

$$\mu_0 \varepsilon_0 = \frac{1}{c^2}. \tag{3.12}$$

Applying the vector relation $\nabla \times (\nabla \times \mathbf{E}) = \nabla (\nabla \cdot \mathbf{E}) - \nabla^2 \mathbf{E}$ to the LHS of Equation 3.11 yields

$$\nabla (\nabla \cdot \mathbf{E}) - \nabla^2 \mathbf{E} = -\frac{1}{c^2} \frac{\partial^2}{\partial t^2} \mathbf{E} - \mu_0 \frac{\partial^2}{\partial t^2} \mathbf{P}. \tag{3.13}$$

From Equation 3.5,

$$\mathbf{E} = \frac{\mathbf{D} - \mathbf{P}}{\varepsilon_0}, \tag{3.14}$$

which when substituted into Equation 3.13 will result in

$$\nabla \left(\frac{\nabla \cdot \mathbf{D} - \nabla \cdot \mathbf{P}}{\varepsilon_0} \right) - \nabla^2 \mathbf{E} = -\frac{1}{c^2} \frac{\partial^2}{\partial t^2} \mathbf{E} - \mu_0 \frac{\partial^2}{\partial t^2} \mathbf{P}. \tag{3.15}$$

It is already known from Equation 3.7 that $\nabla \cdot \mathbf{D} = 0$. After some arrangement one will get the nonhomogeneous wave equation

$$\left(\nabla^2 - \frac{1}{c^2} \frac{\partial^2}{\partial t^2} \right) \mathbf{E} = -\frac{1}{\varepsilon_0} \left(\nabla \nabla \cdot - \frac{1}{c^2} \frac{\partial^2}{\partial t^2} \right) \mathbf{P}. \tag{3.16}$$

Here, the polarization $\mathbf{P}$ acts as the source term for the electric field $\mathbf{E}$. Equation 3.16 can be rewritten in a simpler form as

$$\mathcal{L} \mathbf{E} (\mathbf{R}, t) = f (\mathbf{R}, t) \tag{3.17}$$

where the operator $\mathcal{L} = \nabla^2 - \frac{1}{c^2} \frac{\partial^2}{\partial t^2}$ and $f (\mathbf{R}, t) = -\frac{1}{\varepsilon_0} \left(\nabla \nabla \cdot - \frac{1}{c^2} \frac{\partial^2}{\partial t^2} \right) \mathbf{P} (\mathbf{R}, t)$ is the inhomogeneous term (source term). This differential equation may be solved by employing the

Green function method where a Green function G has to be searched such that

$$\mathcal{L}G\left(\mathbf{R},t,\mathbf{r},t'\right)=\delta\left(\mathbf{R}-\mathbf{r}\right)\delta\left(t-t'\right), \tag{3.18}$$

so that the solution for the electric field $\mathbf{E}\left(\mathbf{R},t\right)$ may be obtained as

$$\mathbf{E}\left(\mathbf{R},t\right)=\int\int G\left(\mathbf{R},t,\mathbf{r},t'\right)f\left(\mathbf{r},t'\right)dt'd\mathbf{r}. \tag{3.19}$$

To verify Equation 3.19, one may apply $\mathcal{L}$ to the equation from the left and get

$$\begin{aligned}\mathcal{L}\mathbf{E}\left(\mathbf{R},t\right) &= \int\int \mathcal{L}G\left(\mathbf{R},t,\mathbf{r},t'\right)f\left(\mathbf{r},t'\right)d\mathbf{r}dt' \\ &= \int\int \delta\left(\mathbf{R}-\mathbf{r}\right)\delta\left(t-t'\right)f\left(\mathbf{r},t'\right)d\mathbf{r}dt' \\ &= f\left(\mathbf{R},t\right),\end{aligned} \tag{3.20}$$

which returns Equation 3.17. The Green function which satisfies Equation 3.18 is

$$G\left(\mathbf{R},t,\mathbf{r},t'\right)=\frac{1}{4\pi\left|\mathbf{R}-\mathbf{r}\right|}\delta\left(t-t'\right), \tag{3.21}$$

with the retarded time $t'=t-\frac{|\mathbf{R}-\mathbf{r}|}{c}$, which results in the integral solution

$$\mathbf{E}\left(\mathbf{R},t\right)=-\int_V\left(\nabla\nabla\cdot-\frac{1}{c^2}\frac{\partial^2}{\partial t^2}\right)\frac{\mathbf{P}\left(\mathbf{r},t-\frac{|\mathbf{R}-\mathbf{r}|}{c}\right)}{4\pi\varepsilon_0\left|\mathbf{R}-\mathbf{r}\right|}d^3r, \tag{3.22}$$

where $\int_V$ denotes integration over the entire volume of the spherical particle. The definition for $\mathbf{R}$ and $\mathbf{r}$ here is consistent with Figure 3.1.

It is particularly convenient to solve the wave equation in frequency domain. Fourier transformation of Equation 3.16 into frequency domain yields

$$\left(\nabla^2 + \frac{\omega^2}{c^2}\right)\mathbf{E}(\mathbf{R},\omega) = -\frac{1}{\varepsilon_0}\left(\nabla\nabla\cdot + \frac{\omega^2}{c^2}\right)\mathbf{P}(\mathbf{R},\omega). \tag{3.23}$$

The definition of Fourier transformation used here is

$$\mathbf{E}(\omega) = \int_{-\infty}^{\infty}\mathbf{E}(t)\,e^{i\omega t}dt \tag{3.24}$$

and the same definition applies for the macroscopic polarization $\mathbf{P}(\omega)$. The polarization $\mathbf{P}(\mathbf{R},\omega)$ consists of linear and nonlinear contributions expressed as

$$\mathbf{P}(\mathbf{R},\omega) = \varepsilon_0\chi^{(1)}(\omega)\,\mathbf{E}(\mathbf{R},\omega) + \mathbf{P}^{NL}(\mathbf{R},\omega). \tag{3.25}$$

Substitution of Equation 3.25 into Equation 3.7 gives the following relation

$$\nabla\cdot\mathbf{E} = -\frac{\nabla\cdot\mathbf{P}^{NL}}{\varepsilon_0\varepsilon(\omega)}, \tag{3.26}$$

where $\varepsilon(\omega) = 1 + \chi^{(1)}(\omega)$ is the frequency-dependent dielectric function of the spherical particle which describes linear dispersion. Applying Equations 3.25 and 3.26 on the RHS of Equation 3.23 results in

$$\begin{aligned}\left(\nabla^2 + \frac{\omega^2}{c^2}\right)\mathbf{E}(\mathbf{R},\omega) &= \nabla\nabla\cdot\frac{\mathbf{P}^{NL}(\mathbf{R},\omega)}{\varepsilon_0\varepsilon(\omega)}\chi^{(1)}(\omega) - \frac{1}{\varepsilon_0}\nabla\nabla\cdot\mathbf{P}^{NL}(\mathbf{R},\omega)\\ &\quad -\frac{\omega^2}{c^2}\chi^{(1)}(\omega)\,\mathbf{E}(\mathbf{R},\omega)(\omega) - \frac{1}{\varepsilon_0}\frac{\omega^2}{c^2}\mathbf{P}^{NL}(\mathbf{R},\omega).\end{aligned} \tag{3.27}$$

Recalling the relation $\chi^{(1)}(\omega) = \varepsilon(\omega) - 1$, the above equation may again be simplified

into a non-homogeneous wave equation in frequency domain

$$\left(\nabla^2 + \frac{\omega^2}{c^2}\varepsilon(\omega)\right)\mathbf{E}(\mathbf{R},\omega) = -\frac{1}{\varepsilon_0}\left(\frac{\nabla\nabla\cdot}{\varepsilon(\omega)} + \frac{\omega^2}{c^2}\right)\mathbf{P}^{NL}(\mathbf{R},\omega). \tag{3.28}$$

Just as in Equation 3.16, the solution for $\mathbf{E}(\mathbf{R},\omega)$ in Equation 3.28 can be obtained by applying the Green function which satisfies

$$\left(\nabla^2 + \frac{\omega^2}{c^2}\varepsilon(\omega)\right)G(\mathbf{R},\omega,\mathbf{r},\omega') = \delta(\mathbf{R}-\mathbf{r})\,\delta(\omega-\omega'). \tag{3.29}$$

This Green function is found to be of the form (Jackson, 1999)

$$G(\mathbf{R},\omega,\mathbf{r},\omega') = \frac{e^{ik(\omega)|\mathbf{R}-\mathbf{r}|}}{4\pi|\mathbf{R}-\mathbf{r}|}\delta(\omega-\omega'), \tag{3.30}$$

which then leads to the solution for the electric field in frequency domain

$$\mathbf{E}(\mathbf{R},\omega) = -\int_V \left(\frac{\nabla\nabla\cdot}{\varepsilon(\omega)} + \frac{\omega^2}{c^2}\right)\frac{\mathbf{P}^{NL}(\mathbf{r},\omega)\,e^{ik(\omega)|\mathbf{R}-\mathbf{r}|}}{4\pi\varepsilon_0|\mathbf{R}-\mathbf{r}|}d^3r, \tag{3.31}$$

where the wave vector is given by $k(\omega) = \frac{\omega}{c}\sqrt{\varepsilon(\omega)}$. As mentioned in section 3.1, it is assumed in this study that the detection distance is sufficiently large such that the far-field approximation can be made, that is,

$$|\mathbf{R}-\mathbf{r}| \simeq R - \hat{R}\cdot\mathbf{r}. \tag{3.32}$$

Expressing the polarization in spherical polar coordinate, $\mathbf{P}^{NL}(\mathbf{r},\omega) = \hat{R}P_R^{NL} + \hat{\Theta}P_\Theta^{NL} + \hat{\Phi}P_\Phi^{NL}$ and using

$$\frac{\nabla\nabla\cdot\left[\mathbf{P}^{NL}(\mathbf{r},\omega)\,e^{ik|\mathbf{R}-\mathbf{r}|}\right]}{|\mathbf{R}-\mathbf{r}|} \simeq -\frac{k^2P_R^{NL}e^{ik\left(R-\hat{R}\cdot\mathbf{r}\right)}}{R}\hat{R}, \tag{3.33}$$

one can rewrite Equation 3.31 as

$$\mathbf{E}(\mathbf{R},\omega) = \frac{\omega^2}{c^2}\int_V \frac{\left(\hat{\Theta}P_{\Theta}^{NL} + \hat{\Phi}P_{\Phi}^{NL}\right)e^{ik(\omega)|\mathbf{R}-\mathbf{r}|}}{4\pi\varepsilon_0|\mathbf{R}-\mathbf{r}|}d^3r. \tag{3.34}$$

Note that only the transverse (angular) component of the polarization contribute to the far field. The derivation will stop at this point.

3.3 Quantum Langevin Formalism for Coherences

In this section, the analytical expressions of the coherences $\hat{\sigma}_{bd}$ and $\hat{\sigma}_{ac}$ associated with the Stokes and anti-Stokes transitions, respectively in the four-level double Raman scheme (Figure 2.1(a)) will be derived utilizing quantum Langevin formalism with noise operators as highlighted in section 2.2. The results from this section will be useful for deriving the scattered Stokes and anti-Stokes electric field in the next section. One may just proceed from the results in Equations 2.50-2.59, which are the 16 coupled Langevin equations describing the time-evolution of the atomic operators. Due to the high nonlinearity of the Langevin equations, analytical solutions are only possible when some assumptions are made. Here, it is assumed that the Stokes $\hat{\mathbf{E}}_s(t)$ and anti-Stokes $\hat{\mathbf{E}}_a(t)$ fields are weak so that both the populations $\hat{\sigma}_{ii}\,(i = a, d, b, c)$ and the coherences associated with the laser transitions $\hat{\sigma}_{dc}$ and $\hat{\sigma}_{ab}$ can be approximated as time-independent complex numbers. This results in just four coupled equations describing the time-evolution of $\hat{\sigma}_{ac}, \hat{\sigma}_{ad}, \hat{\sigma}_{bc}$ and $\hat{\sigma}_{bd}$. The closed coupled equations for the slowly varying atomic envelope operators of these four coherences $\hat{p}_{ac} = \hat{\sigma}_{ac}e^{-i\nu_a t}, \hat{p}_{ad} = \hat{\sigma}_{ad}e^{-i\nu_{cs}t}, \hat{p}_{bc} = \hat{\sigma}_{bc}e^{-i\nu_{ac}t}$ and $\hat{p}_{bd} = \hat{\sigma}_{bd}e^{i\nu_s t}$ are given by

$$\begin{aligned}\frac{d}{dt}\hat{p}_{ac} &= -\gamma_{ac}\hat{p}_{ac} + i\omega_{ac}\hat{p}_{ac} - i\nu_a\hat{p}_{ac} + i\mathbf{g}_a^*\cdot\tilde{\mathbf{E}}_a^{\dagger}(\hat{p}_{aa} - \hat{p}_{cc}) \\ &\quad -i\Omega_c^*\hat{p}_{bc} + i\Omega_p^*\hat{p}_{ad} + e^{-i\nu_a t}\hat{F}_{ac}(t),\end{aligned} \tag{3.35}$$

$$\frac{d}{dt}\hat{p}_{ad} = -\gamma_{ad}\hat{p}_{ad} + i\omega_{ad}\hat{p}_{ad} - i\nu_{cs}\hat{p}_{ad} - i\mathbf{g}_a^*\cdot\tilde{\mathbf{E}}_a^\dagger\hat{p}_{cd} + i\mathbf{g}_s\cdot\tilde{\mathbf{E}}_s\hat{p}_{ab}$$
$$-i\Omega_c^*\hat{p}_{bd} + i\Omega_p\hat{p}_{ac} + e^{-i\nu_{cs}t}\hat{F}_{ad}(t), \tag{3.36}$$

$$\frac{d}{dt}\hat{p}_{bc} = -\gamma_{bc}\hat{p}_{bc} + i\omega_{bc}\hat{\sigma}_{bc} - i\nu_{ac}\hat{p}_{bc} - i\mathbf{g}_s\cdot\tilde{\mathbf{E}}_s\hat{p}_{dc} + i\mathbf{g}_a^*\cdot\tilde{\mathbf{E}}_a^\dagger\hat{p}_{ba}$$
$$-i\Omega_c\hat{p}_{ac} + i\Omega_p^*\hat{p}_{bd} + e^{-i\nu_{ac}t}\hat{F}_{bc}(t), \tag{3.37}$$

$$\frac{d}{dt}\hat{p}_{bd} = -\gamma_{bd}\hat{p}_{bd} + i\omega_{bd}\hat{\sigma}_{bd} + i\nu_s\hat{p}_{bd} - i\mathbf{g}_s\cdot\tilde{\mathbf{E}}_s(\hat{p}_{dd} - \hat{p}_{bb})$$
$$-i\Omega_c\hat{p}_{ad} + i\Omega_p\hat{p}_{bc} + e^{i\nu_s t}\hat{F}_{bd}(t), \tag{3.38}$$

where $\nu_{ij} = \nu_i - \nu_j$ and $\nu_i\,(i, j = p, s, c, a)$ denote the carrier frequency of the pump, Stokes, control and anti-Stokes fields, respectively, all of which satisfy $\nu_p + \nu_c = \nu_s + \nu_a$ for the parametric four photons transitions. The complex decoherences are given by

$$T_{ac} = i\Delta_a + \gamma_{ac}, \tag{3.39}$$
$$T_{ad} = i(\Delta_c - \Delta_s) + \gamma_{ad}, \tag{3.40}$$
$$T_{bc} = i(\Delta_p - \Delta_s) + \gamma_{bc}, \tag{3.41}$$
$$T_{db} = i\Delta_s + \gamma_{db}, \tag{3.42}$$

with the detunings $\Delta_a = \nu_a - \omega_{ac}, \Delta_c = \nu_c - \omega_{ab}, \Delta_s = \nu_s - \omega_{db}$, and $\Delta_p = \nu_p - \omega_{dc}$ of the pump, Stokes, control, and anti-Stokes fields, respectively. Here, ω_{ac} simply means the transition frequency between energy level a and c and the same definition applies to all other cases. As mentioned in section 3.1, the spatial dependence of the pump and control laser fields is retained but the temporal dependence is neglected, i.e. Ω_p

and Ω_c are constants in time. Hence, the Rabi frequencies for the lasers $l = p, c$ are $\Omega_l(\mathbf{r}) = \mathbf{g}_l \cdot \tilde{\mathbf{E}}_l = \sum_{q=x,y,z} g_{lq} \tilde{E}_{lq}$, where $g_{lq} = \frac{\wp_{lq}}{\hbar}$ is the coupling strength with $\wp_{lq}$ as the $q-$component transition dipole moment. In order to solve for the coherences $\hat{p}_{bd}(\mathbf{r}, \omega)$ and $\hat{p}_{ac}(\mathbf{r}, \omega)$, which are respectively associated with the Stokes and anti-Stokes transitions the following assumptions need to be made

$$\hat{p}_{aa} - \hat{p}_{cc} \approx w_{cc}^{st} = \langle \hat{p}_{aa} - \hat{p}_{cc} \rangle, \tag{3.43}$$

$$\hat{p}_{dd} - \hat{p}_{bb} \approx w_{bb}^{st} = \langle \hat{p}_{dd} - \hat{p}_{bb} \rangle, \tag{3.44}$$

$$\hat{p}_{ab} \approx \left\langle \hat{p}_{ab}^{st} \right\rangle = p_{ab}^{st}, \tag{3.45}$$

$$\hat{p}_{dc} \approx \left\langle \hat{p}_{dc}^{st} \right\rangle = p_{dc}^{st}, \tag{3.46}$$

where the populations and the coherences operators at the laser transitions are taken as steady state expectation values. Taking this into account and performing Fourier transformation $\tilde{Q}(\omega) = \int_{-\infty}^{\infty} \tilde{Q}(t) e^{i\omega t} dt$ $\left(\tilde{Q} = \tilde{E}_s, \tilde{E}_a^{\dagger}, \hat{p}_x, \hat{G}_x \text{ where } x = ac, ad, bc, bd\right)$ on the four coupled equations results in

$$\hat{p}_{ac}(\omega) = \frac{1}{T_{ac}(\omega)} \left[i\tilde{A}^{\dagger}(\omega) w_{cc}^{st} - i\Omega_c^* \hat{p}_{bc}(\omega) + i\Omega_p^* \hat{p}_{ad}(\omega) + \hat{G}_{ac}(\omega) \right], \tag{3.47}$$

$$\hat{p}_{ad}(\omega) = \frac{1}{T_{ad}(\omega)} \left[i\tilde{S}(\omega) p_{ab}^{st} - i\tilde{A}^{\dagger}(\omega) p_{cd}^{st} + i\Omega_p \hat{p}_{ac}(\omega) - i\Omega_c^* \hat{p}_{bd}(\omega) + \hat{G}_{ad}(\omega) \right], \tag{3.48}$$

$$\hat{p}_{bc}(\omega) = \frac{1}{T_{bc}(\omega)} \left[-i\tilde{S}(\omega) p_{dc}^{st} + i\tilde{A}^{\dagger}(\omega) p_{ba}^{st} - i\Omega_c \hat{p}_{ac}(\omega) + i\Omega_p^* \hat{p}_{bd}(\omega) + \hat{G}_{bc}(\omega) \right], \tag{3.49}$$

$$\hat{p}_{bd}(\omega) = \frac{1}{T_{db}^*(\omega)} \left[-i\tilde{S}(\omega) w_{bb}^{st} + i\Omega_p \hat{p}_{bc}(\omega) - i\Omega_c \hat{p}_{ad}(\omega) + \hat{G}_{bd}(\omega) \right], \tag{3.50}$$

where we have defined $\tilde{S} = \mathbf{g}_s \cdot \tilde{\mathbf{E}}_s = \sum_{q=x,y,z} g_{sq} \tilde{E}_{sq}$ and $\tilde{A} = \mathbf{g}_a \cdot \tilde{\mathbf{E}}_a = \sum_{q=x,y,z} g_{aq} \tilde{E}_{aq}$ with the coupling strengths $g_{sq} = \frac{\wp_{db,q}}{\hbar}$ and $g_{aq} = \frac{\wp_{ac,q}}{\hbar}$, and the complex decoherences

after Fourier transformation are $T_x(\omega) = T_x - i\omega$ $(x = ac, ad, bc)$ and $T^*_{db}(\omega) = T^*_{db} - i\omega$. At this point, readers should bear in mind that the pump and control laser fields inside the spherical particle depend on the spatial coordinate of the particle. This is due to the refraction and focusing by the geometry of the particle which are taken into account by the Lorentz-Mie theory (Ooi et al., 2005; Bohren & Huffman, 1983) given in Appendix A, with the assumption that the incident laser fields are x polarized. Now, the aim is to solve for $\hat{p}_{ac}(\omega)$ and $\hat{p}_{bd}(\omega)$ by rewriting the four coupled equations in Equations 3.47-3.50 in matrix form

$$\begin{pmatrix} \hat{p}_{ac}(\omega) \\ \hat{p}_{ad}(\omega) \\ \hat{p}_{bc}(\omega) \\ \hat{p}_{bd}(\omega) \end{pmatrix} = -M \begin{pmatrix} i\tilde{A}^{\dagger}(\omega) w^{st}_{cc} + \hat{G}_{ac}(\omega) \\ i\tilde{S}(\omega) p^{st}_{ab} - i\tilde{A}^{\dagger}(\omega) p^{st}_{cd} + \hat{G}_{ad}(\omega) \\ -i\tilde{S}(\omega) p^{st}_{dc} + i\tilde{A}^{\dagger}(\omega) p^{st}_{ba} + \hat{G}_{bc}(\omega) \\ -i\tilde{S}(\omega) w^{st}_{bb} + \hat{G}_{bd}(\omega) \end{pmatrix}, \tag{3.51}$$

where

$$M = \begin{pmatrix} -T_{ac}(\omega) & i\Omega^*_p & -i\Omega^*_c & 0 \\ i\Omega_p & -T_{ad}(\omega) & 0 & -i\Omega^*_c \\ -i\Omega_c & 0 & -T_{bc}(\omega) & i\Omega^*_p \\ 0 & -i\Omega_c & i\Omega_p & -T^*_{db}(\omega) \end{pmatrix}^{-1}. \tag{3.52}$$

At the end, the following results will be obtained

$$\hat{p}_{bd}(\omega) = -\left(\sum_{j=1}^{4} M_{4j} \hat{G}_j + X_s \tilde{A}^{\dagger} + G_s \tilde{S} \right), \tag{3.53}$$

$$\hat{p}_{ac}(\omega) = -\left(\sum_{j=1}^{4} M_{1j} \hat{G}_j + G_a \tilde{A}^{\dagger} + X_a \tilde{S} \right), \tag{3.54}$$

with the coefficients

$$G_s = i\left(p_{ab}^{st}M_{42} - p_{dc}^{st}M_{43} - w_{bb}^{st}M_{44}\right), \tag{3.55}$$

$$G_a = i\left(w_{cc}^{st}M_{11} - p_{cd}^{st}M_{12} + p_{ba}^{st}M_{13}\right), \tag{3.56}$$

$$X_s = i\left(w_{cc}^{st}M_{41} - p_{cd}^{st}M_{42} + p_{ba}^{st}M_{43}\right), \tag{3.57}$$

$$X_a = i\left(p_{ab}^{st}M_{12} - p_{dc}^{st}M_{13} - w_{bb}^{st}M_{14}\right). \tag{3.58}$$

In Equations 3.53 and 3.54, the noise operators are labelled as $\hat{G}_1 = \hat{G}_{ac}, \hat{G}_2 = \hat{G}_{ad}, \hat{G}_3 = \hat{G}_{bc}, \hat{G}_4 = \hat{G}_{bd}$. The steady-state solutions for the populations and coherences at laser transitions are provided in Appendix C.

3.4 Analytical Solutions for Stokes and Anti-Stokes Fields

The nonhomogeneous wave equation in frequency domain in Equation 3.23 can be modified to include the subscript $f = s, a$ which denotes Stokes and anti-Stokes fields, respectively. The result is

$$\left(\nabla^2 + \frac{\omega^2}{c^2}\right)\hat{\mathbf{E}}_f(\mathbf{R},\omega) = -\frac{1}{\varepsilon_0}\left\{\nabla\nabla\cdot + \frac{\omega^2}{c^2}\right\}\hat{\mathbf{P}}_f(\mathbf{R},\omega). \tag{3.59}$$

Note that both the electric field $\hat{\mathbf{E}}_f$ and polarization $\hat{\mathbf{P}}_f$ vectors are now treated as quantum-mechanical operators as we are now considering the wave equation for the quantum fields. The quantum coherences operators $\hat{\sigma}_{bd}$ and $\hat{\sigma}_{ac}$ of the quantum particles are coupled to the electric field operators of the Stokes and anti-Stokes fields via the quantum-mechanical expression of the macroscopic polarization

$$\hat{\mathbf{P}}_f(\mathbf{r},\omega) = N\vec{\wp}_f\hat{\sigma}_f(\mathbf{r},\omega), \tag{3.60}$$

where N is the number density, $\vec{\wp}_s = \vec{\wp}_{bd} = \langle b| \mathbf{d} |d\rangle$ and $\vec{\wp}_a = \vec{\wp}_{ca} = \langle c| \mathbf{d} |a\rangle$ are the dipole matrix elements, and $\hat{\sigma}_s = \hat{\sigma}_{bd} = |b\rangle \langle d|$ and $\hat{\sigma}_a = \hat{\sigma}_{ca} = |c\rangle \langle a|$ are the coherences operators corresponding to the Stokes and anti-Stokes transitions, respectively.

Similarly, the far-field solution for a mesoscopic spherical particle can be modified from Equation 3.34 as

$$\hat{\mathbf{E}}_f(\mathbf{R}, \omega) = \frac{\omega^2}{c^2} \int_V \frac{\left\{ \hat{\Theta} \hat{P}^{NL}_{\Theta,f} + \hat{\Phi} \hat{P}^{NL}_{\Phi,f} \right\} e^{ik_f(\omega)|\mathbf{R}-\mathbf{r}|}}{4\pi\varepsilon_0 |\mathbf{R}-\mathbf{r}|} d^3r, \tag{3.61}$$

where the dispersive wave vector is related to the dielectric function through $k_f(\omega) = \sqrt{\varepsilon_f(\omega)}\frac{\omega}{c}$. In spherical polar coordinate, the observation point is at $\mathbf{R} = R(\sin\Theta\cos\Phi, \sin\Theta\sin\Phi, \cos\Theta)$ whereas the position of the dipole is at $\mathbf{r} = r(\sin\theta\cos\phi, \sin\theta\sin\phi, \cos\theta)$. The magnitude of the distance is $|\mathbf{R}-\mathbf{r}| = \sqrt{\Delta_x^2 + \Delta_y^2 + \Delta_z^2}$, where $\Delta_x = X - x$, etc. The $\Theta-$ and $\Phi-$component of the nonlinear polarization $\hat{\mathbf{P}}^{NL}_f$ can be written as $\hat{P}^{NL}_{\Theta,f} = \hat{\Theta} \cdot \hat{\mathbf{P}}^{NL}_f$ and $\hat{P}^{NL}_{\Phi,f} = \hat{\Phi} \cdot \hat{\mathbf{P}}^{NL}_f$, respectively and they are related to the Cartesian components $\hat{P}^{NL}_{q,f}$ $(q = x, y, z)$ by the transformation unit vectors $\hat{\Theta} = (\cos\Theta\cos\Phi, \cos\Theta\sin\Phi, -\sin\Theta)$ and $\hat{\Phi} = (-\sin\Phi, \cos\Phi, 0)$. The electric field can also be decomposed into Cartesian components $\hat{\mathbf{E}}_f = \left(\hat{E}_{fx}, \hat{E}_{fy}, \hat{E}_{fz}\right)$. To couple the Stokes and anti-Stokes fields to the atomic coherences operators, Equation 3.61 an be written as

$$\begin{pmatrix} \hat{\mathbf{E}}_s(\mathbf{R}, \omega) \\ \hat{\mathbf{E}}^{\dagger}_a(\mathbf{R}, \omega) \end{pmatrix} = \int_V \begin{pmatrix} K_s(\mathbf{R}, \mathbf{r}, \omega) \vec{\wp}^{\perp}_{bd} \hat{\sigma}^{NL}_{bd}(\mathbf{r}, \omega) \\ K^*_a(\mathbf{R}, \mathbf{r}, \omega) \vec{\wp}^{\perp}_{ac} \hat{\sigma}^{NL}_{ac}(\mathbf{r}, \omega) \end{pmatrix} d^3r, \tag{3.62}$$

where $K_f(\mathbf{R}, \mathbf{r}, \omega) = \frac{\omega^2}{c^2} \frac{N}{4\pi\varepsilon_0|\mathbf{R}-\mathbf{r}|} e^{ik_f(\omega)|\mathbf{R}-\mathbf{r}|}$ and the transverse dipole moment vector is given by $\vec{\wp}^{\perp}_g = \hat{\Theta}\wp_{\Theta,g} + \hat{\Phi}\wp_{\Phi,g}$ with the angular components $\wp_{\Theta,g} = \hat{\Theta} \cdot \vec{\wp}_g$ and $\wp_{\Phi,g} = \hat{\Phi} \cdot \vec{\wp}_g$ where $g = bd, ac$.

Now, the original atomic $\hat{\sigma}_x$ and field $\hat{\mathbf{E}}_f(\omega)$ operators will be connected to their

slowly varying envelop operators in frequency domain. The slowly varying envelop of the field is defined by $\hat{\mathbf{E}}_f(t) = \tilde{\mathbf{E}}_f(t)\, e^{-i\nu_f t}$. Hence, the Fourier transforms of the original operators are related to their envelop operators as

$$\begin{pmatrix} \hat{\sigma}_{bd}(\omega) \\ \hat{\mathbf{E}}_s(\omega) \end{pmatrix} = \int e^{i(\omega-\nu_s)t} \begin{pmatrix} \hat{p}_{bd}(t) \\ \tilde{\mathbf{E}}_s(t) \end{pmatrix} dt = \begin{pmatrix} \hat{p}_{bd}(\omega-\nu_s) \\ \tilde{\mathbf{E}}_s(\omega-\nu_s) \end{pmatrix}, \tag{3.63}$$

$$\begin{pmatrix} \hat{\sigma}_{ac}(\omega) \\ \hat{\mathbf{E}}_a^{\dagger}(\omega) \end{pmatrix} = \int e^{i(\omega+\nu_a)t} \begin{pmatrix} \hat{p}_{ac}(t) \\ \tilde{\mathbf{E}}_a^{\dagger}(t) \end{pmatrix} dt = \begin{pmatrix} \hat{p}_{ac}(\omega+\nu_a) \\ \tilde{\mathbf{E}}_a^{\dagger}(\omega+\nu_a) \end{pmatrix}. \tag{3.64}$$

This means that one can rewrite Equation 3.62 as

$$\begin{pmatrix} \hat{\mathbf{E}}_s(\omega) \\ \hat{\mathbf{E}}_a^{\dagger}(\omega) \end{pmatrix} = \int_V \begin{pmatrix} K_s(\mathbf{R},\mathbf{r},\omega)\, \vec{\wp}_{bd}^{\perp} \hat{p}_{bd}^{NL}(\omega-\nu_s) \\ K_a^*(\mathbf{R},\mathbf{r},\omega)\, \vec{\wp}_{ac}^{\perp} \hat{p}_{ac}^{NL}(\omega+\nu_a) \end{pmatrix} d^3r, \tag{3.65}$$

where the $\mathbf{R}$ and $\mathbf{r}$ dependence of $\hat{\mathbf{E}}_f$ and $\hat{p}_f^{NL}$, respectively has been suppressed for clarity. However, $\hat{p}_{bd}^{NL}(\omega)$ and $\hat{p}_{ac}^{NL}(\omega)$ have to be used (instead of $\hat{p}_{bd}^{NL}(\omega-\nu_s)$ and $\hat{p}_{ac}^{NL}(\omega+\nu_a)$) as these two are the solutions of the coupled equations obtained in Equations 3.53 and 3.54. Thus, using $\tilde{\mathbf{E}}_s(\omega) = \hat{\mathbf{E}}_s(\omega+\nu_s)$ and $\tilde{\mathbf{E}}_a^{\dagger}(\omega) = \hat{\mathbf{E}}_a^{\dagger}(\omega-\nu_a)$ as obtained from Equations 3.63 and 3.64, one may write

$$\begin{pmatrix} \tilde{\mathbf{E}}_s(\omega) \\ \tilde{\mathbf{E}}_a^{\dagger}(\omega) \end{pmatrix} = N \int_V \begin{pmatrix} C_s(\mathbf{r},\omega)\, \vec{\wp}_{bd}^{\perp} \hat{p}_{bd}^{NL}(\omega) \\ C_a^*(\mathbf{r},\omega)\, \vec{\wp}_{ac}^{\perp} \hat{p}_{ac}^{NL}(\omega) \end{pmatrix} d^3r, \tag{3.66}$$

where $C_s(\mathbf{r},\omega) = \frac{(\omega+\nu_s)^2}{c^2} \frac{e^{ik_s(\omega+\nu_s)|\mathbf{R}-\mathbf{r}|}}{4\pi\varepsilon_0|\mathbf{R}-\mathbf{r}|}$ and $C_a(\mathbf{r},\omega) = \frac{(\omega-\nu_a)^2}{c^2} \frac{e^{ik_a(\omega-\nu_a)|\mathbf{R}-\mathbf{r}|}}{4\pi\varepsilon_0|\mathbf{R}-\mathbf{r}|}$. The dispersive wave vectors are $k_s(\omega+\nu_s) = \sqrt{\varepsilon_s(\mathbf{r},\omega+\nu_s)}\frac{(\omega+\nu_s)}{c}$ and $k_a(\omega-\nu_a) = \sqrt{\varepsilon_a(\mathbf{r},\omega-\nu_a)}\frac{(\omega-\nu_a)}{c}$

with the dielectric functions

$$\begin{pmatrix} \varepsilon_s(\mathbf{r},\omega+\nu_s) \\ \varepsilon_a(\mathbf{r},\omega-\nu_a) \end{pmatrix} = 1 + \frac{N}{\hbar\varepsilon_0} \begin{pmatrix} G_s(\mathbf{r},\omega)\,|\wp_{db}|^2 \\ G_s(\mathbf{r},\omega)\,|\wp_{ca}|^2 \end{pmatrix}, \tag{3.67}$$

which are derived from the linear parts of $\hat{p}_{bd}^{NL}(\omega)$ and $\hat{p}_{ac}^{NL}(\omega)$. The details on the derivation of Equation 3.67 is provided in Appendix B. Since the superscript NL (which means nonlinear) in Equation 3.66 excludes the term proportional to the respective quantum fields,

$$\hat{p}_{bd}^{NL}(\omega) = -\left(\sum_{j=1}^{4} M_{4j}\hat{G}_j + X_s\tilde{A}^{\dagger}\right), \tag{3.68}$$

$$\hat{p}_{ac}^{NL}(\omega) = -\left(\sum_{j=1}^{4} M_{1j}\hat{G}_j + X_a\tilde{S}\right). \tag{3.69}$$

3.5 Stokes Spectra

In this section the normal- and antinormal-order spectra of the Stokes and anti-Stokes fields will be derived. Then, simulation results of the spectra together with discussions on the findings will be provided in Chapter 6.

3.5.1 Normal-Order Stokes Spectra

For weak fields, only the first term in Equations 3.53 and 3.54 involving the noise operators are significant. It follows from Equation 3.66 that electric field vector of the Stokes signal is given by

$$\hat{\mathbf{E}}_s(\omega) = -N\vec{\wp}_{bd}^{\perp}\int_V C_s(\mathbf{r},\omega)\sum_{j=1}^{4} M_{4j}(\mathbf{r},\omega)\,\hat{G}_j(\mathbf{r},\omega)\,d^3r. \tag{3.70}$$

Considering the $q-$component ($q = x, y, z$) of the Stokes electric field, the normal-order correlation is

$$\begin{aligned}
&\left\langle \hat{E}^{\dagger}_{sq}\left(-\omega'\right)\hat{E}_{sq}\left(\omega\right)\right\rangle \\
= \;& N^2\left|\wp^{\perp}_{bd,q}\right|^2\int_V\left[C_s\left(\mathbf{r}',\omega'\right)\right]^* C_s\left(\mathbf{r},\omega\right) \\
&\times\sum_{j,l=1}^{4}\left[M_{4j}\left(\mathbf{r}',\omega'\right)\right]^* M_{4l}\left(\mathbf{r},\omega\right)\left\langle\left[\hat{G}_{j'}\left(\mathbf{r}',\omega'\right)\right]^{\dagger}\hat{G}_l\left(\mathbf{r},\omega\right)\right\rangle d^3r'd^3r. \qquad (3.71)
\end{aligned}$$

The normal-order noise correlation products in the frequency domain are

$$\begin{aligned}
\left\langle\left[\hat{G}_j\left(\mathbf{r}',\omega'\right)\right]^{\dagger}\hat{G}_l\left(\mathbf{r},\omega\right)\right\rangle &= \left\langle\int e^{-i\omega' t'}e^{i\nu_j t'}F_j^{\dagger}\left(\mathbf{r}',t'\right)dt'\int e^{i\omega t}e^{-i\nu_l t}F_l\left(\mathbf{r},t\right)dt\right\rangle \\
&= \int e^{-i\omega' t'}dt'\int e^{i\omega t}dte^{i\nu_j t'}e^{-i\nu_l t}\left\langle F_j^{\dagger}\left(\mathbf{r}',t'\right)F_l\left(\mathbf{r},t\right)\right\rangle \\
&= \int e^{i\left(\omega-\omega'+\nu_j-\nu_l\right)t}2D_{j\dagger,l}\left(\mathbf{r},t\right)dt\frac{\left(2\pi\right)^3}{N}\delta\left(\mathbf{r}'-\mathbf{r}\right) \\
&= \frac{\left(2\pi\right)^3}{N}2\tilde{D}_{j\dagger,l}\left(\mathbf{r},\omega'-\omega\right)\delta\left(\mathbf{r}'-\mathbf{r}\right) \\
&= \frac{\left(2\pi\right)^3}{N}2\tilde{D}^{n}_{j,l}\left(\mathbf{r},\omega'-\omega\right)\delta\left(\mathbf{r}'-\mathbf{r}\right), \qquad (3.72)
\end{aligned}$$

where the normal-order diffusion coefficients in the frequency domain are related to that in time domain via Fourier transformation $2\tilde{D}^{n}_{j,l}\left(\omega\right) = \int 2\tilde{D}_{j\dagger,l}\left(t\right)e^{i\omega t}dt$ and $\tilde{D}_{j\dagger,l}\left(t\right) = e^{i\left(\nu_j-\nu_l\right)}D_{j\dagger,l}\left(t\right)$ where $j,l = ac, ad, bc, bd$ and $j\dagger, l\dagger = ca, da, cb, db$. In deriving Equation 3.72 we have used $\left\langle F_j^{\dagger}\left(\mathbf{r}',t'\right)F_l\left(\mathbf{r},t\right)\right\rangle = \frac{\left(2\pi\right)^3}{N}2D_{j\dagger,l}\left(\mathbf{r},t\right)\delta\left(\mathbf{r}'-\mathbf{r}\right)\delta\left(t'-t\right)$ as taken from Ooi et al., 2007. The calculations for all the diffusion coefficients are provided in Appendix C.

In spherical polar coordinates, $d^3r = r^2\sin\theta dr d\theta d\phi$ and in the far-field approxima-

tion,

$$\begin{aligned} |\mathbf{R}-\mathbf{r}| &\simeq R-\hat{R}\cdot\mathbf{r} \\ &= R-\frac{\mathbf{R}}{R}\cdot\mathbf{r} \\ &= R-r\left[\sin\Theta\sin\theta\cos\left(\Phi-\phi\right)+\cos\Theta\cos\theta\right]. \end{aligned} \tag{3.73}$$

Since

$$R^2 \gg \left|-2Rr\left[\sin\Theta\sin\theta\cos\left(\Phi-\phi\right)+\cos\Theta\cos\theta\right]+r^2\left[\sin\Theta\sin\theta\cos\left(\Phi-\phi\right)+\cos\Theta\cos\theta\right]^2\right|, \tag{3.74}$$

one can approximate $|\mathbf{R}-\mathbf{r}|^2 \approx R^2$ in the denominator of $|C_s(\mathbf{r},\omega)|^2$. Recalling the relation $S^n_{sq}(\omega) = \left\langle \tilde{E}^{\dagger}_{sq}(\omega')\,\tilde{E}_{sq}(\omega)\right\rangle$ from section 2.3 and putting Equations 3.71 and 3.72 together, one will have the normal-order Stokes spectrum as

$$\begin{aligned} S^n_{sq}(\omega) &= AN\left|\wp^{\perp}_{bd,q}\right|^2(\omega+\nu_s)^4\sum_{j,l=1}^{4}\int_{r=0}^{\rho}\int_{\theta=0}^{\pi}\int_{\phi=0}^{2\pi}e^{2\,\mathrm{Im}\,k_s(\omega+\nu_s)\hat{R}\cdot\mathbf{r}} \\ &\quad\times M^*_{4j}(\mathbf{r}',\omega')\,M_{4l}(\mathbf{r},\omega)\,2\tilde{D}^n_{j,l}(\mathbf{r},0)\,d^3r, \end{aligned} \tag{3.75}$$

where $A = \left(\frac{1}{4\pi\varepsilon_0 c^2 R}\right)^2(2\pi)^3$ and ρ is the radius of the spherical particle.

If the pump and control laser fields are homogeneous across the particle, the matrix elements of M would be independent of position and the spectra would be similar to the one obtained for a single atom. In this case, the normal-order Stokes spectrum would become

$$S^n_{sq}(\omega) = AN\left|\wp^{\perp}_{bd,q}\right|^2\frac{4\pi}{3}\rho^3(\omega+\nu_s)^4\sum_{j,l=1}^{4}M^*_{4j}(\mathbf{r}',\omega')\,M_{4l}(\mathbf{r},\omega)\,2\tilde{D}^n_{j,l}(\mathbf{r},0). \tag{3.76}$$

3.5.2 Antinormal-Order Stokes Spectra

To obtain the antinormal-order field correlation, one may start from the antinormal-order noise correlation

$$\left\langle \hat{G}_{j'}\left(\mathbf{r}',\omega'\right)\hat{G}_{l}^{\dagger}\left(\mathbf{r},\omega\right)\right\rangle = \frac{\left(2\pi\right)^{3}}{N}2\tilde{D}_{j,l}^{an}\left(\omega'-\omega\right)\delta\left(\mathbf{r}'-\mathbf{r}\right), \tag{3.77}$$

while the rest remains the same as the normal-order case. The only difference between the normal- and antinormal-correlation is in the diffusion coefficients where $2\tilde{D}_{j,l}^{n}$ is replaced by $2\tilde{D}_{j,l}^{an} = 2\tilde{D}_{j,l\dagger}$. Hence, the antinormal-order spectrum for the $q-$component Stokes signal is given by

$$S_{sq}^{an}\left(\omega\right) = AN\left|\wp_{bd,q}^{\perp}\right|^{2}\frac{4\pi}{3}\rho^{3}\left(\omega+\nu_{s}\right)^{4}\sum_{j,l=1}^{4}M_{4j}\left(\mathbf{r}',\omega'\right)M_{4l}^{*}\left(\mathbf{r},\omega\right)2\tilde{D}_{j,l}^{an}\left(\mathbf{r},0\right). \tag{3.78}$$

3.6 Normal- and Antinormal-Order Anti-Stokes Spectra

From Equation 3.66, the electric field vector of the anti-Stokes signal is given by

$$\hat{\mathbf{E}}_{a}\left(\omega\right) = -N\vec{\wp}_{ac}^{\perp}\int_{V}C_{a}\left(\mathbf{r},\omega\right)\sum_{j=1}^{4}M_{1j}\left(\mathbf{r},\omega\right)\hat{G}_{j}\left(\mathbf{r},\omega\right)d^{3}r, \tag{3.79}$$

where again it is assumed that the anti-Stokes field is weak. Following the same procedures as in subsection 3.5.1 and 3.5.2, the $q-$component normal-order power spectrum of the anti-Stokes signal is obtained as

$$S_{aq}^{n}\left(\omega\right) = AN\left|\wp_{ac,q}^{\perp}\right|^{2}\left(\omega-\nu_{a}\right)^{4}\sum_{j,l=1}^{4}\int_{V}e^{2\,\mathrm{Im}\,k_{a}\left(\omega-\nu_{a}\right)\hat{R}\cdot\mathbf{r}}M_{1j}\left(\mathbf{r}',\omega'\right)M_{1l}^{*}\left(\mathbf{r},\omega\right)2\tilde{D}_{j,l}^{an}\left(\mathbf{r},0\right)d^{3}r \tag{3.80}$$

and the antinormal-order anti-Stokes spectrum as

$$S_{aq}^{an}(\omega) = AN\left|\wp_{ac,q}^{\perp}\right|^2(\omega-\nu_a)^4\sum_{j,l=1}^{4}\int_V e^{2\,\mathrm{Im}\,k_a(\omega-\nu_a)\hat{R}\cdot\mathbf{r}}M_{1j}^{*}(\mathbf{r}',\omega')\,M_{1l}(\mathbf{r},\omega)\,2\tilde{D}_{j,l}^{n}(\mathbf{r},0)\,d^3r. \tag{3.81}$$

In summary, the Stokes and anti-Stokes fields emitted from a mesoscopic spherical particle in double Raman scheme have been analytically solved using quantum Langevin formalism with noise operators. The analytical expression of the emitted fields obtained allow us to compute the spectra from which the quantum properties of the Stokes and anti-Stokes photons could be studied. Simulations of the spectra, particularly their dependence on the particle size and angle of detection for different cases of laser fields strengths and detunings are provided and analyzed in Chapter 6.

CHAPTER 4: QUANTUM SYSTEM INTERACTING WITH METALLIC PARTICLE: SPECTRA FROM LANGEVIN THEORY

This chapter concerns the main theme of this thesis: the quantum optical properties of a hybrid nanostructure comprising of a metallic nanoparticle (MP) in close proximity with a quantum system (QS) in double Raman configuration. Just like in Chapter 3, quantum Langevin formalism with noise operators will be used to solve for the Stokes and anti-Stokes fields scattered from the QS but this time the plasmonic effects caused by a nearby MP will also be taken into account. In general, there will be a long-range Coulomb interaction between the two particles, thus leading to excitation transfer which will then result in interesting optical properties such as local field enhancement effect. The local fields of QS and MP as well as the scattered fields at arbitrary observation point will first be analytically solved and the then quantum fields spectra will be computed. In Chapter 6, the quantum properties of the emitted Stokes and anti-Stokes photons will be interpreted from the spectra and the dependence of the spectra on various parameters such as interparticle distance, angle of observation, size of the particles, etc. will be analyzed.

The organization of this chapter is as follows. In section 4.1, the model of the system under study will be established and at the same time, the assumptions or approximations made throughout the chapter will be highlighted. Then, the analytical form of the scattered field from a polarizing source under dipole approximation will be derived in section 4.2. This expression will be helpful in the search for the explicit expression of scattered fields at arbitrary point in section 4.3 as well as the local fields of QS and MP in section 4.4. Then, in section 4.5, the scattered Stokes and anti-Stokes fields at arbitrary point will be put in their final form. The final section of this chapter is on the computation of the Stokes and anti-Stokes spectra, both of which are going to be simulated and studied in Chapter 6 in order to gain insights into the plasmonic effects on the quantum fields emitted by the

hybrid nanostructure.

4.1 Model

The model considered in this study consists of a spherical MP of radius a in close proximity with a spherical QS of radius b. As shown in Figure 4.1, the center of the QS is located at the origin of the Cartesian coordinate whereas the spherical MP is located at some point along the $x-$axis. We define $\mathbf{R} = R\hat{R}$ as the vector of the observation point from the origin, $\mathbf{r} = r\hat{x}$ as the vector of the center of MP from the origin and $\mathbf{r}' = \mathbf{R} - \mathbf{r} = r'\hat{r}'$ as the vector of the observation point from the center of MP. Here, the MP is a nanosized particle made of noble-metal such as silver (Ag) with dispersive dielectric function $\varepsilon_{MP,f}(\omega)$ $(f = s, a)$ and polarizibility $\alpha_{MP,f}(\omega)$. On the other hand, the QS is modelled as a single collective dipole, practically as a quantum dot or nanoparticle comprising of atoms in four-level double Raman configuration and with well-defined Stokes and anti-Stokes dielectric functions $\varepsilon_{QS,f}(\omega)$. The formalism adopted in this chapter is considered a semiclassical approach in which the MP is treated as a classical dielectric particle with continuous spectral response whereas the QS is treated quantum-mechanically using Heisenberg-Langevin formalism as in sections 2.2 and 3.3. For the sake of simplicity, it is assumed that the dimension of the QS is sufficiently small such that any finite-size related effect such as laser focusing can be neglected. This means that in this chapter the Lorentz-Mie theory which account for the spatial dependence of the incident laser fields will not be incorporated into the formalism as in Chapter 3 and the QS will be treated as a point particle. Also, to give a more realistic picture of the MP spectral response the effect of spatial nonlocality (McMahon et al., 2010) will be considered through the k_d-dependent dielectric function, $\varepsilon_{MP,f}(\mathbf{k}_d, \omega)$ (where $k_d = \frac{2\pi}{d}$, $d = 2a$ is the diameter of the MP). The retardation effect (Meier & Wokaun, 1983; Moroz, 2009) will also be included via the correction terms in the polarizibility, $\alpha_{MP,f}(\omega)$.

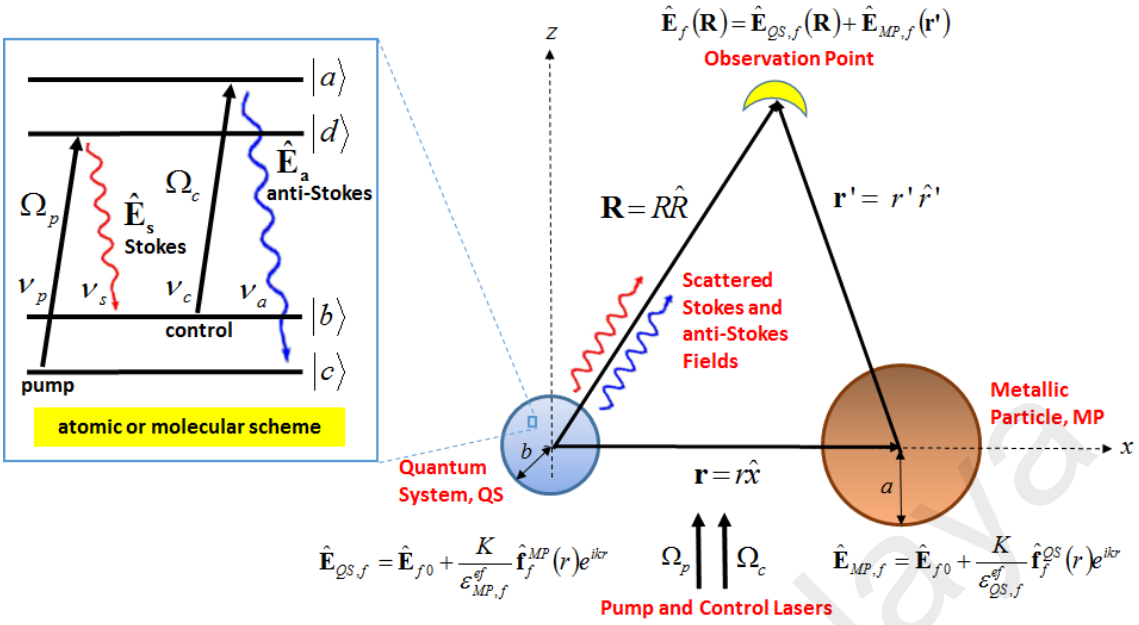

Figure 4.1: Schematic showing the hybrid nanostructure comprising of a quantum system (QS) located at the origin in close proximity with a metallic nanoparticle (MP) located at some point along the $x-$axis. The QS is made of quantum particles in double Raman configuration. Here, $\hat{\mathbf{E}}_{QS,f}(0)$ and $\hat{\mathbf{E}}_{MP,f}(\mathbf{r})$ $(f = s, a)$ are the Stokes and anti-Stokes local fields of the QS and MP, respectively and $\hat{\mathbf{E}}_f(\mathbf{R})$ is the scattered field at arbitray position $\mathbf{R}$. We assume that the incident pump and control laser fields are polarized along the $x-$axis and propagate in the $+z-$direction. The inset shows the energy-level diagram for the four-level double Raman scheme similar to the one in Figure 3.1(b).

In this model, the electromagnetic fields of the lasers excite the discreet transitions between the energy levels in the QS and the plasmons on the surface of MP which provide strong continuous spectral response. A long-range Coulomb interaction exists between MP and QS which couples the two particles and leads to excitation transfer. The theoretical treatment given in this chapter considers only the dipole-dipole interaction although several multipole interactions are also involved in the Coulomb coupling. This dipole approximation approach in modelling MP-QS interactions has been extensively used in the literatures (Zhang et al., 2006; Zhang & Govorov, 2011; Artuso & Bryant, 2010; Ridolfo et al., 2010; Sadeghi, 2009; Artuso & Bryant, 2008; Kosionis et al., 2013; Kosionis et al., 2012; Ooi & Tan, 2013) and is valid when the sizes of both particles are much smaller than the wavelengths of the radiation fields $\lambda_{s(a)} >> a, b$ as well as

the interparticle distance $r >> a, b$ (Kosionis et al., 2012; Yan et al., 2008). As a mathematical proof, it is shown in Appendix E that the dipole-dipole interaction becomes dominant under these two conditions. The advantage of this approximation is that it greatly simplifies the rigorous calculations involved without losing the essential physics behind MP-QS interaction.

4.2 Scattered Fields from a Polarizing Source under Dipole Approximation

In this section, the analytical form of the scattered fields from a polarizing source within the dipole approximation will be the main focus. The expression obtained will be useful for the calculation of the scattered field at arbitrary point in section 4.3 and local fields in section 4.4.

The scattered electric field (in frequency domain) from a polarizing source at arbitrary point **R** within the dipole approximation is formally given by (Jackson, 1999)

$$\hat{\mathbf{E}}_{I,f}(\mathbf{R},\omega) = \frac{K}{\varepsilon^{ef}_{I,f}(\omega)}\hat{\mathbf{f}}^{I}_{f}(R,\omega)\, e^{ikR}, \tag{4.1}$$

where $I = QS$ or MP denotes the source particle, $K = \frac{1}{4\pi\varepsilon_0}$, $k = \frac{\omega}{c}$ is the wavevector and $\varepsilon^{ef}_{I,f}$ is the effective dielectric function of the source particle given by

$$\varepsilon^{ef}_{I,f}(\omega) = \frac{2\varepsilon_b + \varepsilon_{I,f}(\omega)}{3\varepsilon_b}, \tag{4.2}$$

with ε_b and $\varepsilon_{I,f}$ as the dielectric function of the background and source particle, respectively. Since one is now dealing with quantum fields (Stokes and anti-Stokes fields), the

vectorial part of the electric field in Equation 4.1 takes the operator form

$$\begin{aligned}\hat{\mathbf{f}}_f^I(R,\omega) &= \frac{k^2}{R}\left(\hat{n}_I \times \hat{\mathbf{p}}_f^I(\omega)\right)\times \hat{n}_I \\ &\quad + \left[3\hat{n}_I\left(\hat{n}_I \cdot \hat{\mathbf{p}}_f^I(\omega)\right) - \hat{\mathbf{p}}_f^I(\omega)\right]\left(\frac{1}{R^3} - \frac{ik}{R^2}\right),\end{aligned} \tag{4.3}$$

where $\hat{\mathbf{p}}_f^I$ is the dipole moment operator and the unit vectors $\hat{n}_{QS} = \hat{R} = \frac{\mathbf{R}}{R}$ and $\hat{n}_{MP} = \hat{r}' = \frac{\mathbf{r}'}{r'} = \frac{\mathbf{R}-\mathbf{r}}{|\mathbf{R}-\mathbf{r}|}$ point along the vectors from the respective source particle (QS or MP) to the observation point $\mathbf{R}$. It can be shown (Ooi & Tan, 2013) that by using the vector triple product identity $(\mathbf{a}\times\mathbf{b})\times\mathbf{c} = (\mathbf{c}\cdot\mathbf{a})\,\mathbf{b} - (\mathbf{c}\cdot\mathbf{b})\,\mathbf{a}$, Equation 4.3 can be further simplified into

$$\hat{\mathbf{f}}_f^I(R,\omega) = A(R,\omega)\,\hat{\mathbf{p}}_f^I(\omega) + B(R,\omega)\left(\hat{n}_I \cdot \hat{\mathbf{p}}_f^I(\omega)\right)\hat{n}_I \tag{4.4}$$

with the coefficients given by

$$A(R,\omega) = \frac{k^2}{R} - \frac{1}{R^3} + \frac{ik}{R^2}, \tag{4.5}$$

$$B(R,\omega) = \frac{3}{R^3} - \frac{3ik}{R^2} - \frac{k^2}{R}. \tag{4.6}$$

The formula for the electric field scattered from a particle in Equation 4.1 is valid for any vector dipole moment over a wide range of interparticle distances through the terms A and B, provided R is larger than the dimension of the particle.

The dielectric functions of the QS are related to the density matrix elements via

$$\varepsilon_{QS,f}(\omega) = 1 + \frac{\eta_f}{\Omega_f}\bar{\rho}_f(\omega), \tag{4.7}$$

where $\eta_s = \frac{N|\wp_{bd}|^2}{\hbar\varepsilon_0}$ and $\eta_a = \frac{N|\wp_{ca}|^2}{\hbar\varepsilon_0}$, N is the number density of the QS, $\wp_{bd}$ and $\wp_{ca}$ are the dipole moments, Ω_s and Ω_a are respectively the Rabi frequencies of the Stokes and

anti-Stokes fields and $\bar{\rho}_s = \bar{\rho}^{st}_{db}$ and $\bar{\rho}_a = \bar{\rho}^{st}_{ac}$ are the steady state coherences corresponding to the Stokes and anti-Stokes transitions, respectively. These steady state coherences are computed self-consistently from the 16 density matrix equations given in section 2.2 and the details of the computation are provided in Appendix F.

On the other hand, the dielectric functions of the MP are approximated by (McMahon et al., 2010)

$$\varepsilon_{MP}(\mathbf{k}_d, \omega) = \varepsilon_\infty - \frac{\omega_p^2}{\omega[\omega + i\Gamma_m] - \beta^2 k_d^2}, \tag{4.8}$$

where ε_∞ is the dielectric function at infinity, ω_p is the plasma frequency, $\Gamma_m = \Gamma_m^\infty + C\frac{v_F}{a}$ (Derkachova et al., 2015; Khlebtsov et al., 1996) is the electron relaxation rate that depends on a the radius of the MP, v_F is the Fermi velocity, C is a theory-dependent quantity, $\beta^2 = \frac{3v_F^2}{D+2}$ (for free electron gas) (McMahon, Gray, & Schatz, 2010; Fetter, 1973), where D is the dimension of the system ($D = 3$ in our case), $k_d = \frac{2\pi}{d}$, and $d = 2a$ is the diameter of MP.

A point to note here is that in Equation 4.8, the phenomenological relaxation term $C\frac{v_F}{a}$ has been added to the relaxation rate Γ_m^∞ to account for the increased electron-interface scattering when the dimension of the MP is smaller or comparable to the mean free path of the conduction electrons, λ_m. For gold (Au), $\lambda_m = 37.7$ nm at room temperature (Gall, 2016) and $C = 0.33$ (Derkachova et al., 2015), whereas for silver, $\lambda_m = 53.3$ nm with $C = 1$ (Hövel et al., 1993). Moreover, the size-dependent correction term $-\beta^2 k_d^2$ has also been added in the denominator of Equation 4.8 to account for the **spatial nonlocality** which originates from the finite penetration of the charges induced by the EM fields in the MP by an amount not negligible compared to the size of the nanostructure (David & de Abajo, 2011). This effect is known to cause an effective reduction in permitivity which leads to blue shift of the spectral peak (Palombaa et al., 2008; Kosionis et al., 2012). Take note that all the parameters used in this study are for silver (Ag) nanoparticle. For this

reason, here the effect of interband transition on the dielectric function in Equation 4.8 is not included because for spherical silver nanoparticle such effect is not important as the energy position of the LSPR is around 3.5 eV which does not coincide with the interband transition at around 4.0 eV (Andrews et al., 2010). This approximation will break down if the incident field with which the silver nanoparticle interacts is a broadband light with linewidth above 100THz, where interband transitions could occur. Such cases will not be considered here but instead the incident field is assumed to be a coherent laser with narrow linewidth, and any other external sources of light that could stimulate interband transitions are assumed to be too weak to bring any observable features in the dielectric function.

4.3 Scattered Stokes and Anti-Stokes Fields at Arbitrary Point from the Hybrid Nanostructure

The scattered Stokes and anti-Stokes fields at arbitrary point $\mathbf{R}=R(\sin\Theta\cos\Phi, \sin\Theta\sin\Phi, \cos\Theta)$ are due to the contribution from the polarization fields emitted by both QS and MP. Hence, using the vector notation in Figure 4.1, the scattered Stokes $\hat{\mathbf{E}}_s(\mathbf{R})$ and anti-Stokes $\hat{\mathbf{E}}_a^{\dagger}(\mathbf{R})$ fields operators at point $\mathbf{R}$ are written as

$$\hat{\mathbf{E}}_f(\mathbf{R},t) = \hat{\mathbf{E}}_{QS,f}(\mathbf{R},t) + \hat{\mathbf{E}}_{MP,f}(\mathbf{r}',t), \tag{4.9}$$

where the subscript $f = s, a$ refers to the Stokes and anti-Stokes fields, respectively. Since both QS and MP are modelled as dipole emitters, $\hat{\mathbf{E}}_{QS,f}(\mathbf{R})$ and $\hat{\mathbf{E}}_{MP,f}(\mathbf{r}')$ are the Stokes and anti-Stokes polarization fields operators from the QS and MP, respectively.

Next, by substituting Equations 4.1, 4.4, 4.5 and 4.6 into Equation 4.9 will lead to

$$\begin{aligned}\hat{\mathbf{E}}_s(\mathbf{R},\omega) &= \frac{Ke^{ikR}}{\varepsilon^{ef}_{QS,s}(\omega)}P^{QS}(\mathbf{R},\omega)\,\vec{\wp}_{bd}\hat{\sigma}_{bd}(\omega) \\ &\quad+\frac{K\alpha_{MP,s}(\omega)\,e^{ikr'}}{\varepsilon^{ef}_{MP,s}(\omega)}P^{MP}(\mathbf{r}',\omega)\,\hat{\mathbf{E}}^{loc}_{MP,s}(\omega),\end{aligned} \tag{4.10}$$

$$\begin{aligned}\hat{\mathbf{E}}_a(\mathbf{R},\omega) &= \frac{Ke^{ikR}}{\varepsilon^{ef}_{QS,a}(\omega)}P^{QS}(\mathbf{R},\omega)\,\vec{\wp}_{ca}\hat{\sigma}_{ca}(\omega) \\ &\quad+\frac{K\alpha_{MP,a}(\omega)\,e^{ikr'}}{\varepsilon^{ef}_{MP,a}(\omega)}P^{MP}(\mathbf{r}',\omega)\,\hat{\mathbf{E}}^{loc}_{MP,a}(\omega).\end{aligned} \tag{4.11}$$

In the process the expressions for the quantum-mechanical dipole moment operator for the QS, $\hat{\mathbf{p}}^{QS}_f = \vec{\wp}_f\hat{\sigma}_f$ $(f \in s,a)$ and MP, $\hat{\mathbf{p}}^{MP}_f = \alpha_{MP,f}\hat{\mathbf{E}}^{loc}_{MP,f}$ have been used, where $\hat{\mathbf{E}}^{loc}_{MP,f}$ is the local field of the MP. The dipole matrix elements are $\vec{\wp}_{bd} = \langle b|\,\mathbf{d}\,|d\rangle$ and $\vec{\wp}_{ca} = \langle c|\,\mathbf{d}\,|a\rangle$ and the coherences operators corresponding to the Stokes and anti-Stokes transitions are $\hat{\sigma}_s = \hat{\sigma}_{bd} = |b\rangle\langle d|$ and $\hat{\sigma}_a = \hat{\sigma}_{ca} = |c\rangle\langle a|$, respectively. The dipole moment of the MP, $\hat{\mathbf{p}}^{MP}_f$ depends on the local fields $\hat{\mathbf{E}}^{loc}_{MP,f}$ through the polarizability $\alpha_{MP,f} = \frac{1}{K}\gamma_f a^3$ (a is the radius of the MP) where (Moroz, 2009)

$$\gamma_f = \frac{\varepsilon_{MP,f}(\mathbf{k}_d,\omega)-\varepsilon_b}{\varepsilon_{MP,f}(\mathbf{k}_d,\omega)+2\varepsilon_b-\left[\varepsilon_{MP,f}(\mathbf{k}_d,\omega)-\varepsilon_b\right]x^2-i\frac{2x^3}{3}\left[\varepsilon_{MP,f}(\mathbf{k}_d,\omega)-\varepsilon_b\right]}, \tag{4.12}$$

with $\varepsilon_{MP,f}(\mathbf{k}_d,\omega)$ and ε_b as the dielectric functions of MP and background, respectively and $x = ka$ where $k = \frac{2\pi}{\lambda}$ and a is the MP radius. Note that if the last two terms $-\left[\varepsilon_{MP,f}(\mathbf{k}_d,\omega)-\varepsilon_b\right]x^2-i\frac{2x^3}{3}\left[\varepsilon_{MP,f}(\mathbf{k}_d,\omega)-\varepsilon_b\right]$ in the denominator of Equation 4.12 are ignored, the original expression $\gamma_f = \frac{\varepsilon_{MP,f}-\varepsilon_b}{\varepsilon_{MP,f}+2\varepsilon_b}$ as obtained from the well-known Clausius-Mossotti relation will recover. The x^2-dependent term is added to account for the **retardation effect** which arises from the dephasing between the fields emitted by

different parts of the MP sphere whereas the x^3-dependent term is the **radiative reaction correction** which applies to any oscillating dipole (Moroz, 2009). These two terms can be ignored when the size of the MP is sufficiently small such that $x \ll 1$.

The matrix P^{QS} in Equations 4.10 and 4.11 is obtained by first representing all the vectors as 3×1 matrices, such as

$$\hat{\mathbf{p}}_f^{QS} = \begin{pmatrix} \hat{p}_{f,x}^{QS} \\ \hat{p}_{f,y}^{QS} \\ \hat{p}_{f,z}^{QS} \end{pmatrix} \tag{4.13}$$

and then simplifying Equation 4.4 using matrix multiplication. This provides a convenient way for evaluating each vector component of the fields without involving too many unit vectors such as $\hat{\imath}$, $\hat{\jmath}$ and $\hat{\mathbf{k}}$. One will finally arrive at

$$P^{QS}(\mathbf{R}, \omega) = A(R, \omega) I + B(R, \omega) \begin{pmatrix} n_{QS,x}^2 & n_{QS,y} n_{QS,x} & n_{QS,z} n_{QS,x} \\ n_{QS,x} n_{QS,y} & n_{QS,y}^2 & n_{QS,z} n_{QS,y} \\ n_{QS,x} n_{QS,z} & n_{QS,y} n_{QS,z} & n_{QS,z}^2 \end{pmatrix}, \tag{4.14}$$

where $A(R, \omega)$ and $B(R, \omega)$ are respectively given by Equations 4.5 and 4.6, $n_{QS,q}$ $(q = x, y, z)$ is the Cartesian component of the unit vectors $\hat{n}_{QS} = \hat{R} = \frac{\mathbf{R}}{R}$, from which P^{QS} acquires its $\mathbf{R}$ dependence. $P^{MP}(\mathbf{r}', \omega)$ can be obtained by simply replacing all the R's in Equation 4.14 by r' and $n_{QS,q}$ by $n_{MP,q}$. Also, according to Figure 4.1, $\mathbf{r}' = \mathbf{R} - r\hat{x}$.

It is obvious from Equations 4.10 and 4.11 that the scattered Stokes and anti-Stokes fields depend directly on the local fields at MP, $\hat{\mathbf{E}}_{MP,f}^{loc}$ as well as the coherences operators $\hat{\sigma}_{bd}(\omega)$ and $\hat{\sigma}_{ca}(\omega)$ whose analytical solutions depend on the local fields at the position of QS as given in Equations 3.53 and 3.54 in section 3.3 in their slowly varying form.

4.4 Exact Vectorial Local Fields

In this section, the local electric fields of the QS and MP which are required to evaluate the scattered Stokes and anti-Stokes electric fields in Equations 4.10 and 4.11 will be derived. Since the system considered here contains only two particles, the scatterings between the two particles lead to only two coupled equations. If there were many particles, there would be multiple scatterings involving many coupled equations.

4.4.1 Local Fields of Metallic Nanoparticle

The local electric fields of the MP, $\hat{\mathbf{E}}^{loc}_{MP,f}$ $(f = s, a)$ are due to the intrinsic quantum Stokes and anti-Stokes fields $\hat{\mathbf{E}}_{f0}$ (which are independent of the exciton-plasmon coupling) as well as the polarization fields emitted by the QS. Again, Equation 4.1 is used to write the local Stokes and anti-Stokes electric fields at the MP as

$$\hat{\mathbf{E}}^{loc}_{MP,s}(r,\omega) = \hat{\mathbf{E}}_{s0}(\omega) + \frac{Ke^{ikr}}{\varepsilon^{ef}_{QS,s}(\omega)} \mathcal{P}(r,\omega)\, \vec{\wp}_{bd} \hat{\sigma}_{bd}(\omega), \tag{4.15}$$

$$\hat{\mathbf{E}}^{loc}_{MP,a}(r,\omega) = \hat{\mathbf{E}}_{a0}(\omega) + \frac{Ke^{ikr}}{\varepsilon^{ef}_{QS,a}(\omega)} \mathcal{P}(r,\omega)\, \vec{\wp}_{ca} \hat{\sigma}_{ca}(\omega), \tag{4.16}$$

with the definition of the matrix $\mathcal{P}(r,\omega)$ given by

$$\mathcal{P}(r,\omega) = \begin{pmatrix} A(r,\omega) + B(r,\omega) & 0 & 0 \\ 0 & A(r,\omega) & 0 \\ 0 & 0 & A(r,\omega) \end{pmatrix}. \tag{4.17}$$

Here, the definitions for $A(r,\omega)$ and $B(r,\omega)$ are the same as in Equations 4.5 and 4.6 except that all the R's are replaced by r, the separation distance between QS and MP. Note that Equation 4.17 is obtained from Equation 4.14 by simply taking into account the fact that both QS and MP are placed along the $x-$axis ($n_{QS,x} = 1, n_{MP,x} = -1$).

Equations 4.15 and 4.16 are derived by including the dipole moment operator for the QS, $\hat{\mathbf{p}}_f^{QS} = \vec{\wp}_f \hat{\sigma}_f$ $(f = s, a)$ mentioned earlier which couples the local fields at MP to the coherences operators at QS.

4.4.2 Local Fields of Quantum Emitter

Similarly, the local electric fields at the QS $\hat{\mathbf{E}}_{QS,f}^{loc}$ are due to the intrinsic quantum fields from the QS as well as the polarization fields from the MP. They are written as

$$\hat{\mathbf{E}}_{QS,s}^{loc}(r,\omega) = \hat{\mathbf{E}}_{s0}(\omega) + \frac{K\alpha_{MP,s}(\omega)}{\varepsilon_{MP,s}^{ef}(\omega)} \mathcal{P}(r,\omega)\, \hat{\mathbf{E}}_{MP,s}^{loc}(\omega)\, e^{ikr}, \tag{4.18}$$

$$\hat{\mathbf{E}}_{QS,a}^{loc}(r,\omega) = \hat{\mathbf{E}}_{a0}(\omega) + \frac{K\alpha_{MP,a}(\omega)}{\varepsilon_{MP,a}^{ef}(\omega)} \mathcal{P}(r,\omega)\, \hat{\mathbf{E}}_{MP,a}^{loc}(\omega)\, e^{ikr}. \tag{4.19}$$

In deriving Equations 4.18 and 4.19, the dipole moment operator for the MP, $\hat{\mathbf{p}}_f^{MP} = \alpha_{MP,f} \hat{\mathbf{E}}_{MP,f}^{loc}$ which couples the local fields at QS to the local fields at MP has been used. Substitution of the expressions for the local fields at MP in Equations 4.15 and 4.16 into Equations 4.18 and 4.19, respectively yields

$$\hat{\mathbf{E}}_{QS,s}^{loc}(r,\omega) = \mathbf{N}_s(r,\omega)\, \hat{\mathbf{E}}_{s0}(\omega) + \mathbf{R}_s(r,\omega)\, \hat{\sigma}_{bd}(\omega), \tag{4.20}$$

$$\hat{\mathbf{E}}_{QS,a}^{loc}(r,\omega) = \mathbf{N}_a(r,\omega)\, \hat{\mathbf{E}}_{a0}(\omega) + \mathbf{R}_a(r,\omega)\, \hat{\sigma}_{ca}(\omega), \tag{4.21}$$

where

$$\mathbf{N}_f(r,\omega) = I + \frac{K\alpha_{MP,f}(\omega)}{\varepsilon_{MP,f}^{ef}(\omega)} \mathcal{P}(r,\omega)\, e^{ikr} \tag{4.22}$$

and

$$\mathbf{R}_f(r,\omega) = \frac{K^2\alpha_{MP,f}(\omega) e^{2ikr}}{\varepsilon_{MP,f}^{ef}(\omega)\varepsilon_{QS,f}^{ef}(\omega)} \mathcal{P}^2(r,\omega)\, \vec{\wp}_g. \tag{4.23}$$

The subscript g in $\vec{\wp}_g$ is defined by $g(f) = bd(s), ca(a)$.

4.5 Scattered Stokes and Anti-Stokes Fields: Final Form

Now, the analytical expressions of the scattered Stokes and anti-Stokes fields will be derived given the expressions of the local fields in Equations 4.15 and 4.16. The vectorial scattered Stokes and anti-Stokes fields at point **R** (in frequency domain) are found to be

$$\hat{\mathbf{E}}_s(\mathbf{R},\omega) = \mathbf{M}_s(R, r, r', \omega)\,\hat{\sigma}_{bd}(\omega) + \hat{\mathbf{D}}_s(r', \omega), \tag{4.24}$$

$$\hat{\mathbf{E}}_a(\mathbf{R},\omega) = \mathbf{M}_a(R, r, r', \omega)\,\hat{\sigma}_{ca}(\omega) + \hat{\mathbf{D}}_a(r', \omega), \tag{4.25}$$

where

$$\begin{aligned}\mathbf{M}_f(R, r, r', \omega) &= \frac{K}{\varepsilon^{ef}_{QS,f}(\omega)} P^{QS}(R, \omega)\,\vec{\wp}_g e^{ikR} \\ &\quad + \frac{K^2 \alpha_{MP,f}(\omega)}{\varepsilon^{ef}_{MP,f}(\omega)\,\varepsilon^{ef}_{QS,f}(\omega)} P^{MP}(r', \omega)\,\mathcal{P}(r,\omega)\,\vec{\wp}_g e^{ik(r+r')},\end{aligned} \tag{4.26}$$

$$\hat{\mathbf{D}}_f(r', \omega) = Q_f(r', \omega)\,\hat{\mathbf{E}}_{f0}(\omega), \tag{4.27}$$

$$Q_f(r', \omega) = \kappa_f P^{MP}(r', \omega), \tag{4.28}$$

and

$$\kappa_f = \frac{K \alpha_{MP,f}(\omega)}{\varepsilon^{ef}_{MP,f}(\omega)} e^{ikr'}. \tag{4.29}$$

In order to make use of the results in Equations 3.53 and 3.54, the Fourier transform of the slowly varying envelope fields operators defined by $\hat{\mathbf{E}}_f(\mathbf{R}, t) = \tilde{\mathbf{E}}_f(\mathbf{R}, t)e^{-i\nu_f t}$ instead of the original fields operators in Equations 4.24 and 4.25 have to be computed. The

Fourier transforms of the original fields and coherences are related to their envelopes via

$$\begin{pmatrix} \hat{\sigma}_{bd}(\omega) \\ \hat{\mathbf{E}}_s(\omega) \\ \hat{\mathbf{E}}_{s0}(\omega) \end{pmatrix} = \int e^{i\omega t} e^{-i\nu_s t} \begin{pmatrix} \hat{p}_{bd}(t) \\ \tilde{\mathbf{E}}_s(t) \\ \tilde{\mathbf{E}}_{s0}(t) \end{pmatrix} dt = \begin{pmatrix} \hat{p}_{bd}(\omega - \nu_s) \\ \tilde{\mathbf{E}}_s(\omega - \nu_s) \\ \tilde{\mathbf{E}}_{s0}(\omega - \nu_s) \end{pmatrix}, \tag{4.30}$$

$$\begin{pmatrix} \hat{\sigma}_{ca}(\omega) \\ \hat{\mathbf{E}}_a(\omega) \\ \hat{\mathbf{E}}_{a0}(\omega) \end{pmatrix} = \int e^{i\omega t} e^{-i\nu_a t} \begin{pmatrix} \hat{p}_{ca}(t) \\ \tilde{\mathbf{E}}_a(t) \\ \tilde{\mathbf{E}}_{a0}(t) \end{pmatrix} dt = \begin{pmatrix} \hat{p}_{ca}(\omega - \nu_a) \\ \tilde{\mathbf{E}}_a(\omega - \nu_a) \\ \tilde{\mathbf{E}}_{a0}(\omega - \nu_a) \end{pmatrix}. \tag{4.31}$$

Hence, Equations 4.24 and 4.25 can be rewritten as

$$\tilde{\mathbf{E}}_s(\omega - \nu_s) = \mathbf{M}_s(\omega)\,\hat{p}_{bd}(\omega - \nu_s) + Q_s(\omega)\,\tilde{\mathbf{E}}_{s0}(\omega - \nu_s), \tag{4.32}$$

$$\tilde{\mathbf{E}}_a(\omega - \nu_a) = \mathbf{M}_a(\omega)\,\hat{p}_{ca}(\omega - \nu_a) + Q_a(\omega)\,\tilde{\mathbf{E}}_{a0}(\omega - \nu_a). \tag{4.33}$$

However, the solutions given in Equations 3.53 and 3.54 are $\hat{p}_{bd}(\omega)$ and $\hat{p}_{ca}(\omega)$ instead of $\hat{p}_{bd}(\omega - \nu_s)$ and $\hat{p}_{ca}(\omega - \nu_a)$. Hence, the Fourier frequency in the entire expression has to be shifted and doing so leads to

$$\tilde{\mathbf{E}}_s(\omega) = \mathbf{M}_s(\omega + \nu_s)\,\hat{p}_{bd}(\omega) + \tilde{\mathbf{D}}_s(\omega), \tag{4.34}$$

$$\tilde{\mathbf{E}}_a(\omega) = \mathbf{M}_a(\omega + \nu_a)\,\hat{p}_{ca}(\omega) + \tilde{\mathbf{D}}_a(\omega), \tag{4.35}$$

where

$$\tilde{\mathbf{D}}_f(\omega) = Q_f\left(\omega + \nu_f\right)\tilde{\mathbf{E}}_{f0}(\omega). \tag{4.36}$$

4.6 Stokes and Anti-Stokes Spectra

In this section, the normal-order Stokes and anti-Stokes spectra of the hybrid nanostructure will be computed. It is already known from section 2.3 that the q-component ($q = x, y, z$) spectra for the Stokes and anti-Stokes fields at position $\mathbf{R}$ are defined as

$$S_{fq}(\mathbf{R},\omega) = \left\langle \hat{E}^{\dagger}_{fq}(\mathbf{R},\omega)\hat{E}_{fq}(\mathbf{R},\omega)\right\rangle, \tag{4.37}$$

with $\left\langle \hat{\mathbf{E}}^{\dagger}_{f}(\mathbf{R},\omega)\cdot\hat{\mathbf{E}}_{f}(\mathbf{R},\omega)\right\rangle = \sum_{q=x,y,z} S_{fq}(\mathbf{R},\omega)$. This means that one needs to evaluate the q-component of the fields correlations $\left\langle \hat{E}^{\dagger}_{fq}(\omega)\hat{E}_{fq}(\omega)\right\rangle$. From the scattered fields expressions in Equations 4.34 and 4.35, one obtains

$$\begin{aligned}
&\left\langle \hat{E}^{\dagger}_{sq}(\omega')\hat{E}_{sq}(\omega)\right\rangle \\
&= C_s\bar{n}_s \sum_{m=x,y,z} \left|Z^{s}_{qm}(\omega+\nu_s)\right|^2 + \left|M_{sq}(\omega+\nu_s)\right|^2 \left\langle \hat{p}^{\dagger}_{bd}(\omega)\,\hat{p}_{bd}(\omega)\right\rangle \\
&\quad + M_{sq}(\omega+\nu_s)\left\langle \tilde{D}^{\dagger}_{sq}(\omega)\,\hat{p}_{bd}(\omega)\right\rangle + M^{*}_{sq}(\omega+\nu_s)\left\langle \hat{p}^{\dagger}_{bd}(\omega)\,\tilde{D}_{sq}(\omega)\right\rangle
\end{aligned} \tag{4.38}$$

and

$$\begin{aligned}
&\left\langle \tilde{E}^{\dagger}_{aq}(\omega)\,\tilde{E}_{aq}(\omega)\right\rangle \\
&= C_a\bar{n}_a \sum_{m=x,y,z} \left|Z^{a}_{qm}(\omega+\nu_a)\right|^2 + \left|M_{aq}(\omega+\nu_a)\right|^2 \left\langle \hat{p}_{ac}(\omega)\,\hat{p}^{\dagger}_{ac}(\omega)\right\rangle \\
&\quad + M_{aq}(\omega+\nu_a)\left\langle \tilde{D}^{\dagger}_{aq}(\omega)\,\hat{p}^{\dagger}_{ac}(\omega)\right\rangle + M^{*}_{aq}(\omega+\nu_a)\left\langle \hat{p}_{ac}(\omega)\,\tilde{D}_{aq}(\omega)\right\rangle.
\end{aligned} \tag{4.39}$$

Here, M_{fq} is the q-component of the vector quantity in Equation 4.26, $C_f = \frac{\hbar\nu_f\pi}{\varepsilon_0 Ac}$, $\bar{n}_f = \left[\exp(\theta_f) - 1\right]^{-1}$, $\theta_f = \hbar\nu_f/k_BT$ is the average number of thermal photons at temperature T (in Kelvin), $\nu_f\,(f = s, a)$ are the carrier frequencies of the Stokes and

anti-Stokes fields, A is the effective interaction area and Z^f_{qm} is the element of the matrix

$$Z^f(\omega) = \begin{pmatrix} 1+\kappa_f(\omega) P^{MP}_{11}(\omega) & \kappa_f(\omega) P^{MP}_{12}(\omega) & \kappa_f(\omega) P^{MP}_{13}(\omega) \\ \kappa_f(\omega) P^{MP}_{21}(\omega) & 1+\kappa_f(\omega) P^{MP}_{22}(\omega) & \kappa_f(\omega) P^{MP}_{23}(\omega) \\ \kappa_f(\omega) P^{MP}_{31}(\omega) & \kappa_f(\omega) P^{MP}_{32}(\omega) & 1+\kappa_f(\omega) P^{MP}_{33}(\omega) \end{pmatrix}. \quad (4.40)$$

The subscript q and m $(q, m = x, y, z)$ in $Z^f_{qm}(\omega)$ are related to the elements of the matrix Z^f $(f = s, a)$ via the relation $Z^f_{xx} = Z^f_{11}, Z^f_{xy} = Z^f_{12}, Z^f_{yy} = Z^f_{22}, Z^f_{zx} = Z^f_{31}$, ..., etc. Matrix Z^f actually comes from the new definition for $\tilde{D}_{fq}(\omega)$ as

$$\tilde{D}_{fq}(\omega) = \sum_{m=x,y,z} Z^f_{qm}(\omega + \nu_f)\, \tilde{E}_{f0m}(\omega). \quad (4.41)$$

Now 6 operator products are left: $\left\langle \hat{p}^\dagger_{bd}(\omega)\, \hat{p}_{bd}(\omega) \right\rangle$, $\left\langle \tilde{D}^\dagger_{sq}(\omega)\, \hat{p}_{bd}(\omega) \right\rangle$, $\left\langle \hat{p}^\dagger_{bd}(\omega)\, \tilde{D}_{sq}(\omega) \right\rangle$, $\left\langle \hat{p}_{ac}(\omega)\, \hat{p}^\dagger_{ac}(\omega) \right\rangle$, $\left\langle \tilde{D}^\dagger_{aq}(\omega)\, \hat{p}^\dagger_{ac}(\omega) \right\rangle$ and $\left\langle \hat{p}_{ac}(\omega)\, \tilde{D}_{aq}(\omega) \right\rangle$ to be evaluated. After a rather rigorous calculations, the atomic operators products are found to be

$$\left\langle \hat{p}^\dagger_{bd}(\omega)\, \hat{p}_{bd}(\omega) \right\rangle = \sum_{i=1}^{4} H_{4i} J_i, \quad (4.42)$$

$$\left\langle \hat{p}_{ac}(\omega)\, \hat{p}^\dagger_{ac}(\omega) \right\rangle = \sum_{i=1}^{4} H^*_{1i} K_i, \quad (4.43)$$

where the matrices H, J and K are given in Appendix G. Other operator products are

given by

$$\begin{aligned}
&\left\langle \tilde{D}^{\dagger}_{sq}(\omega)\,\hat{p}_{bd}(\omega)\right\rangle \\
= \;& -C_s\bar{n}_s G_s \sum_m g_{sm}N_{sm}(\omega+\nu_s)\,Z^{s*}_{qm}(\omega+\nu_s) \\
& -X_s \sum_m \mathcal{R}^*_a Z^{s*}_{qm}(\omega+\nu_s)\left\langle \tilde{E}^{\dagger}_{s0m}(\omega)\,\hat{p}_{ac}(\omega)\right\rangle \\
& -G_s \sum_m \mathcal{R}_s Z^{s*}_{qm}(\omega+\nu_s)\left\langle \tilde{E}^{\dagger}_{s0m}(\omega)\,\hat{p}_{bd}(\omega)\right\rangle, \qquad (4.44)
\end{aligned}$$

$$\begin{aligned}
&\left\langle \tilde{D}^{\dagger}_{aq}(\omega)\,\hat{p}^{\dagger}_{ac}(\omega)\right\rangle \\
= \;& -C_a\bar{n}_a G^*_a \sum_m g_{am}N_{am}(\omega+\nu_a)\,Z^{a*}_{qm}(\omega+\nu_a) \\
& -G^*_a \sum_m \mathcal{R}_a Z^{a*}_{qm}(\omega+\nu_a)\left\langle \tilde{E}^{\dagger}_{a0m}(\omega)\,\hat{p}^{\dagger}_{ac}(\omega)\right\rangle \\
& -X^*_a \sum_m \mathcal{R}^*_s Z^{a*}_{qm}(\omega+\nu_a)\left\langle \tilde{E}^{\dagger}_{a0m}(\omega)\,\hat{p}^{\dagger}_{bd}(\omega)\right\rangle, \qquad (4.45)
\end{aligned}$$

where $\mathcal{R}_a = \sum_{q'} g_{aq'}R_{aq'}(\omega+\nu_a), \mathcal{R}_s = \sum_{q'} g_{sq'}R_{sq'}(\omega+\nu_s)$ and the other two terms can be obtained as

$$\left\langle \hat{p}^{\dagger}_{bd}(\omega)\,\tilde{D}_{sq}(\omega)\right\rangle = \left\langle \tilde{D}^{\dagger}_{sq}(\omega)\,\hat{p}_{bd}(\omega)\right\rangle^*, \qquad (4.46)$$

$$\left\langle \hat{p}_{ac}(\omega)\,\tilde{D}_{aq}(\omega)\right\rangle = \left\langle \tilde{D}^{\dagger}_{aq}(\omega)\,\hat{p}^{\dagger}_{ac}(\omega)\right\rangle^*. \qquad (4.47)$$

The solutions for the field-atomic operator products (such as $\left\langle \tilde{E}^{\dagger}_{s0m}(\omega)\,\hat{p}_{ac}(\omega)\right\rangle$) in $\left\langle \tilde{D}^{\dagger}_{sq}(\omega)\,\hat{p}_{bd}(\omega)\right\rangle$ and $\left\langle \tilde{D}^{\dagger}_{aq}(\omega)\,\hat{p}^{\dagger}_{ac}(\omega)\right\rangle$ are given in Appendix H.

To summarize, the spectra of the scattered fields from a hybrid nanostructure comprising of a MP in close proximity with a QS in double Raman scheme have been analytically solved, taking into account the long-range Coulomb interaction between the two particles. The spectra obtained will allow us to gain insights into the quantum properties of the emitted Stokes and anti-Stokes at arbitrary position, particularly the plasmonic enhance-

ment effects caused by the presence of the MP. These will be discussed in Chapter 6 where simulations showing the dependence of the spectra on various parameters such as the interparticle distance, size of the particles, angle of observation, etc. will be presented and analyzed.

CHAPTER 5: QUANTUM SYSTEM-METALLIC PARTICLE INTERACTION: ANALYTICAL THEORY FOR THE GENERAL CASE

In this chapter, a general analytical theory for the problem of metallic nanoparticle-quantum system (MP-QS) interaction which includes electric multipole effects and is valid for arbitrary interparticle separation, observation distance as well as particle shape and size will be developed. Most of the previous theoretical studies on MP-QS interaction were based on dipole approximation which is only valid for the case when both the interparticle separation and the wavelength of the electromagnetic field is much larger compared to the sizes of the components. However, the most interesting regime of strong MP-QS interaction occurs when the interparticle distance is sufficiently small such that the dipole approximation is no longer valid. To describe this interesting regime of strong coupling, in this chapter the Coulomb interaction between MP and QS will be treated exactly by including electric multipole effects instead of making the dipole approximation as in chapter 4. Furthermore, most of the related studies, including the one with multipole effects (Yan et al., 2008), neglect the finite size effects due to the geometry of the MP and QS and consider only the far-field of the hybrid nanostructure. This causes the theories developed to lose generality since they could be invalid for near-field and for the cases where the sizes of the MP and QS are comparable to the wavelength. To overcome this, the formalism used in this chapter will take into account the finite size of the particles via the volume integral and at the same time, will be valid for near-, intermediate- and far-field zone. The ultimate aim is to obtain the exact and general solution to the problem of MP-QS interaction.

Section 5.1 concerns the model of the problem studied in this chapter. This is followed by section 5.2 which gives the general expression for the scattered multipole field from the MP and QS at arbitrary position $\mathbf{R}$. Derivations of the local fields of MP and QS are

provided in section 5.3. Finally in section 5.4, the expression for the scattered multipole field at point **R** will be written down in its final form. The general expression obtained will be useful for studying MP-QS interaction involving any energy level configuration of the QS, any sizes and shapes of the QS and MP, any value of interparticle separation and arbitrary observation point in the Cartesian coordinate.

5.1 Model

Figure 5.1 shows the hybrid system under consideration in this chapter. Similar to the system in chapter 4, the system considered here consists of a QS of radius b with its center located at the origin of the Cartesian coordinate and a spherical MP of radius a with its center located at some point along the $x-$axis. However, unlike the previous chapter, the finite dimensions of both QS and MP will now be considered. For this reason, the vector notation used in Figure 4.1 has to be modified. As shown in Figure 5.1, $\mathbf{R} = R\hat{R}$ is the vector of the observation point from the origin, $\mathbf{r} = r\hat{r}$ is the vector of the electric multipoles within the QS, $\mathbf{R}' = R'\hat{R}'$ is the vector of the observation point from the center of MP, $\mathbf{r}' = r'\hat{r}'$ is the vector of the electric multipoles within the MP and $\mathbf{d} = d\hat{x}$ is the vector of the center of MP from the origin. The semiclassical approach will again be utilized in this study where the MP is modelled using classical electrodynamics whereas the QS is treated quantum-mechanically using either the density matrix equations or Heisenberg-Langevin formalism. Here, the energy level configuration of the QS will not be specified like what has been done in chapter 4 but rather keeping our formalism general by leaving the atomic coherences associated with the field as ρ_{ij}, where i and j are the labels for the row and column of the density matrix $\hat{\rho}$ which describes the state of the QS. Hence, the formalism developed in this chapter will concern only the scattered and local fields and not the quantum-mechanical solution associated with the QS.

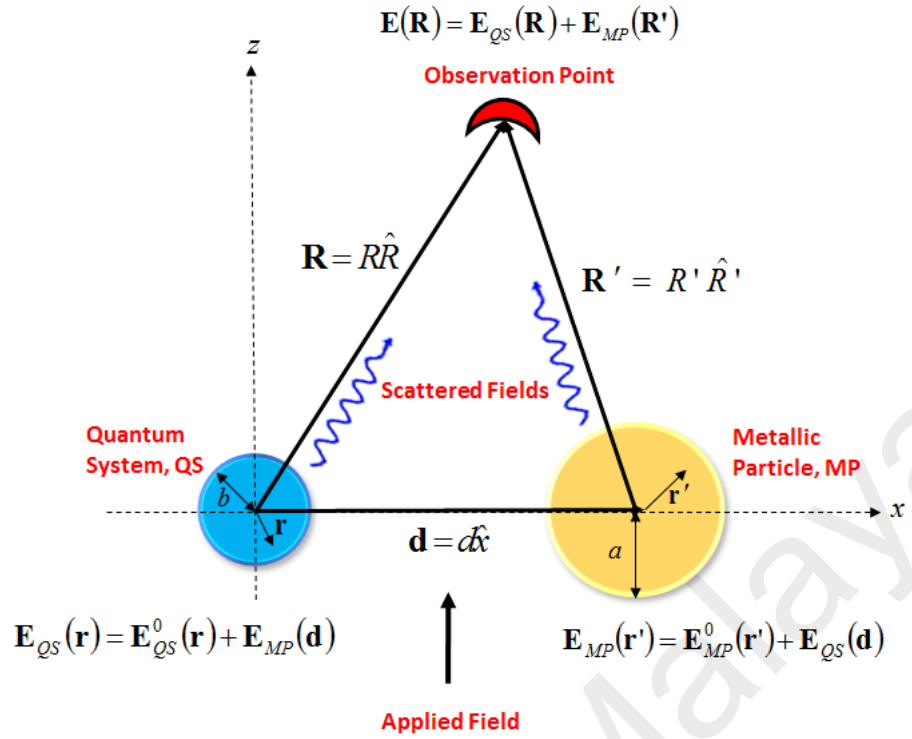

Figure 5.1: Schematic of the hybrid nanostructure under study. Note that the model is similar to the one in Figure 4.1 except that the vector notations have been changed to account for the finite sizes of the MP and QS and the QS can be in any energy configuration.

5.2 Scattered Multipole Fields at Arbitrary Distance from a Polarizing Source of Arbitrary Size: General Form

The field scattered from a polarizing source can be obtained from solution of the Maxwell's equations as highlighted in section 3.2. From Equation 3.16, the nonhomogeneous wave equation is given by

$$\left(\nabla^2 - \frac{1}{c^2}\frac{\partial^2}{\partial t^2}\right)\mathbf{E}(\mathbf{R},t) = -\frac{1}{\varepsilon_0}\left(\nabla\nabla\cdot - \frac{1}{c^2}\frac{\partial^2}{\partial t^2}\right)\mathbf{P}(\mathbf{R},t)\,. \tag{5.1}$$

After Fourier transformation into the frequency domain using $\mathbf{E}(\mathbf{R},\omega) = \int_{-\infty}^{\infty}\mathbf{E}(\mathbf{R},t)\,e^{i\omega t}dt$, one will get the nonhomogeneous wave equation in frequency domain

$$\left(\nabla^2 + \frac{\omega^2}{c^2}\right)\mathbf{E}(\mathbf{R},\omega) = -\frac{1}{\varepsilon_0}\left(\nabla\nabla\cdot + \frac{\omega^2}{c^2}\right)\mathbf{P}(\mathbf{R},\omega)\,. \tag{5.2}$$

Using the Green's function

$$G\left(\mathbf{R},\omega,\mathbf{r},\omega'\right)=\frac{1}{|\mathbf{R}-\mathbf{r}|}\delta\left(\omega-\omega'\right), \tag{5.3}$$

the electric field outside the particle can be solved as

$$\mathbf{E}\left(\mathbf{R},\omega\right)=\int_{V}\left[\nabla\nabla\cdot+k^{2}\left(\omega\right)\right]\frac{\mathbf{P}\left(\mathbf{r},\omega\right)e^{ik(\omega)|\mathbf{R}-\mathbf{r}|}}{4\pi\varepsilon_{0}\left|\mathbf{R}-\mathbf{r}\right|}d^{3}r, \tag{5.4}$$

where $k\left(\omega\right)=\omega/c$. In spherical polar coordinates, the exponential term on the RHS of Equation 5.4 can be expanded as (Jackson, 1999)

$$\frac{e^{ik(\omega)|\mathbf{R}-\mathbf{r}|}}{|\mathbf{R}-\mathbf{r}|}=4\pi ik\sum_{l=0}^{\infty}h_{i}^{(1)}\left(kR\right)j_{l}\left(kr\right)\sum_{m=-l}^{l}Y_{lm}^{*}\left(\theta,\phi\right)Y_{lm}\left(\Theta,\Phi\right), \tag{5.5}$$

where the value of $l=0,1,2,3,\ldots$ actually corresponds to different order of multipole polarization in the source particle. For example, $l=0$ is for dipole, $l=1$ is for quadrupole, $l=2$ is for octupole, and so on. Hence, by keeping all the terms in l, the electric multipole effects are automatically included into the scattered field expression. Also, the volume integration $\int_{V}$ over the dimension of the source particle at the RHS of Equation 5.4 means that the finite size of the source particle has already been taken into account. Furthermore, by not making the far-field approximation $|\mathbf{R}-\mathbf{r}|\simeq R-\hat{R}\cdot\mathbf{r}$ and using the exact expression for $|\mathbf{R}-\mathbf{r}|$ instead, Equation 5.4 will be valid for any distance outside the particle, not just at the far-field zone. After all of the above considerations, Equation 5.4 is now considered the exact scattered multipole field expression valid for arbitrary particle size and observation distance.

Now, the multipole field scattered from the QS will be derived using the vector notation in Figure 5.1. Starting from the expression for microscopic polarization,

$$\mathbf{P}_{QS}(\mathbf{r},\omega) = N_{QS}\vec{\wp}\rho_{ij}(\mathbf{r},\omega), \tag{5.6}$$

where N_{QS} is the number density of QS, $\vec{\wp}$ is the dipole moment and $\rho_{ij}(\mathbf{r},\omega)$ is the density matrix element (atomic coherence) obtained from the ith row and jth column of the density matrix $\hat{\rho}(\mathbf{r},\omega)$ that describes the evolution of the atomic states. When Equation 5.6 is substituted into Equation 5.4, one gets

$$\mathbf{E}_{QS}(\mathbf{R},\omega) = X(\omega)\int\left[\nabla\nabla\cdot+k^2(\omega)\right]\frac{\vec{\wp}\rho_{ij}(\mathbf{r},\omega)\,e^{ik(\omega)|\mathbf{R}-\mathbf{r}|}}{|\mathbf{R}-\mathbf{r}|}d^3r, \tag{5.7}$$

where $X(\omega) = \frac{N_{QS}}{4\pi\varepsilon_0\varepsilon_{QS}^{ef}(\omega)}$, $\varepsilon_{QS}^{ef}(\omega) = \frac{2\varepsilon_b+\varepsilon_{QS}(\omega)}{3\varepsilon_b}$ is the effective dielectric function of QS which consists of the dielectric function of the QS $\varepsilon_{QS}(\omega)$ as well as the background permitivity ε_b, $\mathbf{R} = (X,Y,Z) = R(\sin\Theta\cos\Phi, \sin\Theta\sin\Phi, \cos\Theta)$, $\mathbf{r} = (x,y,z) = r(\sin\theta\cos\phi, \sin\theta\sin\phi, \cos\theta)$ and $|\mathbf{R}-\mathbf{r}| = \sqrt{\Delta_x^2+\Delta_y^2+\Delta_z^2}$ with $\Delta_x = X - x$, etc.

As for the field scattered from the MP, the expression for polarization $\mathbf{P}_{MP}(\mathbf{r}',\omega) = \alpha_{MP}\mathbf{E}_{MP}(\mathbf{r}',\omega)$ which couples with the local field of the MP will be used instead of Equation 5.6. This gives the result

$$\mathbf{E}_{MP}(\mathbf{R}',\omega) = Y(\omega)\int\left[\nabla'\nabla'\cdot+k'^2(\omega)\right]\frac{\mathbf{E}_{MP}(\mathbf{r}',\omega)\,e^{ik'(\omega)|\mathbf{R}'-\mathbf{r}'|}}{|\mathbf{R}'-\mathbf{r}'|}d^3r', \tag{5.8}$$

where $Y(\omega) = \frac{\alpha_{MP}}{4\pi\varepsilon_0\varepsilon_{MP}^{ef}}$, α_{MP} is the polarizibility of the MP, $\varepsilon_{MP}^{ef}(\omega) = \frac{2\varepsilon_b+\varepsilon_{MP}(\omega)}{3\varepsilon_b}$ is the effective dielectric function of MP, $\mathbf{R}' = (X',Y',Z') = R'(\sin\Theta'\cos\Phi', \sin\Theta'\sin\Phi', \cos\Theta')$, $\mathbf{r}' = (x',y',z') = r'(\sin\theta'\cos\phi', \sin\theta'\sin\phi', \cos\theta')$ and $|\mathbf{R}'-\mathbf{r}'| = \sqrt{\Delta_x'^2+\Delta_y'^2+\Delta_z'^2}$ with $\Delta_x' = X' - x'$, etc. Note that in Equations 5.7 and 5.8, $k(\omega)$ and ∇ are defined as the

wavevector and Del operator associated with the QS whereas $k'(\omega)$ and ∇' are the corresponding quantity and operator associated with the MP. The operators ∇ and ∇' operate on coordinates of the observation point $\mathbf{R}$ and $\mathbf{R}'$, respectively.

At this point, it is appropriate to focus on the nonlocal dielectric response of the MP (David & de Abajo, 2011; de Abajo, 2008) which is taken into account via the (wavevector) $\mathbf{k}-$dependence of the MP dielectric function $\varepsilon_{MP}(\omega)$ as mentioned in section 4.2. Such effect will become important when the size of the MP is much smaller than the wavelength. Reader should recall that in the local treatment, the dielectric function of the MP is provided by the Drude formula

$$\varepsilon_{MP}(\omega) = \varepsilon_{\infty} - \frac{\omega_p^2}{\omega[\omega + i\Gamma_m]}, \tag{5.9}$$

where ε_{∞} is the dielectric function at infinity, ω_p is the plasma frequency, $\Gamma_m = \Gamma_m^{\infty} + C\frac{v_F}{a}$ is the electron relaxation rate that depends on a the radius of the MP (Derkachova et al., 2015; Khlebtsov et al., 1996), v_F is the Fermi velocity and C is a theory-dependent quantity as mentioned in section 4.2. In the nonlocal case, however, the MP dielectric function is given by (Dasgupta & Fuchs, 1981; Kosionis, et al., 2012)

$$\varepsilon_{MP}(\omega) = \left[\frac{6}{\pi}a\int_0^{\infty}\frac{j_1^2(ka)}{\varepsilon_{MP}(\mathbf{k},\omega)}dk\right]^{-1}, \tag{5.10}$$

where j_1 is the first-order spherical Bessel function, $k = |\mathbf{k}|$ and $\varepsilon_{MP}(\mathbf{k},\omega)$ is the nonlocal dielectric function in $\mathbf{k}-$space, which according to the hydrodynamic model (Agarwal & ONeil, 1983; Fuchs & Claro, 1987), is given by

$$\varepsilon_{MP}(\mathbf{k},\omega) = \varepsilon_{\infty} - \frac{\omega_p^2}{\omega[\omega + i\Gamma_m] - \beta^2 k^2}. \tag{5.11}$$

In this expression, $\beta^2 = \frac{3v_F^2}{D+2}$ (McMahon et al., 2010; Fetter, 1973) with D as the dimension of the system ($D = 3$ in our three-dimensional case). The nonlocal dielectric function in Equation 5.10 can be derived from the problem of a small MP interacting with an electrostatic field where dipole approximation can be made. Its detailed derivation is provided in Appendix I. Substituting Equation 5.11 into Equation 5.10,

$$\varepsilon_{MP}(\omega) = \left[\frac{1}{\varepsilon_{MP,D}(\omega)} + 3\left(\frac{a\omega_p}{\beta u}\right)^2 I_{3/2}(u) K_{3/2}(u)\right]^{-1}, \tag{5.12}$$

where I_ν and K_ν are the modified Bessel functions, $\varepsilon_{MP,D}(\omega)$ is given by the Drude formula in Equation 5.9 and

$$u = \frac{a\sqrt{\omega_p^2 - \omega(\omega + i\Gamma_m)}}{\beta}. \tag{5.13}$$

Lastly, the total multipole field at arbitrary position $\mathbf{R}$ is due to the contribution from both QS and MP. Hence, its expression is just the addition of Equations 5.7 and 5.8,

$$\begin{aligned}
\mathbf{E}(\mathbf{R},\omega) &= \mathbf{E}_{QS}(\mathbf{R},\omega) + \mathbf{E}_{MP}(\mathbf{R}',\omega) \\
&= X(\omega)\int \left[\nabla\nabla\cdot + k^2(\omega)\right]\frac{\vec{\wp}\rho_{ij}(\mathbf{r},\omega)\, e^{ik(\omega)|\mathbf{R}-\mathbf{r}|}}{|\mathbf{R}-\mathbf{r}|}d^3r \\
&\quad + Y(\omega)\int \left[\nabla'\nabla'\cdot + k'^2(\omega)\right]\frac{\mathbf{E}_{MP}(\mathbf{r}',\omega)\, e^{ik'(\omega)|\mathbf{R}'-\mathbf{r}'|}}{|\mathbf{R}'-\mathbf{r}'|}d^3r'.
\end{aligned} \tag{5.14}$$

5.3 Local Fields of Metallic Nanoparticle and Quantum System

Since Equation 5.14 couples to the local field of MP, $\mathbf{E}_{MP}(\mathbf{r}',\omega)$, the next task is to search for the analytical form of $\mathbf{E}_{MP}(\mathbf{r}',\omega)$ as in section 4.4. The local field of MP is due to the intrinsic field (which is independent of the MP-QS coupling) as well as the

polarization field from the QS. One may write this as

$$\mathbf{E}_{MP}(\mathbf{r}',\omega) = \mathbf{E}^0_{MP}(\mathbf{r}',\omega) + \mathbf{E}_{QS}(\mathbf{d},\omega)$$

$$= \mathbf{E}^0_{MP}(\mathbf{r}',\omega) + X(\omega)\int \left[\nabla_d \nabla_d \cdot + k^2(\omega)\right] \frac{\vec{\wp}\rho_{ij}(\mathbf{r},\omega)\, e^{ik(\omega)|\mathbf{d}-\mathbf{r}|}}{|\mathbf{d}-\mathbf{r}|} d^3r, \tag{5.15}$$

where from the diagram, $\mathbf{d}=(d,0,0)$ and therefore $|\mathbf{d}-\mathbf{r}| = \sqrt{(d-x)^2+y^2+z^2}$. The Del operator ∇_d acts on $\mathbf{d}$ while the wavevector $k(\omega)$ is associated with the field from the QS. Though not explicitly written here, the atomic coherence $\rho_{ij}(\mathbf{r},\omega)$ will most likely contain the local field of QS, $\mathbf{E}_{QS}(\mathbf{r},\omega)$. Hence, it is of interest to search for $\mathbf{E}_{QS}(\mathbf{r},\omega)$.

The local field of QS is due to the intrinsic field and the polarization field from the MP, which can be written as

$$\mathbf{E}_{QS}(\mathbf{r},\omega) = \mathbf{E}^0_{QS}(\mathbf{r},\omega) + \mathbf{E}_{MP}(\mathbf{d},\omega)$$

$$= \mathbf{E}^0_{QS}(\mathbf{r},\omega) + Y(\omega)\int \left[\nabla_d \nabla_d \cdot + k'^2(\omega)\right] \frac{\mathbf{E}_{MP}(\mathbf{r}',\omega)\, e^{ik'(\omega)|\mathbf{d}-\mathbf{r}'|}}{|\mathbf{d}-\mathbf{r}'|} d^3r', \tag{5.16}$$

where $|\mathbf{d}-\mathbf{r}'| = \sqrt{(d-x')^2+y'^2+z'^2}$ and the wavevector $k'(\omega)$ is associated with the field from the MP. This shows that Equations 5.15 and 5.16 form two coupled equations which describe the long range Coulomb coupling between MP and QS. Substituting Equation 5.15 into Equation 5.16,

$$\begin{aligned}\mathbf{E}_{QS}(\mathbf{r},\omega) \;=\; & \mathbf{E}^0_{QS}(\mathbf{r},\omega) + Y(\omega)\int \left[\nabla_d \nabla_d \cdot + k'^2(\omega)\right] \frac{\mathbf{E}^0_{MP}(\mathbf{r}',\omega)\, e^{ik'(\omega)|\mathbf{d}-\mathbf{r}'|}}{|\mathbf{d}-\mathbf{r}'|} d^3r' \\ & + X(\omega)\,Y(\omega)\int \left[\nabla_d \nabla_d \cdot + k'^2(\omega)\right] \\ & \times \left\{\int \left[\nabla_d \nabla_d \cdot + k^2(\omega)\right] \frac{\vec{\wp}\rho_{ij}(\mathbf{r},\omega)\, e^{ik(\omega)|\mathbf{d}-\mathbf{r}|}}{|\mathbf{d}-\mathbf{r}|} d^3r \right\} \frac{e^{ik'(\omega)|\mathbf{d}-\mathbf{r}'|}}{|\mathbf{d}-\mathbf{r}'|} d^3r'. \end{aligned} \tag{5.17}$$

A point to note here is that it has been mentioned earlier that the coherence $\rho(\mathbf{r},\omega)$ will mostly contain $\mathbf{E}_{QS}(\mathbf{r},\omega)$. This causes Equation 5.17 to be highly nonlinear and obtaining the analytical solution for $\mathbf{E}_{QS}(\mathbf{r},\omega)$ would be a tedious task.

5.4 Scattered Multipole Fields at Arbitrary Point: Final Form

After getting the expression for the local fields of MP and QS, one can further expand Equation 5.14 into

$$\mathbf{E}(\mathbf{R},\omega) = \mathbf{E}_{QS}(\mathbf{R},\omega) + \mathbf{E}_{MP}(\mathbf{R}',\omega), \tag{5.18}$$

where

$$\mathbf{E}_{QS}(\mathbf{R},\omega) = X(\omega)\int \left[\nabla\nabla\cdot + k^2(\omega)\right]\frac{\vec{\wp}\rho_{ij}(\mathbf{r},\omega)\,e^{ik(\omega)|\mathbf{R}-\mathbf{r}|}}{|\mathbf{R}-\mathbf{r}|}d^3r, \tag{5.19}$$

$$\begin{aligned}\mathbf{E}_{MP}(\mathbf{R}',\omega) &= Y(\omega)\int \left[\nabla'\nabla'\cdot + k'^2(\omega)\right]\frac{\mathbf{E}^0_{MP}(\mathbf{r}',\omega)\,e^{ik'(\omega)|\mathbf{R}-\mathbf{d}-\mathbf{r}'|}}{|\mathbf{R}-\mathbf{d}-\mathbf{r}'|}d^3r' \\ &\quad + X(\omega)Y(\omega)\int \left[\nabla'\nabla'\cdot + k'^2(\omega)\right] \\ &\times\left\{\int \left[\nabla\nabla\cdot + k^2(\omega)\right]\frac{\vec{\wp}\rho_{ij}(\mathbf{r},\omega)\,e^{ik(\omega)|\mathbf{d}-\mathbf{r}|}}{|\mathbf{d}-\mathbf{r}|}d^3r\right\}\frac{e^{ik'(\omega)|\mathbf{R}-\mathbf{d}-\mathbf{r}'|}}{|\mathbf{R}-\mathbf{d}-\mathbf{r}'|}d^3r',\end{aligned} \tag{5.20}$$

and the vector relation $\mathbf{R}' = \mathbf{R} - \mathbf{d}$ which can easily be obtained from Figure 5.1 has been used. For problems dealing with quantum fields, the electric fields vectors in Equation 5.18 can be written in operator form

$$\hat{\mathbf{E}}(\mathbf{R},\omega) = \hat{\mathbf{E}}_{QS}(\mathbf{R},\omega) + \hat{\mathbf{E}}_{MP}(\mathbf{R}',\omega), \tag{5.21}$$

where

$$\hat{\mathbf{E}}_{QS}(\mathbf{R},\omega) = X(\omega)\int \left[\nabla\nabla\cdot + k^2(\omega)\right]\frac{\vec{\wp}\hat{\sigma}_{ji}(\mathbf{r},\omega)\,e^{ik(\omega)|\mathbf{R}-\mathbf{r}|}}{|\mathbf{R}-\mathbf{r}|}d^3r, \tag{5.22}$$

$$\hat{\mathbf{E}}_{MP}(\mathbf{R}',\omega) = Y(\omega)\int\left[\nabla'\nabla'\cdot+k'^{2}(\omega)\right]\frac{\hat{\mathbf{E}}^{0}_{MP}(\mathbf{r}',\omega)\,e^{ik'(\omega)|\mathbf{R}-\mathbf{d}-\mathbf{r}'|}}{|\mathbf{R}-\mathbf{d}-\mathbf{r}'|}d^{3}r'$$
$$+X(\omega)Y(\omega)\int\left[\nabla'\nabla'\cdot+k'^{2}(\omega)\right]$$

$$\times\left\{\int\left[\nabla\nabla\cdot+k^{2}(\omega)\right]\frac{\vec{\wp}\hat{\sigma}_{ji}(\mathbf{r},\omega)\,e^{ik(\omega)|\mathbf{d}-\mathbf{r}|}}{|\mathbf{d}-\mathbf{r}|}d^{3}r\right\}\frac{e^{ik'(\omega)|\mathbf{R}-\mathbf{d}-\mathbf{r}'|}}{|\mathbf{R}-\mathbf{d}-\mathbf{r}'|}d^{3}r', \tag{5.23}$$

with $\hat{\sigma}_{ji}(\mathbf{r},\omega) = |j\rangle\langle i|$ as the atomic coherence operator obtained from Heisenberg equations.

The result in Equation 5.18 can be further solved once the atomic coherence $\rho_{ij}(\mathbf{r},\omega)$ is known. Similarly, knowledge of the analytical form of atomic coherence operator $\hat{\sigma}_{ji}(\mathbf{r},\omega)$ will bring about the solution for Equation 5.21. Once the scattered field expression is obtained, the spectra of the fields can be computed and analyzed. Study of the spectra will provide insights into the quantum properties of the emitted fields and the plasmonic effects caused by the MP.

CHAPTER 6: RESULTS AND DISCUSSION

This chapter presents the MATLAB simulations of the Stokes and anti-Stokes spectra derived in Chapter 3 and 4 along with the discussion of the results. The first section of this chapter focuses on the spectra of the Stokes and anti-Stokes fields (Equations 3.76 and 3.80) emitted from a mesoscopic spherical particle composed of atoms in double Raman configuration without the presence of the metallic nanoparticle (MP). In particular, the variation of the spectra across different radii of the mesoscopic particle for various cases of laser fields strengths will be studied. The directionality of the fields emission will also be studied and analyzed from the angular dependence of the spectra. The next section is concerned with the Stokes and anti-Stokes spectra (Equation 4.37) of a hybrid nanostructure comprising of a quantum system (QS) in double Raman scheme in close proximity with a metallic nanoparticle (MP). The Stokes and anti-Stokes fields spectra of the hybrid nanostructure are shown to change with the interparticle distance r, observation angles Φ and Θ as well as number density N. Furthermore, effect of the configuration of the laser parameters and the presence of surface plasmon resonance (SPR) on the spectra will be studied. In both sections, analysis and interpretation of the results are provided.

6.1 Quantum Spectra of Raman Photon Pair from a Mesoscopic Spherical Particle

In this section, the results obtained from the simulations of the quantum spectra in Equations 3.76 and 3.80 will be discussed. It is plot in Figures 6.1-6.7 the normal-order spectra of the Stokes and anti-Stokes fields emitted by a mesoscopic spherical particle of radius ρ containing atoms in double Raman configuration. In particular, Figure 6.1 shows the change of the spectra with particle radius ρ for the case without linear dispersion where the permitivity $\varepsilon_f\,(f = s, a)$ of the mesoscopic particle is taken to be a constant value (independent of frequency). On the other hand, Figures 6.3 and 6.4 show similar

plot for the case where the frequency dependence of the wavevector is included through $\varepsilon_f(\omega)$ in Equation 3.67. The angular dependence of the spectra is shown in Figures 6.5, 6.6 and 6.7 where linear dispersion is included. In all of the above-mentioned figures the spectra for four different cases of laser parameters at resonance $(\Delta_p = \Delta_s = \Delta_c = \Delta_a = 0)$ are studied: (i) weak and symmetric pump and control laser strengths $\Omega_p = \Omega_c = \gamma_{ac}$, (ii) strong and symmetric laser strengths $\Omega_p = \Omega_c = 10\gamma_{ac}$, (iii) asymmetric laser strengths $\Omega_p = 3\gamma_{ac}, \Omega_c = 7\gamma_{ac}$ and (iv) the opposite $\Omega_p = 7\gamma_{ac}, \Omega_c = 3\gamma_{ac}$. Other cases include Raman electromagnetically induced transparency (EIT) scheme with $\Delta_p = \Delta_s = -20\gamma_{ac}, \Delta_c = \Delta_a = 0, \Omega_p = \gamma_{ac}$ and $\Omega_c = 10\gamma_{ac}$ as well as off-resonance configurations $\Delta_p = \Delta_s = \Delta_c = \Delta_a = -20\gamma_{ac}, \Omega_p = \gamma_{ac}$ and $\Omega_c = 3\gamma_{ac}$. Also in these figures, instead of plotting the original spectra $S_{s(a)q}(\omega)$ in Equations 3.76 and 3.80, the dimensionless spectra (denoted by an overbar) given by

$$\bar{S}_{s(a)q}(\omega) = S_{s(a)q}(\omega)\,\frac{\Gamma_{db(ac)}}{ANV\left|\wp_{db(ac)}\right|^2 \nu_{s(a)}^4}, \tag{6.1}$$

is plotted where the subscript s and a denote Stokes and anti-Stokes fields, respectively, $q = x, y, z$ denotes the Cartesian components, $A = \left(\frac{1}{4\pi\varepsilon_0 c^2 R}\right)^2 (2\pi)^3$, N is the number density of the mesoscopic particle, $V = \frac{4\pi}{3}\rho^3$ is the volume of the particle, $\wp_{db(ac)}$ is the dipole moment associated with the Stokes (anti-Stokes) field and $\nu_{s(a)}$ is the Stokes (anti-Stokes) carrier frequency. As mentioned in section 3.3, due to the finite size of the spherical particle, the focusing effect which gives rise to spatially inhomogeneous pump and control laser fields inside the particle becomes significant. Here, this effect is taken into account using the Mie theory provided in Appendix A with n_p= 1.5 and n_c = 1.4

(refractive indices associated with the pump and control laser fields inside the mesoscopic particle). The main features of the spectra together with their physical interpretation will

be discussed in the following subsections.

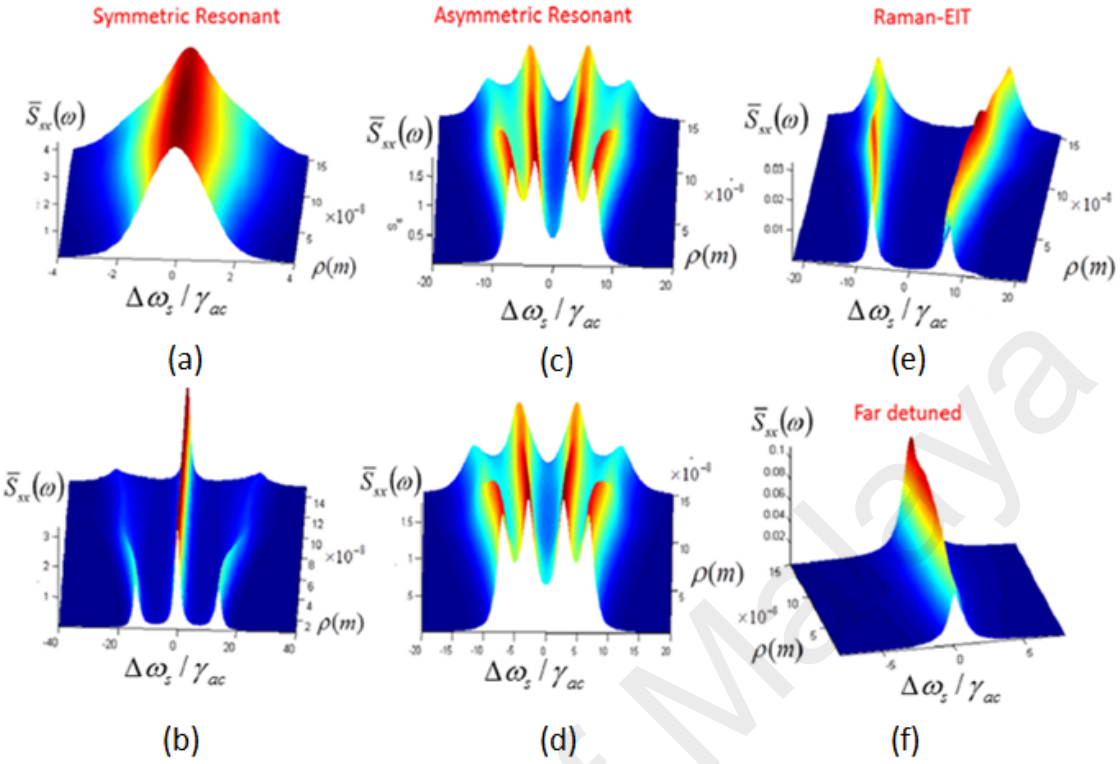

Figure 6.1: The $x-$component of the normal-order Stokes spectra (identical to anti-Stokes spectra) versus particle radius ρ without linear dispersion (with constant permitivities $n_p = 1.5, n_c = 1.4, n_s = n_a = 1.3$) for cases of resonant $(\Delta_p = \Delta_s = \Delta_c = \Delta_a = 0)$ and symmetric pump and control laser fields (a) $\Omega_p = \Omega_c = \gamma_{ac}$ and (b) $\Omega_p = \Omega_c = 10\gamma_{ac}$; resonant and asymmetric laser fields (c) $\Omega_p = 3\gamma_{ac}, \Omega_c = 7\gamma_{ac}$ and (d) $\Omega_p = 7\gamma_{ac}, \Omega_c = 3\gamma_{ac}$; (e) Raman-EIT scheme $\Delta_p = \Delta_s = -20\gamma_{ac}, \Delta_c = \Delta_a = 0, \Omega_p = \gamma_{ac}$ and $\Omega_c = 10\gamma_{ac}$; and (f) off-resonance configurations $\Delta_p = \Delta_s = \Delta_c = \Delta_a = -20\gamma_{ac}, \Omega_p = \gamma_{ac}$ and $\Omega_c = 3\gamma_{ac}$. Here, $\Delta\omega_f = \omega - \nu_f\,(f = s, a)$ denotes the detuning from the Stokes and anti-Stokes carrier frequencies. Other parameters used are given by $\Gamma_x = \Gamma = 5 \times 10^7$ s^{-1} with $x = ac, ab, db, dc$, $\bar{n}_x = [\exp(\theta_x) - 1]^{-1}$ with $\theta_x = \hbar\omega_x / k_B T$ at temperature $T = 300$ K, $N \simeq 10^{27}$ m^{-3}, $\Theta = \Phi = 0$ and $\wp_{ac,q} = \wp_{db,q} = 2 \times 10^{-29}$ C m with $q = x, y, z$.

6.1.1 Effects of Laser Fields Strengths

It can be observed clearly from Figure 6.1(a) that when the pump and control laser fields strengths are weak and equal $(\Omega_p = \Omega_c = \gamma_{ac})$, side peaks occur at around $\pm(\Omega_p + \Omega_c) = \pm 2\gamma_{ac}$ which cannot be seen clearly due to their overlapping with the central peak. In another case where the laser fields strengths are strong and equal $(\Omega_p = \Omega_c = 10\gamma_{ac})$, Mollow triplets (Mollow, 1969; Cohen-Tannoudji & Reynaud, 1977) become clearly visible (Figure 6.1(b)) with side peaks at around $\pm(\Omega_p + \Omega_c) = \pm 10\gamma_{ac}$, particularly for

the case of small particle radius (which describes well the single atom scenario). From these two results it can be observed that the separation between the side peaks grows wider as the laser strengths increases which is due to stronger ac Stark shift induced by the laser fields. When the pump and control laser fields strengths have different values $\Omega_p \neq \Omega_c$, four strong resonant peaks (Figures 6.1(c) and (d)) appear at around $-\left(\Omega_p + \Omega_c\right), -\left|\Omega_p - \Omega_c\right|, \left|\Omega_p - \Omega_c\right|$ and $\Omega_p + \Omega_c$ which all can be explianed as due to Autler Townes splittings. In the Raman-EIT case, one can clearly observe the EIT peaks at around $\pm\Omega_p = \pm 10\gamma_{ac}$ together with the "transparency window" between the peaks in Figure 6.1(e).

A closer look at Figures 6.1(b)-(d) reveals that the side peaks (at small particle radius) are actually shifted slightly less than $\pm\left(\Omega_p + \Omega_c\right)$ from the center. This can be understood by looking at the pump-field distributions inside the particle shown in Figure 6.2 for different values of the particle radius ρ. It can be observed from the figure the presence of regions with normalized intensity $\frac{\left|E_{px}\right|^2+\left|E_{pz}\right|^2}{E_{p0}^2}$ less than unity which corresponds to effective Rabi frequencies less than the input value Ω_p. This reduced laser intensity effect is due to the refraction and focusing by the geometry of the particle and is the origin for the unexpected shifts of the side peaks in Figures 6.1(b)-(d). Similar explanation could be given for the slight shift of the EIT peaks from $\pm\Omega_p = \pm 10\gamma_{ac}$ in Figure 6.1(e). This feature distinguishes the spectra for mesoscopic particles from the spectra of an isolated particle or single atom.

Similar spectral peaks are also observed in Figures 6.3 and 6.4 (where dispersion is taken into account) for all four cases of resonant laser fields, except that the spectra exhibit narrow morphology-dependent resonant (MDR) peaks at large ρ. This feature will be discussed in subsection 6.1.5.

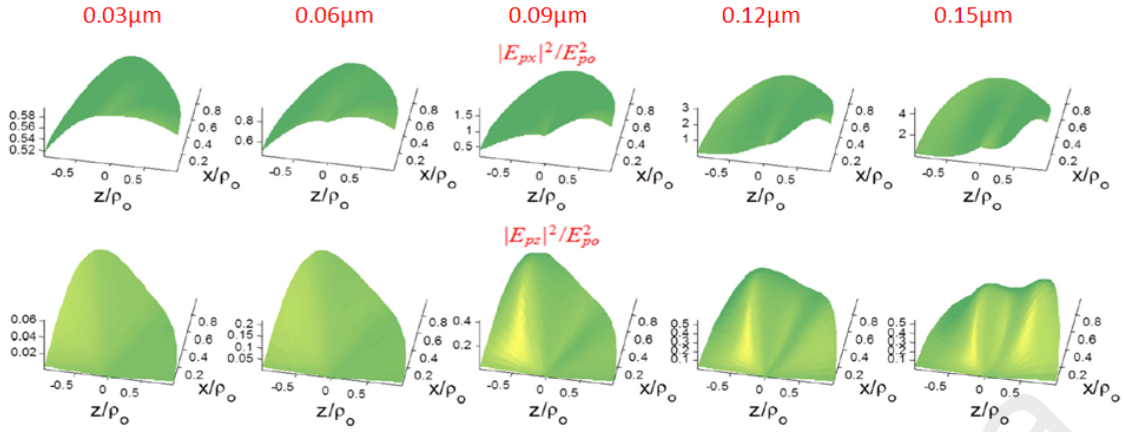

Figure 6.2: Normalized field intensity distributions $|E_{px}|^2/E_{po}^2$ and $|E_{pz}|^2/E_{po}^2$ for the pump laser for five different particle radii ρ. Note that $|E_{pz}|^2$ is smaller than $|E_{px}|^2$ in all five cases.

6.1.2 Comparison Between Normal- and Antinormal-Order Spectra

As mentioned in section 2.3, normal-order correlations are used to describe photodetection based on absorption of photons whereas antinormal-order correlations describe the opposite process, i.e. stimulated emission. Mathematically, the difference between Equations 3.76 and 3.78 and Equations 3.80 and 3.81 is in the diffusion coefficients $2\tilde{D}_{j,l}^{n(an)}(\mathbf{r})$ which are frequency independent. This results in identical shape and profile of the normal- and antinormal-order spectra for both Stokes and anti-Stokes (so it is trivial to show the antinormal-order spectra). In fact, the results show that both normal- and antinormal-order spectra yield identical features for all cases of resonant fields strengths with or without dispersion. In the small particle regime, any differences between the normal- and antinormal-order spectra would actually yield the quantum nature of the fields since classically there would be no distinctions between the two orderings.

6.1.3 Comparison Between Stokes and Anti-Stokes Spectra

In the absence of dispersion, the Stokes and anti-Stokes spectra exhibit identical features (so it is trivial to show both) not only for the resonant (Figures 6.1(a)-(d)) cases but also for the Raman-EIT case (Figure 6.1(e)) and off-resonance case (Figure 6.1(f)),

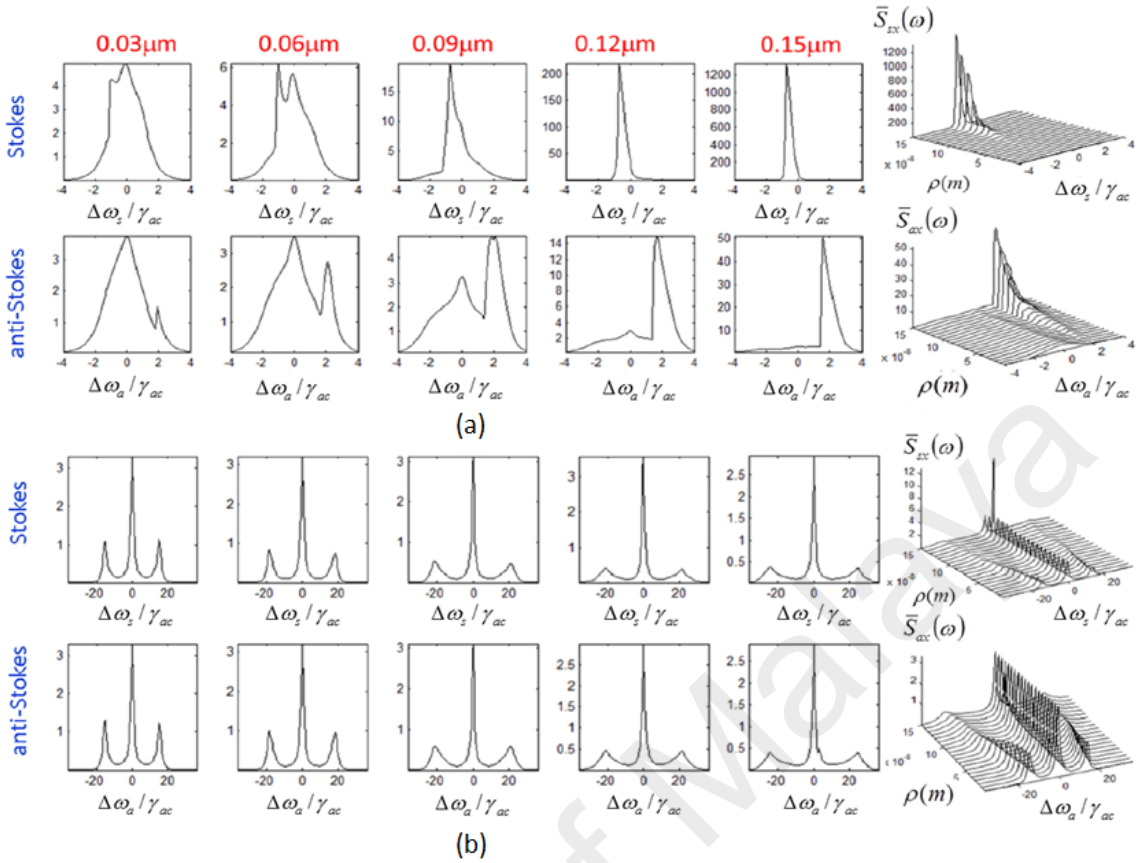

Figure 6.3: The $x-$component of the normal-order Stokes spectra (upper panels) and anti-Stokes spectra (lower panels) versus particle radius ρ with linear dispersion. The pump and control lasers are resonant $(\Delta_p = \Delta_s = \Delta_c = \Delta_a = 0)$ and equal in strengths with (a) $\Omega_p = \Omega_c = \gamma_{ac}$ (weak fields) and (b) $\Omega_p = \Omega_c = 10\gamma_{ac}$ (strong fields). All other parameters are the same as in Figure 6.1.

though there are minor differences that are immaterial as they are not the main features. In the presence of dispersion however, both Stokes and anti-Stokes spectra show significant differences as can be observed from Figures 6.3-6.7.

Careful observation of Figures 6.3 and 6.4 reveals that generally, Stokes spectra acquires higher central peak (MDR peak) as compared to anti-Stokes spectra, especially at large particle radius ρ. Higher peaks indicate higher efficiency of detection so this means that Stokes fields strengths are much higher than that of anti-Stokes. Also, Stokes central peaks are also shown to be narrower at large particle size, thus indicating narrower spectral widths.

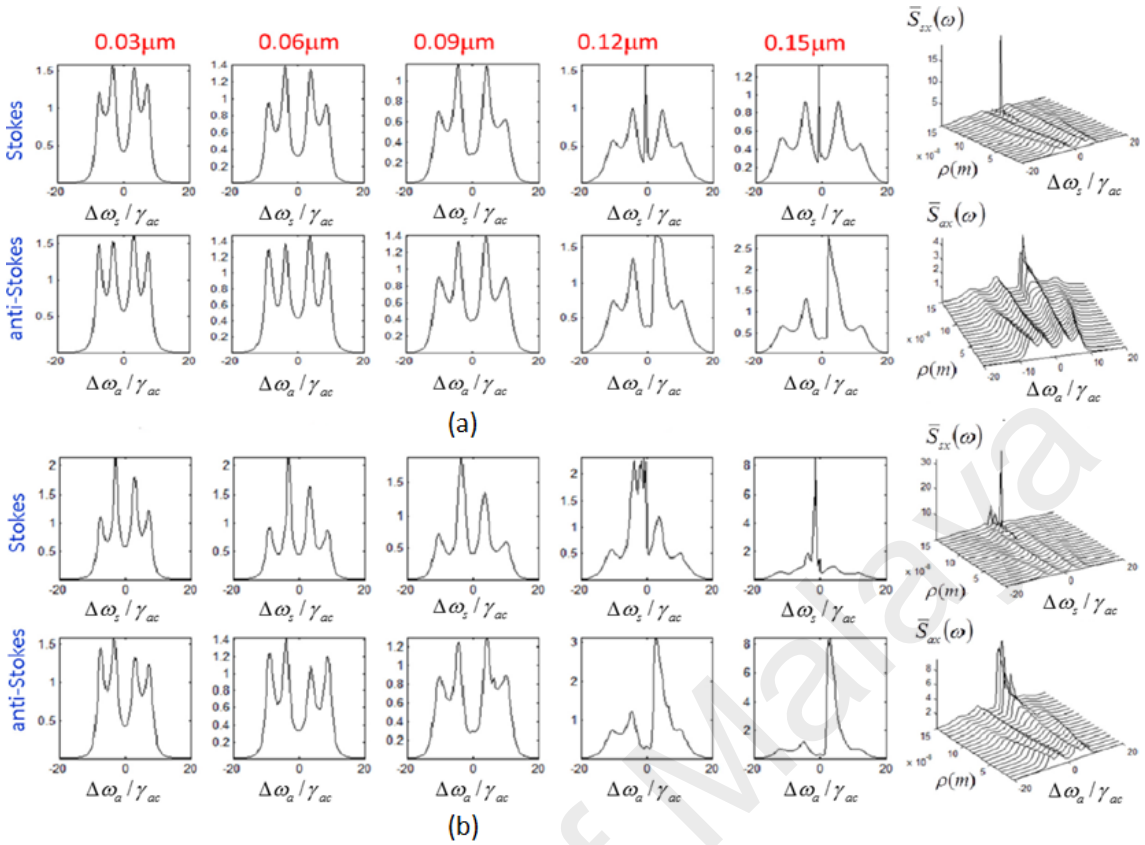

Figure 6.4: The $x-$component of the normal-order Stokes spectra (upper panels) and anti-Stokes spectra (lower panels) versus particle radius ρ with linear dispersion for the cases of asymmetric resonant lasers with (a) $\Omega_p = 3\gamma_{ac}, \Omega_c = 7\gamma_{ac}$ and (b) $\Omega_p = 7\gamma_{ac}, \Omega_c = 3\gamma_{ac}$. All other parameters are the same as in Figure 6.1.

6.1.4 Finite Size Effects: Spectral Broadening

A first glance at Figures 6.3 and 6.4 reveals that the side peaks become unresolved as the particle size ρ increases due to spectral broadening caused by the finite size of the mesoscopic particle. One can observe in Figure 6.3(a) that the three (Mollow) peaks of the spectra for the case of weak and symmetric laser fields $\left(\Omega_p = \Omega_c = \gamma_{ac}\right)$ can no longer be resolved at around $\rho = 0.1\mu$m. Similar feature is found in Figure 6.4 for the asymmetric lasers case $\Omega_p \neq \Omega_c$ where the two side peaks broadens and then coalesce into a single peak with the increase in particle size ρ. However, for the case of strong and symmetric fields $\left(\Omega_p = \Omega_c = 10\gamma_{ac}\right)$, the Mollow triplets are clearly visible and still can be resolved even at large particle size ρ. Also, broadening does not affect the central peak in this case.

One may also observe the shifting of the side peaks away from the center in Figures 6.3(b) and 6.4. This is due to the collective effect of spatially inhomogeneous laser fields inside the mesoscopic particle which causes a position-dependent ac Stark shift in the energy levels. The focusing effect caused by the geometry of the spherical particle creates a large ac Stark shift around a small spatial region. Most parts in the entire volume of the spherical particle experience a range of ac Stark shifts. This means that the shift and broadening of the resonance lines are actually due to the superpositions of a range of ac Stark shifted peaks. The nature of this spectral broadening is due to spatial factor of the mesoscopic particle, an entirely different mechanism from other known broadenings, such as the ones due to atomic collision, Doppler effect, high intensity laser fields, etc. This feature also differentiate the spectra for mesoscopic particles from the spectra for single particles.

6.1.5 Effects of Linear Dispersion

When linear dispersion is taken into account through the inclusion of the frequency-dependent dielectric functions (Equation 3.67) in the wavevector $k_f(\omega) = \sqrt{\varepsilon_f}\frac{\omega}{c}$, the spectra exhibit significant difference at certain particle size. Comparison between Figure 6.1 and Figures 6.3 and 6.4 show that the difference is due to the presence of morphology-dependent resonant (MDR) peaks near the center of the spectra at large ρ. For example, one can see in Figure 6.3(a) (for the case $\Omega_p = \Omega_c = \gamma_{ac}$) a narrow MDR peak appears in the Stokes spectra at around $-\gamma_{ac}$ and a slightly broader MDR peak appears in the anti-Stokes spectra at around $2\gamma_{ac}$ for $\rho \simeq 0.01\mu$m. For stronger fields with $\Omega_p = \Omega_c = 10\gamma_{ac}$, the MDR peaks are not seen until $\rho \simeq 0.1\mu$m. Also, the MDR peaks grow with the particle radius and their spectral position do not change with laser parameters. These features hold for asymmetric laser fields as well, as shown in Figure 6.4. Hence, one may say that strong fields can reduce the effect of particle size on the spectra.

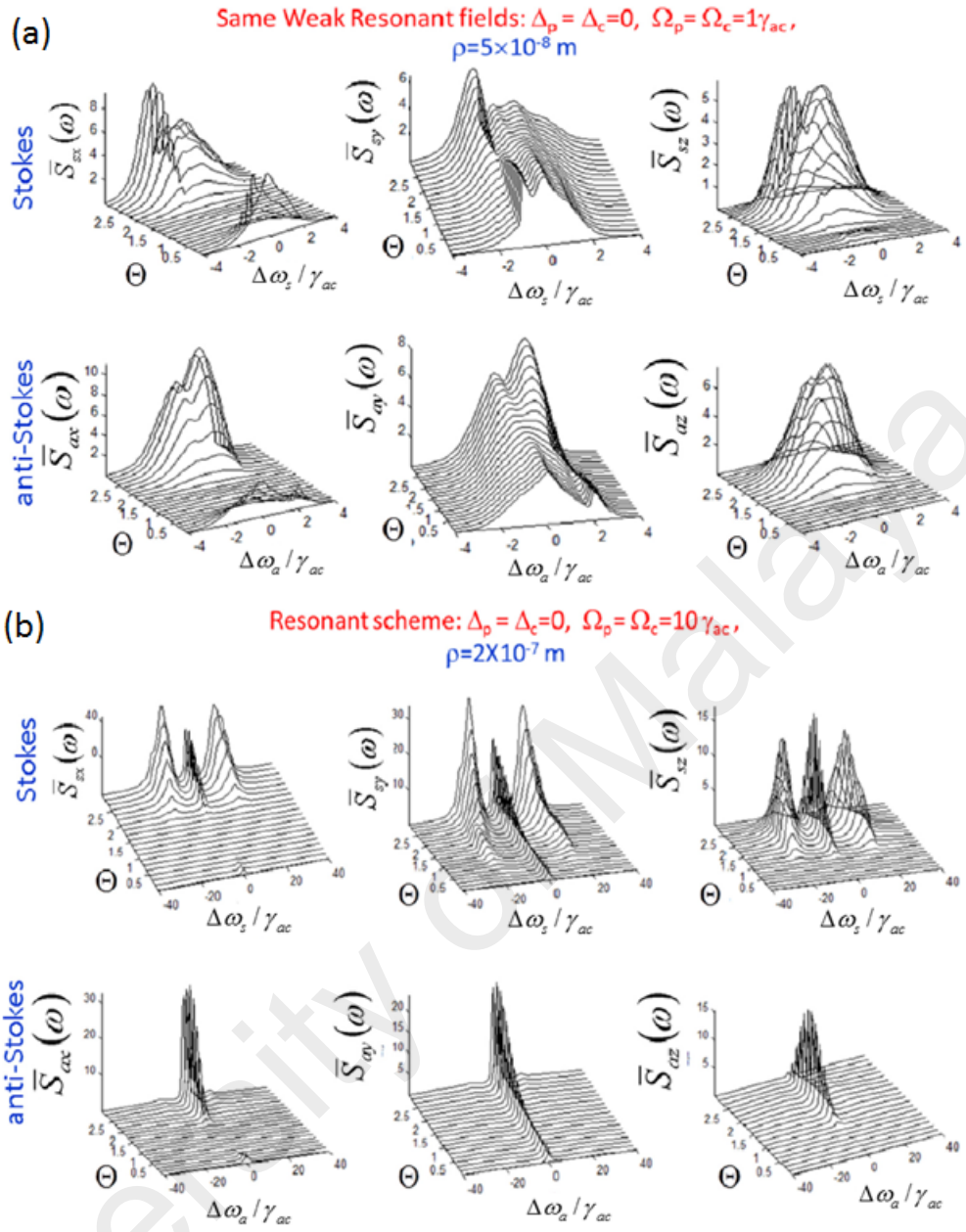

Figure 6.5: Angular Θ−dependence of the normal-order Stokes and anti-Stokes spectra with linear dispersion for the cases of symmetric resonant laser fields with (a) $\Omega_p = \Omega_c = \gamma_{ac}$ (weak fields) and (b) $\Omega_p = \Omega_c = 10\gamma_{ac}$ (strong fields). All other parameters are the same as in Figure 6.1.

6.1.6 Angular Dependence of the Spectra

In the absence of dispersion, both Stokes and anti-Stokes spectra of all components do not change with the angle of observation Θ. It is found that the variation of the spectra with Θ and Φ only occurs when the frequency-dependent dielectric function $\varepsilon_{s,a}(\omega)$ (Equation 3.67) is taken into account through the wavevector $k(\omega)$. The Θ− and

$\Phi-$dependence of the spectra originates from Equation 3.73 and the presence of dispersive loss and gain from the terms $e^{2\,\mathrm{Im}\,k_s(\omega)\hat{R}\cdot\mathbf{r}}$ and $e^{2\,\mathrm{Im}\,k_a(\omega)\hat{R}\cdot\mathbf{r}}$ in the integrals of $S_{sq}(\omega)$ and $S_{aq}(\omega)$, respectively. For $\rho = 1$ nm, only the magnitude of the peaks changes with Θ and Φ and no change is seen in the profile of the spectra across the frequencies. For $\rho = 10$ nm or larger, the frequency profile of the spectra begin to change with Θ, as shown in Figures 6.5 and 6.6 for various configurations of laser parameters. It can be clearly seen from the spectra in Figure 6.5 for the case of weak and symmetric resonant fields ($\Omega_p = \Omega_c = \gamma_{ac}$) that Fano-like dips appear at certain angular and spectral position for all of the three components. When the symmetric laser fields become stronger, the side peaks of the Mollow triplets become comparable or higher than the central peak. As for the case of asymmetric laser fields, the four peaks from Autler-Townes splittings are not clearly visible in Figures 6.6(a) and (b). The Stokes peaks in the Raman-EIT scheme are displaced from the center due to large detuning while the anti-Stokes exhibit narrow peaks at certain angles. The scattered Stokes and anti-Stokes fields actually acquire the $y-$component after the scattering process. It can also be observed from Figures 6.5 and 6.6 that the $y-$component spectra resemble the $x-$component but are quite different from the $z-$component which vanishes at $\Theta = 0, \pi$ due to the transversality of the waves.

In Figure 6.7 where the variation of the spectra across angle Φ at $\Theta = 0$ is studied, one also observes that the $z-$component spectra do not depend on Φ due to the azimuthal rotational symmetry. The $x-$component spectra vanishes at $\Phi = 0^0, 180^0$ and peaks at $\Phi = 90^0$ and 270^0 due to the transversality of the fields. The same $\Phi-$dependence is found in all other cases of laser configurations so it is trivial to show all.

6.2 Quantum Stokes and Anti-Stokes Spectra from MP-QS Hybrid Nanostructure

In this section, the optical properties of a hybrid nanostructure comprising of a plasmonic MP and a QS in four-level double Raman scheme will be studied based on the

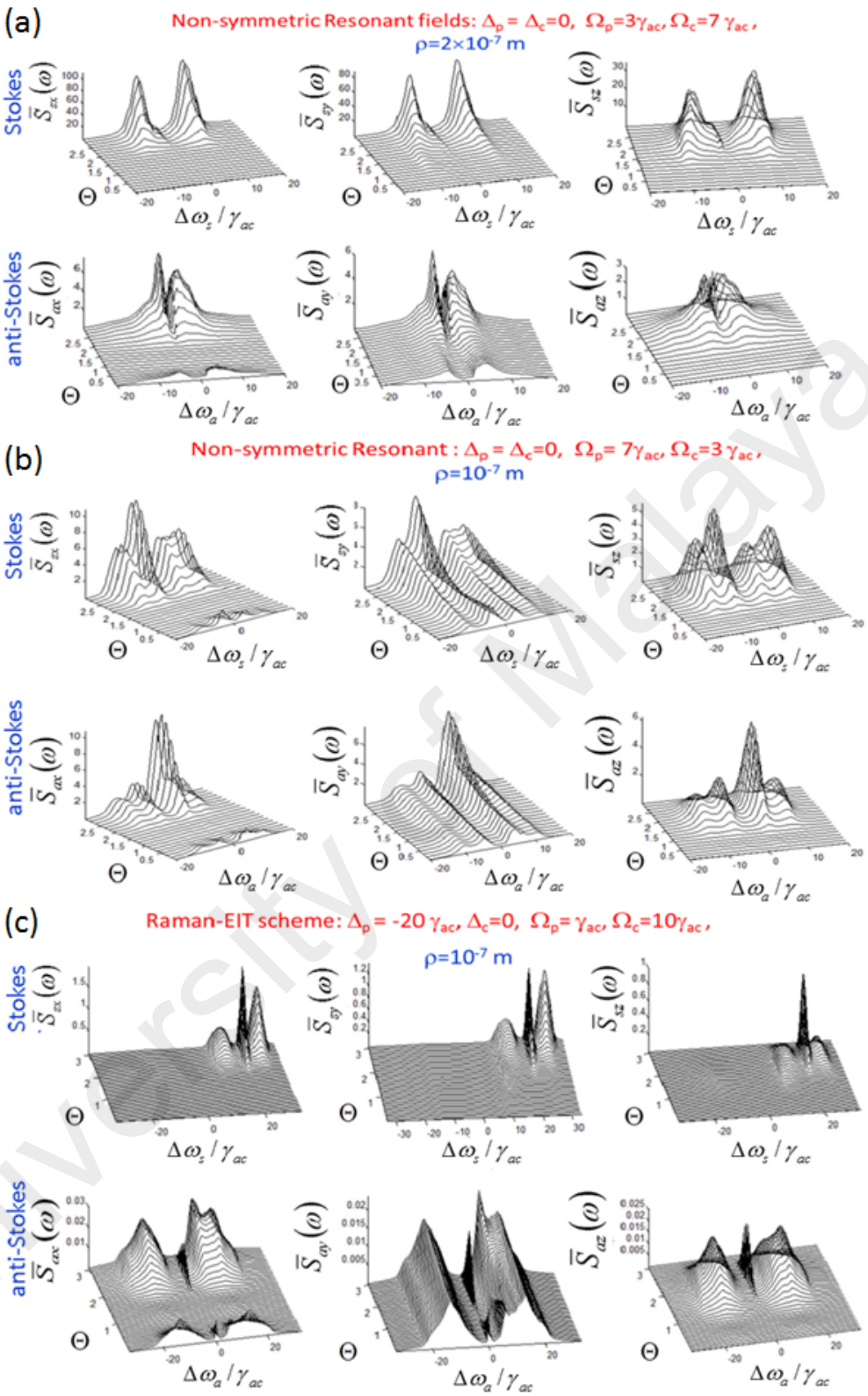

Figure 6.6: Angular $\Theta-$dependence of the normal-order Stokes and anti-Stokes spectra with linear dispersion for the cases of asymmetric resonant laser fields with (a) $\Omega_p = 3\gamma_{ac}, \Omega_c = 7\gamma_{ac}$, (b) $\Omega_p = 7\gamma_{ac}, \Omega_c = 3\gamma_{ac}$ and (c) $\Omega_p = \gamma_{ac}, \Omega_c = 10\gamma_{ac}$. All other parameters are the same as in Figure 6.1.

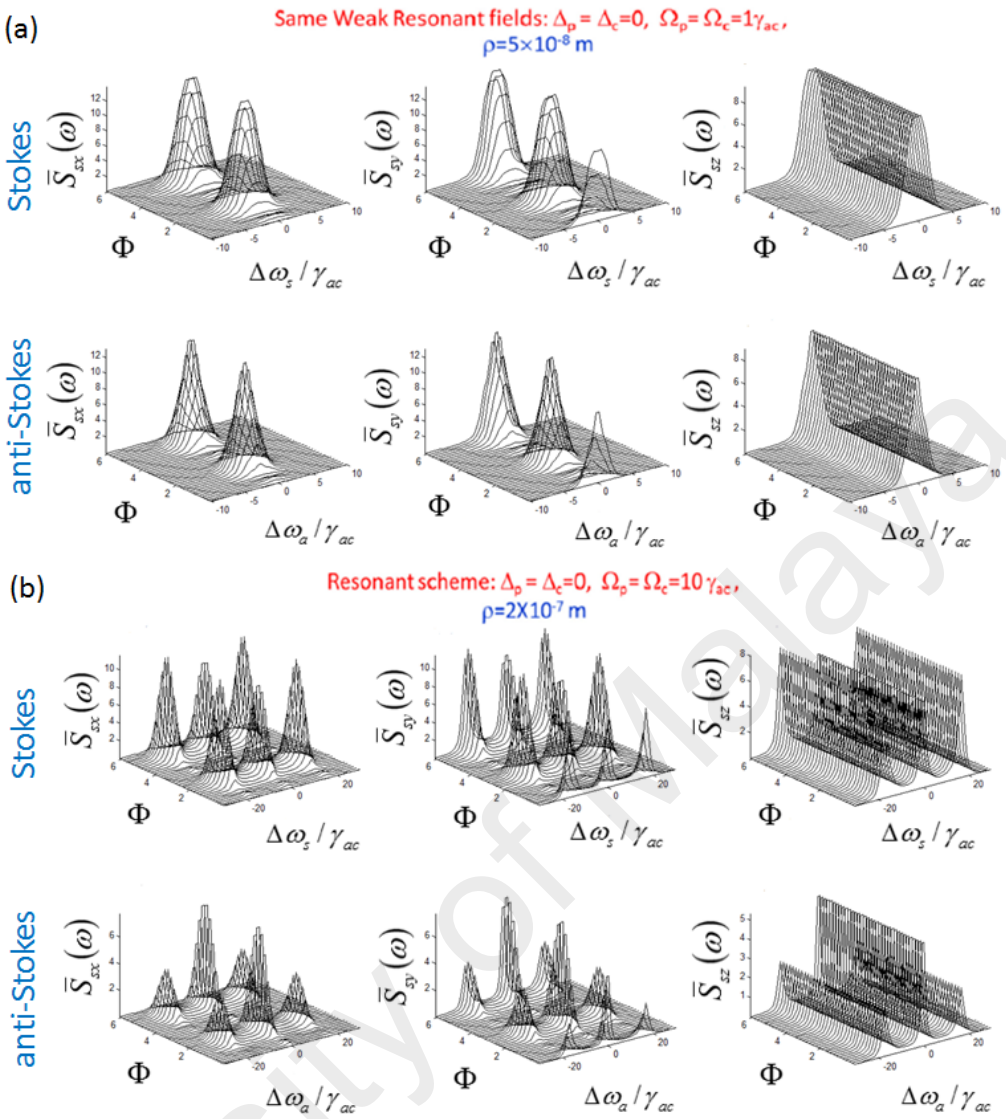

Figure 6.7: Angular Φ−dependence of the normal-order Stokes and anti-Stokes spectra with linear dispersion for the cases of symmetric resonant laser fields with (a) $\Omega_p = \Omega_c = \gamma_{ac}$ (weak fields) and (b) $\Omega_p = \Omega_c = 10\gamma_{ac}$ (strong fields). All other parameters are the same as in Figure 6.1.

simulations of the spectra (Equation 4.37) of scattered quantum (Stokes and anti-Stokes) fields. The Stokes and anti-Stokes fields spectra are plotted in Figures 6.9-6.17, showing how the spectra change with the separation distance r between QS and MP, observation angles Φ and Θ as well as number density N. For the sake of clarity, throughout this section the dimensionless $q-$component ($q = x, y, z$) Stokes and anti-Stokes spectra $\bar{S}_{s(a)q} = S_{s(a)q}\frac{R^6}{K^2\left|\wp_{bd(ca)}\right|^2}$ are plotted instead of the original spectra. Also, the spectra are numerically normalized by dividing all the values in the spectra by the maximum value

attained by the $z-$component spectra, so that all the peaks values are in the order of 1-100. This allows clearer presentation of the results and at the same time, comparison between different components of the spectra.

Also, throughout this section the radius of the MP is fixed to be $a = 50$ nm and 70 nm (to compare the spectra between the two values) and the radius of the QS is fixed to be $b = 10$ nm (Khlebtsov & Khlebtsov, 2007) (in other similar studies the radii values are even smaller, about $a = 5$ nm and $b = 1.5 - 2.0$ nm (Malyshev & Malyshev, 2011)), all of which are much smaller than the wavelength of the Stokes ($\lambda_{db} = 632.10$ nm) and anti-Stokes ($\lambda_{ac} = 570.07$ nm) fields, thus fulfilling the condition for dipole approximation $\lambda >> a, b$. Also, in Figures 6.9-6.13 the plots start from the minimum interparticle distance of $r = 1000$ nm ($k_0 r \simeq 11$, where $k_0 = \omega_{ac}/c$) so as to fulfill the condition $r >> a, b$ for the validity of dipole approximation. Unless stated otherwise, the range of number density considered in this study is $2.39 \times 10^{23} \mathrm{m}^{-3} < N < 5.01 \times 10^{25}$ m^{-3}. Here, the minimum density is obtained based on the requirement that there must consist of at least one atom in the QS volume whereas the maximum density is the highest density below which the collective effects can be ignored, based on the simulation results of Equation 39 in Ref. (Ficek & Tanaś, 2002) given by

$$\Omega_{ij} = -\frac{3\Gamma_x}{4}\left\{\left[1-\left(\bar{\mu}\cdot\bar{r}_{ij}\right)^2\right]\frac{\cos\left(k_x r_{ij}\right)}{k_x r_{ij}} - \left[1-3\left(\bar{\mu}\cdot\bar{r}_{ij}\right)^2\right]\left[\frac{\sin\left(k_x r_{ij}\right)}{\left(k_x r_{ij}\right)^2}+\frac{\cos\left(k_x r_{ij}\right)}{\left(k_x r_{ij}\right)^3}\right]\right\}, \tag{6.2}$$

which characterizes the strength of the collective interactions between atoms. Here, Γ_x ($x = ab, ac, db.dc$) is the spontaneous emission rate in Appendix C, $k_x = \omega_x/c$, $r_{ij} = N^{-1/3}$ is the distance between the ith and jth atom (interatomic distance), $\bar{\mu}$ is the unit vector of the dipole moment and $\bar{r}_{ij}$ is the unit vector for the displacement vector $\mathbf{r}_{ij}$ from the ith to the jth atom. The left side of Figure 6.8(a) shows the plot of Equation 6.2 versus

number density in logarithmic scale, $\log_{10} N$ and atomic dipole orientation $\bar{\mu} \cdot \bar{r}_{ij}$ (with respect to the interatomic axis) for the anti-Stokes transition. From the figure, it can be observed that for number densities $N < 10^{25}$ m^{-3}, the interaction strengths between 2 nearest atoms in the QS responsible for collective emission becomes zero for all atomic dipole orientations. This means that $N \simeq 10^{25}$ m^{-3} can be regarded as an upper limit below which collective effects between atoms can be ignored. From the numerical values obtained, a more accurate upper limit to the number density would be $N = 5.01 \times 10^{25}$ m^{-3} as stated above. For a more detailed study of Equation 6.2 one may refer to the left panel of Figure 6.8(b) where the quantity is plotted versus interatomic distance r_{ij}. It can be observed from the figure that Ω_{ij} shows strong oscillatory behavior at small r_{ij} (which corresponds to high number density) and such oscillations undergo damping as r_{ij} increases (which corresponds to decreasing number density), giving an almost constant value of zero. This zero value of Ω_{ij} implies negligible collective interaction between atoms at large r_{ij}. Hence, the result in Figure 6.8(b) is consistent with that of Figure 6.8(a). The absence of oscillation in Figure 6.8(a) is due to the large range of N (and therefore r_{ij}) Ω_{ij} is plotted against. It can also be observed from Figure 6.8(b) that oscillation of Ω_{ij} undergoes damping at smaller r_{ij} for the case where the dipole moment is parallel to the interatomic axis defined by vector $\mathbf{r}_{ij}$ as compared to other dipole orientations. A point to note here is that all four transitions in the double Raman scheme exhibit similar feature so it is trivial to show all. The plot for F_{ac} in Figure 6.8 will be discussed in subsection 6.2.7.

Furthermore, with such large size of the MP considered here the retardation effect which causes redshift of the plasmon resonance peak could be important. In fact, our simulations (Figure 6.10) show that for $a > 50$ nm, the retardation effect becomes significant. In Figure 6.10, a comparison is made between the polarizibility $\alpha_{MP,f}$ $(f = s, a)$ with

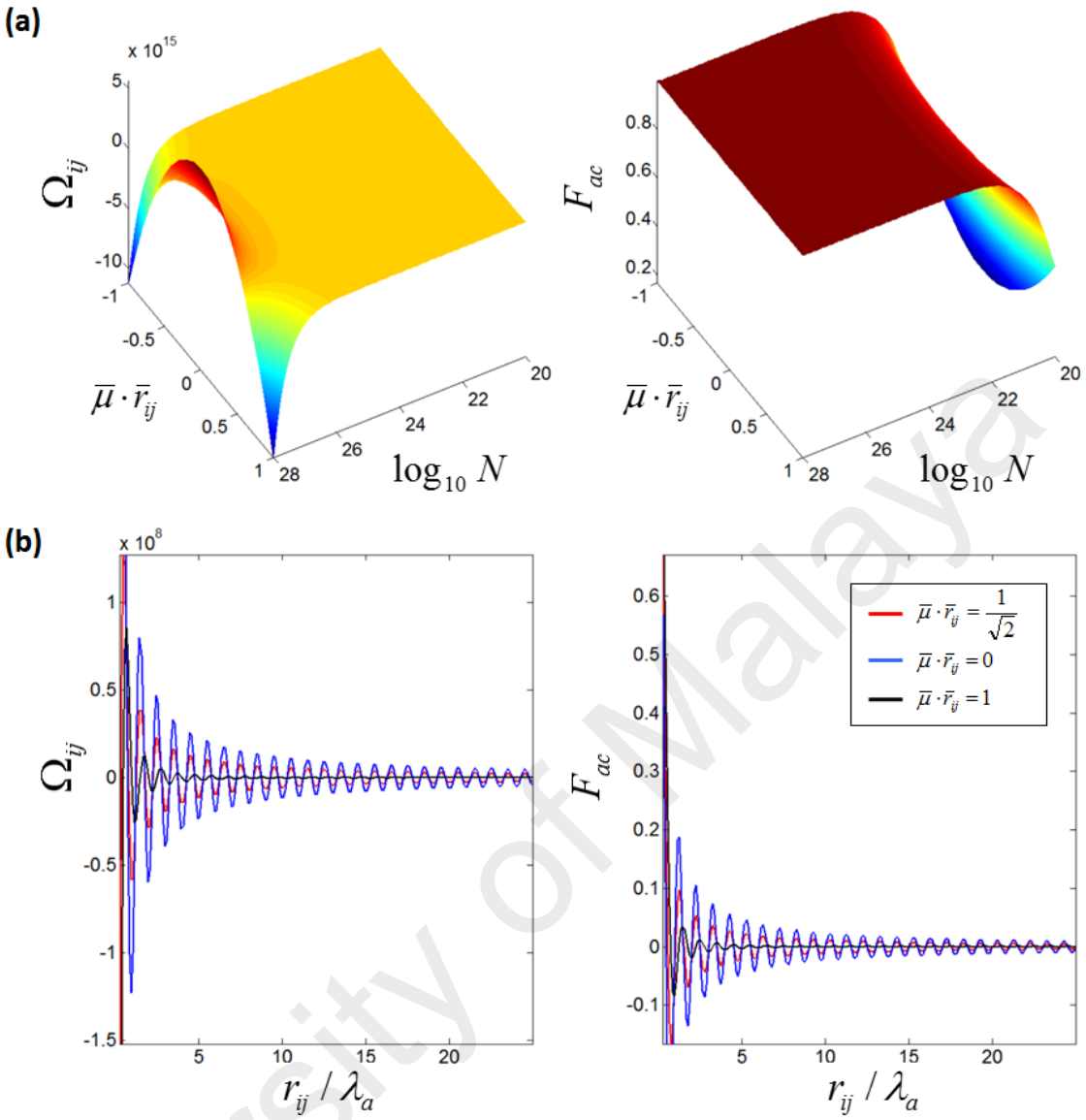

Figure 6.8: (a) Plot of the collective interaction strength Ω_{ij} (left) and F_{ac} (right) versus number density in log scale, $\log_{10} N$ and atomic dipole orientation (with respect to the interatomic axis) $\bar{\mu} \cdot \bar{r}_{ij}$ for the anti-Stokes transition in double Raman scheme with $k_a = \omega_{ac}/c$. (b) Plot of the anti-Stokes collective interaction strength Ω_{ij} (left) and F_{ac} (right) versus interatomic distance r_{ij}/λ_a for three different cases atomic dipole orientation $\bar{\mu} \cdot \bar{r}_{ij} = 1/\sqrt{2}$ (red line), $\bar{\mu} \cdot \bar{r}_{ij} = 0$ (blue line) and $\bar{\mu} \cdot \bar{r}_{ij} = 1$ (black line).

and without taking into account the retardation effect. It is shown that the polarizibility obtained from the retarded and non-retarded model exhibit departure starting from the particle radius $a = 50$nm and beyond. This indicates that retardation effect could be important for the two cases of particle radii $a = 50$ nm and 70 nm considered in this section. Our model here takes into account not only the retardation effect via the two correction terms $-\left[\varepsilon_{MP,f}(\mathbf{k}_d, \omega) - \varepsilon_b\right] x^2 - i\frac{2x^3}{3}\left[\varepsilon_{MP,f}(\mathbf{k}_d, \omega) - \varepsilon_b\right]$ in the denominator

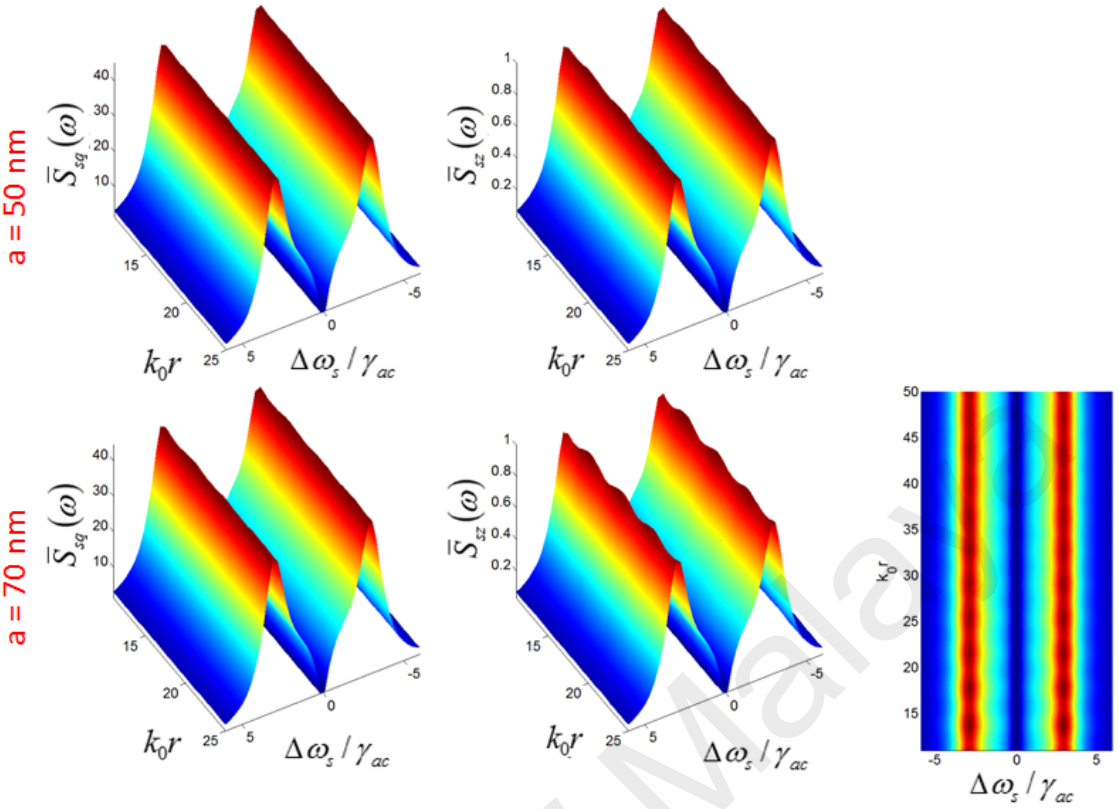

Figure 6.9: Raman Stokes-EIT: Stokes spectra versus interparticle distance r for the case $\Omega_p = 3\gamma_{ac}, \Omega_c = 0$ at $\Theta = \Phi = 0^0$ with initial condition $\bar{\rho}_{bb}(0) = 1$ and without surface plasmon resonance (SPR) ($\omega_{ac} \neq \omega_{SPR}$)**.** We compare between the spectra for two different cases of metallic nanoparticle radius, $a = 50$ nm and $a = 70$ nm. The $x-$ and $y-$component spectra are combined into one plot as $\bar{S}_{sq}$ $(q = x, y)$ due to their similarity. The plot starts from $r = 1000$ nm ($k_0 r > 11$, where $k_0 = \omega_{ac}/c$) so as to fulfill the condition $r >> a, b$ for the validity of dipole approximation. The number density used, $N = 2.52 \times 10^{25}$ m^{-3} is the middle value of the range of number densities 2.39×10^{23} m^{-3} $< N < 5.01 \times 10^{25}$ m^{-3}. The parameters used in $\varepsilon_{MP}(\mathbf{k}_d, \omega)$ (Equation 4.8) are those for silver (Ag) nanoparticle with $\omega_p = 9.1$ eV$= 2.2 \times 10^{15}$ s^{-1}, $\Gamma_m^{\infty} = 18$ meV $= 2.73 \times 10^{13}$ s^{-1}and $\varepsilon_{\infty} = 3.7$. Other parameters are $\varepsilon_b = 1.5$, quantum particle radius $b = 10$ nm and the probe field amplitude $E_{s0,q} = \frac{0.1\hbar\gamma_{ac}}{\wp_{db,q}}$, where the dipole moments are taken to be isotropic: $\wp_{ac,q} = \wp_{db,q} = 2 \times 10^{-29}$C m.

of Equation 4.12 but also the effect of spatial nonlocality via the term $-\beta^2 k_d^2$ in Equation 4.8. Figure 6.11 shows that the real part of the nonlocal dielectric function $\varepsilon_{MP,f}$ $(f = s, a)$ only deviates from the Drude model when $a < 15$ nm whereas its imaginary part deviates when $a < 40$ nm. Since the real part is much higher in magnitude compare to imaginary part, one can just take the limit $a < 15$ nm as the particle size below which nonlocal effect is important. Although in this section the values $a = 50$ nm and 70 nm (which are

much larger than $a = 15$ nm) are used, nonlocal effect is still included here for the sake of completeness.In the following subsections the main results from the spectra will be highlighted based on how they are affected by various parameters.

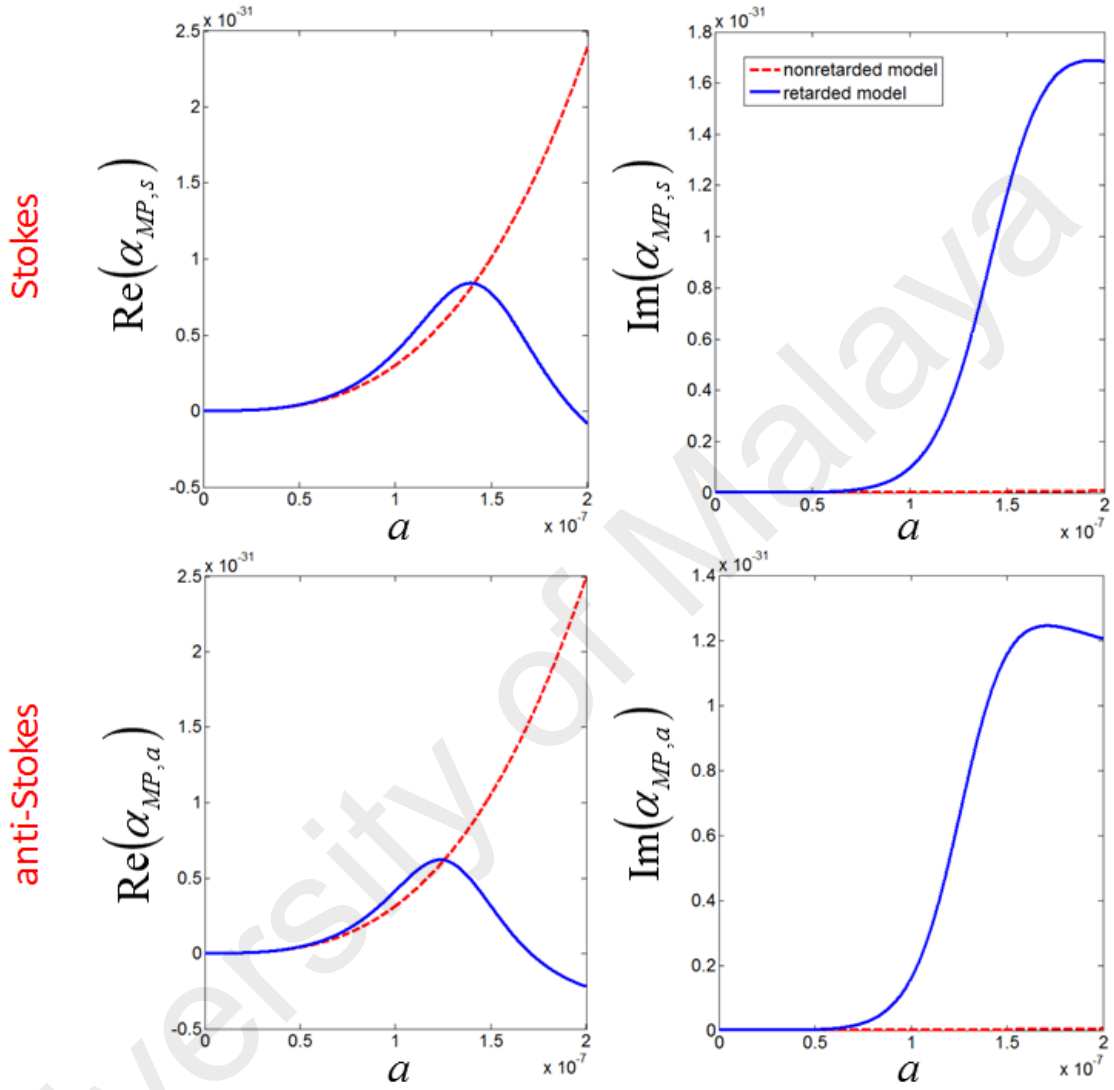

Figure 6.10: Dependence of the polarizibility $\alpha_{MP,f}$ $(f = s, a)$ on the radius a of the MP at the resonant frequencies $\omega = \omega_{db}$ (for Stokes) and $\omega = \omega_{ac}$ (for anti-Stokes). We compare between the polarizibility with (blue continuous line) and without (red dashed line) retardation effect. All other parameters are the same as in Figure 6.9

6.2.1 Effects of Resonant Laser Fields Strengths

As in section 6.1, here the Stokes and anti-Stokes spectra for various cases of resonant laser fields will be studied: (i) Raman-EIT utilizing the $\Lambda-$system associated with the Stokes field as the three-level EIT system, (ii) weak symmetric laser fields

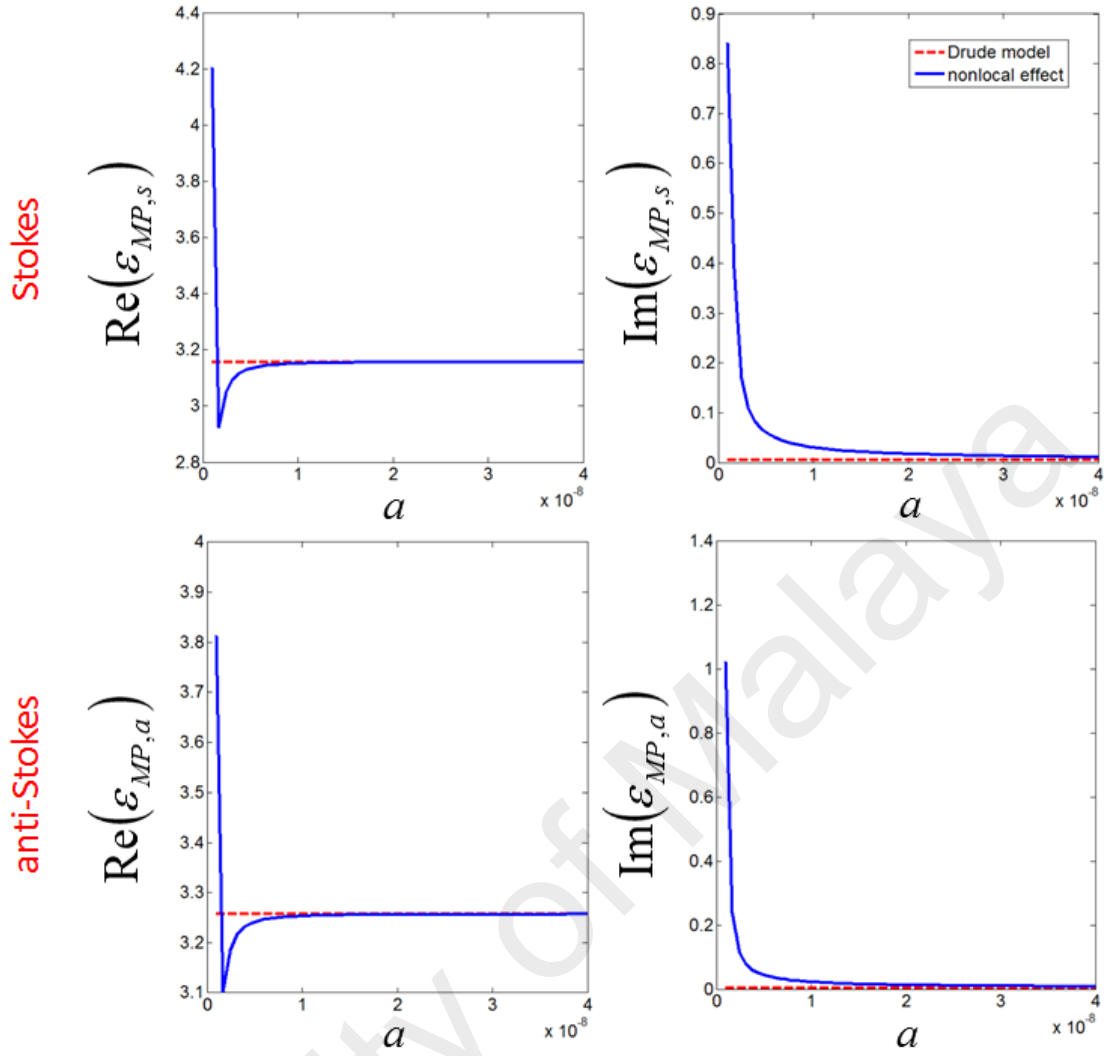

Figure 6.11: Dependence of the MP dielectric function $\varepsilon_{MP,f}$ $(f = s, a)$ on the radius a of the MP at the resonant frequencies $\omega = \omega_{db}$ (for Stokes) and $\omega = \omega_{ac}$ (for anti-Stokes). We compare the MP dielectric function obtained from the Drude model (red dashed line) with the one including nonlocal effect (blue continuous line). All other parameters are the same as in Figure 6.9.

($\Omega_p = \Omega_c = \gamma_{ac}$), (iii) strong symmetric laser fields ($\Omega_p = \Omega_c = 15\gamma_{ac}$) and (iv) asymmetric laser fields ($\Omega_p = 7\gamma_{ac}, \Omega_c = 3\gamma_{ac}$). For all these cases the value of number density $N = 2.52 \times 10^{25}\text{m}^{-3}$ which is the middle value of the range of number densities mentioned above is used. This value of N corresponds to about 105 atoms within the QS volume. Since both the x- and y-component Stokes and anti-Stokes spectra for all cases of resonant laser fields exhibit exactly the same features across the interparticle distances r, both spectra are combined into one plot as $\bar{S}_{fq}$ $(q = x, y)$ in Figures 6.9-6.13. The similarity between the x- and y-component spectra across r is a direct result of our choice

of observation angles, $\Phi = \Theta = 0^0$.

For the Raman-EIT case in Figure 6.9, the Stokes field acts as the weak probe field while the pump Ω_p field serves as the strong coherent laser field. From the figure, one can see how the famous EIT spectra (and other cases of resonant laser fields) is affected by MP, in particular the oscillations of the two peaks and the "breathing" feature of the peaks with varying interparticle distance r.

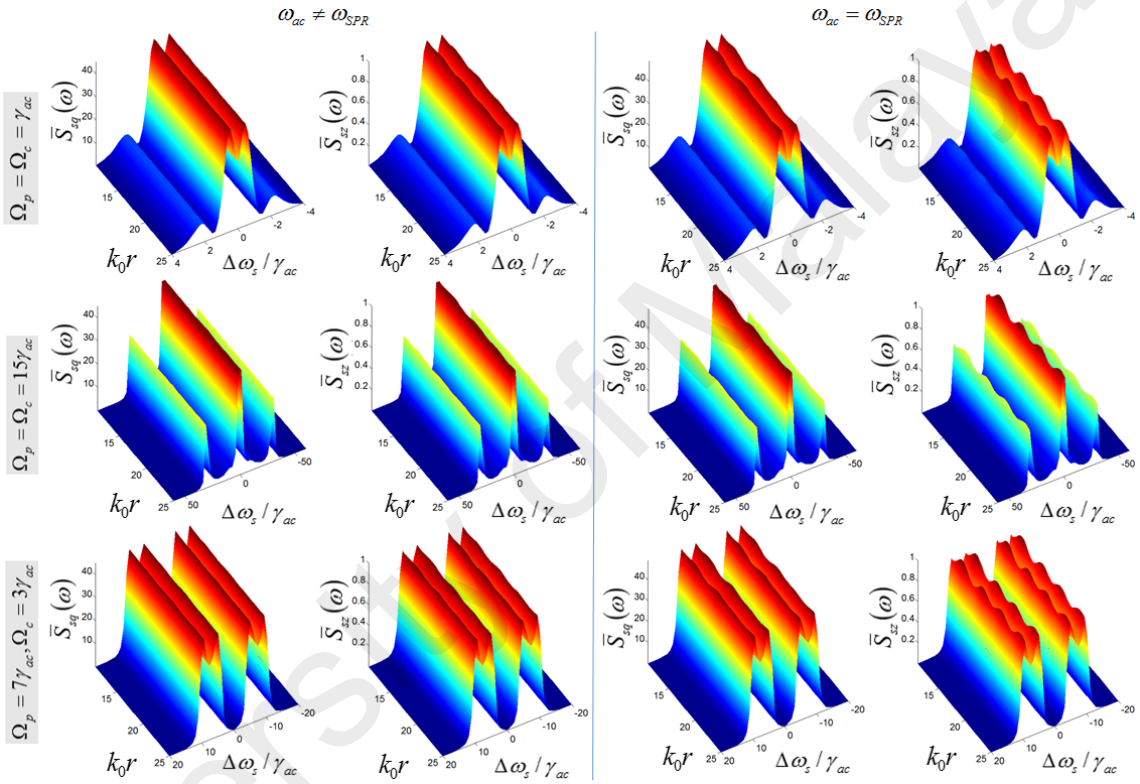

Figure 6.12: Weak, strong and asymmetric resonant pump and control laser fields for Stokes: Stokes spectra versus interparticle distance r for the cases of weak ($\Omega_p = \Omega_c = \gamma_{ac}$), strong ($\Omega_p = \Omega_c = 15\gamma_{ac}$) and asymmetric ($\Omega_p = 7\gamma_{ac}, \Omega_c = 3\gamma_{ac}$) pump and control laser fields with initial condition $\bar{\rho}_{bb}(0) = \bar{\rho}_{cc}(0) = 0.5$. We compare between the spectra for the case with SPR ($\omega_{ac} = \omega_{SPR}$) and the case without SPR ($\omega_{ac} \neq \omega_{SPR}$). The $x-$ and $y-$component spectra are combined into one plot as $\bar{S}_{sq}\,(q = x, y)$ due to their similarity. The metallic nanoparticle radius considered here is $a = 50$ nm. All other parameters are the same as in Figure 6.9.

Other cases of resonant laser excitations (Figures 6.12 and 6.13) exhibit spectra with typical features of QS in double Raman configuration which serve not only to show the correctness of the results but also contain the physics of strong quantum fields resulting from the influence of MP. When both pump and control laser fields strengths are the same

and weak ($\Omega_p = \Omega_c = \gamma_{ac}$), the side peaks at $\pm(\Omega_p + \Omega_c) = \pm 2\gamma_{ac}$ remain for the Stokes and anti-Stokes spectra. However, surprisingly for the Stokes spectra, there is a Fano dip at the higher central peak, creating two peaks at $\pm 0.25\gamma_{ac}$ while for anti-Stokes the central peak is completely absent. This Fano dip and absence of central peak can be interpreted as quenching due to enhancement of the quantum Stokes and anti-Stokes fields by the MP to the extent where the pump and control laser fields become weaker or comparable to the quantum fields. While the dip can be observed in the case of weak laser fields, such is not the case when the laser fields become sufficiently large ($\Omega_p = \Omega_c = 15\gamma_{ac}$). When both pump and control laser fields have strong symmetric fields strength Mollow triplets become clearly visible in the Stokes and anti-Stokes spectra. Surprisingly, the middle peak for the anti-Stokes spectra is much smaller than the side peaks as it has been almost completely suppressed or quenched by the enhanced anti-Stokes field under the influence of the MP.

Figure 6.14 shows the effects of the laser strengths on the Fano resonance. One can see clearly from the figure that as the pump and control laser fields strength increases, the Fano dip at the central peak of the Stokes spectra (blue continuous line) becomes less significant and the usual central peak slowly recovers. Also from Figure 6.14 one can observe the presence of additional small peaks between the central and side peaks of the Stokes spectra for weaker laser fields strengths. These unexpected extra peaks are due to additional ac Stark shifts induced by the enhanced Stokes field which has greater or comparable strength as compared to the input laser fields. These additional peaks become less significant with increasing laser fields strengths such that the ac Stark shifts (which result in Mollow triplets) caused by the laser fields becomes dominant. Similar features are found in anti-Stokes spectra (red dashed line in Figure 6.14) except that the central peaks are suppressed even further. Autler-Townes splittings are also evident in the spectra

for the case where the laser fields are asymmetric ($\Omega_p = 7\gamma_{ac}, \Omega_c = 3\gamma_{ac}$), with four strong resonant peaks at $-\left(\Omega_p + \Omega_c\right), -\left|\Omega_p - \Omega_c\right|, \left|\Omega_p - \Omega_c\right|$ and $\Omega_p + \Omega_c$, but with the two inner peaks suppressed in the anti-Stokes spectra. As expected, due to stronger ac Stark shift, the separation between the side peaks increases as the laser fields get stronger.

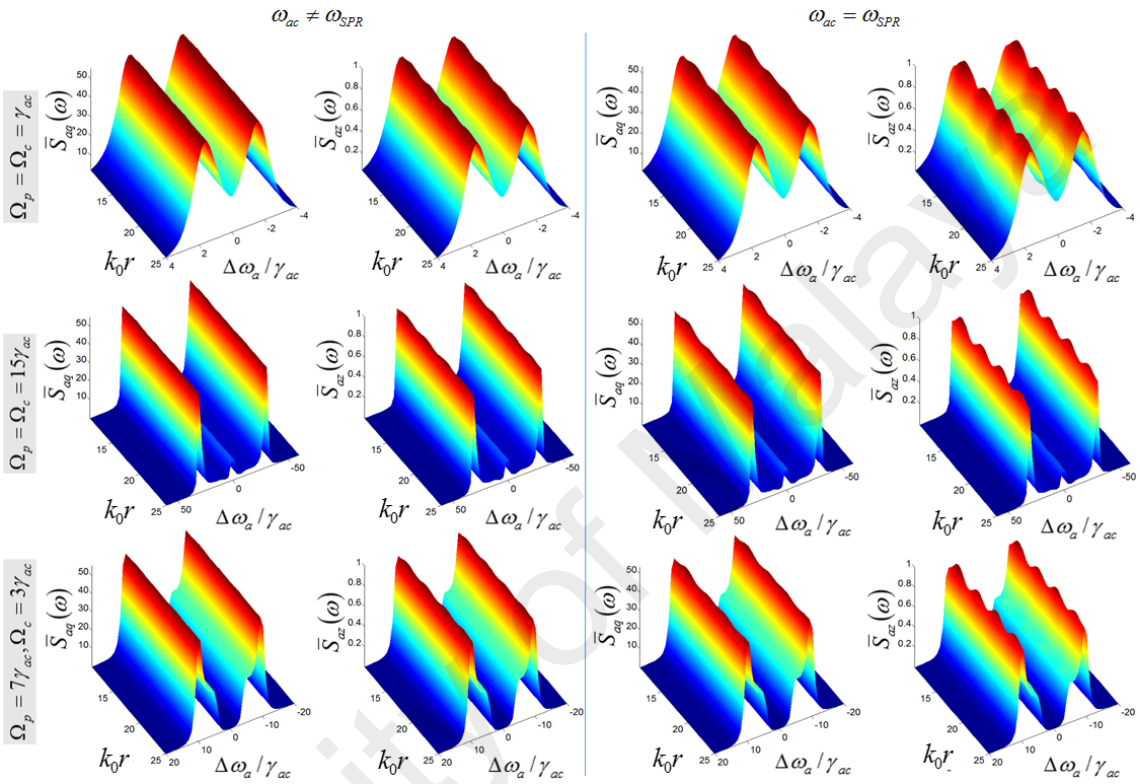

Figure 6.13: Weak, strong and asymmetric resonant pump and control laser fields for anti-Stokes: Anti-Stokes spectra versus interparticle distance r for the cases of weak ($\Omega_p = \Omega_c = \gamma_{ac}$), strong ($\Omega_p = \Omega_c = 15\gamma_{ac}$) and asymmetric ($\Omega_p = 7\gamma_{ac}, \Omega_c = 3\gamma_{ac}$) pump and control laser fields with initial condition $\bar{\rho}_{bb}(0) = \bar{\rho}_{cc}(0) = 0.5$. We compare between the spectra for the case with SPR ($\omega_{ac} = \omega_{SPR}$) and the case without SPR ($\omega_{ac} \neq \omega_{SPR}$). The $x-$ and $y-$component spectra are combined into one plot as $\bar{S}_{aq}(q = x, y)$ due to their similarity. The metallic nanoparticle radius considered here is $a = 50$ nm. All other parameters are the same as in Figure 6.9.

6.2.2 Effects of Detunings

In Figures 6.9-6.15 the spectra plotted are for the cases where the fields are resonant i.e. detunings, $\Delta_x = 0\,(x = p, c, s, a)$. In this subsection, the effects of detunings on the Stokes and anti-Stokes spectra will be studied. Here, readers should refer to Figure 6.16 where a comparison of Stokes and anti-Stokes spectra for four different cases of detunings

is made. At a first glance of Figure 6.16, one can tell that the presence of detunings causes the spectra to look asymmetrical and that it affects the anti-Stokes spectra much more significantly than the Stokes spectra. As shown in Figure 6.16(a), when all the fields are detuned by the same amount ($\Delta_x = 5\gamma_{ac}$), the anti-Stokes spectra exhibit asymmetrical shape where the side peak at $+(\Omega_p + \Omega_c) = +30\gamma_{ac}$ becomes higher than the peak at $-(\Omega_p + \Omega_c) = -30\gamma_{ac}$, indicating higher fields at the positive frequency. This is reasonable since all the fields are detuned towards the positive frequencies. Although the Stokes spectra look symmetrical at the first glance, careful observation reveals that in both Stokes and anti-Stokes spectra, small additional peak actually occurs at around $+(\Omega_p + \Omega_c) = +10\gamma_{ac}$ while the same is not true at $-(\Omega_p + \Omega_c) = -10\gamma_{ac}$. This additional peak is caused by the additional ac Stark shift due to the non-resonant pump and control laser fields which have frequencies ν_p and ν_c with magnitude $5\gamma_{ac}$ higher than the transition frequencies. When the sign of the detuning is reversed, i.e. $\Delta_x = -5\gamma_{ac}$ (carrier frequencies of the fields is lower than transition frequencies), the shape of both the Stokes and anti-Stokes peaks becomes reversed (with higher anti-Stokes side peaks at the negative frequency instead of positive frequency), as shown in Figure 6.16(b).

Figure 6.16(c) shows what happens to the spectra when only the pump and control laser fields are detuned from their transition frequencies but not the quantum fields. The result shows that while the additional peaks at around $+(\Omega_p + \Omega_c) = +10\gamma_{ac}$ still occurs in both Stokes and anti-Stokes spectra as in Figure 6.16(a), but the side peaks at $+(\Omega_p + \Omega_c) = +30\gamma_{ac}$ in both the Stokes and anti-Stokes spectra become suppressed. This is because as the laser fields are detuned towards the positive frequency, the Stokes and anti-Stokes transitions becomes stronger at the negative frequency. This causes peak at the negative frequency to be higher, indicating higher detection efficiency.

In contrast to Figure 6.16(c), Figure 6.16(d) is for the case where both the pump and control laser fields are resonant but the Stokes and anti-Stokes fields are detuned by $+5\gamma_{ac}$. It can be observed from the figure that the anti-Stokes side peak at the positive frequency is higher due to the enhancement of the quantum field at this frequency while the Stokes spectra remains almost symmetrical.

6.2.3 Effects of Interparticle Distance

In this subsection, Figures 6.9-6.13 will be analyzed to study the effects of interparticle distance r on the spectra. One can clearly observe from the figures that while the profile of the spectra across the frequencies does not change with r, the main feature on the $r-$dependence is the oscillations in the spectra with period of $k_0 r = 2\pi$, due to the interference effect of the fields from the two particles. Since the Stokes and anti-Stokes fields in Equations 4.34 and 4.35 comprise of the scattered fields from both QS and MP, the crests and troughs on the peaks correspond respectively to the constructive and destructive interference of the fields from both particles. An interesting feature here is that the interference between the fields is correlated to interparticle distance in a periodic manner, with certain values of r giving constructive interference and other values resulting in destructive interference. This is likened to a cavity effect formed by two particles close to each other that dictates the phases of the fields scattered from both particles which in turn determine the outcome of the interference at point **R**. At small r, the stronger interference between the polarization fields from the QS and MP leads to larger amplitude of oscillations of the spectral peaks, as can be seen from Figures 6.9-6.13. The oscillations in the spectra experience damping as r increases and eventually die off at large separation distance, where the interference effect is less significant, as clearly shown in the bottom-right top-view plot in Figure 6.9 for the case $a = 70$ nm in Raman-EIT scheme. The same oscillatory behaviour applies to all other cases of laser strengths including EIT.

At $k_0 r > 50$, the spectra for all the cases of laser strengths resemble that of the case for a single QS in the absence of MP.

In Figures 6.12 and 6.13 it can be observed that for the case without surface plasmon resonance (SPR) ($\omega_{ac} \neq \omega_{SPR}$), the $x-$ and $y-$components spectra actually contain oscillations across $k_0 r$ but appear to be less visible than the $z-$component spectra. This is due to the fact that the $z-$component spectrum is 40 to 50 times lower in magnitude (due to the nonvanishing $B(R, \omega)$ in Equation 4.14) as compared to the other two components, hence causing the oscillations across $k_0 r$ to have higher visibility. This is also due to our choice of observation angles , $\Phi = \Theta = 0^0$ which corresponds to $n_{I,x} = n_{I,y} = 0$ and $n_{I,z} \neq 0$, thus leading to stronger $r-$dependence (via the nonvanishing $B(R, \omega)$) of the $z-$component field as compared to the $x-$ and $y-$component (with vanishing $B(R, \omega)$). Figure 6.15 reveals that if we choose other values of Φ and Θ, for example, $\Phi = \Theta = 45^0$,(Figure 6.15(a)) the oscillations can be seen more clearly in the $x-$ and $y-$components spectra which now have magnitudes comparable to the $z-$component. For the case $\Phi = 0^0, \Theta = 90^0$, it is the $y-$component spectrum that has much higher magnitude and exhibit weaker oscillations than the rest while for the case $\Phi = \Theta = 90^0$, the oscillations of the $y-$component spectral peaks are the most significant. All these can be similarly explained based on the values of the terms $n_{I,x}, n_{I,y}$ and $n_{I,z}$ in Equation 4.14.

For the case with SPR ($\omega_{ac} = \omega_{SPR}$), all three components of the spectra in Figures 6.12 and 6.13 exhibit visible oscillations across $k_0 r$ due to the plasmonic enhancement effect which will be discussed in subsection 6.2.5.

6.2.4 Effects of MP Size

One can observe from Figure 6.9 that the oscillations in the spectra is stronger for the case where $a = 70$ nm. In fact, the results show that the interference effect for all cases of resonant laser fields becomes more significant as the size of MP gets larger. This

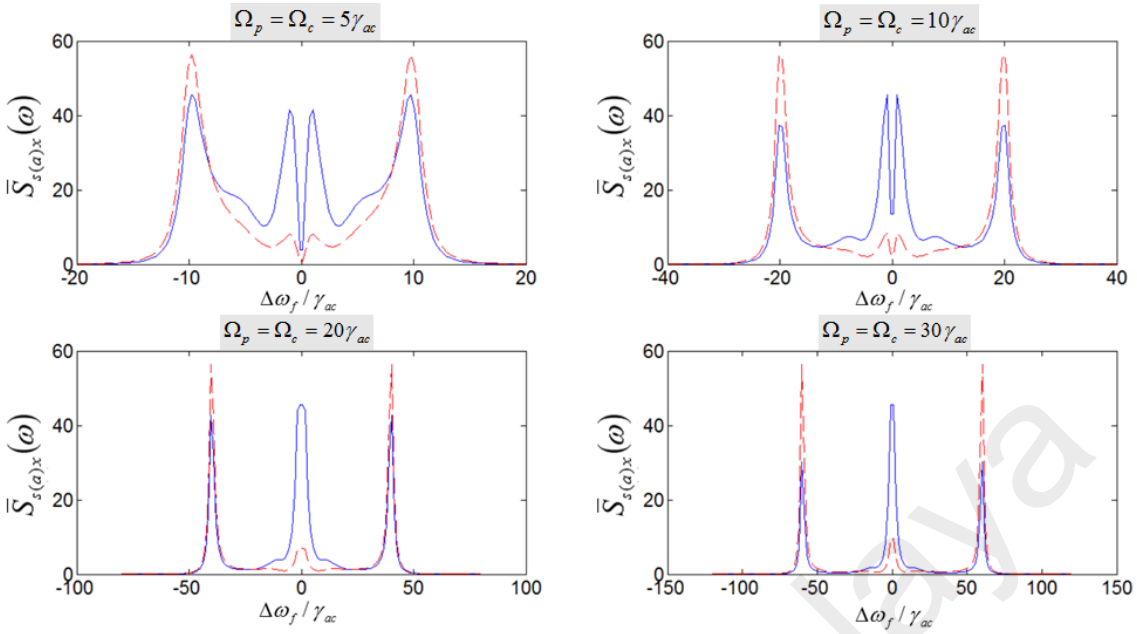

Figure 6.14: Symmetric resonant pump and control laser fields: $x-$component Stokes (blue continuous line) and anti-Stokes (red dashed line) spectra at $k_0 r = 15$ for the case of symmetric pump and control laser fields ($\Omega_p = \Omega_c$) with initial condition $\bar{\rho}_{bb}(0) = \bar{\rho}_{cc}(0) = 0.5$. We compare among the spectra for four different cases of laser fields strengths. The metallic nanoparticle radius considered here is $a = 50$ nm and SPR is absent ($\omega_{ac} \neq \omega_{SPR}$). All other parameters are the same as in Figure 6.9.

phenomenon can be explained by referring to the polarizibility $\alpha_{MP,f} = \frac{1}{K}\gamma_f a^3$ which characterizes the dynamical response of the MP to the external fields (polarization fields from the QS), particularly the ability of the particle to form dipoles which will then take part in the long-range Coulomb interaction responsible for the MP-QS coupling. The cubic dependence of $\alpha_{MP,f}$ on a implies that larger MP will give stronger response and thus stronger long-range Coulomb interaction between the two particles which manifests itself in the form of oscillatory behaviour of the spectral peaks across $k_0 r$. This explains the stronger oscillations in the spectra for larger MP size. Our simulations (not shown here) show that the spectra start to exhibit little oscillations at around $a = 25$ nm and the oscillations become stronger as a increases.

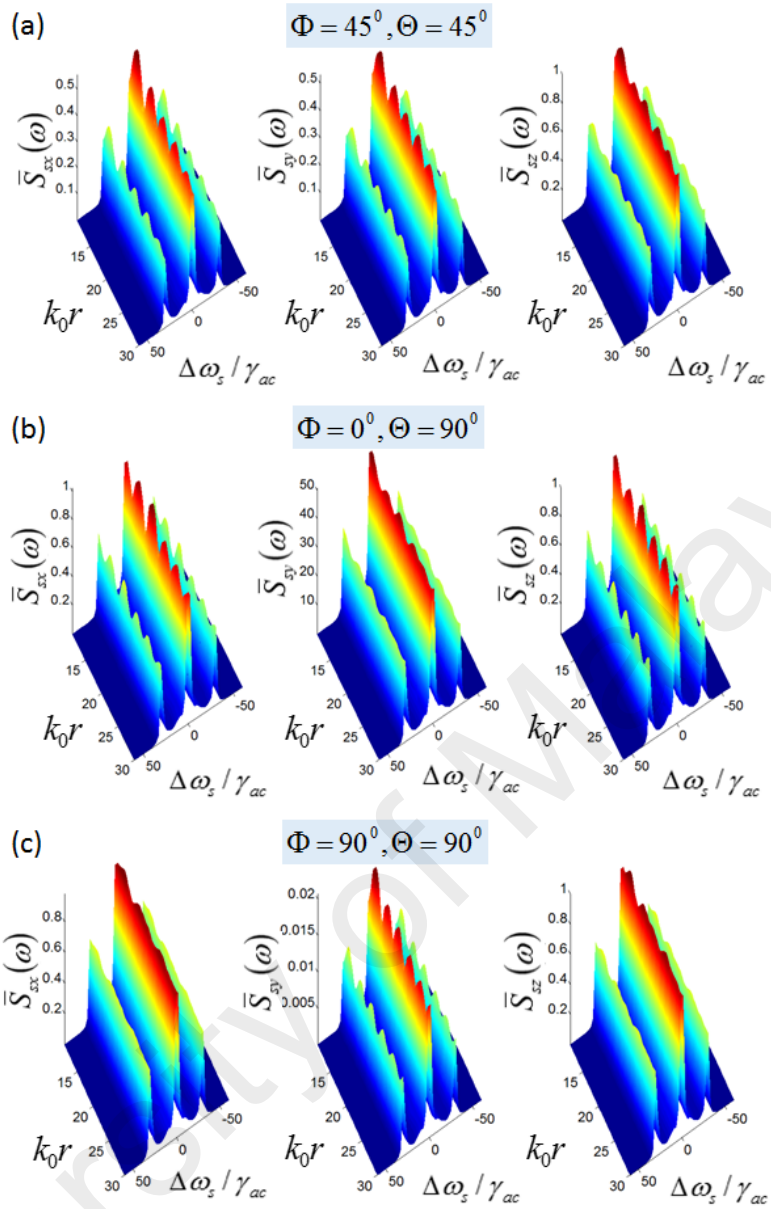

Figure 6.15: Stokes spectra versus interparticle distance r for the case of strong ($\Omega_p = \Omega_c = 15\gamma_{ac}$) symmetric resonant pump and control laser fields with initial condition $\bar{\rho}_{bb}(0) = \bar{\rho}_{cc}(0) = 0.5$. We compare between the Stokes spectra at (a) $\Phi = \Theta = 45^0$, (b) $\Phi = 0^0, \Theta = 45^0$ and (c) $\Phi = \Theta = 90^0$. The metallic nanoparticle radius considered here is $a = 70$ nm and SPR is presence ($\omega_{ac} = \omega_{SPR}$). All other parameters are the same as in Fig. 6.9.

6.2.5 Effects of Surface Plasmon Resonance (SPR)

In this subsection, the effects of surface plasmon resonance (SPR) on the Stokes and anti-Stokes spectra will be studied. To observe strong plasmonic enhancement effect one has to make sure that the SPR condition is fulfilled, that is, when the factor γ_f in Equation

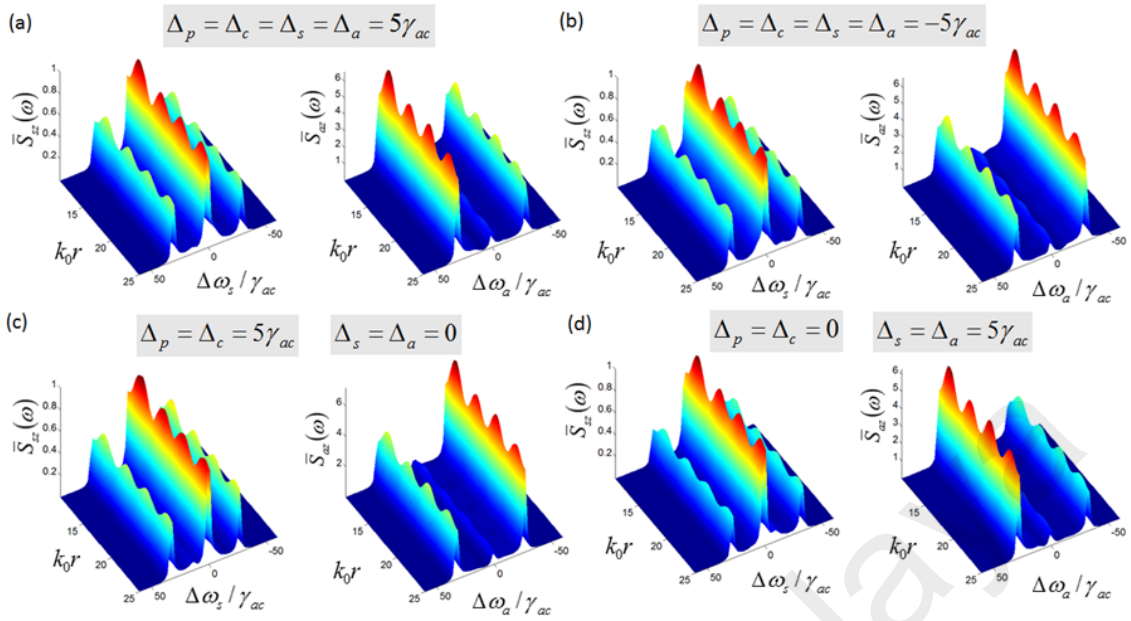

Figure 6.16: Strong symmetric non-resonant pump and control laser fields: $z-$component Stokes and anti-Stokes spectra at $k_0 r = 15$ for the case of strong symmetric nonresonant pump and control laser fields ($\Omega_p = \Omega_c = 15\gamma_{ac}$) with initial condition $\bar{\rho}_{bb}(0) = \bar{\rho}_{cc}(0) = 0.5$ in the presence of SPR ($\omega_{ac} = \omega_{SPR}$). We compare between the spectra for various cases of detunings: (a) $\Delta_p = \Delta_c = \Delta_s = \Delta_a = 5\gamma_{ac}$, (b) $\Delta_p = \Delta_c = \Delta_s = \Delta_a = -5\gamma_{ac}$, (c) $\Delta_p = \Delta_c = 5\gamma_{ac}, \Delta_s = \Delta_a = 0$ and (d) $\Delta_p = \Delta_c = 0, \Delta_s = \Delta_a = 5\gamma_{ac}$. The metallic nanoparticle radius considered here is $a = 70$ nm. All other parameters are the same as in Figure 6.9.

4.12 is maximum. This occurs at the SPR frequency given by

$$\omega_{SPR} = \sqrt{\frac{\omega_p^2}{\varepsilon_\infty + 2\varepsilon_b} + \beta^2 k_d^2 - \frac{\Gamma_m^2}{4}}, \tag{6.3}$$

where the retardation effect has been neglected by dropping the x^2 and x^3 terms in the denominator of Equation 4.12 to simplify the calculations. It can be calculated from Equation 6.3 that the SPR frequency for silver (Ag) nanoparticle is $\omega_{SPR} \simeq 5.3544 \times 10^{15}\text{s}^{-1}$ when $a = 50$ nm and $\omega_{SPR} \simeq 5.3469 \times 10^{15}\text{s}^{-1}$ when $a = 70$ nm.

In Figures 6.12 and 6.13 the plasmonic enhancement effect on the Stokes and anti-Stokes spectra for different cases of resonant laser fields is studied by setting $\omega_{ac} = \omega_{SPR}$. Comparison between the spectra for the case with and without SPR in Figures 6.12 and 6.13 reveals that the oscillations of the spectra across $k_0 r$ become much stronger in the

presence of SPR for all three cases of resonant laser fields. This enhanced oscillations is the result of the plasmonic enhancement effect which enhances the local Stokes fields at QS and MP, leading to stronger interference of the fields from both particles.

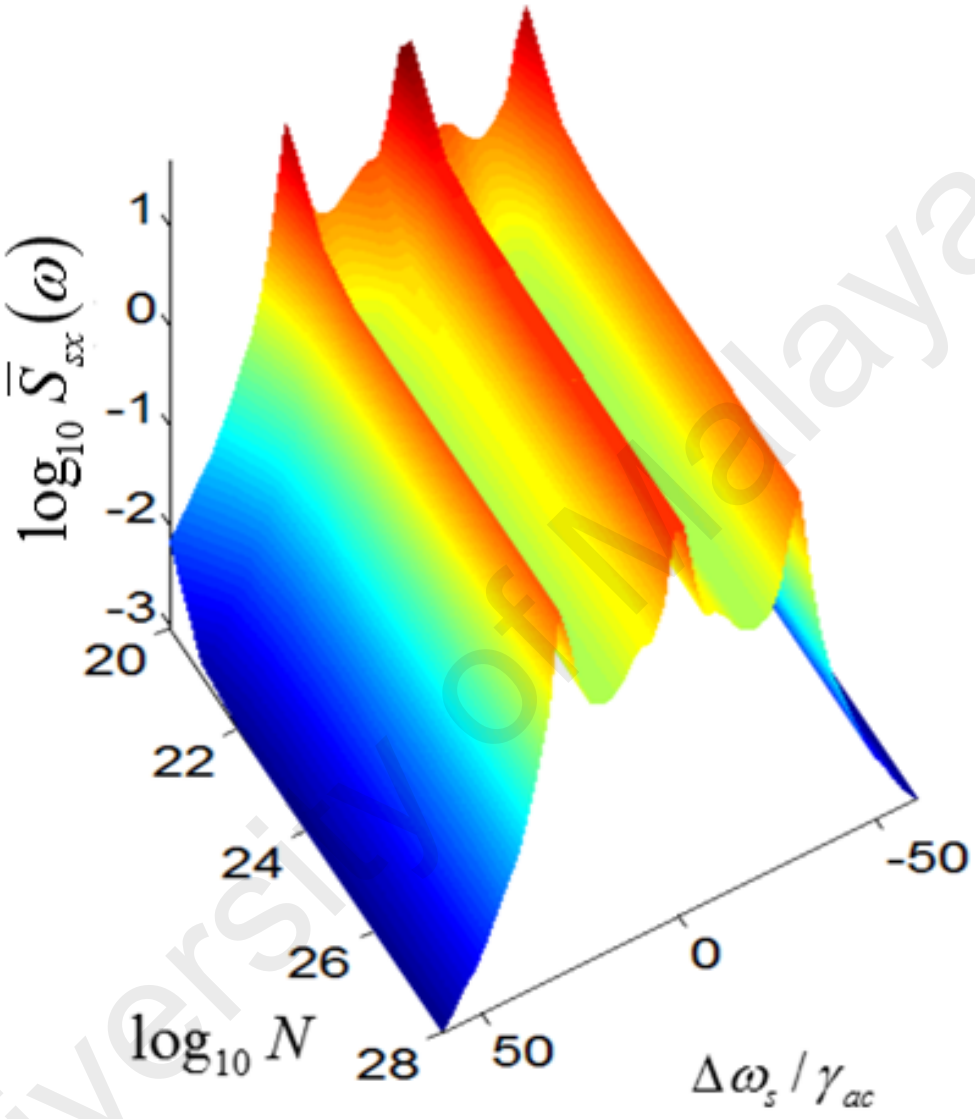

Figure 6.17: Dependence on number density N: (leaft panel) x-component Stokes spectra in log scale versus number density in log scale, $\log_{10} N$ for the case of strong symmetric pump and control laser fields ($\Omega_p = \Omega_c = 15\gamma_{ac}$) with initial condition $\bar{\rho}_{bb}(0) = \bar{\rho}_{cc}(0) = 0.5$ at $k_0 r = 25$ (corresponds to $r \simeq 2268$ nm). (right panel) The profile of the spectra across frequencies at minimum and maximum number densities. The metallic nanoparticle radius used here is $a = 50$ nm and the quantum particle radius is $b = 134$ nm. SPR is not considered here ($\omega_{ac} \neq \omega_{SPR}$). All other parameters are the same as in Figure 6.9.

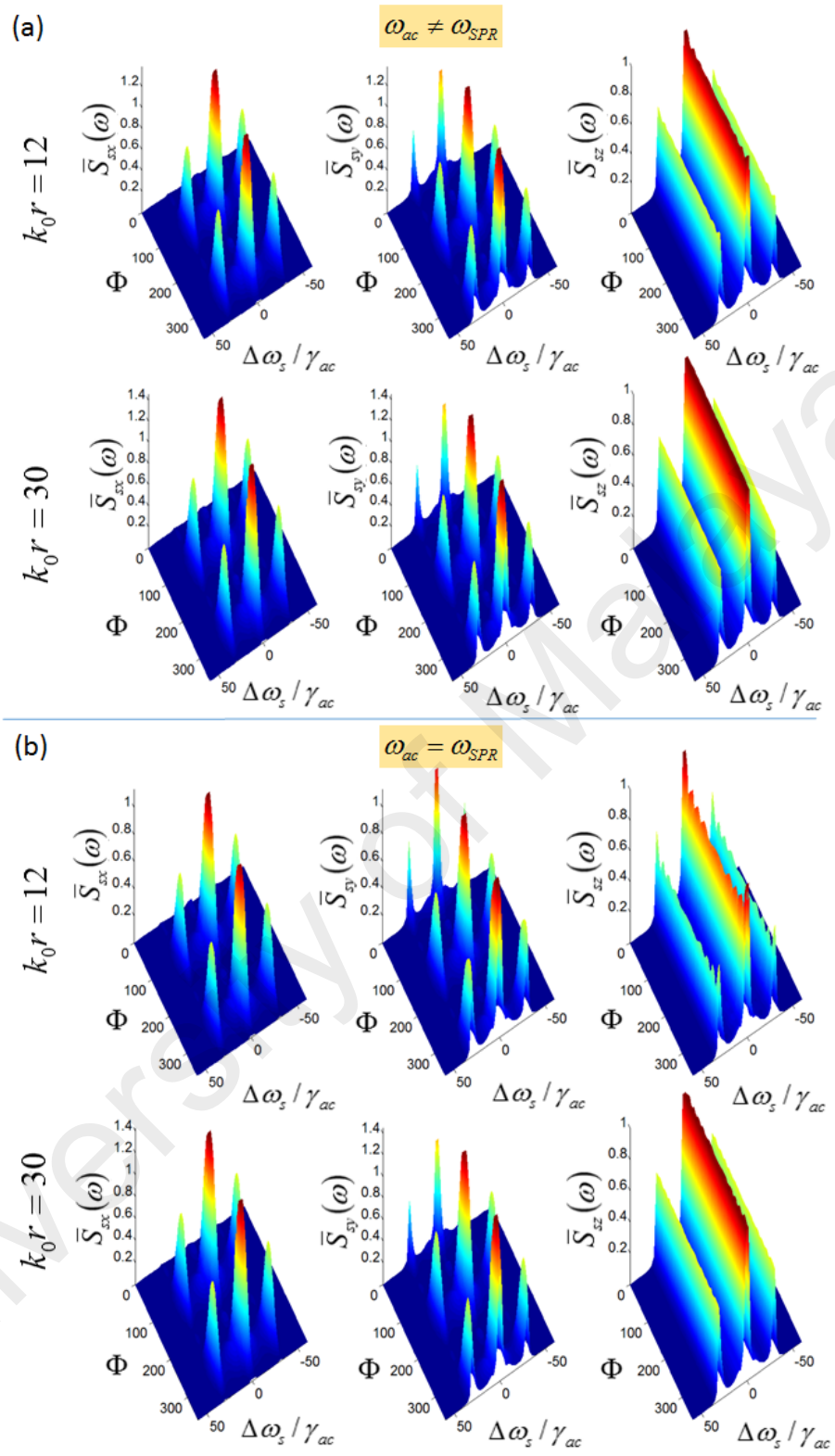

Figure 6.18: Angular Φ−dependence: Stokes spectra versus Φ for the case of strong symmetric pump and control laser fields ($\Omega_p = \Omega_c = 15\gamma_{ac}$) with initial condition $\bar{\rho}_{bb}(0) = \bar{\rho}_{cc}(0) = 0.5$ at two different interparticle distances $k_0 r = 12$ and 30 and at $\Theta = 90^0$ ($x - y$ plane). We compare between the spectra for the case with SPR ($\omega_{ac} = \omega_{SPR}$) and the case without SPR ($\omega_{ac} \neq \omega_{SPR}$). The metallic nanoparticle radius considered here is $a = 70$ nm. All other parameters are the same as in Figure 6.9.

6.2.6 Angular/Directional Dependence

The spectra also depend on the observation angles Φ and Θ as shown in Figures 6.18 and 6.19 for the Stokes field under the case of strong symmetric laser field. Both Stokes and anti-Stokes spectra show the same angular dependence for all cases of laser strengths so it is trivial to show all. The angular dependence of the spectra lies entirely in the $q-$component unit vectors $n_{I,q}$ in Equation 4.14 which is uncorrelated to any frequency-dependent terms. This explains why only the magnitude of the spectra changes with Φ and Θ, while the spectral positions of the resonant peaks remain invariant. The variation of the spectra across the observation angles occurs in the form of oscillatory behaviour which is due to either the sine and cosine terms in $n_{I,q}$ or the interference between the polarization fields from the QS and MP. For discussion on the variation of spectra across observation angles we refer mainly to the case $a = 70$ nm because for the case $a = 50$ nm, the dependence of the spectra on observation angles are not clearly visible (not shown here) due to the weaker MP-QS coupling.

One can see from Figures 6.18 and 6.19 some interesting results such as the variation of the spectra across Φ and Θ that strongly depends on the interparticle distance r. In Figure 6.18 where it has been set $\Theta = 90^0$ ($x - y$ plane), there is a dependence of all $x, y, z-$components of the spectra on Φ at small $k_0 r$, regardless of whether SPR is present or not. At $k_0 r = 12$, the $z-$component spectral peaks are maximum only at one angle $\Phi = 0^0$ or 360^0. But at larger $k_0 r$, the dependence of the z-component spectra on Φ slowly disappears and only the $x-$ and y-component spectra depend on Φ. The $z-$component spectrum is supposed to be invariant by rotation over Φ on the $x - y$ plane because at $\Theta = 0^0, n_{I,z} = 0$ and the $z-$component spectra whose angular dependence relies entirely on the three terms in the third row of matrix P^I in Equation 4.14 eventually loses its Φ-dependence. Hence, the result for $k_0 r = 12$ shows that the interference effect caused by

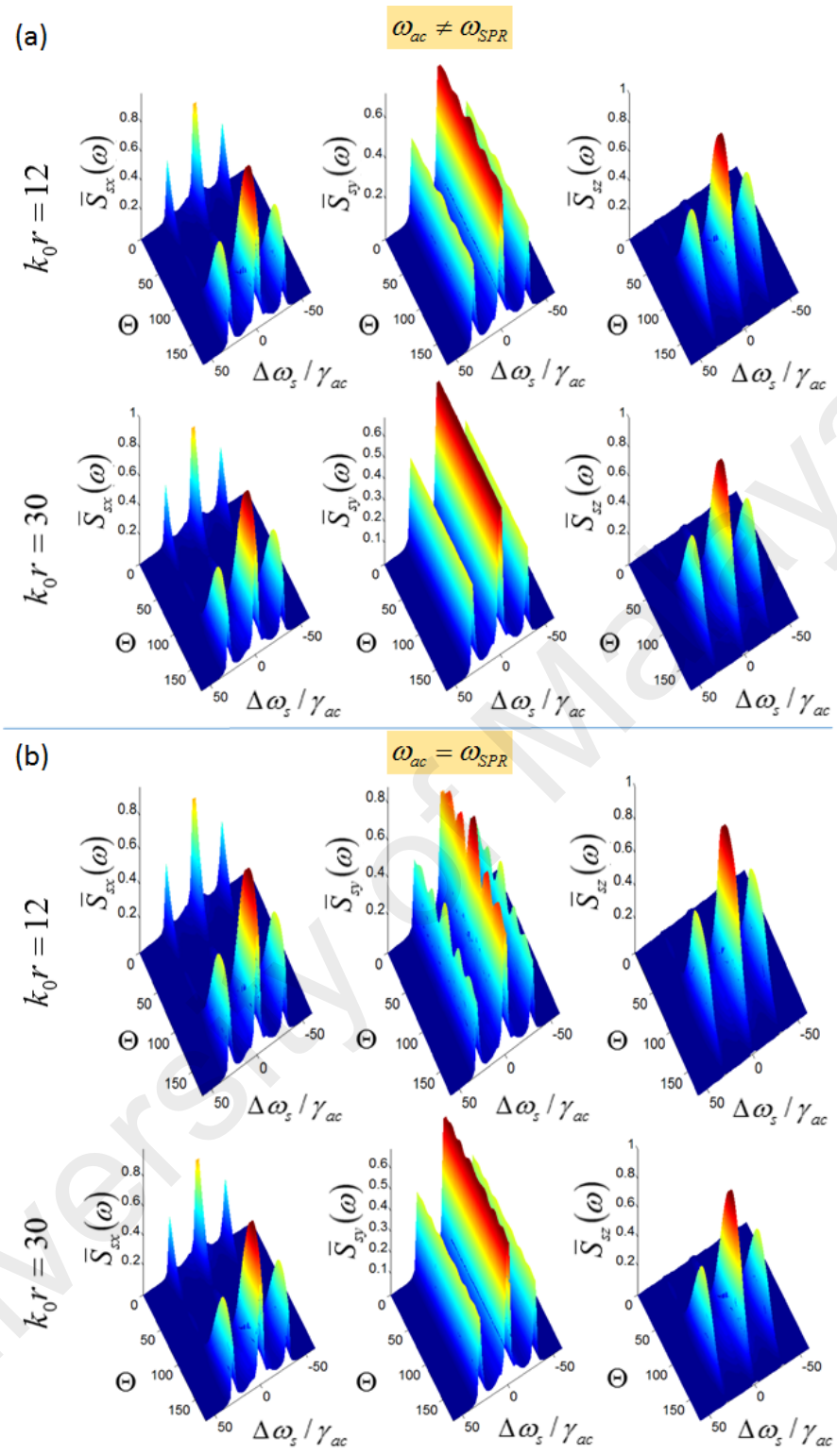

Figure 6.19: Angular Θ−dependence: Stokes spectra versus Θ for the case of strong symmetric pump and control laser fields ($\Omega_p = \Omega_c = 15\gamma_{ac}$) with initial condition $\bar{\rho}_{bb}(0) = \bar{\rho}_{cc}(0) = 0.5$ at two different interparticle distances $k_0 r = 12$ and 30. We compare between the spectra for the case with SPR ($\omega_{ac} = \omega_{SPR}$) and the case without SPR ($\omega_{ac} \neq \omega_{SPR}$). The metallic nanoparticle radius considered here is $a = 70$ nm. All other parameters are the same as in Figure 6.9.

the presence of MP is causing the oscillations in the $z-$component spectra, despite being perpendicular to the plane of Φ rotation ($x-y$ plane of observation). This shows that the influence of MP breaks the azimuthal rotational symmetry. At large $k_0 r$, the interference across Φ on the $x-y$ plane becomes insignificant, i.e. the angular Φ dependence ceases for the $z-$component field because the MP is too far from the QS to exert any significant influence on the fields scattered from the QS. Notice that the x-component spectra vanishes at $\Phi = 0^0, 180^0$ (peaks at $\Phi = 90^0$ and 270^0) due to the transversality of the fields.

Similar argument can be used to explain the results in Figure 6.19 when we set $\Phi = 0^0$ ($x-z$ plane) and allow the spectra to vary with Θ. This time, it is the y-component spectra that is supposed to show invariance across Θ because the y-component field, whose angular dependence lies in the terms in the second row of matrix P^I loses its dependence on Θ since at $\Phi = 0^0, n_{I,y} = 0$. However, at small $k_0 r$, the y-component field shows angular dependence on Θ with maximum around $\Theta = 180^0$ as the influence of the MP has broken the Θ rotational symmetry. As r increases, the MP loses its influence on the QS and thus the $y-$component spectra shows invariance across Θ (absence of oscillations) due to Θ rotational symmetry, as it is perpendicular to the $x-z$ plane of observation. Here, the z-component vanishes at $\Theta = 0^0$ and 180^0. Our simulations (not shown here) also reveal that when we set $\Phi = 90^0$ ($y-z$ plane), it is the $x-$component spectra that is invariant across Θ at large r.

One can also observe in Figures 6.18(b) and 6.19(b) that when the SPR condition is fulfilled ($\omega_{ac} = \omega_{SPR}$), the oscillations of the $z-$component spectra across Φ in Figure 6.18(b) and the $y-$component spectra across Θ in Figure 6.19(b) become stronger, indicating stronger directional dependence of the spectra. This is again due to the plasmonic enhancement of the local quantum fields caused by the MP, thus leading to stronger interference effect which manifests itself in the form of oscillations across the observation

angles. Moreover, a closer look at Figures 6.18(b) and 6.19(b) also tells us that the angular dependence of the spectra under SPR condition is visible up to large interparticle distance, i.e. $k_0 r = 30$, as can be observed in the small oscillations of the $z-$component spectral peaks in Figure 6.18(b) and the $y-$component spectral peaks in Figure 6.19(b). This shows the long-range influence of the plasmonic enhancement of MP on the QS which is not found in cases without SPR.

The magnitudes of the spectra in Figures 6.18 and 6.19 may at first seem contradictory to the results in Figures 6.9-6.14 but careful analysis shows that there is no contradiction at all. In Figure 6.12, the magnitude of the $x-$ and $y-$component Stokes spectra for the case of symmetric strong pump and control laser fields at $\Theta = \Phi = 0^0$ is about 40 times larger than the magnitude of the $z-$component spectra. This is actually in agreement with the results in Fig. 6.19 (with $\Phi = 0$) where the highest magnitude of the $x-$ and $y-$component Stokes spectra at $\Theta = 0^0$ is around 0.8, which is also about 40 times larger than the highest magnitude of the $z-$component spectra (estimated to be ~ 0.02 and $0.02 \times 40 = 0.8$). Also, take note that the magnitudes shown in the figures are not absolute values of the spectra but values relative to the normalized $z-$component spectra as explained in the first paragraph of this section. This provides an explanation for the magnitudes of all the three components of the spectra in Figures 6.18 and 6.19 which attain highest values of ~ 1: that the magnitudes of the highest peaks in all three components are comparable. To see the reason behind this let's focus on the Stokes spectra (for the case $k_0 r = 30$ and $\omega_{ac} \neq \omega_{SPR}$) in Figure 6.18, where $\Theta = 90^0$. It can be seen that the $x-$ and $z-$component spectra are maximum at the angle $\Phi = 90^0$ due to the vanishing $B(R, \omega)$ in Equation 4.14 (as a result of $n_{I,x} = n_{I,z} = 0, n_{I,y} \neq 0$) whereas the $y-$component spectra is minimum at this angular position (due to the nonvanishing $B(R, \omega)$). On the other hand, at $\Phi = 180^0$, where $n_{I,y} = n_{I,z} = 0, n_{I,x} \neq 0$, it is the $y-$ and $z-$component spectra that are maximum and the

$x-$component spectra becomes minimum, also due to the vanishing and nonvanishing of $B(R,\omega)$, respectively. Since each component achieves maximum value at certain values of Φ by similar factor, i.e. vanishing $B(R,\omega)$, it comes as no surprise that the highest peaks in each component of the Stokes spectra are comparable in magnitude. This leads to the ~ 1 peaks magnitude of all three components of the spectra in Figure 6.18. Similar reasoning can be applied to explain the maximum magnitude of all three components of the spectra in Figure 6.19.

6.2.7 Effects of Number Density

As mentioned in the second paragraph of this section the collective effect is ignored in Figures 6.9-6.16 and Figures 6.18 and 6.19 where the value of number density $N = 2.52 \times 10^{25}\mathrm{m}^{-3}$ is used. In this subsection, the variation of the spectra across different number densities beyond the range $2.39 \times 10^{23}\ \mathrm{m}^{-3} < N < 5.01 \times 10^{25}\ \mathrm{m}^{-3}$ will be studied. To do so there is a need to include the collective effect between the atoms in the QS by replacing the spontaneous emission rates $\Gamma_x\,(x = ab, ac, db.dc)$ in Appendix C by the *collective spontaneous emission rates* Γ'_x given by (Ficek & Tanaś, 2002)

$$\Gamma'_x = \Gamma_x F_x\left(k_x r_{ij}\right), \tag{6.4}$$

where

$$F_x\left(k_x r_{ij}\right) = \frac{3}{2}\left\{\left[1-\left(\bar{\mu}\cdot\bar{r}_{ij}\right)^2\right]\frac{\sin\left(k_x r_{ij}\right)}{k_x r_{ij}} + \left[1-3\left(\bar{\mu}\cdot\bar{r}_{ij}\right)^2\right]\left[\frac{\cos\left(k_x r_{ij}\right)}{\left(k_x r_{ij}\right)^2} - \frac{\sin\left(k_x r_{ij}\right)}{\left(k_x r_{ij}\right)^3}\right]\right\}. \tag{6.5}$$

Here, $k_x = \omega_x/c$ and $r_{ij} = N^{-1/3}$ is the distance between the ith and jth atom (interatomic distance). Figure 6.8(a) shows the dependence of F_{ac} on dipole orientation and number density. Unlike Ω_{ij}, F_{ac} remain constant at maximum value in the range of number

densities 10^{22} m^{-3} $< N <$ 10^{28} m^{-3} and decreases dramatically at low number densities $N < 10^{22}$ m^{-3}. Interesting feature of F_{ac} can only be found in Figure 6.8(b) where the dependence of F_{ac} on the interatomic distance r_{ij} is studied for three different cases of dipole moment: $\bar{\mu} \cdot \bar{r}_{ij} = 1/\sqrt{2}$, $\bar{\mu} \cdot \bar{r}_{ij} = 0$ and $\bar{\mu} \cdot \bar{r}_{ij} = 1$. It can be observed from Figure 6.8(b) that the collective spontaneous emission rate exhibits strong oscillations at small interatomic distances (due to collective dipole-dipole interactions between atoms) and undergoes damping with the increase in interatomic distance, just like Ω_{ij}. It also shows the same dependence on dipole moment orientation as Ω_{ij} in this figure.

In Figure 6.17 where the dependence of the spectra on the number density is studied, heavy hole exciton is assumed in the QS which gives the value $\left(\bar{\mu} \cdot \bar{r}_{ij}\right)^2 = 1/2$ (Abdussalam & Machnikowski, 2012). A larger size of QS is also considered so that the minimum number density can be lowered down to 10^{20} m^{-3}. It is assumed that the radius of the QS is $b = 134$ nm so that the entire QS volume contains at least one atom at the minimum number density of $N = 10^{20}$ m^{-3}. This value of b still fulfills the condition for the validity of dipole approximation $\lambda >> b$ whereas the condition $r >> b$ is fulfilled by setting $k_0 r = 25$ in Figure 6.17, which corresponds to $r \simeq 2268$ nm.

It is shown in Figure 6.17 for the case of strong symmetric laser fields without SPR the variation of the x-component Stokes spectra across the range of number densities 10^{20} m^{-3} $< N <$ 10^{28} m^{-3}. One may observe from Figure 6.17 that the Mollow triplets become sharper and narrower at higher number density. This is due to the collective effect which induces stronger ac Stark shifts on the Stokes and anti-Stokes transition levels. On the other hand, the higher and broader peaks at lower number density shows higher efficiency of the photon emission and broader spectral widths of the emitted photons. The spectral position of the peaks do not change with number densities and similar features are found in all other cases of laser fields strengths. Our results (not shown here) also show that

the presence of SPR does not affect the variation of the spectra across different number densities.

6.3 Comparison Between the Two Cases

It is interesting to compare the spectra discussed in section 6.1 with those mentioned in section 6.2. The spectra in section 6.1 are for the case where the finite size of the source particle (mesoscopic spherical particle) is taken into account and the MP is absent. In contrast, the spectra discussed in section 6.2 are for the case where the QS is assumed to be a point-like particle and it is interacting with a nearby MP. Any distinction between the spectra for the two cases is due to either the mesoscopic nature of the particle or the plasmonic effects caused by the MP or both.

Unfortunately, direct comparison cannot be made for most of the spectra due to the different parameters involved. For example, the spectra in Figure 6.1 and Figures 6.3 and 6.4 are plotted with respect to the particle size ρ whereas the spectra in Figure 6.9 and Figures 6.15-6.15 are plotted with respect to the interparticle distance $k_0 r$. However, one can still compare between the Stokes spectra in Figure 6.5(b) and the Stokes spectra in Figure 6.19 as both spectra are plotted with respect to the same parameter, Θ. The first distinction is in the side peaks of the spectra for the mesoscopic particle (Figure 6.5(b)) which are higher than the central peak while the same is not true in the spectra in Figure 6.19 for all cases. This is likely due to the focusing effect caused by the mesoscopic nature of the particle which suppresses the central peak. This feature is absent in the MP-QS hybrid nanostructure where we assume the QS to be point-like. The second distinction is in the occurrence of significant spectral peak in the $x-$ and $y-$component Stokes spectra in Figure 6.19 which is absent in the corresponding spectra in Figure 6.5(b). This peak is due to the presence of a nearby MP which contributes to additional scattered fields at around $\Theta = 0^0$. The third distinction is the absence of oscillation across Θ in the

$y-$component Stokes spectra in Figure 6.5(b) which is present in Figure 6.19 (for the case $k_0 r = 12$). As explained in subsection 6.2.5, this oscillatory dependence is due to the plasmonic effects caused by the nearby MP which breaks the $\Theta-$rotational symmetry.

Another interesting comparison that can be made is between the profile of the spectra across the frequency range for the two cases at specific ρ (for the case in section 6.1) or specific $k_0 r$ (for the case in section 6.2). For this comparison readers should refer mainly to the spectra in Figure 6.3(b) (at smallest ρ) and the spectra in Figure 6.14 for the case $\Omega_p = \Omega_c = 10\gamma_{ac}$. Both the Stokes and anti-Stokes spectra in Figure 6.3(b) actually resemble those obtained for single atom case. One can clearly observe that the only distinction here is the presence of Fano dip in the central peak of the spectra in Figure 6.14 and the occurrence of additional peaks between the central peak and the two side peaks. Both of these features has been explained in subsection 6.2.1 as phenomena due to the enhanced quantum fields as well as the additional ac Stark shifts induced by the plasmon-enhanced quantum fields, respectively.

In summary, the optical properties of two types of quantum systems: (i) A mesoscopic spherical particle composed of double Raman atoms and (ii) A hybrid nanostructure consisting of a double Raman QS and a MP have been studied. In particular, the dependence of the Stokes and anti-Stokes spectra from the two systems on various parameters has been discussed and the explanation for the underlying physical mechanisms has been provided. It is found that the spectra obtained for both systems are dramatically different due to either the mesoscopic nature of the microparticle or the plasmonic effects caused by the nearby MP. Conclusion of the results will be provided in the following chapter.

CHAPTER 7: CONCLUSION

In conclusion, the optical properties of a hybrid nanostructure comprising of a plasmonic metallic nanoparticle (MP) and a quantum system (QS) in four-level double Raman configuration from the spectra of the quantum fields emitted have been studied. A semiclassical approach is adopted in analyzing the MP-QS interaction in which the MP is treated as a classical dielectric spherical particle whereas the QS is treated quantum-mechanically using quantum Langevin formalism with noise operators. Local fields enhancement due to the MP which manifests itself as a Fano dip in the central peak of the spectra is observed, indicating Stokes and anti-Stokes fields strengths that are comparable to or greater than the incident laser fields. The long-range MP-QS interaction also results in cavity interference effect where oscillations of the spectral peaks across interparticle distances are observed, indicating interference of the quantum fields from both particles. Such oscillations experience damping with the increase in interparticle distance as the plasmonic effects due to the MP becoming weaker. The results show that the spectra for single particle without the presence of MP can only be reproduced at sufficiently large interparticle distance, i.e. $k_0 r > 50$. Furthermore, the quantum spectra are sensitive to the observation angles Θ and Φ where oscillatory behaviour is observed and some component will become dominant depending on the the observation angles. The limit of long-range interaction may be inferred from the point where the transversality of the fields no longer applies in the spectra versus angles for the three field components. The oscillatory dependence of the spectra on the interparticle distance and observation angles becomes even more significant in the presence of surface plasmon resonance, where the plasmonic field enhancement effect is at maximum. Finally, the results show that due to collective effects among the atoms, higher number density leads

to stronger enhancement of the quantum fields. It is expected that the findings of this work will have implications on the development of nanostructured devices capable of controlling light-matter interaction at the nanoscale, particularly those with potential applications in spectroscopy of nanomaterials and generation of nonclassical photons for quantum information processing. Possible extensions of this work include the study of a QS placed in the gap of metallic nanoparticle dimer (Nordlander et al., 2004; Savasta et al., 2010b; Wu et al., 2010), computation of Glauber's two-photon correlations $G^{(2)}$, and fully quantum-mechanical treatment of similar MP-QS interaction system.

REFERENCES

Abdussalam, W., & Machnikowski, P. (2012). Collective spontaneous emission from a system of quantum dots. *Acta Physica Polonica A, 122*(6), 994-996.

Agarwal, G. S., & ONeil, S. V. (1983). Effect of hydrodynamic dispersion of the metal on surface plasmons and surface-enhanced phenomena in spherical geometries. *Physical Review B, 28*(2), 487-493.

Alivisatos, P. (2004). The use of nanocrystals in biological detection. *Nature Biotechnology, 22*, 47-52.

Alvarez-Puebla, R., Liz-Marzán, L. M., & de Abajo, F. J. G. (2010). Light concentration at the nanometer scale. *Journal of Physical Chemistry Letters, 1*(16), 2428-2434.

André, A., Duan, L.-M., & Lukin, M. D. (2002). Coherent atom interactions mediated by dark-state polaritons. *Physical Review Letters, 88*, 243602(1-4).

Andrews, D., Scholes, G., & Wiederrecht, G. (2010). *Comprehensive nanoscience and technology*. United Kingdom: Academic Press.

Angelini, I., Artioli, G., Bellintani, P., Diella, V., Gemmi, M., Polla, A., & Rossi, A. (2004). Chemical analyses of bronze age glasses from frattesina di rovigo, northern italy. *Journal of Archaeological Science, 31*(8), 1175 -1184.

Artuso, R. D., & Bryant, G. W. (2008). Optical response of strongly coupled quantum dot-metal nanoparticle systems: Double peaked fano structure and bistability. *Nano Letters, 8*(7), 2106-2111.

Artuso, R. D., & Bryant, G. W. (2010, Nov). Strongly coupled quantum dot-metal nanoparticle systems: Exciton-induced transparency, discontinuous response, and suppression as driven quantum oscillator effects. *Physical Review B, 82*, 195419 (1-10).

Balić, V., Braje, D. A., Kolchin, P., Yin, G. Y., & Harris, S. E. (2005). Generation of paired photons with controllable waveforms. *Physical Review Letters, 94*, 183601 (1-4).

Benkert, C., Scully, M. O., Bergou, J., Davidovich, L., Hillery, M., & Orszag, M. (1990). Role of pumping statistics in laser dynamics: Quantum langevin approach. *Physical Review A, 41*, 2756–2765.

Bennett, C. H., & Shor, P. W. (1998). Quantum information theory. *IEEE Transactionson Information Theory, 44*(6), 2724-2742.

Berman, P. R., & Malinovsky, V. S. (2011). *Principles of laser spectroscopy and quantum optics*. New Jersey: Princeton University Press.

Bharadwaj, P., Deutsch, B., & Novotny, L. (2009). Optical antennas. *Advances in Optics and Photonics, 1*(3), 438-483.

Bohren, C. F., & Huffman, D. R. (1983). *Absorption and scattering of light by small particles*. New York: Wiley.

Boyer, D., Tamarat, P., Maali, A., Lounis, B., & Orrit, M. (2002). Photothermal imaging of nanometer-sized metal particles among scatterers. *Science, 297*(5584), 1160–1163.

Chang, D. E., Sørensen, A. S., Demler, E. A., & Lukin, M. D. (2007). A single-photon transistor using nanoscale surface plasmons. *Nature Physics, 3*, 807-812.

Chou, C. W., Polyakov, S. V., Kuzmich, A., & Kimble, H. J. (2004). Single-photon generation from stored excitation in an atomic ensemble. *Physical Review Letters, 92*, 213601(1-4).

Cohen-Tannoudji, C., & Reynaud, S. (1977). Dressed-atom description of resonance fluorescence and absorption spectra of a multi-level atom in an intense laser beam. *Journal of Physics B: Atomic and Molecular Physics, 10*, 345-363.

Finkelstein-Shapiro, D., Calatayud, M., Atabek, O., Mujia, V., & Keller, A. (2016). Nonlinear Fano interferences in open quantum systems: An exactly solvable model. *Physical Review A, 93*, 063414(1-8).

Dasgupta, B. B., & Fuchs, R. (1981). Polarizibility of a small sphere including nonlocal effects. *Physical Review B, 24*(2), 554-561.

David, C., & de Abajo, F. J. G. (2011). Spatial nonlocality in the optical response of metal nanoparticles. *The Journal of Physical Chemistry C, 115*(40), 19470–19475

Davis, T. J., Gómez, D. E., & Vernon, K. C. (2010). Interaction of molecules with localized surface plasmons in metallic nanoparticles. *Physical Review B, 81*, 045432(1-11).

de Abajo, F. J. G. (2008). Nonlocal effects in the plasmons of strongly interacting nanoparticles, dimers and waveguides. *The Journal of Physical Chemistry C, 112*, 17983-17987.

Derkachova, A., Kolwas, K., & Demchenko, I. (2015). Dielectric function for gold in plasmonics applications: Size dependence of plasmon resonance frequencies and damping rates for nanospheres. *Plasmonics, 11*, 941-951.

Engheta, N. (2007). Circuits with light at nanoscales: Optical nanocircuits inspired by metamaterials. *Science, 317*, 1698-1702.

Fano, U. (1961). Effects of configuration interaction on intensities and phase shifts. *Physical Review, 124*, 1866–1878.

Félidj, N., Aubard, J., Lévi, G., Krenn, J. R., Salerno, M., Schider, G., Lamprecht, B., Leitner, A., Aussenegg, F. R. (2002). Controlling the optical response of regular arrays of gold particles for surface-enhanced raman scattering. *Physical Review B, 65*, 075419(1-9).

Fetter, A. L. (1973). Electrodynamics of a layered electron gas. I. single layer. *Annals of Physics, 81*(2), 367-393.

Ficek, Z., & Tanas, R. (2002). Entangled states and collective nonclassical effects in two atom systems. *Physics Reports, 372*(5), 369 - 443.

Fleischhauer, M., & Lukin, M. D. (2002). Quantum memory for photons: Dark-state polaritons. *Physical Review A, 65*, 022314(1-12).

Fox, M. (2006). Quantum optics, an introduction. New York: Oxford University Press.

Fuchs, R., & Claro, F. (1987). Multipolar response of small metallic sphere: Nonlocal theory. *Physical Review B, 35*(8), 3722-3727.

Gall, D. (2016). Electron mean free path in elemental metals. *Journal of Applied Physics, 119*, 085101(1-5).

Gantzounis, G., & Stefanou, N. (2006). Cavity-plasmon waveguides: Multiple scattering calculations of dispersion in weakly coupled dielectric nanocavities in a metallic host material. *Physical Review B, 74*, 085102(1-6).

Genet, C., & Ebbesen, T. W. (2007). Light in tiny holes. *Nature, 445*, 39-46.

Glauber, R. J. (1963). The quantum theory of optical coherence. *Physical Review, 130*, 2529–2539.

Govorov, A. O. (2010). Semiconductor-metal nanoparticle molecules in a magnetic field: Spin-plasmon and exciton-plasmon interactions. *Physical Review B, 82*, 155322(1-11).

Govorov, A. O., Bryant, G.W., Zhang, W., Skeini, T., Lee, J., Kotov, N. A., Slocik, J. M., & Naik, R. R. (2006). Exciton-plasmon interaction and hybrid excitons in semiconductore-metal nanoparticle assemblies. *Nano Letters, 6*(5), 984-994.

Govorov, A. O., & Carmeli, I. (2007). Hybrid structures composed of photosynthetic system and metal nanoparticles: Plasmon enhancement effect. *Nano Letters, 7*(3), 620-625.

Hammerer, K., Sørensen, A. S., & Polzik, E. S. (2010). Quantum interface between light and atomic ensembles. *Reviews of Modern Physics, 82*, 1041–1093.

Hövel, H., Fritz, S., Hilger, A., Kreibig, U., & Vollmer, M. (1993). Width of cluster plasmon resonances: Bulk dielectric functions and chemical interface damping. *Physical Review B, 48*, 18178–18188.

Huver, S. D., Wildfeuer, C. F., & Dowling, J. P. (2008). Entangled fock states for robust quantum optical metrology, imaging, and sensing. *Physical Review A, 78*, 063828(1-5).

Jackson, J. D. (1999). *Classical electrodynamics.* New York: Wiley.

Jiang, W., Han, C., Xue, P., Duan, L.-M., & Guo, G.-C. (2004). Nonclassical photon pairs generated from a room-temperature atomic ensemble. *Physical Review A, 69*, 043819(1-5).

Khlebtsov, B. N., & Khlebtsov, N. G. (2007). Biosensing potential of silica/gold nanoshells: Sensitivity of plasmon resonance to the local dielectric environment. *Journal of Quantitative Spectroscopy and Radiative Transfer, 106*(1–3), 154-169.

Khlebtsov, N. G., Bogatyrev, V. A., Dykman, L. A., & Melnikov, A. G. (1996). Spectral extinction of colloidal gold and its biospecific conjugates. *Journal of Colloid and Interface Science, 180*(2), 436-445.

Kim, S., Jin, J., Kim, Y.-J., Park, I.-Y., Kim, Y., & Kim, S.-W. (2008). High-harmonic generation by resonant plasmon field enhancement. *Nature, 453*, 757-760.

Kolchin, P., Du, S., Belthangady, C., Yin, G.Y., & Harris, S. E. (2006). Generation of narrow-bandwidth paired photons: Use of a single driving laser. *Physical Review Letters*, *97*, 113602(1-4).

Kosionis, S. G., Terzis, A. F., Sadeghi, S. M., & Paspalakis, E. (2013). Optical response of a quantum dot–metal nanoparticle hybrid interacting with a weak probe field. *Journal of Physics: Condensed Matter*, *25*(4), 045304(1-10).

Kosionis, S. G., Terzis, A. F., Yannopapas, V., & Paspalakis, E. (2012). Nonlocal effects in energy absorption of coupled quantum dot–metal nanoparticle systems. *The Journal of Physical Chemistry C, 116*(44), 23663-23670.

Kozhekin, A. E., Mølmer, K., & Polzik, E. (2000). Quantum memory for light. *Physical Review A, 62*, 033809(1-5).

Kumar, C. S. S. R. (2013). *Uv-vis and photoluminescence spectroscopy for nanomaterials characterization.* Berlin: Springer-Verlag Berlin Heidelberg.

Kurtsiefer, C., Oberparleiter, M., & Weinfurter, H. (2001). Generation of correlated photon pairs in type-ii parametric down conversion—revisited. *Journal of Modern Optics, 48*(13), 1997-2007.

Kuzmich, A., Bowen, W. P., Boozer, A. D., Boca, A., Chou, C. W., Duan, L.-M., & Kimble, H. J. (2003). Generation of nonclassical photon pairs for scalable quantum communication with atomic ensembles. *Nature, 423*, 731-734.

Li, J. F., Huang, Y. F., Ding, Y., Yang, Z. L., Li, S. B., Zhou, X. S., Fan, F. R., Zhang, W., Zhou, Z. Y., Wu, D. Y., Ren, B., Wang, Z. L., & Tian, Z. Q. (2010). Shell-isolated nanoparticle-enhanced raman spectroscopy. *Nature, 464*, 392-395.

Lia, Z., Cao, D.-Z., & Wang, K. (2005). Manipulating synchronous optical signal with a double-Λ atomic ensemble. *Physics Letters A, 341*(5-6), 366-370.

Lukin, M. D., Hemmer, P. R., Löffler, M., & Scully, M. O. (1998). Resonant enhancement of parametric processes via radiative interference and induced coherence. *Physical Review Letters, 81*, 2675–2678.

Lukin, M. D., Matsko, A. B., Fleischhauer, M., & Scully, M. O. (1999). Quantum noise and correlations in resonantly enhanced wave mixing based on atomic coherence. *Physical Review Letters, 82*, 1847–1850.

Maier, S. A. (2007). *Plasmonics: Fundamentals and applications.* New York: Springer Science+Business Media LLC.

Maier, S. A., & Atwater, H. A. (2005). Plasmonics: Localization and guiding of electromagnetic energy in metal/dielectric structures. *Journal of Applied Physics, 98*, 011101(1-10).

Malyshev, A. V., & Malyshev, V. A. (2011). Optical bistability and hysteresis of a hybrid metal-semiconductor nanodimer. *Physical Review B, 84*, 035314(1-6).

Mandel, L. (1966). Antinormally ordered correlations and quantum counters. *Physical Review, 152*, 438–451.

Manjavacas, A., de Abajo, F. J. G., & Nordlander, P. (2011). Quantum plexcitonics: Strongly interacting plasmons and excitons. *Nano Letters, 11*(6), 2318-2323.

Matsudaa, K., Ito, Y., & Kanemitsu, Y. (2008). Photoluminescence enhancement and quenching of single CdSe/ZnS nanocrystals on metal surfaces dominated by plasmon resonant energy transfer. *Applied Physics Letters, 92*, 211911(1-10).

McMahon, J. M., Gray, S. K., & Schatz, G. C. (2010). Calculating nonlocal optical properties of structures with arbitrary shape. *Physical Review B, 82*, 035423(1-12).

Meier, M., & Wokaun, A. (1983). Enhanced fields on large metal particles: Dynamic depolarization. *Optics Letters, 8*(11), 581–583.

Moiseev, S. A., & Ham, B. S. (2005). Generation of entangled lights with temporally reversed photon wave packets. *Physical Review A, 71*, 053802(1-7).

Mollow, B. R. (1969). Power Spectrum of Light Scattered by two-level systems. *Physical Review, 188*, 1969-1975.

Moroz, A. (2009). Depolarization field of spheroidal particles. *Journal of the Optical Society of America B, 26*(3), 517–527.

Mühlschlegel, P., Eisler, H.-J., Martin, O. J. F., Hecht, B., & Pohl, D.W. (2005). Resonant optical antennas. *Science, 308*(5728), 1607-1609.

Noginov, M. A., Zhu, G., Belgrave, A. M., Bakker, R., Shalaev, V. M., Narimanov, E. E., Stout, S., Herz, E., Suteewong, T., & Wiesner, U. (2009). Demonstration of a spaser-based nanolaser. *Nature, 460*, 1110-1112.

Nordlander, P.,&Avouris, P. (1986). Structure of adsorbate inverse photoemission spectra: A model hamiltonian study. *Surface Science Letters, 177*(2), L1004-L1010.

Nordlander, P., Oubre, C., Prodan, E., Li, K., & Stockman, M. I. (2004). Plasmon hybridization in nanoparticle dimers. *Nano Letters, 4*(5), 899-903.

Novotny, L., & Hecht, B. (2006). *Principles of nano-optics*. United Kingdom: Cambridge University Press.

Ooi, C. H. R. (2007a). Continuous source of phase-controlled entangled two photon laser. *Physical Review A, 76*, 013809(1-7).

Ooi, C. H. R. (2007b). Quenching the collective effects on the two-photon correlation from two double-raman atoms. *Physical Review A, 75*, 043817(1-6).

Ooi, C. H. R., Beadie, G., Kattawar, G. W., Reintjes, J. F., Rostovtsev, Y., Zubairy, M. S., & Scully, M. O. (2005). Theory of femtosecond coherent anti-stokes raman backscattering enhanced by quantum coherence for standoff detection of bacterial spores. *Physical Review A, 72*, 023807(1-13).

Ooi, C. H. R., Kim, B.-G., & Lee, H.-W. (2007). Coherent effects on two-photon correlation and directional emission of two two-level atoms. *Physical Review A, 75*, 063801(1-14).

Ooi, C. H. R., & Lan, B. L. (2010). Intense nonclassical light: Controllable two-photon talbot effect. *Physical Review A, 81*, 063832(1-7).

Ooi, C. H. R., Sun, Q., Zubairy, M. S., & Scully, M. O. (2007). Correlation of photon pairs from the double raman amplifier: Generalized analytical quantum langevin theory. *Physical Review A, 75*, 013820(1-13).

Ooi, C. H. R., & Tan, K. S. (2013). Controlling double quantum coherence and electromagnetic induced transparency with plasmonic metallic nanoparticle. *Plasmonics, 8*(2), 891–898.

Ozbay, E. (2006). Plasmonics: Merging photonics and electronics at nanoscale dimensions. *Science, 311*(5758), 189-193.

Palombaa, S., Novotnyb, L., & Palmera, R. (2008). Blue-shifted plasmon resonance of individual size-selected gold nanoparticles. *Optics Communications, 281*(3), 480-483.

Patnaik, A. K., Agarwal, G. S., Ooi, C. H. R., & Scully, M. O. (2005). Quantum correlations between a pair of raman photons from a single atom under arbitrary excitation condition. *Physical Review A, 72,* 043811(1-5).

Perkins, D. H. (2000). *Introduction to high energy physics.* United Kingdom: Cambridge University Press.

Pike, E. R., & Swain, S. (1971). A general approach to nonequilibrium quantum statistics. *Journal of Physics A: General Physics, 4*(4), 555-563.

Pons, T., Medintz, I. L., Sapsford, K. E., Higashiya, S., Grimes, A. F., English, D. S., & Mattoussi, H. (2007). On the quenching of semiconductor quantum dot photoluminescence by proximal gold nanoparticles. *Nano Letters, 7*(10), 3157-3164.

Puri, R. R. (2001). *Mathematical methods of quantum optics.* Berlin: Springer.

Ridolfo, A., Di Stefano, O., Fina, N., Saija, R., & Savasta, S. (2010). Quantum plasmonics with quantum dot-metal nanoparticle molecules: Influence of the fano effect on photon statistics. *Physical Review Letters, 105*, 263601(1-4).

Rindzevicius, T., Alaverdyan, Y., Dahlin, A., Höök, F., Sutherland, D. S., & Käll, M. (2005). Plasmonic sensing characteristics of single nanometric holes. *Nano Letters, 5*(11), 2335-2339.

Sadeghi, S. M. (2009). The inhibition of optical excitations and enhancement of rabi flopping in hybrid quantum dot–metallic nanoparticle systems. *Nanotechnology, 20*(22), 225401(1-6).

Sadeghi, S. M. (2010). Coherent control of metallic nanoparticles near fields: Nanopulse controllers and functional nanoamplifiers. *Physical Review B, 82*, 035413(1-7).

Sargent, M., Scully, M. O., & Lamb, W. E. (1974). *Laser physics*. London: Addison-Wesley Publishing Company.

Savasta, S., Saija, R., Ridolfo, A., Stefano, O. D., Denti, P., & Borghese, F. (2010a). Nanopolaritons: Vacuum rabi splitting with a single quantum dot in the center of a dimer nanoantenna. *ACS Nano, 4*(11), 6369-6376.

Scully, M. O. (Ed.). (1994). *Proceedings of the conference on effects of atomic coherence and interference in quantum optics, Crested Butte, Colorado, 1993.*

Scully, M. O., & Drühl, K. (1982). Quantum eraser: A proposed photon correlation experiment concerning observation and "delayed choice" in quantum mechanics. *Physical Review A, 25*, 2208–2213.

Scully, M. O.,&Ooi, C. H. R. (2004). Improving quantum microscopy and lithography via raman photon pairs: II. analysis. *Journal of Optics B: Quantum and Semiclassical Optics, 6*(8), S816(1-4).

Scully, M. O., & Zubairy, M. S. (1997). *Quantum optics*. Cambridge: Cambridge University Press.

Shimizu, K. T., Woo, W. K., Fisher, B. R., Eisler, H. J., & Bawendi, M. G. (2002). Surface-enhanced emission from single semiconductor nanocrystals. *Physical Review Letters, 89*, 117401(1-4).

Talley, C. E., Jackson, J. B., Oubre, C., Grady, N. K., Hollars, C. W., Lane, S. M., Huser, T. R., Nordlander, P., & Halas, N. J. (2005). Surface-enhanced raman scattering from individual Au nanoparticles and nanoparticle dimer substrates. *Nano Letters, 5*(8), 1569-1574.

Taminiau, T. H., Stefani, F. D., Segerink, F. B., & van Hulst, N. F. (2008). Optical antennas direct single-molecule emission. *Nature Photonics, 2*, 234-237.

Theiss, J., Pavaskar, P., Echternach, P. M., Muller, R. E., & Cronin, S. B. (2010). Plasmonic nanoparticle arrays with nanometer separation for high-performance lasers substrates. *Nano Letters, 10*(8), 2749-2754.

Tsukada, M., & Brenig, W. (1985). Theory of optical excitation of adsorbed rare gas atoms. *Surface Science, 151*(2-3), 503-520.

van der Wal, C. H., Eisaman, M. D., André, A., Walsworth, R. L., Phillips, D. F., Zibrov,A. S., & Lukin, M. D. (2003). Atomic memory for correlated photon states. *Science, 301*(5630), 196-200.

Wu, L.-A., Xiao, M.,&Kimble, H. J. (1987). Squeezed states of light from an optical parametric oscillator. *Journal of the Optical Society of America B, 4*(10), 1465–1475.

Wu, X., Gray, S. K., & Pelton, M. (2010). Quantum-dot-induced transparency in a nanoscale plasmon resonator. *Optics Express, 18*(23), 23633-23645.

Xu, H., Bjerneld, E. J., Käll, M., & Börjesson, L. (1999). Spectroscopy of single hemoglobin molecules by surface enhanced raman scattering. *Physical Review Letters, 83*, 4357–4360.

Yamamoto, Y., & Imamoglu, A. (1999). *Mesoscopic quantum optics.* Canada: JohnWiley & Sons Inc.

Yan, J.-Y., Zhang, W., Duan, S., Zhao, X.-G., & Govorov, A. O. (2008). Optical properties of coupled metal-semiconductor and metal-molecule nanocrystal complexes: Role of multipole effects. *Physical Review B, 77*, 165301(1-9).

Yang, X.-X., Wu, X., & Wu, Y. (2005). Matched ultra slow optical solitons in double-Λ media. *Chinese Physics Letters, 22*(11), 2816-2821.

Yang, X.-X., & Wu, Y. (2005). Achieving an ultra-slowly propagating maximally entangled state of two light beams via four-wave mixing in a double-Λ system. *Journal of Optics B: Quantum and Semiclassical Optics, 7*(2), 54-56.

Yariv, A. (1989). *Quantum electronics.* Canada: John Wiley & Sons. Inc.

Zhang, W., & Govorov, A. O. (2011). Quantum theory of the nonlinear fano effect in hybrid metal-semiconductor nanostructures: The case of strong nonlinearity. *Physical Review B, 84*, 081405(1-5).

Zhang, W., Govorov, A. O., & Bryant, G. W. (2006). Semiconductor-metal nanoparticle molecules: Hybrid excitons and the nonlinear fano effect. *Physical Review Letters, 97*, 146804(1-4).

Zubarev, D. N. (1960). Double-time green functions in statistical physics. *Soviet Physics Uspekhi*, *3*(3), 320-345.

LIST OF PUBLICATIONS AND PAPERS PRESENTED

Loh, W. M. E., & Ooi, C. H. R. (2017). Quantum particle interacting with a metallic particle: Spectra from quantum langevin theory. *Physical Review A, 95*, 013836(1-20).

Ooi, C. H. R., **Loh, W. M. E.,** & Kam, C. H. (2015). Quantum spectra of raman photon pairs from a mesoscopic particle. *Physical Review A, 91*, 063826(1-12).